UNIVERSIDAD DE GRANADA

Doctoral Thesis

Development of 2D and 3D structures for millimeter-wave communications and future applications

---

Author:
Salvador Moreno Rodríguez

Thesis supervisors:
Dr. Carlos Molero Jiménez
Dr. Antonio Alex Amor

Department of Signal Theory, Telematics and Communications
University of Granada
Programa de Doctorado en Tecnologías de la Información y la Comunicación

Granada, Julio, 2024

Editor: Universidad de Granada. Tesis Doctorales
Autor: Salvador Moreno Rodríguez
ISBN: 978-84-1195-540-9
URI: https://hdl.handle.net/10481/97394

"Lo que hoy no se alcanza, mañana se pisa."
- Luis Donaldo Colosio

Preface

This is a collection of articles submitted in fulfillment of the requirements set by the University of Granada (Spain) to obtain the International PhD in the Doctoral Programme in Information and Communications Technologies. Dr. Carlos Molero Jiménez and Dr. Antonio Alex Amor supervised the research presented in this document. The research results were primarily developed at the University of Granada.

This thesis have been supported in part by the grant *PID2020-112545RB-C54* funded by MCIN/AEI/10.13039/50110001103, the grants *P18-RT-4830* and *A-TIC-608-UGR20* funded by Junta de Andalucía and ERDF A way of making Europe, and the grants *TED2021-129938B-I00* and *TSI-064100-2022-20* funded by MCIN/AEI/10.13039/501100011033 and by the European Union NextGenerationEU/PRTR.

Acknowledgements

Primero que todo, me gustaría agradecer y destacar la gran labor de mis directores, Carlos Molero y Antonio Alex, por su enorme generosidad, paciencia, humildad y dedicación desde que comencé este camino llamado Tesis. Gracias por enseñarme, exigirme y acompañarme en todo el proceso, así como por ayudarme a madurar y crecer tanto a nivel profesional como personal. No puedo olvidar a uno de mis directores del Trabajo Fin de Máster y mi otro gran mentor en esta etapa, Ángel Palomares, quien me introdujo en el mundo de la investigación y en el grupo SWAT de la Universidad de Granada. Este grupo, que gracias al esfuerzo de sus fundadores, Juan Francisco Valenzuela y Pablo Padilla, ha logrado posicionarse y darse a conocer a nivel nacional e internacional. No solo por su trabajo y dedicación diaria, sino también por el compañerismo y solidaridad que imponen a los integrantes una vez que entras en él. Gracias a esta filosofía de colaboración y no de competición, hemos avanzado juntos y vivido muy buenos momentos que han ayudado a hacer más liviana esta desafiante etapa. Gracias a todos los compañeros y amigos como Cleo, Alex, Nacho, Carmelo, Natalia, Migue, Sorah, Mario, Marcos, Andrés, Juane, Ginés, Sergio, Fran y a los profesionales con los que he trabajado durante estos cuatro intensos años.

Es inevitable que, después de estos diez años desde que comencé el Grado en Ingeniería de Tecnologías de la Telecomunicación en la UGR, me vengan a la mente los nombres de muchos de mis amigos y compañeros con los que compartí momentos y experiencias memorables en la carrera, como Gloria, Zapata, Adri, Ramos, Reda, Domo, Bailón, Yosape, Guzmán, Castillo, Ivanzu, Isi, Manu, Salcedo, Irigaray, Javi, Quiles y Clemen.

No podría dejar de agradecer a toda mi gente del Barrio de la Cruz por ser quienes siempre me han animado desde fuera y me han apoyado en los momentos más dificiles. Personas como Irene, Josi, Alberto, Víctor, Ismael, Rufi, Toni, Nacho, Gonzalo, Belmonte, Garrido, Ángel, Nano, Ramón, Jesús, Raúl, Carrillo, Urbano, Luis, Álvaro, Martínez, Rafa y todos con los que he compartido momentos inolvidables en mi vida fuera del ámbito profesional.

Pero, sin duda alguna, el mayor agradecimiento y dedicación es para mi familia y mi pareja, quienes realmente han confiado en mí y me han

apoyado siempre de manera incondicional dentro y fuera del trabajo. Me han educado, mantenido, aconsejado, soportado, consolado, esperado y, en definitiva, me han querido y cuidado durante todo este largo viaje. Gracias por el ejemplo de resiliencia que habeis demostrado a lo largo de vuestras vidas y por el que solo puedo mostrar mi más sincera admiración. Gracias por haberme impulsado a llegar hasta aquí.

Gracias a todos por ser parte de lo que soy.

"El trabajo en equipo es la habilidad de trabajar juntos hacia una visión común. La habilidad de dirigir logros individuales hacia objetivos organizacionales. Es el combustible que permite a gente común obtener resultados poco comunes."
- Andrew Carnegie

Abstract

Over the last few decades, the exponential growth of smart devices has drastically increased the demand for high-capacity communication links. The rapid increase in the data transmission, especially for streaming applications, has driven to the search for wireless links operating at higher frequencies. Consequently, the primary goal in current Fifth Generation (5G) and future Sixth Generation (6G) mobile networks is to utilize channels in the millimeter-wave bands (from 30 to 300 GHz) and even the sub-THz band (up to 1 THz) to achieve greater bandwidth and capacity in communication links.

However, at these frequencies, propagation losses in the channels and antenna directivity become more pronounced. In this context, *broadcasting*, where a single user sends information to multiple users, becomes challenging. Thus, new communication systems focusing on point-to-point links with beam-steering capabilities have emerged as promising solutions. Additionally, frequency mixing, which allows antennas to transmit information across different frequency bands (such as for telephony or geolocation), presents a viable alternative to design more efficient devices.

This Doctoral Thesis focuses on the development of radiating systems and metastructures that address these technological challenges. In particular, we research the use of periodically-modulated metamaterials to modify the properties of antennas in the millimeter-wave bands. We divide this extensive topic into three main categories: spatial modulations, time modulations and spacetime modulations. In each of them, we propose different devices that present interesting capabilities in the millimeter-wave bands.

On the one hand, concerning spatial modulations, we propose several passive metamaterials/metasurfaces, including: a Fresnel lens-antenna designed to enhance directivity and introduce beam-steering capabilities to a conventional waveguide at 60 GHz, and a metasurface for polarization control in reflection at K/Ka satellite bands. Additionally, we develop analytical frameworks based on Floquet-Bloch expansions of the electromagnetic fields and integral-equation methods to simulate these spatially-modulated metamaterials from a circuit-based perspective. Specifically, we use the circuit theory, previously applied to static spatial metasurfaces, in a 3D metadevice and a 2D metagrating loaded with lumped elements (diodes, resistors, capacitors and inductors).

On the other hand, regarding time modulations, we propose a theoretical framework to simulate a time-varying metasurface that alternates its electrical properties (air, metal and grating states). Due to the lack of commercial full-wave software to simulate this kind of devices in an efficient manner, this solution arises as a good alternative in this topic. Furthermore, we implement a finite-difference time-domain (FDTD) method to test the obtained analytical results.

These works lead to the development of a comprehensive theoretical tool for simulating spacetime-modulated metasurfaces. The proposed spacetime device demonstrates both beamforming and frequency mixing capabilities in the microwave bands, offering promising and intriguing features for future telecommunications systems.

Additionally, a setup for electromagnetic characterisation of materials is proposed with the aim of understanding the constitutive parameters of homogeneous dielectrics that can be useful for the design of metamaterials in the millimeter-wave bands.

Keywords: Metamaterials, metasurfaces, periodic structures, spatial modulation, temporal modulation, spacetime modulation, material characterization, telecommunications, beamforming, beam steering, frequency mixing, millimeter bands, FDTD.

Resumen

En las últimas décadas, el crecimiento exponencial de los dispositivos inteligentes ha aumentado drásticamente la demanda de enlaces de comunicación de alta capacidad. El rápido incremento en la transmisión de datos, especialmente para aplicaciones de streaming, ha impulsado la búsqueda de enlaces inalámbricos que operen a frecuencias más altas. En consecuencia, el objetivo principal en las redes móviles actuales 5G y futuras 6G es utilizar canales en las bandas de ondas milimétricas (de 30 a 300 GHz) e incluso en la banda sub-THz (hasta 1 THz) para lograr un mayor ancho de banda y capacidad en los enlaces de comunicación.

Sin embargo, a estas frecuencias, las pérdidas de propagación en los canales y la directividad de las antenas se vuelven más pronunciadas. En este contexto, el *broadcasting*, donde un único usuario envía información a múltiples usuarios, se vuelve complejo. Por lo tanto, los nuevos sistemas de comunicación que se centran en enlaces punto a punto con capacidades de direccionamiento de haz han surgido como soluciones prometedoras. Además, la mezcla de frecuencias, que permite a las antenas transmitir información a través de diferentes bandas de frecuencia (como para telefonía o geolocalización), presenta una alternativa viable para diseñar dispositivos más eficientes.

Esta Tesis Doctoral se centra en el desarrollo de sistemas radiantes y metaestructuras que aborden estos desafíos tecnológicos. En particular, investigamos el uso de metamateriales modulados periódicamente para modificar las propiedades de las antenas en las bandas de ondas milimétricas. Dividimos este amplio campo en tres categorías principales: modulaciones espaciales, modulaciones temporales y modulaciones espaciotemporales. En cada una de ellas, proponemos diferentes dispositivos que presentan capacidades interesantes en las bandas de ondas milimétricas.

Por un lado, en lo que respecta a las modulaciones espaciales, proponemos varios metamateriales/metasuperficies pasivos, incluyendo: una antena tipo lente de Fresnel diseñada para mejorar la directividad e introducir capacidades de direccionamiento de haz en una guía de ondas convencional a 60 GHz, y una metasuperficie para controlar la polarización en reflexión en las bandas satelitales K/Ka. Además, desarrollamos marcos analíticos basados en expansiones de Floquet-Bloch de los campos electromagnéticos y en métodos de ecuaciones integrales para simular estos metamateriales modulados espacialmente desde una perspectiva basada en cir-

cuitos. Específicamente, utilizamos la teoría de circuitos, previamente aplicada a metasuperficies espaciales estáticas, en un dispositivo metálico 3D y en un *metagrating* 2D cargado con elementos activos (diodos, resistores, condensadores y bobinas).

Por otro lado, en lo que respecta a las modulaciones temporales, proponemos un marco teórico para simular una metasuperficie variable en el tiempo que alterna sus propiedades eléctricas (entre estados aire, metal y *grating*). Debido a la falta de softwares comerciales de onda completa para simular este tipo de dispositivos de manera eficiente, esta solución surge como una buena alternativa en este campo. Además, implementamos un método de diferencias finitas en el dominio del tiempo (FDTD) para comprobar los resultados analíticos obtenidos.

Estos trabajos llevan al desarrollo de una herramienta teórica completa para simular metasuperficies moduladas en el espacio y tiempo simultáneamente. El dispositivo propuesto demuestra capacidades tanto de formación de haces como de mezclado de frecuencias en las bandas de microondas, ofreciendo características prometedoras e intrigantes para los sistemas de telecomunicaciones futuros.

Además, se propone un *setup* para la caracterización electromagnética de materiales con el objetivo de comprender los parámetros constitutivos de dieléctricos homogéneos que puedan ser útiles para el diseño de metamateriales en las bandas de ondas milimétricas.

Palabras Clave: Metamateriales, metasuperficies, estructuras periódicas, modulación espacial, modulación temporal, modulación espaciotemporal, caracterización de materiales, telecomunicaciones, *beam forming*, *beam steering*, mezclado de frecuencias, bandas milimétricas, FDTD.

Contents

Acronyms

1D One-Dimensional.

2D Two-Dimensional.

3D Three-Dimensional.

4D Four-Dimensional.

5G Fifth Generation.

6G Sixth Generation.

ABC Absorbing Boundary Condition.

AFSS Active Frequency Selective Surface.

BJ Baker-Jarvis.

CFL Courant-Friedrichs-Lewy.

COMSOL COMSOL Multiphysics.

CST CST Studio Suite.

D2D Device-to-Device.

DLP Digital Light Processing.

DMLS Direct Metal Laser Sintering.

DoA Direction-of-Arrival.

DUT Device Under Test.

FDM Fused Deposition Modelling.

FDTD Finite-Difference Time-Domain.

FETD Finite-Element Time-Domain.

FSS Frequency Selective Surface.

GRL Gated-Reflect-Line.

HWG Hard Waveguide.

IoT Internet of Things.

LP-to-CP Linear Polarization to Circular Polarization.

LWA Leaky-Wave Antenna.

MJ Material Jetting.

mmWave Millimeter Wave.

MoM Method of Moments.

NRW Nicholson-Ross-Weir.

OAM Orbital-Angular-Momentum.

P2P Point-to-Point.

PA Phased Array.

PBC Periodic Boundary Condition.

PEC Perfect Electric Conductor.

PMC Perfect Magnetic Conductor.

PML Perfectly Matched Layer.

RF Radio-Frequency.

RIS Reconfigurable Intelligent Surface.

RLC Resistor-Inductor-Capacitor.

RWG Rectangular Waveguide.

SatCom Satellite Communication.

SLA Stereolithography.

SLM Selective Laser Melting.

SLS Selective Laser Sintering.

SWG Slotted Waveguide.

TE Transverse Electric.

TEM Transverse Electromagnetic.

TG Time-Gating.

TM Transverse Magnetic.

TRL Thru-Reflect-Line.

VNA Vector Network Analyzer.

Chapter 1

Introduction

1.1 Background and motivation

Since the beginnings, the history of communications has been a constant pursuit to improve the transmission of information. Early communication systems, such as the telegraph [1] and the telephone [2], used electrical signals through wires to send messages over relatively short distances. With the invention of radio [3] and television [4], it became possible to transmit audio and video signals through electromagnetic waves, which allowed for greater geographic coverage and a larger volume of information. With the advent of the digital era and the exponential growth of the Internet, the demand for data transmission has drastically increased [5]. The need to share large amounts of real-time information, such as high-definition videos, online gaming, and augmented and virtual reality applications, has highlighted the limitations of traditional communication systems [6].

The increase of the bandwidth is crucial to cover this growing demand. Greater bandwidths enable the transmission of more data at higher speeds, reducing latency and improving the quality of communication services. To achieve this, it is essential that the antennas operate at higher frequencies, where more bandwidth is available. It allows the increase of the capacity of the systems, which is essential for advanced and emerging applications in future communication of the Sixth Generation (6G) [7, 8]. Therefore, moving to higher frequencies, such as Millimeter Wave (mmWave) and sub-Terahertz bands, opens up the possibility to unlock new capabilities and support the massive connectivity requirements of the future.

The implementation of the Fifth Generation (5G) has revealed numerous challenges that need to be still addressed, particularly in urban scenarios [9–11]. This generation is characterized by the use of the mmWave bands (from 30 to 300 GHz), where the data transmission rate could reach up to 100 Gbps [12, 13]. Nonetheless, the use of these frequencies presents several fundamental challenges in communication [14]. To name a few, it

is highlighted the inherent high directivity of the antennas that forces the Point-to-Point (P2P) links, the sensivity to blockage produced by the foliage [15], human blockage [16], or material penetration [17], the severe path loss due to the rain [18], gas molecules into the atmosphere [19], and general channel attenuation imposed by the Friis formula [20]. For instance, several of these issues are found in Satellite Communications (SatComs) where polarization alterations by the Faraday rotation in the ionosphere are also added [21]. Furthermore with the growth of the Internet of Things (IoT), new Device-to-Device (D2D) communications have emerged, including vehicles, mobile users, networks, and infrastructures, where the beam steering [22], beam forming [23] and frequency conversion [24] capabilities become crucial.

With all these challenges, Radio-Frequency (RF) engineers have focused their efforts on designing new prototypes that mitigate some of the previously presented drawbacks. For instance, lens-antennas [25] have become widely adopted as an excellent solution for P2P links, as they can concentrate power into specific regions, thereby increasing antenna directivity and compensating for path losses [26, 27]. In addition to their capability to operate across a wide range of frequencies [28, 29], they have beam-steering capabilities depending on: on the one hand, the feeder [30, 31]; and, on the other hand, the relationship between the position of the radiating element and the lens [32]. Furthermore, the continuous improvement in additive manufacturing has facilitated the fabrication of these devices using dielectric or metallic materials through various Three-Dimensional (3D) printing techniques [33, 34], such as Stereolithography (SLA), Fused Deposition Modelling (FDM), Selective Laser Sintering (SLS), Material Jetting (MJ), Digital Light Processing (DLP), Selective Laser Melting (SLM), or Direct Metal Laser Sintering (DMLS). These facilities, along with the inclusion of Frequency Selective Surfaces (FSSs) [35, 36], have enabled the creation of more sophisticated reconfigurable lens-based prototypes which are ideal for communication scenarios where the beam steering is desired [37, 38].

FSSs are periodic structures that selectively transmit or reflect electromagnetic waves at certain frequencies [39]. They generally consist of an array of elements, such as patches or apertures, arranged in a spatial periodic pattern on a substrate. The behavior of a FSS is determined by the shape, size, and arrangement of these elements (whose periodicity is established as the distance between two consecutive elements or cells), as well as the dielectric properties of the substrate. In recent decades, they have gained significant prominence due to their multiple applications, such as absorptive filters [40], radome filters in aircraft, the medical and military sectors by means of special textiles, or their easy implementation in antennas [41], among others. Furthermore, the subsequent design of multilayer FSSs [42, 43] and the use of the longitudinal dimension to create 3D FSSs [44], increases the operational bandwidth of the filters and facilitates

the integration of active elements [45,46]. These last lead to the development of Active Frequency Selective Surfaces (AFSSs) [47], resulting in overall superior performance in terms of reconfigurability, dual-band responses, beam steering, beam forming, or beam switching. The improvement in the manufacturing, characterization, and measurement methods of these devices has enabled the development of FSSs in the sub-Terahertz ranges [48], allowing the creation of high-capacity links with frequency selection, reflection, transmission, and absorption characteristics for the communications of the future generation [49].

FSSs have also been proposed in SatComs for their ability to adjust polarization and operate across various frequency bands [50, 51]. Their capability to switch between Linear Polarization to Circular Polarization (LP-to-CP) [52], or reverse spin direction with rotators [53], combined with their functionality in both reflection and transmission modes [54], makes them an excellent choice for communication systems where channel conditions can affect the electromagnetic signal polarization [55]. Particularly, there is special interest in *K/Ka* bands SatCom terminals that operate in the 17.7-21.2 GHz range for downlink and the 27.5-31 GHz range for uplink. Therefore, the use of FSSs has made it possible to design prototypes that work in both bands together [56, 57]. On the other hand, the emergence of fully-metallic polarizers has provided a robust solution for satellite integration, utilizing multilayer FSSs [58] or employing 3D-printed prototypes [59, 60].

Spatial modulations have been the primary technique for tailoring the classical systems for beam forming or polarization conversion, such as FSSs, multilayer antennas [61],Leaky-Wave Antennas (LWAs) [62, 63], metagratings [64–66], metamirrors [67, 68] or Phased Array (PA)-based devices like reflectarrays [69], transmitarrays [70] or Reconfigurable Intelligent Surfaces (RISs) [71,72]. However, the recent inclusion of time modulation has opened a new range of intriguing applications for future communications [73–84]. These applications include non-reciprocal devices [85–87], amplification [88, 89], Direction-of-Arrival (DoA) estimation [90], imaging [91], digital computing [92], isolation [93], lensing [94] or frequency beam scanning at fixed input frequency in LWAs [95] to name just a few. Many of these applications will be very useful in 6G [96] highlighting the frequency conversion [97–99] and beam steering [100–102] for the future D2D communications. Several of these spacetime-modulated prototypes are able to modify their properties in time by means of PIN diodes [103–105] or varactors [106, 107] in the mmWave range. Furthermore, the fast improvement of the switching systems have enabled the mannufacturing of novel prototypes even in the teraherzt range [108–110].

With all these new possibilities that spacetime-modulated devices enable, it is mandatory to develop simulation tools to understand the physical insight and test the electromagnetic response of the designed structures. Nevertheless, classical full-wave commercial software widely used by RF en-

ginieers, such as *CST Studio Suite (CST)* [111] or *Ansys HFSS* [112], lack of temporal modulations without the support of external tools [113]. Thus, to the best of our knowledge, the only commercial software available to simulate the electromagnetic response of time-varying systems in a convincing and practical manner is *COMSOL Multiphysics (COMSOL)* [114]. However, it presents the inherent limitations of general-purpose electromagnetic simulators, such as low efficiency or the complexity of adaptation to specific problems. Moreover, *COMSOL* is a powerful tool for solving many physics problems, but it is not specifically designed to be an user-friendly tool for engineering purposes like *CST* or *HFSS*. For these reasons, the development of numerical and analytical methods to simulate spacetime-varying systems has become a priority.

Therefore, for problems that require knowledge of the time-domain behaviour of the systems, the community typically uses numerical techniques such as a Finite-Difference Time-Domain (FDTD) [115–118], Method of Moments (MoM) [119] or Finite-Element Time-Domain (FETD) [120] among others, to analyze or compare the electromagnetic response of these structures. Due to the high computational cost of these method, several solutions have emerged to reduce simulation times, such as the adaptive mesh-based approach [121]. Nonetheless, other available alternatives for simulating time-varying systems found in the literature that provide physical insight into the problems are based on semianalytic [122–124] or analytic [125, 126] models. The main difference compared to heuristic models is that in these cases, the topology and elements used arise from the analytical formulation itself, unlike in heuristic models where the components and topology are predetermined by the designer.

In order to design and simulate all prototypes referenced in this section, it is vital to know the electromagnetic properties of each material in real life. The extraction of the intrinsic properties of the materials from the measurement of the scattering parameters in a known surrounding medium is a well-established technique. The method was introduced in 1970 by Albert F. Nicholson and Glen F. Ross, who analyzed the impulse response of systems using Transverse Electromagnetic (TEM)-mode in a coaxial air-filled line [127]. They examined the transmission and reflection coefficients of a material slab placed within the system, analyzing these parameters in the time domain. Four years later, William B. Weir extended this method to microwave frequencies, where the extraction of the scattering parameters could be performed in a waveguide or a TEM transmission line [128]. The method was applied directly in the frequency domain using the extracted results from the Vector Network Analyzer (VNA). Since then, many material characterization systems have been proposed to reduce uncertainty in the measurement and extract the constitutive parameters of the materials at higher frequencies [129–131]. Furthermore, the need to determine constitutive parameters in the sub-Terahertz range for developing prototypes

for future communications has prompted the proposal of several broadband methods in the literature [132–135].

Therefore, this Thesis fundamentally aims to contribute to the field of the RF devices designed for future communications in mmWave bands. The organization of the document is divided in three Chapters:

- Chapter 1: Section 1.1 focuses on the exposition of the main challenges found in current and future mobile generations: 5G and 6G. Moreover, it provides a preliminary introduction to the solutions proposed in this document. In the subsequent subsections, we consider crucial aspects for the realization of this Doctoral Thesis. Primarily, in Subsection 1.1.1, we present the constitutive relations of the linear and isotropic materials used in this Thesis. Next, Subsection 1.1.2 highlights the importance of the (spacetime) boundary conditions for solving electromagnetic problems. Subsequently, Subsection 1.1.3 briefly introduces metamaterials and their main applications nowadays. In Subsection 1.1.4, we discuss on periodic structures and the Floquet-Bloch theorem. Afterwards, Subsection 1.1.5 focuses on the numerical technique used to compare the results of time-varying systems. Particularly, we discuss on the implementation of a finite-difference time-domain (FDTD) method. In Subsection 1.1.6, the general formulation of the circuit analysis proposed in this Doctoral Thesis is detailed. Finally, in Subsection 1.1.7, we present the main setups configured in the laboratory for the experimental validations.

- Chapter 2: Publications. This chapter is divided into four main sections. Sections 2.1, 2.2, and 2.3 group the papers related to spatial, temporal, and space-time modulation, respectively. Section 2.4 is dedicated to explaining the setup utilized for the extraction of scattering parameters and the methods applied to determine the constitutive parameters of the materials.

- Chapter 3: Conclusions and Future Work. Section 3.1 details the main observations of each paper published in this Doctoral Thesis. Finally, Section 3.2 outlines possible future directions of the research line for more complex applications.

1.1.1 Constitutive relations

The physical insight into the interaction between electromagnetic waves and the media is governed by Maxwell's equations, primarily published in [136]. There, a complete set of closed equations were unified to describe the electric and magnetic behavior in a single coherent theory, among other milestones. Since then, a plethora of books have referenced this theory to explain the electromagnetic properties of different materials applied to physics and

engineering [137–140], to name just a few. Maxwell's equations [141] are summarized in:

$$\nabla \times \mathbf{E} = -\frac{\partial \mathbf{B}}{\partial t} - \mathbf{M}, \tag{1.1}$$

$$\nabla \times \mathbf{H} = \frac{\partial \mathbf{D}}{\partial t} + \mathbf{J}, \tag{1.2}$$

$$\nabla \cdot \mathbf{D} = \rho, \tag{1.3}$$

$$\nabla \cdot \mathbf{B} = 0, \tag{1.4}$$

where eq. (1.1) is the Faraday's law of induction, eq. (1.2) is the Ampere's law and eqs. (1.3) and (1.4) are the Gauss's laws for the electric and magnetic fields, respectively. In these equations, the volume charge density (ρ), the electric current density ($\mathbf{J}$) and the *fictitious* magnetic current ($\mathbf{M}$), may be considered as the sources of the electromagnetic fields. The relation between the electric($\mathbf{D}$)/magnetic($\mathbf{B}$) flux densities and the electric($\mathbf{E}$)/magnetic($\mathbf{H}$) fields in linear, homogeneous and isotropic materials is expressed through the constitutive relations:

$$\mathbf{D} = \varepsilon \mathbf{E} = \varepsilon_0 \mathbf{E} + \mathbf{P_e} = \varepsilon_0 (1 + \chi_e) \mathbf{E}, \tag{1.5}$$

$$\mathbf{B} = \mu \mathbf{H} = \mu_0 (\mathbf{H} + \mathbf{P_m}) = \mu_0 (1 + \chi_m) \mathbf{H}. \tag{1.6}$$

These relations are governed by the constitutive parameters such as electric permittivity (ε) and magnetic permeability (μ), which may be complex inducing losses in the materials. Moreover, when an electric/magnetic field is applied to materials, additional polarization vectors appear due to the alignment of the electric/magnetic dipole moments within them. These last two new parameters are: the electric polarization ($\mathbf{P_e}$), and the magnetic polarization or magnetization ($\mathbf{P_m}$). The existing relationship between these four parameters ($\varepsilon, \mu, \mathbf{P_e}, \mathbf{P_m}$) is summarized by the complex susceptibilities (χ_e, χ_m) that defines the nature of the material. For instance, a material will be spacetime invariant if its susceptibility does not depend on space or time, or spacetime nondispersive if its susceptibility does not depend on the wavenumber or frequency [142].

Although it is true that these susceptibilities can be tensors, inducing anisotropy in the materials, in this doctoral Thesis we have worked with linear and isotropic materials. Thus, in Section 2.4, we explain the extraction of the complex constitutive parameters in certain homogeneous dielectrics to fully characterize them.

1.1.2 Boundary conditions

Boundary conditions are crucial to understand the interaction between electromagnetic waves and the surrounding media. Depending on the spacetime

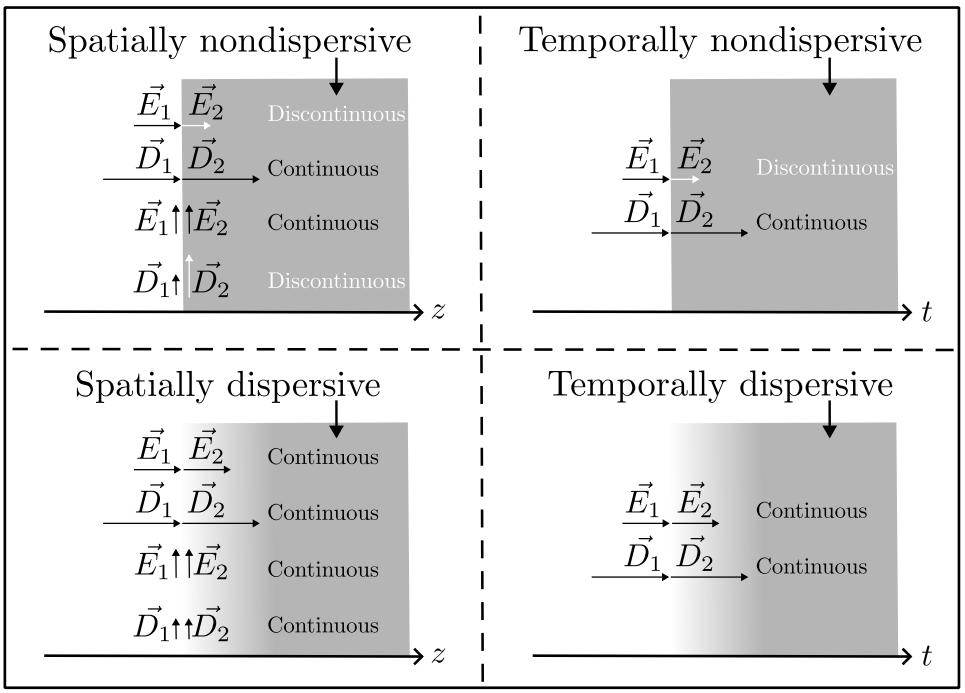

Figure 1.1: Boundary conditions at the interface with different materials depending on their spacetime dispersion [145]. At the interface with spatially or temporally dispersive materials, the electric field and electric flux density are continuous through the interface. However, in nondispersive materials, some considerations must be taken into account. On the one hand, in spatially nondispersive materials, the normal component of $\vec{E}$ and the tangential component of $\vec{D}$ are discontinuous. On the other hand, in temporally nondispersive materials, the electric field is discontinuous meanwhile the electric flux density is continuous.

nature of these boundaries, the solutions of Maxwell's equations change drastically [143]. Taking into account the dispersive nature of certain materials, explained through the relationship between their constitutive parameters and the wavenumber or frequency, the spatiotemporal boundary condition assumes different considerations [144–146].

For instance, in a conventional case of scattering where a plane wave traveling in a nondispersive medium impinges on a different nondispersive medium, the resulting diffraction pattern will vary significantly depending on the spatial or temporal interface found by the wave [147].

On the one hand, for a spatial static interface between two different nondispersive media, the normal component of $\mathbf{D}/\mathbf{B}$ and the tangential component of $\mathbf{E}/\mathbf{H}$ across the interface between both media is continuous. Thus, the frequency in the second medium is preserved while the wavenumber varies.

On the other hand, assuming the dual scenario where the properties of

the entire nondispersive medium change instantaneously from certain constitutive parameters to others at a temporal instant, a time boundary condition may be imposed. Thus, at the interface of temporally nondispersive materials, the continuity of the vectors **D** and **B** is maintained, as depicted in Figure 1.1 for the electric case (being similar for the magnetic field). Under these conditions, the wavenumber is not affected in this problem, while the frequency is altered.

For these reasons, imposing the correct boundary conditions is essential for the accuracy of the results. In many electromagnetic problems, spatial boundary conditions are imposed in the limit of the unit cells by Perfect Electric Conductors (PECs) or Perfect Magnetic Conductors (PMCs), where the value of the electric or magnetic fields on them is known. Furthermore, with the correct imposition of these assumptions in periodic structures, other classical boundary conditions, such as Periodic Boundary Conditions (PBCs), can be obtained [148]. All these points have been taking into account for the correct performance of the circuit analysis proposed in Sections 2.1, 2.2 and 2.3.

1.1.3 Metamaterials

The beginning of metamaterials was around the middle of the last century when Victor Veselago studied the properties of materials with a negative refractive index [149]. This milestone, along with the work of John Pendry on the creation of magnetic materials with values not accessible in nature from nonmagnetic conductor sheets [150] and structures with negative refraction index [151], has lead to the conception of new materials that have revolutionized the field of electromagnetism [152].

Metamaterials have been commonly defined as artificial, *effectively* homogeneous electromagnetic structures with unusual properties not readily available in nature [153,154]. Due to their spatial effective homogeneous condition, the size of the average cell of these materials may be much smaller than the wavelength of the waves that interact with them. Due to their wide versatility, the metamaterials can be catalogued as a function of their spatial or temporal dimension. Thus, One-Dimensional (1D) metamaterials are referred as elements whose spatial modulation is applied only in a single spatial dimension [155]. On the other hand, Two-Dimensional (2D) metamaterials exhibit periodic spatial modulation along a plane. They have adopted the term *metasurfaces* due to their thin spatial condition and have been widely utilized for the design of FSSs, high impedance surfaces, perfect absorbers, polarization transformers, radiating surfaces, wavefront shaping, flat lenses, among others [156–158]. Taking advantage of the third dimension in bulk structures, 3D metamaterials [159] offer an extra degree of freedom that is very useful, for instance, in beam steering, beam splitting, absorption, and polarization selectivity applications [160] or for the creation of

epsilon-near zero metamaterials [161, 162]. The inclusion of time as a new degree of freedom in the design of systems [79] prompts the emergence of Four-Dimensional (4D) metamaterials [142, 163]. It supposes new intriguing applications as magnetic-free nonreciprocal isolators, phased shifthers or circulators [164], power combining [165], efficient phase conjugation [166] or mode-wavelength-division multiple access trough nonreciprocal Orbital-Angular-Momentum (OAM) [167], among others [168].

In this Doctoral Thesis, different metasurfaces and metamaterials have been circuitly analyzed and some of them manufactured in Sections 2.1, 2.2 and 2.3.

1.1.4 Periodic structures

A periodic structure is an arrangement of elements whose electromagnetic response repeats at regular intervals in space, time, or both. Several metamaterials found in the literature have been designed following periodic conditions [169]. The use of PBC is a classical technique to solve complex electromagnetism problems by the analysis of their periodic unit cell. They account the phase difference between the top and bottom and the right and left walls of the unit cell and allow to reduce the original problem to waveguide point of views [170]. The ability to analyze a complex structure formed by the repetition of the same pattern as a simple study of the response of its unit cell is facilitated by Floquet [171] and Bloch [172] theorems. The combination of these theorems states that in a system periodic in both time and space, the value of the electric or magnetic field at a specific point in space and at a specific instant in time will be equal to its value at the next spatial or temporal period, multiplied by a certain complex exponential factor. This exponential factor corresponds to the phase shift imposed by the incident wave between two consecutive periodic elements (in time or space). Therefore, the electromagnetic response of a complex metamaterial that follows a periodic spacetime pattern will be completely characterized if the response in the unit cell is known. Thus, these analyzes have been widely applied to extract the electromagnetic response of waves interacting with periodic structures [173, 174] and periodic metamaterials [175, 176].

In Chapters 2.1, 2.2 and 2.3, PBCs has been assumed for the correct and efficient simulation of the metamaterials.

1.1.5 FDTD method

The finite-difference time-domain (FDTD) method is a numerical technique that provides direct time-domain solutions of Maxwell's differential equations on spatial grids or lattices. This powerful computational technique was introduced by Kane S. Yee in 1966 [177] and extended by many researchers as Allen Taflove in 1995 [178]. The entire simulation space is

discretized with a sub-wavelength spatial sampling, and the time step is selected to ensure numerical stability. At each time step, the components of the electric and magnetic fields are alternately updated (staggered grid), allowing precise capture of the propagation of electromagnetic waves in the medium. For simulations where the spatial region may be considered infinite, Absorbing Boundary Conditions (ABCs) or Perfectly Matched Layers (PMLs) are added to avoid reflections at the edges of the mesh. Particularly, in this Doctoral Thesis, a 2D FDTD method has been programmed applying the second-order Engquist-Majda ABC [179]. To ensure the numerical stability in the simulations, a Courant-Friedrichs-Lewy (CFL) stability condition [180] was imposed. This condition relates the time step size, spatial grid resolution, and the speed of electromagnetic waves in the medium, ensuring that the numerical scheme remains stable throughout the simulation. Furthermore, it has been assumed that the metals involved in the simulations are PECs and nondispersive, meaning that their electromagnetic properties do not vary with frequency. Additionally, homogeneous and isotropic dielectric materials, whose constitutive parameters are summarized by ε_r and μ_r, have been considered as the entire surrounding medium in the simulations.

1.1.6 Circuit analysis

The analytical method development in this Doctoral Thesis is based in circuit models previously applied to 1D [181,182] and 2D [42,43,183] spatially-modulated structures [184]. In this Doctoral Thesis, we have extended the applications of this analytical framework by applying it to a 2D spatial modulation with the inclusion of lumped elements, considering the longitudinal spatial dimension (3D structures), or incorporating the new degree of freedom with a nondispersive time-varying metamaterial that periodically alternates electromagnetic states such as fully-reflectivity and full transmission. Thus, the classical static structures become dynamic, achieving enhanced beam-steering and frequency mixing capabilities.

Thus, in general terms, assuming a spatiotemporal discontinuity described by a spatial interface at $z = 0$ placed in a dielectric medium with relative constitutive parameters ε_r and μ_r, and a temporal interface at $t = 0$, as depicted Figure 1.2, the electromagnetic field in each of the regions on the left side (1) and the right side (2) can be described by a Floquet-Bloch expansion of harmonics

$$\mathbf{E}(x,y,z,t)^{(1),(2)} = \sum_{\forall m}\sum_{\forall n}\sum_{\forall i} E_{nmi}^{(1),(2)}\mathbf{e}_{nmi} \tag{1.7}$$

$$\mathbf{H}(x,y,z,t)^{(1),(2)} = \sum_{\forall m}\sum_{\forall n}\sum_{\forall i} Y_{nmi}E_{nmi}^{(1),(2)}\mathbf{e}_{nmi} \tag{1.8}$$

where each of the indexes $n, m, i \in \mathbb{Z}$ refer to a single periodicity in the problem. On the one hand, the transverse spatial directions x and y have the

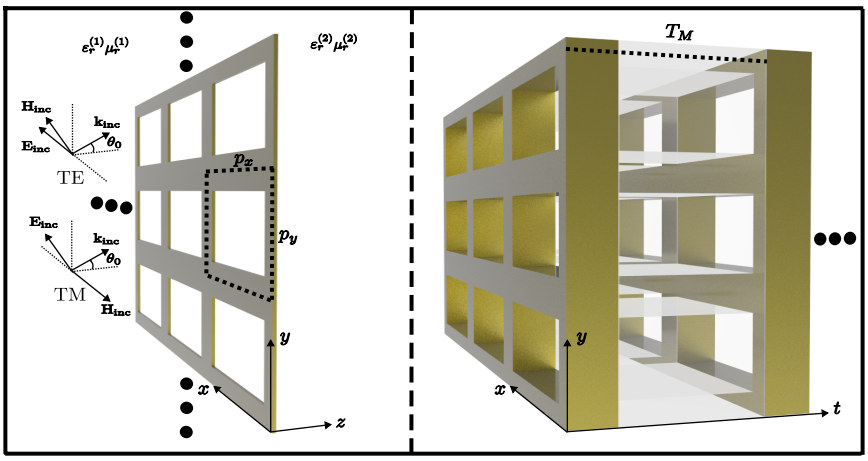

Figure 1.2: Sketch of the general scenario where the circuit method can be applied when a monochromatic wave impinges in a metamaterial under TE/TM incidence. In the left panel, the 2D spatial problem is depicted, with the unit cell defined by the dashed rectangle and governed by the spatial periodicities p_x and p_y. In the right panel, the (2+1)D spacetime scenario including the temporal periodicity T_M is plotted.

spatial periodicities p_x and p_y taken into account by means of the indexes m and n, respectively. On the other hand, the time periodicity is given by T_M, governed by the index i. Periodicity along the longitudinal direction z is not considered. The coefficients $E_{nmi}^{(1),(2)}$ represent the amplitude associated with the nmi-th spacetime harmonic in the leftmost region (1) and rightmost region (2), whereas $\mathbf{e}_{nmi}$ denotes its vector form which is proportional to $\mathbf{e}_{nmi} \propto \exp\left[-j(k_m x + k_n y + \beta_{nmi} z) + j\omega_i t\right]$. The admittances Y_{nmi} are also modal and can be of TM or TE nature. For the sake of simplicity, the incident harmonic ($n = m = i = 0$) has unit amplitude. Its contribution is described via the incident- and reflected-waves in region (1), $E_{000}^{(1)} = 1 + R$, and the transmitted one in region (2), $E_{000}^{(2)} = T$.

One of the key aspects to obtain the equivalent circuit is the knowledge, a priori, of the electric-field profile $\mathbf{E}_{\text{bf}}(x, y, t)$ at the spacetime discontinuity ($z = 0$). Since the tangential electric field must be continuous through the spatial discontinuity, we therefore impose

$$\mathbf{E}(x, y, z = 0, t)^{(1),(2)} = \mathbf{E}_{\text{bf}}(x, y, t)\,. \tag{1.9}$$

After mathematical manipulations of (1.9) (detailed in [182]), we reach the following expression for the Floquet coefficients

$$E_{nmi}^{(1),(2)} = E_{000}\frac{\displaystyle\int_{p_x}\int_{p_y}\int_{T_M} \mathbf{E}_{\text{bf}}(x, y, t)\cdot[\mathbf{e}_{nmi}]^*\,\mathrm{d}x\,\mathrm{d}y\,\mathrm{d}t}{\displaystyle\int_{p_x}\int_{p_y}\int_{T_M} \mathbf{E}_{\text{bf}}(x, y, t)\cdot[\mathbf{e}_{000}]^*\,\mathrm{d}x\,\mathrm{d}y\,\mathrm{d}t}, \tag{1.10}$$

which can be rewritten as

$$E_{nmi}^{(1),(2)} = E_{000} N_{nmi}\,, \tag{1.11}$$

where the term N_{nmi} is circuitly interpreted as a complex transformer with turn ratio $1 : N_{nmi}$, as depicted Figure 1.3.

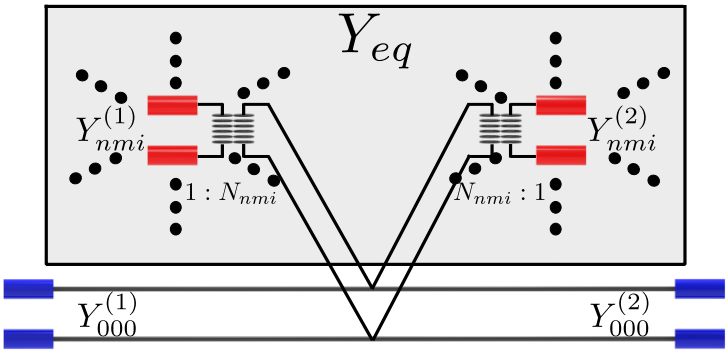

Figure 1.3: General topology of the equivalent circuit model, including the (2+1)D sum of infinite transmission lines representing each spacetime *nmi*-harmonic. The dashed points simulate the expansion around the three dimensions of the admittances and transformers.

By imposing the instantaneous continuity of the Poynting vector across the spacetime interface

$$\mathbf{H}^{(1)}(x,y,z,t) \times \mathbf{E}_{\text{bf}}(x,y,t) = \mathbf{H}^{(2)}(x,y,z,t) \times \mathbf{E}_{\text{bf}}(x,y,t)\,, \tag{1.12}$$

and introducing (1.8) and (1.11) in (1.12), we reach an expression for the reflection coefficient R of the incident wave in the following form

$$R = \frac{Y_{000}^{(1)} - Y_{000}^{(2)} - Y_{eq}}{Y_{000}^{(1)} + Y_{000}^{(2)} + Y_{eq}}\,. \tag{1.13}$$

The term Y_{eq} is the *equivalent admittance* that models the spacetime metasurface. Depending on the studied problem, this equivalent admittance will take different forms. Nonetheless, it will include the modal admittances $Y_{nmi}^{(1),(2)}$ that, depending of their nature, are calculated as

$$Y_{nmi}^{(1),(2)} = \begin{cases} \frac{\beta_{nmi}^{(1),(2)}}{\mu_r^{(1),(2)} \mu_0\, \omega_i}, & \text{TE polarization}\,, \\ \frac{\varepsilon_r^{(1),(2)} \varepsilon_0\, \omega_i}{\beta_{nmi}^{(1),(2)}}, & \text{TM polarization}\,. \end{cases} \tag{1.14}$$

$\beta_{nmi}^{(1),(2)}$ denotes the longitudinal wavevector of the *nmi*-harmonic and it is defined as

$$\beta_{nmi}^{(1),(2)} = \sqrt{\varepsilon_r^{(1),(2)} \mu_r^{(1),(2)} \left[\frac{\omega_0 + i\frac{2\pi}{T_M}}{c}\right]^2 - [k_{nm}]^2}\,, \tag{1.15}$$

with

$$k_{nm} = \sqrt{\left[k_t + n\frac{2\pi}{p_y}\right]^2 + \left[m\frac{2\pi}{p_x}\right]^2}, \tag{1.16}$$

being $k_t = \frac{\omega_0}{c}\sin(\theta_0)\sqrt{\varepsilon_r^{(1),(2)}\mu_r^{(1),(2)}}$ the transverse wavevector of the nmi-th harmonic for the topology sketched in Figure 1.2.

This method have been applied in several papers of this Doctoral Thesis. In Section 2.1, the spatially-modulated 2D case has been exploited for the simulation of the proposed devices presented in [J2] and [J3]. The time-only case, corresponding to a temporal 1D periodicity, is analyzed in Section 2.2 in [J4] and [J5]. Finally, the spacetime (1+1)D case involving a time-varying metagrating is studied in Section 2.3 in [J6].

1.1.7 Experimental validations

To characterize the constitutive parameters of the materials and validate the performance of the prototypes manufactured in this Doctoral Thesis, it is mandatory to accurately extract the experimental scattering parameters in the laboratory. Therefore, different setups, as shown in Figure 1.4, have been configured depending on the requirements of the prototypes.

To achieve the same de-embedding as in commercial full-wave software, various calibration techniques have been employed in the setups sketched in Figure 1.4(a). On the one hand, to eliminate the effects of the VNA, coaxial cables, and transitions on standard waveguides, a classical Thru-Reflect-Line (TRL) calibration [185] has been consistently applied at the antenna interfaces. This technique avoids systematic errors in the measured scattering parameters of the Device Under Test (DUT). It involves three measurements: "Thru," where both antennas are placed directly in front of each other to establish a reference for the amplitude and phase of the reflected and transmitted signals; "Reflect," where a metal is used to provide a reference for the maximum reflection obtained; and "Line," where the antennas are placed at a length different from that of "Thru" to obtain a phase difference.

On the other hand, to address the multiple reflections that can occur in systems including several horns and lenses, we employed temporal filtering using the well-known Time-Gating (TG) technique [186]. This method modifies the temporal response of an arbitrary signal by applying a windowing function, such as rectangular, Hann, or Hamming, to filter out unwanted reflections. Additionally, to account for path losses in free space, we applied the Gated-Reflect-Line (GRL) calibration technique [187]. This technique involves two specific measurements: one with an empty fixture and another with a metal plate of known thickness. Thus, the reference planes are finally defined by the walls of the metal plate.

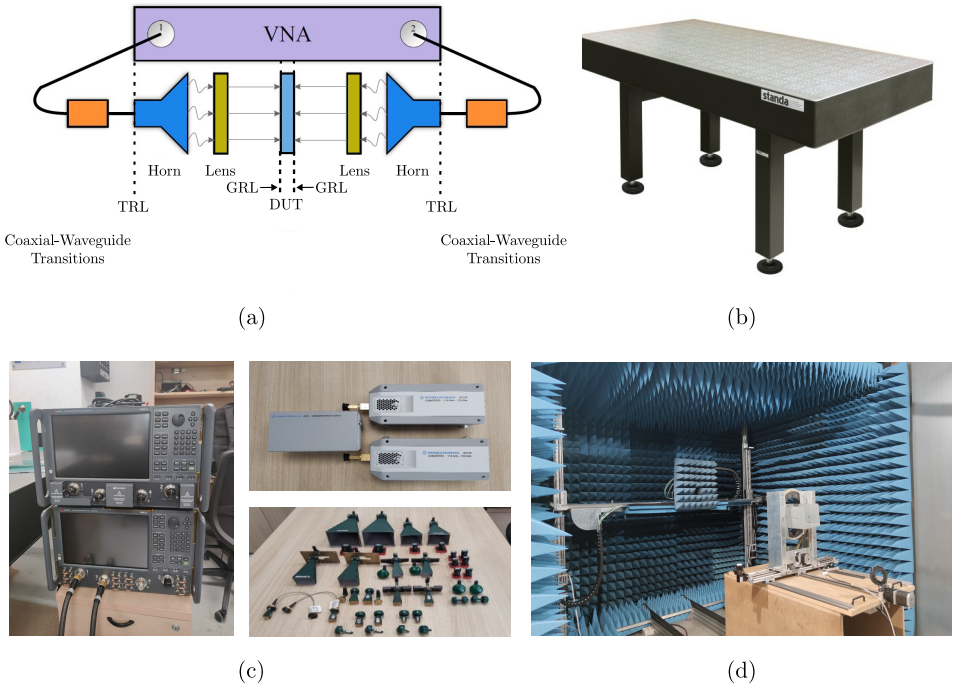

Figure 1.4: (a) General schematic of the setup used for material characterization. (b) Image of the quasi-optic bench used for precise measurements. (c) Photographs of the VNAs, frequency converters, and horns. (d) Anechoic chamber with capabilities for planar, cylindrical, and spherical acquisitions of radiation patterns and gain measurements.

Using these techniques, we have configured an accurate setup for material characterization by extracting cleaned and normalized scattering parameters of the devices with the facilities shown in Figures 1.4(b)-(c). Lenses were employed for the lowest frequencies to ensure proper illumination of the sample. However, for frequencies ranging from 33 GHz to 330 GHz, the collimation of the wavefront produced by the horns was sufficient. Additionally, using the anechoic chamber depicted in Figure 1.4(d), we have obtained the gain measurements and the planar acquisitions of the radiation patterns necessary to evaluate the performance of the spatially-modulated metamaterials.

1.2 Objectives

The main focus of this Doctoral Thesis is the investigation of periodically-modulated metamaterials in the mmWave range for communications and future applications. Specifically, we aim to develop solutions for beamforming, beam steering, frequency conversion, and polarization control of the

radiating devices. Additionally, we pretend to analyze the real response of the materials in these bands for the correct simulation with numerical or analytical approaches. Thus, the objectives can be summarized in:

- **Design, simulation, and measurement of metasurfaces and metamaterials with spatial modulations.** The intrinsic property of spatially-modulated metamaterials to alter the momentum of waves makes them an excellent solution for beamforming and polarization control. The potential of analyzing the scattering properties of these devices using circuit approaches means in the valuable physical insight that they provide and the low computation times, making it a strong alternative to full-wave simulation software. For these reasons, we aim to offer an alternative framework for highest time consuming simulations of periodic structures and test the beamforming and polarization control of the devices experimentally. Therefore, in Section 2.1, we present a Fresnel lens antenna that increases the gain of conventional waveguides and enables the beam-steering capabilities that have been experimentally validated. Additionally, diagonal symmetry is proposed in polarization converters as a methodology to achieve both asymmetric and wideband responses. Finally, we introduce various analytical tools for simulating 3D metastructures that utilize the longitudinal dimension, as well as metasurfaces that can be loaded with lumped elements. These tools aim to incorporate active devices for reconfigurability or the inclusion of time modulations.

- **Simulation tools for metasurfaces with temporal modulations.** Due to the lack of commercial tools for efficiently simulating metamaterials that modify their properties over time, research in this area is crucial. For this reason, we aim to develop a theoretical framework that provides physical insight into time-varying metamaterials. In Section 2.2, we introduce an analytical technique that offers information about the scattering and diffraction phenomena of zero-thickness time-varying metal-based metasurfaces. It allows us to study the physical properties of these complex structures with the aim of applying them to telecommunications systems. Additionally, we have programmed a numerical FDTD method to compare and validate the analytical results. Furthermore, we extend the beamforming capabilities of the metasurface and broad the spectrum where the analytical approach can be applied by the incorporation of new temporal parameters.

- **Theoretical predictions for metasurfaces with spacetime modulation.** Space-time metamaterials are an emerging topic that opens up intriguing new possibilities. To increase the degrees of freedom of conventional time-invariant metamaterials, in Section 2.3, we leverage the intrinsic frequency conversion properties of time-modulated

systems to achieve frequency mixers and beamformers using a zero-thickness time-varying metagrating. Analyzing this through a circuit approach provides valuable information about the complex diffraction patterns associated with the propagative and evanescent nature of space-time harmonics, their diffraction angles, and the scattering parameters as a function of space-time modulation.

- **Material characterization in the mmWave bands.** Knowledge of the complex constitutive parameters of materials in microwave and mmWaves is essential for designing prototypes in these bands. However, many setups of material characterization are based in resonant cavities where the scalability of frequency in this methods is limited. Moreover, many of them need of optimization processes or electromagnetic simulations for achieving accurate solutions. Thus, in Section 2.4, a broadband free-space non-iterative reference-plane invariant setup of material characterization is proposed for extracting the complex constitutive parameters of linear, homogeneous and isotropic materials.

In summary, the manipulation of electromagnetic properties facilitated by metamaterials has revolutionized radiant systems, presenting numerous opportunities for utilization in communications. This Doctoral Thesis aims to empirically examine some of these devices, evaluating their performance and providing simulation tools for periodically-modulated metamaterials.

1.3 Research Methodology

The above objectives have been achieved by means of the following methodology. First, an exhaustive search into the state-of-the-art was carried out to understand the theory around metamaterials and their wide range of possibilities. Some reference books and numerous papers from different journals specializing in antennas, optics, photonics, electronics, instrumentation, and measurements were a great support for this research. Once the potential improvements in this field were identified, we decided to implement and develop some prototypes with spatial modulations to validate the simulations in a real environment. Moreover, a closed analytical method was programmed in *MatLab* [188] for periodically-modulated metamaterials, eliminating the need for any external full-wave tool. This included the incorporation of lumped elements for future implementation of more sophisticated and reconfigurable metasurfaces. Due to the detected lack of simulation tools for spacetime-varying metamaterials, we applied our previous knowledge based on the circuit analysis of spatially-modulated metastructures to ideal and theoretical cases of time-varying metal-based metasurfaces. Additionally, the setup of a material characterization system was key to gaining experience in instrumentation and measurement of antenna devices in the whole

range of microwave bands.

The full-wave commercial software used to compare the results obtained for space-modulated metamaterials with our circuit analysis was *CST*. Among its various solvers, we typically used the *Time Solver* and *Frequency Solver* with periodic boundary conditions and either Floquet's ports or waveguide ports. For time-varying systems, a self-implemented FDTD was programmed *in-house* to verify the theoretical approximations assumed in our model.

The fabrication and experimental validation of the prototypes were made possible thanks to the facilities available at the SWAT research group of the University of Granada (UGR) [189]. For the manufactured prototypes, a Formlabs 3D printer using the SLA additive technique was employed to print the Fresnel lens. The main process to eliminate undesired copper on the Rogers sheets for the polarizers was laser isolation carried out in the microwave group of the University of Sevilla. The scattering parameters for the measurements of the radiation patterns from 10 MHz to 67 GHz were extracted using the VNA (model: ZVA67 from R&S). To avoid reflections and reduce possible interferences, the measurements were realized in an anechoic chamber. Additionally, the material characterization setup was implemented on a quasi-optic bench due to the required accuracy. The configuration of the frequency converters for the highest frequencies was set in the VNA (model: Keysight N5247B) and to cover the complete band from 10 GHz to 330 GHz, a wide variety of standard horns were utilized (WR75, WR51, WR22, WR15, WR10, WR6, WR5, and WR3).

1.4 Thesis Results

This is the list of included **publications** in renowned **journals** and **conferences** that support the results achieved in this Thesis:

- [J1] **S. Moreno-Rodríguez**, M. A. Balmaseda-Márquez, J. Carmona-Murillo and Á. Palomares-Caballero, "Polarization-insensitive unit cells for a cost-effective design of a 3-D-Printed fresnel-lens antenna," *Electronics*, vol. 11, no. 3, p. 338, Jan. 2022.

- [C1] **S. Moreno**, J. L. Medrán-Del-Río, Á. Palomares-Caballero, A. Alex-Amor, A. Fernández-Prieto and C. Molero, "On the Design of Unit Cells with Diagonal Symmetry for Wideband Polarization Converters" in *2022 16th European Conference on Antennas and Propagation (EuCAP)*, Madrid, Spain, 2022, pp. 1-5.

- [J2] A. Alex-Amor, **S. Moreno-Rodríguez**, P. Padilla, J. F. Valenzuela-Valdés and C. Molero, "Analytical equivalent circuits for three-dimensional metamaterials and metagratings," *Physical Review Applied*, vol. 20, p. 044010, Oct 2023.

- [J3] Mario Perez Escribano, **S. Moreno-Rodríguez**, C. Molero , J. F. Valenzuela-Valdés, P. Padilla and A. Alex-Amor, "Analytical Framework to Model Reconfigurable Metasurfaces including Lumped Elements," *IEEE Transactions on Circuits and Systems II: Express Briefs*, vol. 71, no. 4, pp. 1784-1788, April 2024.

- [J4] A. Alex-Amor, **S. Moreno-Rodríguez**, P. Padilla, J. F. Valenzuela-Valdés and C. Molero, "Diffraction phenomena in time-varying metal-based metasurfaces," *Physical Review Applied*, vol. 19, p. 044014, Apr 2023.

- [J5] **S. Moreno-Rodríguez**, A. Alex-Amor, P. Padilla, J. F. Valenzuela-Valdés and C. Molero, "Time-Periodic Metallic Metamaterials defined by Floquet Circuits," *IEEE Access*, vol. 11, pp. 116 665–116 673, 2023.

- [J6] **S. Moreno-Rodríguez**, A. Alex-Amor, P. Padilla, J. F. Valenzuela-Valdés, and C. Molero, "Space-time metallic metasurfaces for frequency conversion and beam forming," *Physical Review Applied*, vol. 21, p. 064018, Jun. 2024.

- [C2] **S. Moreno-Rodríguez**, M. Pérez-Escribano, S. Ortiz-Ruiz, A. Alex-Amor, B. Plaza-Gallardo, Francisco G. Ruiz, and C. Molero, "Reference-Plane Invariant Free Space Dielectric Material Characterization up to 330 GHz," *2024 4th URSI Atlantic Radio Science Meeting (AT-RASC)*, Meloneras, Spain, 2024.

Other related **journal papers** that have been generated along the development of this Thesis but have not been included:

- [OJ1] M. A. Balmaseda-Márquez, **S. Moreno-Rodríguez**, P. H. Zapata, C. Molero and J. F. Valenzuela-Valdés, "Fully-Metallic 3-D Cells for Wideband Applications," *IEEE Transactions on Antennas and Propagation*, vol. 71, no. 5, pp. 4588-4593, May 2023.

- [OJ2] P. H. Zapata-Cano, **S. Moreno-Rodríguez**, S. Amanatiadis, A. Alex-Amor, Z. D. Zaharis, and C. Molero, "Transient States to Control the Electromagnetic Response of Space-time Dispersive Media," *arXiv preprint*, arXiv:2406. 18376, 2024.

- [OJ3] S. Ortiz-Ruiz, M. Pérez-Escribano, **S. Moreno-Rodríguez**, Á. Palomares-Caballero, J. F. Valenzuela-Valdés, F. G. Ruiz, and C. Molero, "Broadband Frequency Selective Surface Absorber based on Laser-Induced Graphene for Applications from Ku-band to Q-band," *TechRxiv*, July 09, 2024.

Other related **conference papers** that have been generated along the development of this Thesis but have not been included:

- [OC1] **S. Moreno-Rodríguez**, A. Alex-Amor, P. Padilla, J. F. Valenzuela-Valdés and C. Molero,"Analysis of Time-Periodic Metallic Metamaterials," in *2023 17th European Conference on Antennas and Propagation (EuCAP)*, Florence, Italy, 2023, pp. 1-5.

- [OC2] **S. Moreno-Rodríguez**, A. Alex-Amor, P. Padilla, J. F. Valenzuela-Valdés and C. Molero,"Analytical Circuit Models: From Purely Spatial to Space-Time Structures," in *2024 18th European Conference on Antennas and Propagation (EuCAP)*, Glasgow, United Kingdom, 2024, pp. 1-5.

- [OC3] J. E. Galeote-Cazorla, A. Ramirez-Arroyo, **S. Moreno-Rodríguez**, J. M. Molina-García-Pardo, María-Teresa Martinez-Inglés, P. Padilla and J. F. Valenzuela-Valdés "A Study on W-Band Frequency Attenuation in the Presence of Human Blockage," in *2024 18th European Conference on Antennas and Propagation (EuCAP)*, Glasgow, United Kingdom, 2024, pp. 1-5.

- [OC4] M. Pérez-Escribano, **S. Moreno-Rodríguez**, A. Alex-Amor, J. F. Valenzuela-Valdés, P. Padilla, and C. Molero, "Analytical Method to Model Spatiotemporal Metasurfaces," *2024 4th URSI Atlantic Radio Science Meeting (AT-RASC)*, Meloneras, Spain, 2024.

- [OC5] **S. Moreno-Rodríguez**, M. Pérez-Escribano, S. Ortiz-Ruiz, Francisco G. Ruiz, B. Plaza-Gallardo, C. Molero, and E. Márquez-Segura "Setup for Material Characterization in the 110-170 GHz Band," *2024 IEEE International Symposium on Antennas and Propagation and USNC-URSI Radio Science Meeting (AP-S/URSI)*, Florence, Italy, July 2024.

- [OC6] Pablo H. Zapata-Cano, **S. Moreno-Rodríguez**, Stamatios Amanatiadis, A. Alex-Amor, Zaharias D. Zaharis, and C. Molero "Transient Analysis of Space-Time Frequency-Dispersive Metal Slabs," *2024 18th International Congress on Engineered Materials Platforms for Novel Wave Phenomena (Metamaterials)*, Creete, Greece, Sept. 2024.

Some of the research results derived from this Doctoral Thesis have received the following **awards** and recognitions:

- The paper entitled "Space-Time Metallic Metasurfaces for Frequency Conversion and Beamforming," has been selected as an Editor's Suggestion in the journal *Physical Review Applied* in volume 21, issue 6, June 2024.

- Finalist of the Young Researchers Award at URSI 2021 (Vigo, Spain) for the paper "3D-Printed Fresnel Lens At 60 GHz".
- Finalist of the Young Researchers Award at URSI 2022 (Málaga, Spain) for the paper "Full-Metal 3D Metasurface for Wideband Polarizers using phase-resonance".
- Finalist of the INDRA Award at URSI 2023 (Cáceres, Spain) for the paper "Floquet Circuits Applied to Time-Varying Metallic Metasurfaces".
- Finalist of the Young Researchers Award at URSI 2024 (Cuenca, Spain) for the paper "Novel Frequency-Selective Surface Absorber based on Laser-Induced Graphene".

During the realization of the Thesis, the following **international stay** have been carried out in the following research center of recognized prestige:

- Visiting scholar at Instituto Superior Técnico (IST) for three months in Lisbon, Portugal, in 2024. This stay, which focused on the design of a flat wideband LWA for the K/Ka frequency bands, was supervised by Full Professor Carlos Fernandez, Professor Sérgio de Almeida Matos, and Professor João Monteiro Felício. The results of the research stay will be submitted to a journal and are expected to be published within the next few months.

In addition, the PhD candidate's academic training has been complemented by the following **international course**:

- Eledia@Auth School course entitled "Global Optimization Methods: Theory, Techniques, and MatLab Simulations" and organized by Prof. Andrea Massa, University of Trento (Italy), Prof. George Karagiannidis, Prof. K. Sotirios Goudos, Prof. Traianos Yioultsis and Dr. Zaharias D. Zaharis, Aristotle University of Thessaloniki (Greece), Thessaloniki, Greece, 2022.

Chapter 2

Publications

This chapter details the main contributions that summarize the achieved objectives of the Doctoral Thesis. It presents eight papers, with six indexed in high-impact journals and two as contributions to international congresses. Each paper discusses and validates various features outlined in Section 1.1, organized into four sections: space modulation, time modulation, space-time modulation, and material characterization. Additionaly, for each postprint version of the published manuscript, information related to the journal and their quiality indexes are provided.

2.1 Space Modulation

2.1.1 Polarization-Insensitive Unit Cells for a Cost-Effective Design of a 3-D-Printed Fresnel-Lens Antenna

This paper presents a flat Fresnel lens operating at 60 GHz. Its dielectric T-shaped unit cell enables the design of the lens by tailoring each subzone with the required relative permittivity. Additionally, due to the symmetry of the cell, this lens is robust to variation of the polarization angle, allowing similar behavior under both Transverse Magnetic (TM) and Transverse Electric (TE) incidences. The use of SLA for 3D printing has enabled the precise fabrication of the cells in the subzones with the lowest permittivity. The measured results demonstrate a gain increase of up to 26.5 ± 0.5 dBi between 55 GHz and 65 GHz, as well as mechanical beam steering capabilities when the center of the lens is shifted with respect to the central part of the feed section. Therefore, this lens is ideal for broadband P2P communications centered at 60 GHz that require reconfigurability to follow the users.

THIS IS A POSTPRINT VERSION OF THE PAPER:

S. Moreno-Rodríguez, M. A. Balmaseda-Márquez, J. Carmona-Murillo and Á. Palomares-Caballero, "Polarization-insensitive unit cells for a cost-effective design of a 3-D-Printed fresnel-lens antenna," *Electronics*, vol. 11, no. 3, p. 338, Jan. 2022.

- Journal Impact Factor (JIF) in JCR 2022: 2.9
- Category: COMPUTER SCIENCE, INFORMATION SYSTEMS. JIF Rank: 99/158 (Q3).
- Category: ENGINEERING, ELECTRICAL & ELECTRONIC. JIF Rank: 131/275 (Q2).
- Category: TELECOMMUNICATIONS. JIF Rank: 72/160 (Q2).

Disclaimer:
This work has been published in Electronics.
DOI: 10.3390/electronics11030338

electronics

MDPI

Article

Polarization-Insensitive Unit Cells for a Cost-Effective Design of a 3-D-Printed Fresnel-Lens Antenna

Salvador Moreno-Rodríguez [1], Miguel A. Balmaseda-Márquez [1], Javier Carmona-Murillo [2] and Ángel Palomares-Caballero [1,*]

[1] Department of Signal Theory, Telematics and Communications, University of Granada (UGR), 18071 Granada, Spain; salvamr96@ugr.es (S.M.-R.); migbalmar@correo.ugr.es (M.A.B.-M.)
[2] Department of Computing and Telematics Engineering, University of Extremadura (UEx), 06006 Badajoz, Spain; jcarmur@unex.es
* Correspondence: angelpc@ugr.es

Abstract: A 3-D printed Fresnel-lens antenna formed by dielectric unit cells insensitive to polarization is presented in this article. The proposed unit cell can be implemented in any azimuth orientation, simplifying the design and the implementation of the Fresnel subzones, which is an advantage over the previous 3-D-printed Fresnel-lens designs. The unit cell exhibits a T-shaped geometry capable of providing no change in relative permittivity under TE polarizations orthogonal to each other. The novel design of the unit cell also provides robustness under oblique incidence and frequency. These features allow the radial arrangement of the unit cells to configure the subzones of the Fresnel lens, ensuring the desired relative permittivity. Additionally, the geometry of the printed unit cells enables self-supported subzones with the minimum number of unit cells per subzone. A 3-D-printed prototype of the proposed Fresnel lens was manufactured by stereolithography (SLA). The measurement results showed a good agreement with the simulated ones. The measured gain was 26.5 ± 0.5 dBi from 55 GHz to 65 GHz with a mean antenna efficiency of 79%.

Keywords: 3-D printing; Fresnel lens; millimeter-waves; lens antenna; polarization insensitivity

Citation: Moreno-Rodríguez, S.; Balmaseda-Márquez, M.A.; Carmona-Murillo, J.; Palomares-Caballero, Á. Polarization-Insensitive Unit Cells for a Cost-Effective Design of a 3-D-Printed Fresnel-Lens Antenna. *Electronics* **2022**, *11*, 338. https://doi.org/10.3390/electronics11030338

Academic Editor: Reza K. Amineh

Received: 28 December 2021
Accepted: 21 January 2022
Published: 23 January 2022

1. Introduction

Lens antennas are the most-promising antenna solutions for the future of wireless communications at millimeter-wave frequencies [1]. This kind of antennas allow to enhance low-directivity antennas such as open-ended waveguides or patch antennas [2]. The gain, which is closely related to the directivity, must be a large number at millimeter-waves communications to overcome the severe path loss introduced in the link budget of a wireless system.

Two main groups of lens antennas can be distinguished depending on the number of refractive indexes employed. On the one hand, there are the gradient-index (GRIN) lenses that require different refractive indexes in the lens structure [3,4]. On the other hand, there is the homogeneous lens that is implemented with a single refractive index value, but the shape of the lens defines its focusing performance [5].

In the design of lens antennas, the determination of the refractive indexes is crucial for a successful implementation of the lens. Due to the significant evolution of the 3-D-printing technologies and the availability of a wide range of materials with different permittivity, GRIN lenses based on 3-D printing have been reported in the literature. Among the GRIN lenses, Luneburg [6–8], Gutman [9], and flat lenses [10–12] are highlighted. Luneburg and Gutman lenses provide an ultra-wideband performance with low scanning losses. However, to further increment the directivity, a 2-D focusing is needed, but theses lenses become bulky with a non-planar profile. Transformation optics can be applied to achieve the desired planar profile, but unfortunately it introduces greater refractive index values in the lens structure [7,12]. The GRIN flat lenses inherently have a planar profile, but a

larger aperture of this kind of lens requires either increasing the maximum refractive index or thickening the lens. This fact could be a drawback in any case of implementation or manufacturing.

Another type of inhomogeneous lens, in addition to the above mentioned, is the Fresnel lens (FL) [13]. At the expense of reducing the operating bandwidth, this kind of lens is also capable of producing a far-field focusing with a simple and low-profile design. One of the main advantages of the Fresnel lens design is the flexibility in the selection of the required permittivity values [14]. Moreover, there is no need to use matching layers (as commonly employed in GRIN flat lenses [15]) since the thickness of the Fresnel lens can be tuned to avoid reflections. Several FL designs based on 3-D printing have been reported. In [16], a classical grooved-dielectric Fresnel zone plate (FZP) was implemented with fused deposition modeling (FDM). An enhanced version of the FZP antenna designed by printed dielectric posts is presented in [17]. If the multidielectric zone version is selected instead of the grooved-dielectric FZP, more design control of the FL is achieved [14]. The lens antennas presented in [18–20] provide 3-D-printed FL designs in different operating frequency ranges and 3-D manufacturing. In contrast with the previous works, in this article is presented a cost-effective design of a 3-D-printed FL for the 60 GHz band. The unit cells, which form the Fresnel lens, allow to be implemented in an easy manner since they can be oriented in any azimuth direction ϕ without changing its relative permittivity. This enhanced feature reduces the complexity in the implementation of the Fresnel subzones by means of 3-D-printed unit cells. The design of the unit cell provides insensitivity to TEM modes whose electric field points in either the vertical (TE polarization) or horizontal (TM polarization) direction. In addition, the geometry of the unit cell produces self-supporting subzones and effortless 3-D-printing fabrication with SLA.

This article is organized as follows. In Section 2, the proposed FL and unit-cell designs are analyzed by electromagnetic simulations. Section 3 discusses the manufacturing and measurements of the 3-D-printed FL. Finally, in Section 4, the main conclusions are presented.

2. Fresnel Lens Design

The proposed FL design and the chosen feeder is shown in Figure 1a. The lens is illuminated at a distance F by an open-ended waveguide (OEWG) corresponding to a WR15 waveguide that represents a low-directivity radiator (7.5 dBi at 60 GHz). The FL is composed by three zones, each of them composed of four subzones; therefore, there are a total of 12 subzones. In Figure 1b is indicated the subzones by a color coding (yellow, red, blue, and light blue), which is periodically repeated from the center of the lens up to the furthest subzone. The n-th subzone has an outer radius of b_n; as an example, the first zone of the lens will be described as follows. The first subzone is composed by four subzones, and these four subzones are repeated three times along the radius of the lens because the total number of zones implemented in the FL is three. The first subzone is highlighted in yellow at the lens center; the subzone radius is b_1; and its relative permittivity is ε_{r1}. The circular ring next to the previous subzone is the second subzone that is highlighted in red whose radius is b_2, and its relative permittivity is ε_{r2}. Then, the third subzone is highlighted in blue whose radius is b_3, and its relative permittivity is ε_{r3}. Finally, the fourth subzone is highlighted in light blue whose radius is b_4, and its relative permittivity is ε_{r4}. The values of the b_n and the relative permittivities were selected according the design equations presented in [14]. Multidielectric FL provides a great flexibility in the design stage considering the maximum dielectric constant that can be achievable. In our case, the used resin for the SLA printing had a relative permittivity ε_r of 2.6. Simply by modifying the thickness t of the lens, a FL can be effectively designed where the required relative permittivities (ε_{r1}, ε_{r2}, ε_{r3}, and ε_{r4}) are lower than the maximum value set for ε_r. Unlike other types of lenses, where their relative permittivity distribution is already established [7–9], the FL can be adjusted to the employed printed material. In Table 1 are listed the value of parameters used in the proposed FL design. The total diameter (D) of the

lens was 71.4 mm indicated by the radius of the subzone furthest away from the center; this is b_{12}. The value for the thickness of the lens t was selected to reduce undesired reflections in the first subzone b_1 [14], while the F/D ratio had been set to 0.448 in order to improve the lens directivity along the frequency range. This enhancement depends on the illumination provided by the OEWG and, in consequence, to the distance between the lens and its feeder (OEWG in our case).

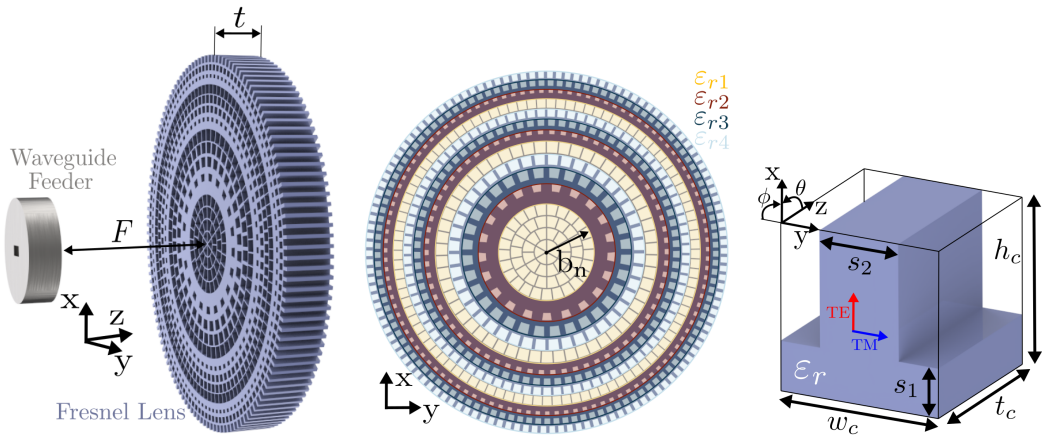

Figure 1. Fresnel lens design: (**a**) 3D view of the lens and the waveguide feeder. (**b**) Planar view of the subzones. (**c**) Dielectric unit cell with T-shaped geometry.

Table 1. Values (in mm) of the parameters used in the design of the Fresnel lens.

Param.	t	F	ε_r	ε_{r1}	ε_{r2}	ε_{r3}	ε_{r4}	b_1	b_2	b_3	b_4	b_5
Value	8.94	32	2.6	1.25	2.36	1.95	1.58	9.4	13.5	16.6	19.4	21.8
Param.	b_6	b_7	b_8	b_9	b_{10}	b_{11}	b_{12}	s_{b1}	s_{b2}	s_{b3}	s_{b4}	
Value	24.1	26.2	28.3	30.2	32.1	33.9	35.7	0.26	2.75	1.32	0.72	

In Figure 1c, it is illustrated the design of the unit cell that forms the subzones of the FL. The unit cell presents a T-shaped geometry that is uniform along the propagation direction z. A typical strategy to reduce the relative permittivity of a dielectric cube is by inserting air zones in the unit-cell structure. In our case, rectangular air slabs are introduced symmetrically (uncolored zones) to allow a tuning of the relative permittivity. Modifying parameters s_1 and s_2 of the T-shaped geometry and keeping fixed the parameters w_c and h_c, the relative permittivity of the unit cell can range from 1 to ε_r. In order to choose the values for s_1 and s_2, which determine the ε_{rn} for each subzone, full-wave simulations in CST Microwave Studio were performed. Frequency-solver and unit-cell boundary conditions along the x- and y-directions were imposed to properly compute the scattering parameters for the TE and TM polarizations. Then, the scattering parameters were analyzed through the formulation proposed in [21] to calculate the modified relative permittivity of the unit cell. It is important to note that the thickness t_c of the unit cell does not affect the computed relative permittivity since there is no change in the structure along the propagation direction.

Since the dimensions of the T-shaped geometry alters the amount of air inside the unit cell, a filling factor f was defined as the ratio between the area with dielectric and the total area in XY plane of the unit cell. Figure 2a shows the relative permittivities for different filling factors when the dimensions of the T-shaped geometry are equal ($s_1 = s_2$) and when they are not ($s_1 \neq s_2$) for a sub-wavelength unit cell. In this figure, the TE and TM polarizations are also assessed. It is important to note that any other incident linear polarization with different azimuth angle ϕ (see axis of Figure 1c) can be decomposed

and analyzed by the orthogonal polarizations TE and TM analyzed in Figure 2a. It is observed the importance of the similarity in the dimensions of the T-shape to obtain a polarization-insensitive unit cell suitable for the radial arrangement in the proposed FL design. The reason for this fact is that both incident polarizations are affected by the same amount of dielectric material. The same conclusions can be extracted if the unit cell or the incident polarization is rotated in ϕ. In this case, the impinging polarization can be decomposed in two vectors aligned with the edges of the unit cell that can be analyzed as TE and TM in Figure 1c. If the dimensions are not equal, the relative permittivity of the unit cell depends on the incident polarization, which results in a non-constant relative permittivity in the subzones of the FL (see Figure 2a). This fact entails that the relative permittivity of each subzone depends on the relative position between incident polarization and the orientation of the unit cell in the subzone. Figure 2b shows the performance of unit cells with different permittivity values along the target frequency range for the case when $s_1 = s_2$ with a normal incidence ($\theta = 0°$). As it was expected because the unit cell is fully dielectric, almost-constant values for the dielectric constant were obtained for TE and TM polarizations, which is also desired for the FL design.

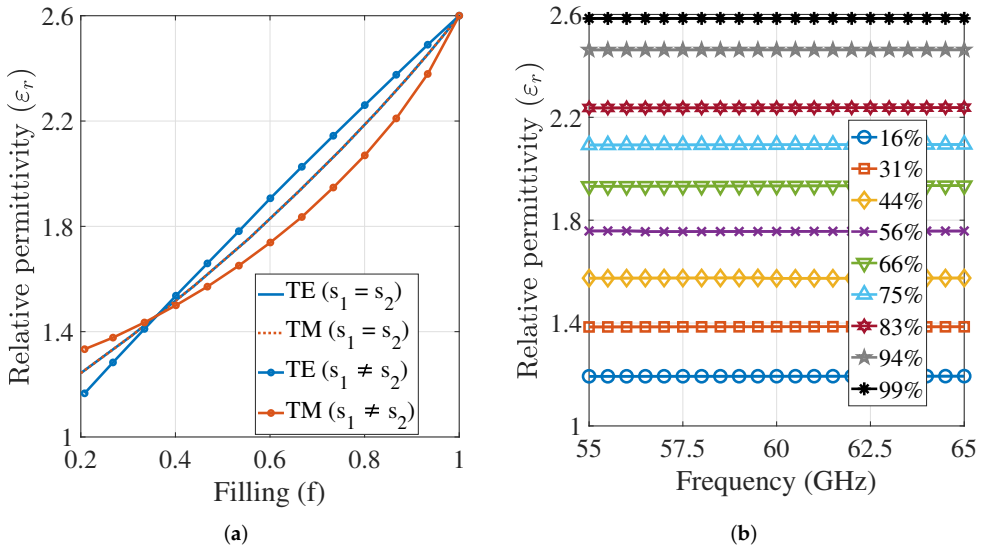

Figure 2. (**a**) Relative permittivity of the unit cell when the filling factor varies at 60 GHz. The dimensions are: $w_c = h_c = t_c = 1$ mm. For the case $s_1 \neq s_2$, $s_2 = 0.2$ mm and s_1 varies. (**b**) Relative permittivity along the frequency for different filling factors.

The S-parameters in phase and magnitude of the unit cell with equal dimensions ($s_1 = s_2$) under oblique incidence was examined in Figure 3. In this case, the thickness t_c of the unit cell was set to 8.94 mm, which is the total thickness of the FL (see Table 1), and dielectric losses ($\tan\delta = 0.02$) were also included to accurately evaluate the performance in the magnitude of the proposed unit cell. The maximum angle assessed for oblique incidence (θ) corresponds to the relative position between the waveguide feeder and the outermost Fresnel subzone. Figure 3a shows the variation in the transmission phase between the normal incidence and the extreme oblique incidence ($\theta = 48°$). The smaller the difference between the transmission-phase values obtained for normal incidence and oblique incidence, the less error is introduced in the Fresnel-lens-design equations (mainly Equation (3) from [14]). Thus, being farther away from the center subzones was found to provide the desired constructive interference at the focus of the lens. The transmission phase implicitly takes into account the relative permittivity produced by each oblique incidence angle. The transmission phase difference was at most 20° for the entire filling-factor range and both orthogonal polarizations. This performance was enabled by the T-shaped unit cell with equal dimensions. Moreover, due to the fully dielectric nature of

the unit cell in which the dielectric material had a relatively low permittivity (2.6), possible resonances in the unit cell structure were avoided in the target frequency range for both normal and oblique incidence (up to $\theta = 48°$). These possible resonances that may appear at oblique incidence drastically modify the electromagnetic response observed at normal incidence. On the other hand, Figure 3b,c present the transmission response in magnitude for the different relative permittivities and oblique incidence angles, respectively. The considered relative permittivities in these simulated results are the ones needed for the FL subzones. Figure 3b shows transmission losses between 0.3 dB and 2 dB for the four required types of unit cell (one for each subzone). The losses observed were produced mainly by two factors: reflection in the dielectric-air interface of the unit cell and dielectric losses due to the loss tangent of the employed resin material. The unit cell with relative permittivity ε_{r1} is the one that produces lower losses because it has the closest relative permittivity (1.25) to that of the free space, and it has the lowest amount of dielectric material in its structure regarding the other types of unit cells. In contrast, a unit cell that provides the ε_{r2} has higher relative permittivity and contains more dielectric material in its structure. In consequence, it provides higher losses in the transmission coefficient as was expected for the two above factors. In Figure 3c, the transmission coefficient for different oblique incidence angles is assessed in the unit cell that provides ε_{r3}. As the incidence angle increased, the transmission magnitude slightly varied with respect to the normal incidence case. Therefore, it was demonstrated that the proposed unit cell provides robustness to large oblique incidence angles beneficial for preserving the behavior of the subzones farthest from the center of the lens. This unit-cell characteristic was scarcely analyzed in previous 3-D-printed Fresnel lenses.

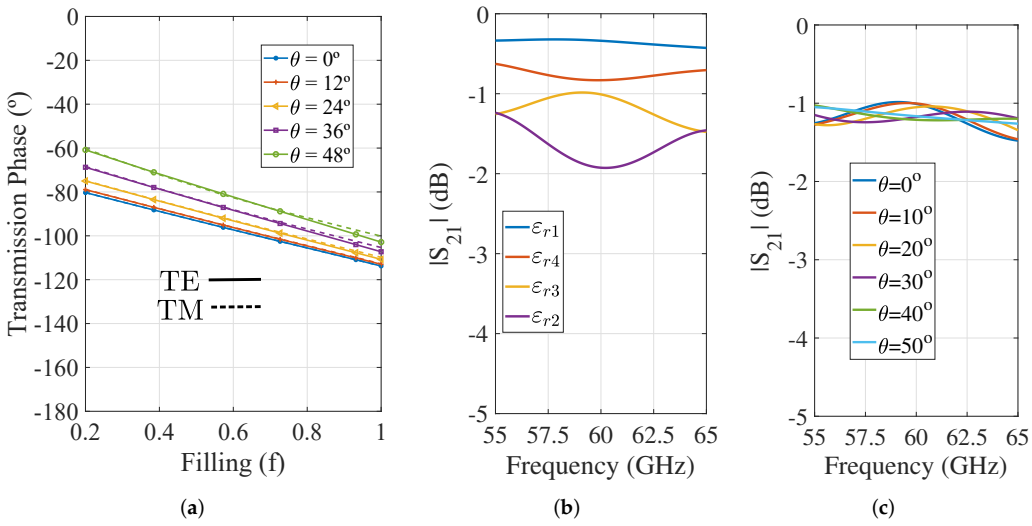

(**a**) (**b**) (**c**)

Figure 3. (**a**) Transmission phase response of the proposed unit cell for different filling factors, oblique incidence angles, and polarizations. The dimensions are: $w_c = h_c = 1$ mm, $t_c = 8.94$ mm, and $s_1 = s_2$. (**b**) Transmission magnitude response for the relative permittivities required in the FL subzones under normal incidence. (**c**) Transmission magnitude response for the unit cell of the third subzone (ε_{r3}) under different oblique incidence angles.

In order to achieve the above required permittivities for the subzones, both dimensions s_1 and s_2 of the T-shaped geometry for each subzone are represented as s_{bn} (see Figure 1b), n being the number of the subzone. Table 1 includes the dimension s_{bn} up to the fourth subzone. The dimensions for the other subzones can be calculated by means of a size scaling knowing the aspect relations of the first four subzones. This scaling process approximately keeps the designed relative permittivity as long as the unit cell is sub-wavelength. For the first subzone of the FL design, four unit cells were implemented, while in the other subzones, a single unit cell in the radial direction was only required. In this manner,

the sizes of all the unit cells, which compose the FL, were sub-wavelength providing the designed relative permittivity. The unit cells were square and had equal dimensions for the T-shaped geometry to preserve the relative permittivity of the subzone under any polarization. This fact enable a cost-effective implementation of the FL subzones by the radial arrangement of the unit cells. Moreover, the proposed unit cell is suitable in the 3-D-printing process because all the subzones are self-supported, avoiding the inclusion of additional supports.

Figure 4a illustrates the phase and amplitude distributions of the electric field in the planes before (framed in gray) and after (framed in black) the FL antenna. The low directivity provided by the waveguide feeder produces a spherical wavefront that impinges in the lens. The FL transforms this spherical wavefront into a flatter wavefront over the entire transverse plane after the lens. Regarding the amplitude distribution in the planes under analysis (illustrated on the right side of the Figure 4a), the amplitude becomes more uniform across the lens due to the phase correction. However some variations in amplitude were still observed caused by the different transmission coefficients provided by the unit cells that form the subzones (Figure 3b). In spite of this fact, the field transformation in the phase wavefront produced by the FL allows a huge increase in directivity. Figure 4b presents the E- and H-plane radiation-patterns comparison between the homogeneous multidielectric, which represents an ideal subzone implementation, and the proposed FL. Good agreement was observed in the comparison, which indicates the effectiveness of the proposed unit cells for the FL design.

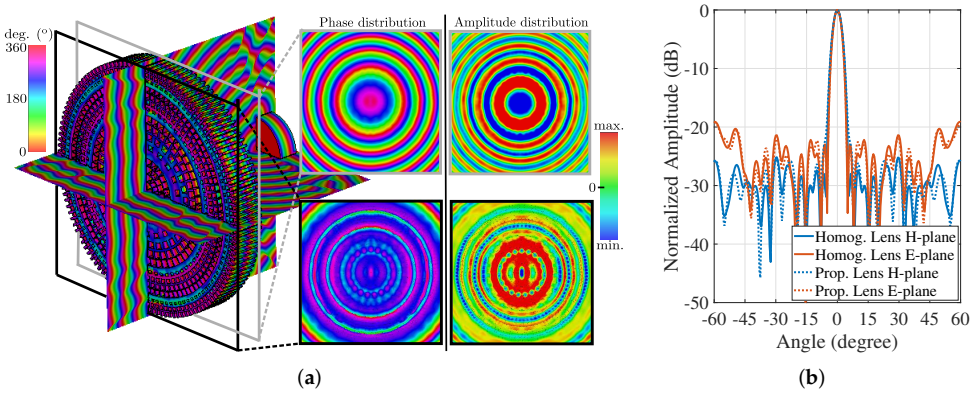

(**a**) (**b**)

Figure 4. Radiation performance of the Fresnel-lens antenna: (**a**) Amplitude and phase distributions at 60 GHz. (**b**) Radiation-patterns comparison with the homogeneous multidielectric Fresnel lens at 60 GHz.

3. Manufacturing and Measurements

The depicted FL design was manufactured with SLA printing. The employed 3-D printer was the Form 3 from Formlabs, and the grey resin was printing material. A 50 µm thickness layer with a horizontal orientation for the printed lens was adopted to achieve a successful printing. This orientation for the FL is very important to correctly print the unit cells where the air zones cannot be covered by resin [17]. Additionally, high vertical supports were included to conserve theses air zones during the printing process. Once the printing was finished, the lens was washed with isopropyl alcohol, cured, and sanded on the surface where the supports were located.

Far-field performance of the printed FL was measured in the anechoic chamber of the University of Granada. Figure 5a shows the measurement setup and the lens prototype. Both insets included in Figure 5a display the same printed Fresnel lens with different light illumination. An antenna holder (illustrated on the right side of the figure) was 3-D printed to align the lens with the OEWG and set the focal distance between them. In addition, the antenna holder contains fixings for moving the FL along its y-direction and, in this manner, assess its scanning performance. These positions are indicated in the figure as well

as the OEWG (waveguide feeder). The distance between positions was 6 mm, achieving an offset between the center of the Fresnel lens and the OEWG of 24 mm at the farthest position. The smaller the distance between positions, the higher the resolution of the beam-steering angle. The simulated and measured results for the reflection coefficient with and without the FL are shown in Figure 5b. The lens antenna system provides a good impedance matching (below −10 dB) along the entire frequency band both with and without the FL. This is because the reflection mainly occurs in the radiation of the OEWG. Some differences between simulated and measured results exist due to the use of a WR15 coax-to-waveguide transition that is necessary to connect the OEWG to the vector-network analyzer (VNA). It was not possible to include this transition in the calibration, but it does not alter the measurements since the measured reflection coefficient level is approximately the simulated one in the target frequency range.

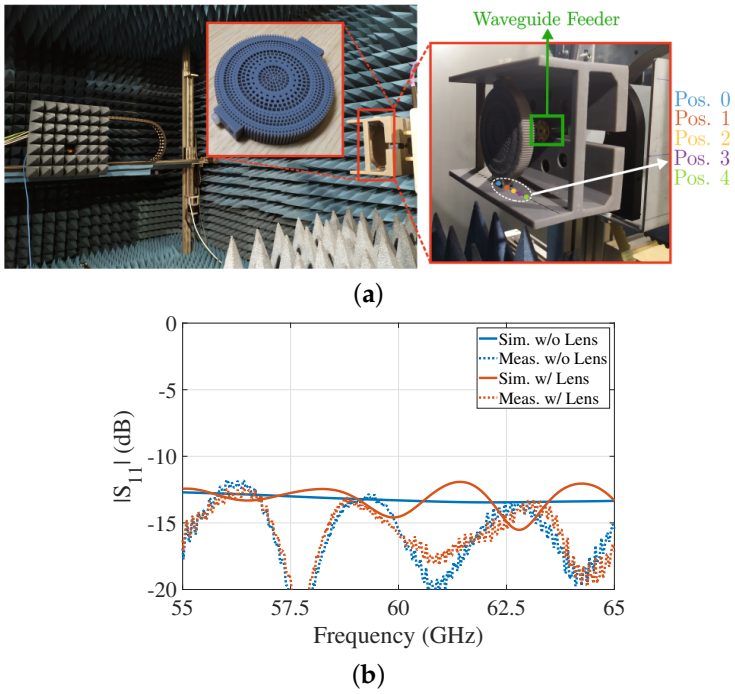

Figure 5. (**a**) 3-D printed prototype and far-field measurement setup. (**b**) Simulated and measured results of the Fresnel-lens antenna.

Figure 6 presents the simulated and measured radiations patterns for the E-plane (see Figure 6a) and H-plane at different positions and frequencies (see Figure 6b–d). Position 0 corresponds when the OEWG is fully aligned with the FL. The rest of the positions represent a 6 mm movement of FL along its y-direction. The larger this movement is, the higher is the pointing angle of the main beam in the H-plane. The measurements reveal that the direction of the main beam is preserved over the frequency and in both planes. Moreover, the beamwidth narrows as the frequency increases, and thus the directivity increases. However, this beamwidth increases, and side lobes appear for larger pointing angles.

In Figure 7a, the simulated and measured gains along the frequency range for the different positions of the lens are shown. It has been included the measured gain of the reference horn antenna (Flann WR15 Standard Gain Horn) used in the measurements to guarantee the correct calculation of the gains. The maximum gain achieved was 27 dBi for the central position. The gain decreased as the pointing angle increased, which was expected from the simulated radiation patterns of Figure 6. For the farthest position (pos. 4), the gain was around 21 dBi, and the pointing angle was 33°. This implies scanning losses of 0.18 dB/°, which are reasonable for this type of lens. In each measured position, the measured gain agrees with the simulated results, which proves the similarity between the estimated-loss tangent ($\tan\delta = 0.02$) and the experimental one. In addition, it is important

to note that the beam-scanning capability of the Fresnel-lens design can be assessed because of the use of a low-directivity feeder. If a feeder with higher directivity had been employed instead, the maximum scanning angle would be smaller because the increase in the lens offset would mean that the lens would receive less power to be re-radiated. In the frequency range, the measured crosspolar level was under −23 dB and the mean antenna efficiency (calculated as the ratio of the simulated directivity, and the measured gain) is 79%. Besides, the aperture efficiency without including the antenna losses, which are taken into account in the antenna efficiency, was about 30% at 60 GHz, which was the design frequency. This value for the aperture efficiency was satisfactory for this kind of antenna system, but it can be improved by the use of a feeder with higher directivity such as a horn antenna. This inclusion would increase, for instance, the spillover efficiency, but also, it would significantly increase the cost of the whole antenna system. In addition, in Figure 7a, the agreement between the simulated and measured gain gets poorer at the end of the frequency range. This is mainly caused by the tolerances in fixing the focal distance F. In order to check the effect of this mechanical tolerance in the gain of the lens for Pos. 0, Figure 7b shows the performance of the simulated gain of the FL along the target frequency range when F varies. As it can be observed, F modifies the behavior of the provided gain along the frequency range. From this figure, we can deduce a lower value for the focal distance in the measurement setup since they are the values that produce a decrease in gain at the end of the measured frequency range. Besides this fact, Figure 7b clearly shows the gain stability at the design frequency (60 GHz) when the focal distance is modified and how the distance F can be tuned to the gain values on both sides of the design frequency.

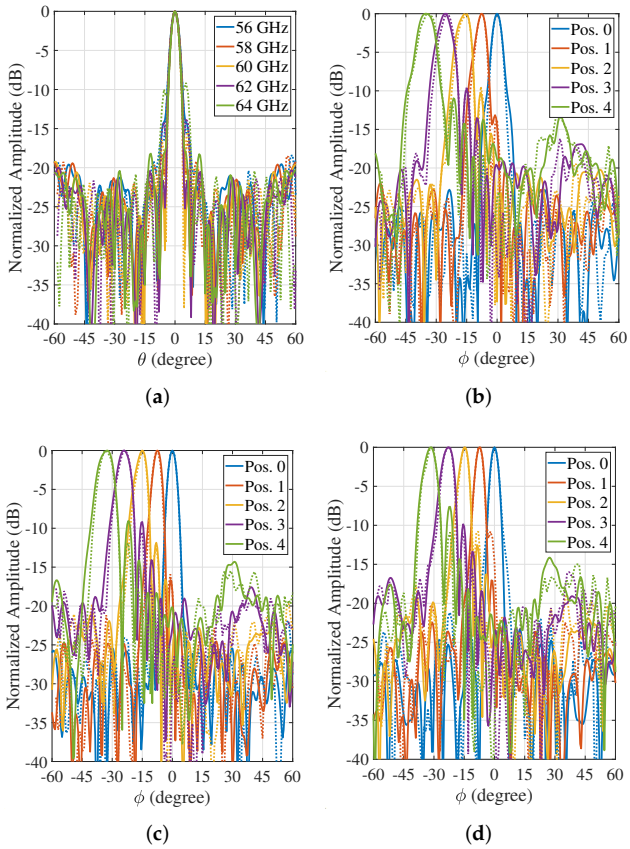

Figure 6. Normalized radiation patterns of the proposed Fresnel lens antenna: (**a**) E-plane for pos. 0. (**b**) H-plane at 56 GHz. (**c**) H-plane at 60 GHz. (**d**) H-plane at 64 GHz. The simulated and measured results are represented by solid and dashed lines, respectively.

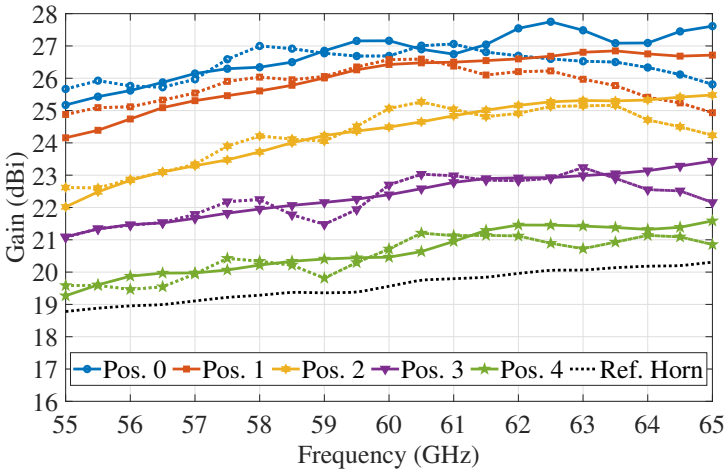

(**a**)

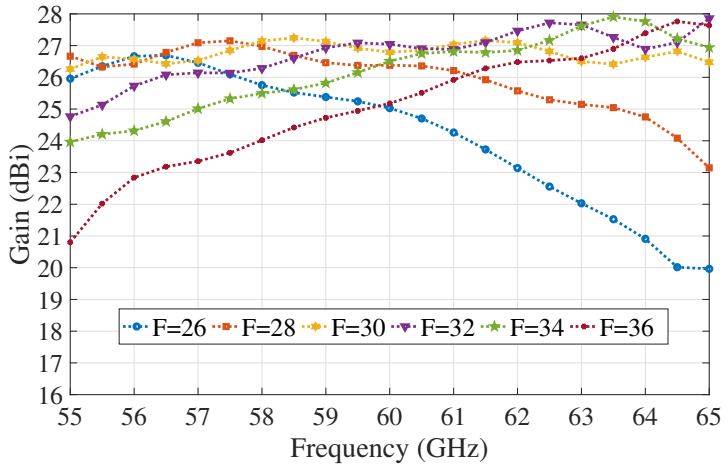

(**b**)

Figure 7. (**a**) Comparison of the gain along the frequency for different lens positions. The simulated and measured results are represented by solid and dashed lines, respectively. (**b**) Simulated gain along the frequency when the focal distance F is modified.

Finally, in Table 2, the proposed FL design is compared with other 3-D-printed FL found in the literature. Our work presents the lowest maximum relative permittivity in the FL design achieving a similar maximum gain even using a low-cost feeder such as OEWG. Due to the geometry of the proposed unit cell, it can be implemented radially in the lens preserving the relative permittivity of the subzones under any incident polarization. In the related works [19,20], their unit cells were analyzed, designed, and implemented in only one orientation, and thus the subzones implementation becomes more complex and limiting. The T-shaped geometry presents greater flexibility in the FL design and a self-supported implementation of the Fresnel subzones for 3-D printing manufacturing. Additionally, the T-shaped unit cell allows to implement unit cells with very low relative permittivity (1.25) without compromising the unit-cell printing and, thus, the lens fabrication. Scanning losses are also included in the comparison table; most of the reported works do not evaluate this radiation characteristic because the employed feeder has a directive radiation diagram, which poorly illuminates the Fresnel lens when the relative position between lens and radiator is varied. The work in [19] can assess the scanning losses because it uses an OEWG as the presented work. Since the same design procedure is followed for the Fresnel lens antenna, similar performance in the scan loss was obtained.

Table 2. Comparison of reported 3-D printed Fresnel-lens antennas with this work.

Ref.	Freq. (GHz)	3-D-Printing Technology	Max. Gain (dBi)	Max. ε_r	Unit-Cell Geometry	Subzone Implement.	Scan Loss (dB/°)
[18]	10	FDM	12.8	4.4	Squared hole	Medium	n. a.
[16]	30	FDM	24.6	2.86	Homogeneous	Easy	n. a.
[19]	22	SLA	27	3.06	Squared hole	Medium	0.16
[20]	60	SLS	28	3.6	Cube shaped	Medium	n. a.
[17]	300	SLA	27.4	2.66	Dielectric post	Medium	n. a.
This Work	60	SLA	27	2.6	T-shaped	Easy	0.18

n. a.: not available.

4. Conclusions

In this study, a cost-effective design for a 3-D-printed Fresnel lens was proposed. The unit cell, which forms the subzones of the Fresnel lens, presents a T-shaped geometry that avoids the modification of the relative permittivity under TE and TM polarizations and oblique incidence. These features are highly desired to enable an effective implementation of the Fresnel subzones by means of a radial arrangement of the unit cell. To validate the proposed design, a 3-D-printed prototype was manufactured by SLA. The experimental results show an operating bandwidth from 55 GHz to 65 GHz where the maximum gain was 27 dBi. Additionally, due to the low-directivity radiator used as the feeder of the lens, the beam-steering capability was produced only by modifying the relative position between the Fresnel lens and the feeder. This radiation feature is of great interest in communications links at millimeter frequencies.

Author Contributions: Conceptualization, Á.P.-C.; methodology, Á.P.-C. and S.M.-R.; formal analysis and investigation, S.M.-R. and M.A.B.-M.; writing—original draft preparation, Á.P.-C., J.C.-M., S.M.-R. and M.A.B.-M.; writing—review and editing, Á.P.-C., J.C.-M., S.M.-R. and M.A.B.-M. All authors have read and agreed to the published version of the manuscript.

Funding: This work was supported in part by the Spanish Government under Project PID2020-112545RB-C54; in part by "Junta de Andalucía" under Project B-TIC-402-UGR18, Project A-TIC-608-UGR20, Project P18.RT.4830, and Project PYC20-RE-012-UGR; in part by the European Regional Development Fund and Junta de Extremadura under Project IB18003; and in part by the Predoctoral Grant FPU18/01965.

Data Availability Statement: Not applicable.

Conflicts of Interest: The authors declare no conflict of interest.

References

1. Quevedo-Teruel, O.; Ebrahimpouri, M.; Ghasemifard, F. Lens Antennas for 5G Communications Systems. *IEEE Commun. Mag.* **2018**, *56*, 36–41. [CrossRef]
2. Liu, K.; Zhao, C.; Qu, S.W.; Chen, Y.; Hu, J.; Yang, S. A 3-D-Printed Multibeam Spherical Lens Antenna with Ultrawide-Angle Coverage. *IEEE Antennas Wirel. Propag. Lett.* **2021**, *20*, 411–415. [CrossRef]
3. Ma, H.F.; Cui, T. Three-dimensional broadband and broad-angle transformation-optics lens. *Nat. Commun.* **2010**, *1*, 124, [CrossRef] [PubMed]
4. Jo, E.S.; Kim, D. 3-D Printer Based Lens Design Method for Integrated Lens Antennas. *IEEE Antennas Wirel. Propag. Lett.* **2018**, *17*, 2090–2093. [CrossRef]
5. Fernandes, C.A.; Lima, E.B.; Costa, J.R. Dielectric Lens Antennas. In *Handbook of Antenna Technologies*; Springer: Singapore, 2016; pp. 1001–1064. [CrossRef]
6. Wang, C.; Wu, J.; Guo, Y.X. A 3-D-Printed Wideband Circularly Polarized Parallel-Plate Luneburg Lens Antenna. *IEEE Trans. Antennas Propag.* **2020**, *68*, 4944–4949. [CrossRef]
7. Lou, Y.H.; Zhu, Y.X.; Fan, G.F.; Lei, W.; Lu, W.Z.; Wang, X.C. Design of Ku-Band Flat Luneburg Lens Using Ceramic 3-D Printing. *IEEE Antennas Wirel. Propag. Lett.* **2021**, *20*, 234–238. [CrossRef]
8. Lei, S.; Han, K.; Li, X.; Wei, G. A Design of Broadband 3-D-Printed Circularly Polarized Spherical Luneburg Lens Antenna for X-Band. *IEEE Antennas Wirel. Propag. Lett.* **2021**, *20*, 528–532. [CrossRef]

9. Bjorkqvist, O.; Zetterstrom, O.; Quevedo-Teruel, O. Additive manufactured dielectric Gutman lens. *Electron. Lett.* **2019**, *55*, 1318–1320. [CrossRef]
10. Garcia-Marin, E.; Filipovic, D.; Masa-Campos, J.; Sanchez-Olivares, P. Low-cost lens antenna for 5G multi-beam communication. *Microw. Opt. Technol. Lett.* **2020**, *62*, 3611–3622. [CrossRef]
11. Imbert, M.; Papió, A.; De Flaviis, F.; Jofre, L.; Romeu, J. Design and Performance Evaluation of a Dielectric Flat Lens Antenna for Millimeter-Wave Applications. *IEEE Antennas Wirel. Propag. Lett.* **2015**, *14*, 342–345. [CrossRef]
12. Poyanco, J.M.; Pizarro, F.; Rajo-Iglesias, E. Wideband hyperbolic flat lens in the Ka-band based on 3D-printing and transformation optics. *Appl. Phys. Lett.* **2021**, *118*, 123503. [CrossRef]
13. Hristov, H.D. *Fresnel Zones in Wireless Links, Zone Plate Lenses and Antennas*, 1st ed.; Artech House, Inc.: Norwood, MA, USA, 2000.
14. Hristov, H.D.; Rodriguez, J.M. Design Equation for Multidielectric Fresnel Zone Plate Lens. *IEEE Microw. Wirel. Components Lett.* **2012**, *22*, 574–576. [CrossRef]
15. He, Y.; Eleftheriades, G.V. Matched, Low-Loss, and Wideband Graded-Index Flat Lenses for Millimeter-Wave Applications. *IEEE Trans. Antennas Propag.* **2018**, *66*, 1114–1123. [CrossRef]
16. Jeong, K.H.; Ghalichechian, N. Design, Fabrication and Measurement of a Millimeter Wave Fresnel Lens using Additive Manufacturing. In Proceedings of the 2018 IEEE International Symposium on Antennas and Propagation USNC/URSI National Radio Science Meeting, Boston, MA, USA, 8–13 July 2018; pp. 1879–1880. [CrossRef]
17. Wu, G.B.; Zeng, Y.S.; Chan, K.F.; Qu, S.W.; Chan, C.H. 3-D Printed Circularly Polarized Modified Fresnel Lens Operating at Terahertz Frequencies. *IEEE Trans. Antennas Propag.* **2019**, *67*, 4429–4437. [CrossRef]
18. Zhang, S. Design and Fabrication of 3D-Printed Planar Fresnel Zone Plate Lens. *Electron. Lett.* **2016**, *52*, 833–835. [CrossRef]
19. Monkevich, J.M.; Le Sage, G.P. Design and Fabrication of a Custom-Dielectric Fresnel Multi-Zone Plate Lens Antenna Using Additive Manufacturing Techniques. *IEEE Access* **2019**, *7*, 61452–61460. [CrossRef]
20. Pourahmadazar, J.; Denidni, T. Towards Millimeter-wavelength: Transmission-Mode Fresnel-Zone Plate Lens Antennas using Plastic Material Porosity Control in Homogeneous Medium. *Sci. Rep.* **2018**, *8*, 5300. [CrossRef] [PubMed]
21. Chen, X.; Grzegorczyk, T.M.; Wu, B.I.; Pacheco, J.; Kong, J.A. Robust method to retrieve the constitutive effective parameters of metamaterials. *Phys. Rev. E* **2004**, *70*, 016608. [CrossRef] [PubMed]

2.1.2 On the Design of Unit Cells with Diagonal Symmetry for Wideband Polarization Converters

In this contribution to an international congress, two reflection polarization converters have been designed and fabricated using a quite similar metasurface. Thanks to its diagonal symmetry, the response of both structures can be analyzed through simple equivalent circuit topologies by decomposing their electric field vector into their main components. Both polarizers exhibit ultra-wideband behavior at normal and oblique incidence in the K/Ka bands. Depending on the length of the metallic strip in the top layer of the unit cell, it is possible to obtain a polarizer that either rotates the plane of polarization or transforms the polarization from linear to circular. The performance of the prototypes was validated experimentally after the submission of this paper, showing good agreement with the simulated results. These prototypes open the possibility for future reconfiguration with PIN diodes or graphene in uplink and downlink satellite communications.

THIS IS A POSTPRINT VERSION OF THE PAPER:

S. Moreno, J. L. Medrán-Del-Río, Á. Palomares-Caballero, A. Alex-Amor, A. Fernández-Prieto and C. Molero, "On the Design of Unit Cells with Diagonal Symmetry for Wideband Polarization Converters" in *2022 16th European Conference on Antennas and Propagation (EuCAP)*, Madrid, Spain, 2022.

Disclaimer:
This work has been published in 16th European Conference on Antennas and Propagation.
DOI: 10.23919/EuCAP53622.2022.9769348

On the Design of Unit Cells with Diagonal Symmetry for Wideband Polarization Converters

Salvador Moreno *, J. Luis Medrán-del-río†, Ángel Palomares-Caballero*, Antonio Alex-Amor‡, Armando Fernández-Prieto†, Carlos Molero*

*Departamento de Teoría de la Señal, Telemática y Comunicaciones, Universidad de Granada, 18071 Granada, Spain

†Departamento de Electrónica y Electromagnetismo, Universidad de Sevilla, Sevilla, Spain

‡Information Technologies Department, Universidad CEU San Pablo, 28003 Madrid, Spain

emails: salvamr96@ugr.es *

***Abstract*—This paper presents a theoretical study of diagonal-symmetric metasurfaces based on very simple transmission-line models in order to achieve wideband polarization converters. The approach profits from the decomposition of the incident-field vector in field components directed along the diagonal-axis, decoupling the problem into two different, individual and independent subproblems. This issue reduces considerably the complexity of the problem, and allows for a better understanding of the physical insight of the structures. Practical examples of wideband rotators/circular polarizers based on very simple metasurface-cells are implemented with the aim of supporting the theoretical conclusions. Experimental prototypes have successfully been manufactured and will soon be tested.**

***Index Terms*—antennas, electromagnetics, propagation, measurements, circuit models, polarizer.**

I. Introduction

Modern satellite communications and 5G standards demand the use of frequency bands close to and beyond millimeter waves. These demands come from the increasing necessity for higher speeds and large data transmission. Bandwidth manipulation has become crucial for data control [1]. Certain applications moreover require an strict control of the polarization state of the electromagnetic waves with the aim of reducing misalignments, Faraday-rotation effects or multipath, non-negligible in these regions of the spectrum [2].

The design of wideband applications supporting polarization conversion is a problem that has historically been faced [3]. The use of frequency selective surfaces (FSSs) based on periodic structures [4] has attracted a lot of attention thanks to the well-known properties of analysis in terms of Floquet modes. This type of analysis reduces the approach to a waveguide problem, where filter theory can, for instance, be applied. Multi-layer FSSs have emerged as good candidates [5]–[7].

The exploitation of FSSs with a certain degree of symmetry-breaking is an another strategy to achieve wideband conversion [8]. These structures profits from being low-profile and very thin, and usually operate in reflection mode when they are fed by a plane wave. They are commonly denominated as metasurfaces. The classical design of a metasurface for this functionality consists of a patch-like periodic (or pseudo-periodic) structure printed on a grounded dielectric slab (single-layer) [8]. Symmetry-breaking is defined when the symmetry axis of the patch do not coincide with the periodicity directions (cell axis). In some cases, the symmetry breaking appears as a sort of anisotropy, where the global effect of the structure on incident vertical polarization (V-pol o $\mathbf{E}_y$) is different from that over horizontal polarization (H-pol or $\mathbf{E}_x$). Examples where a strong anisotropy is manifested are found in [9]. A particular case of symmetry-breaking is that called diagonal symmetry, where the symmetry axis coincides with the diagonal of the unit cell. Examples are found for applications in the THz-regime [10], mid-infrared [11] or the K/Ka bands [12].

Diagonal-symmetric metasurfaces are quite versatile for polarization conversion showing wide bandwidth. Main advantages are associated with the single-layer architecture and thus, being very thin devices [13], possibility of miniaturization and/or extension to cover some other types of operations as efficient wave absorbers [14]. The properties are usually understood in terms of the multiple resonances that can be excited. Some papers provide an explanation of the multi-resonant nature of diagonal-symmetric structures by employing current/field vector diagrams on the patch surface [12]. Here we propose an alternative view based on circuit-model approaches [15]. For this, the electric field is primarily decomposed into components according to the patch-axis unit vectors, which constitute a complete basis. The representation of the electric field in these terms ensures non-coupling between the components. This allows an individual component treatment in terms of individual circuit models. A very simple metasurface example consisting on strip-patches periodic structures will be designed by following the theoretical principles. A real prototype of this particular design has been manufactured.

The paper is organized as follows. Sect. II describes the theoretical requirements for wideband response and simple guidelines based on circuit-models. Sect. III is left for the characterization of the metasurface cell, validating the theoretical assumptions and including information about the manufactured prototype.

II. Theoretical analysis and circuit models

Unit cells showing symmetry break open the window to polarization conversion. That is, the change the polarization state of an original electromagnetic wave. The original electromagnetic wave is, in this case, a plane wave impinging on the

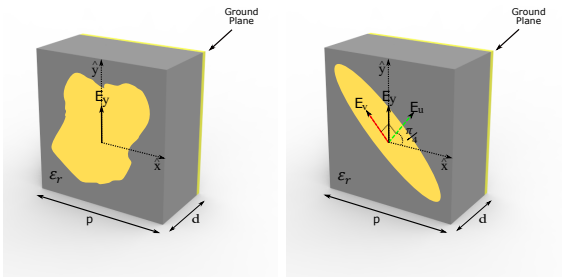

(a) (b)

Fig. 1: Unit cells. Elements in yellow are the patch and the ground plane (metals) and grey color is referred to the dielectric substrate. (a) Example of anisotropic unit cell, having a patch with irregular shape. (b) Cell with diagonal symmetry.

FSS composed by unit cells. Outgoing waves with elliptical, circular or linear polarization with a 90º-rotation of the electric field vector can be attained by a convenient optimization. A generic unit cell example of this type is depicted in Fig. 1(a).

As was aforementioned, these types of architectures are mainly based on a single layer of a two-dimensional periodic distribution of planar patches printed on a grounded dielectric slab. A particular case is the diagonal-symmetric structure as the one shown in Fig. 1(b), where the principal axis of the patch coincides with the diagonal directions of the unit cell. The corresponding unit vectors will be denominated as $\hat{\mathbf{u}}$ and $\hat{\mathbf{v}}$. Assuming arbitrarily an incident wave vertically polarized, we can decompose its electric-field vector into the v- and y-components:

$$\mathbf{E}_{\text{inc}} = E_{\text{y}}\hat{\mathbf{y}} = E_{\text{y}}\left(\frac{1}{\sqrt{2}}\hat{\mathbf{v}} + \frac{1}{\sqrt{2}}\hat{\mathbf{u}}\right), \tag{1}$$

where the factor $\frac{1}{\sqrt{2}}$ comes from the consideration of square unit cells. The representation of the electric field by the use of this base is advantageous due to the non-existence of cross-coupling between the individual v- and u-components. Therefore, the global reflection coefficient of the incident wave $\mathbf{E}_{\text{ref}}$ is expressed as:

$$\mathbf{E}_{\text{ref}} = E_{\text{y}}\frac{1}{\sqrt{2}}\left(\mathrm{e}^{\mathrm{j}\phi_{\text{v}}}\hat{\mathbf{v}} + \mathrm{e}^{\mathrm{j}\phi_{\text{u}}}\hat{\mathbf{u}}\right) \tag{2}$$

where $\phi_{\text{v/u}}$ are the phase shift between the incident and reflected v/u-components respectively. Since

$$\hat{\mathbf{u}} = \cos(\pi/4)\hat{\mathbf{x}} + \sin(\pi/4)\hat{\mathbf{y}} = \frac{1}{\sqrt{2}}(\hat{\mathbf{x}} + \hat{\mathbf{y}}) \tag{3}$$

$$\hat{\mathbf{v}} = -\cos(\pi/4)\hat{\mathbf{x}} + \sin(\pi/4)\hat{\mathbf{y}} = \frac{1}{\sqrt{2}}(-\hat{\mathbf{x}} + \hat{\mathbf{y}}), \tag{4}$$

(2) is rewritten as follows:

$$\mathbf{E}_{\text{ref}} = \frac{E_{\text{y}}}{2}\left[\mathrm{e}^{\mathrm{j}\phi_{\text{v}}}(-\hat{\mathbf{x}} + \hat{\mathbf{y}}) + \mathrm{e}^{\mathrm{j}\phi_{\text{u}}}(\hat{\mathbf{x}} + \hat{\mathbf{y}})\right]. \tag{5}$$

Assuming ϕ_{v} as the phase reference, we define $\phi = \phi_{\text{h}} - \phi_{\text{v}}$ and rewrite (5) as

$$\mathbf{E}_{\text{ref}} = \frac{E_{\text{y}}}{2}\left[\hat{\mathbf{x}}(-1 + \mathrm{e}^{\mathrm{j}\phi}) + \hat{\mathbf{y}}(1 + \mathrm{e}^{\mathrm{j}\phi})\right]. \tag{6}$$

This equation is very illustrative. Controlling the phase shift between the $\hat{\mathbf{v}}$ and $\hat{\mathbf{u}}$ components we can manipulate the polarization state of the global reflected wave $\mathbf{E}_{\text{ref}}$. For instance, if $\phi = 0$ the reflected wave is co-polar to the incident one, in this case directed along y. Otherwise for $\phi = \pi$ the reflected wave is the cross-polar component, say x-component. Circular-polarization can also be attained if $\phi = \pi/2$ or $\phi = 3\pi/2$.

Diagonal-symmetric structures are widely used thanks to their special properties. On the one hand, they provide wide-band response, which results from the concatenation of inherent resonances. In other words, they act as multi-resonant devices. In the literature, the resonances are classified according to its electric or magnetic nature [10]. On the other hand, the behavior of the reflection coefficient under TE- and TM-oblique incidence along the YZ- and XZ-planes behaves identically. This is highly useful for scenarios where the goal of the design is to achieve robustness with respect the incidence angle.

Focusing on the multi-resonant nature, simple interpretations based on circuit models can be invoked. Single-layer patch-like FSSs are circuitally regarded as short-circuited transmission lines (accounting for the propagation inside the grounded dielectric slab) loaded with LC-circuits (accounting for the patch effect at the discontinuity). An input transmission line accounts for the incident/reflected plane wave. See [17] for more information and Fig. 2 for a clearer view. Resonances related to electric moments (called electric resonances, [10], [12]) manifest as a full-reflection typical from electric walls, i. e., a π-radians phase shift between the incident and reflected waves. This is achieved when: the patch resonates; or when a $n\lambda/2$-resonance is induced longitudinally along the transmission line with characteristic impedance Z_1. Resonances related to magnetic moments (magnetic resonances [10]) are phenomenologically exhibited as a 0-radians phase-shift, simulating the typical behavior of magnetic walls. This effect is induced with $\lambda/4$-resonances.

The use of the circuit model facilitates the seek of the desired global response of the structure. For example, if we desire our metasurface to operate as a wideband y-to-x converter or rotator, we can work with independent circuits for v- and u-components, and superpose the individual resulting S_{11} parameters. The design of a wideband rotator requires a wideband π-radians phase difference between the reflection coefficient of both components. For this, we rely on the topologies illustrated in Fig. 2, being resonant for v-component and non-resonant for u-component. The typical response of both circuits is plotted in Fig. 3(a). The green curve refers to S_{11} associated with the u-component. As expected, it is the classical response of a shorted transmission line, with 0-radians phase at 20 GHz corresponding to a $\lambda/4$ resonance, and a π-radians phase at $\lambda/2$ (40 GHz). The red curve, for

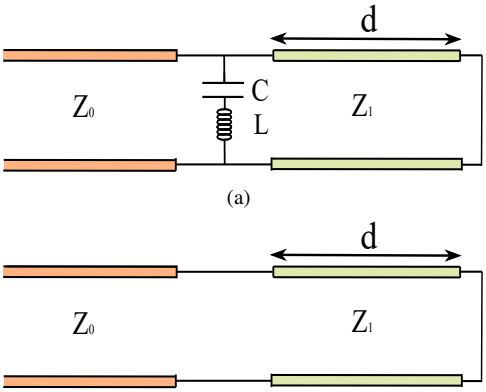

Fig. 2: (a) Equivalent circuit for v-component. (b) Equivalent circuit for u-component.

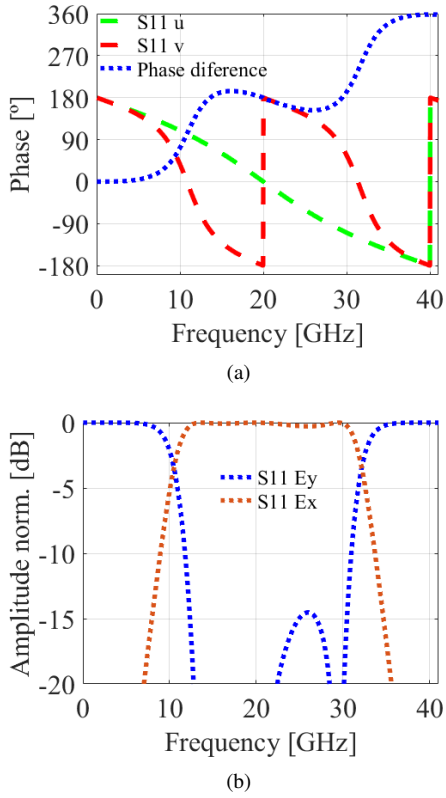

Fig. 3: Results obtained with the equivalent circuits in Fig. 2. Common circuit parameters: $Z_0 = 376\Omega$, $Z_1 = 266.39\Omega$, $d = 2.65$mm. LC-parameters for v-component: $L = 1.85$nH and $C = 34.2$fF. (a) Phase of the v- and u-components of the rotator. (b) Reflection coefficient for the y- and x-components.

v-component, is strongly influenced by the presence of the LC-series resonator. Now, at 20 GHz, a π-radians phase is exhibited. This results from the LC resonance, conveniently tuned to coincide with 20 GHz, ensuring a π-radians phase shift between both components. In fact, this phase shift is approximately kept below and beyond 20 GHz, from 11.9 to

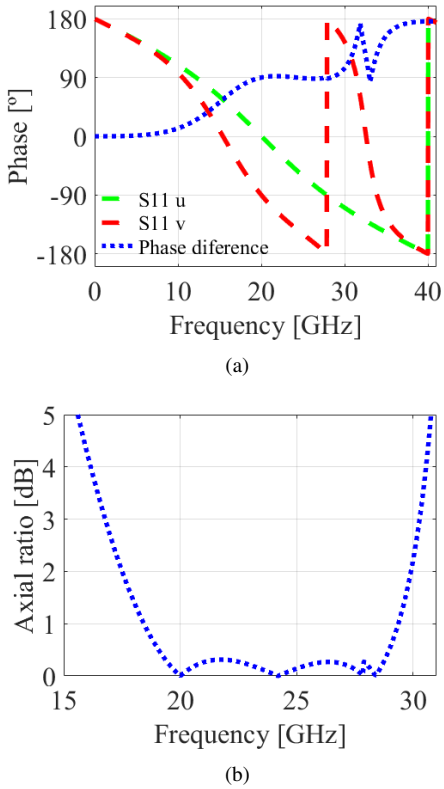

Fig. 4: Results obtained with the equivalent circuits in Fig. 2. Same values for the circuit parameters as in Fig. 3 excepting those for the LC-series connection for v-component: $L = 3.2$nH and $C = 10.2$fF. (a) Phase of the v- and u-components of the rotator. (b) Resulting axial ratio.

30.9 GHz, covering a fractional bandwidth of 89.5%. This is manifested in the global reflection response plotted in Fig. 3(b), where an excellent field-rotation has been obtained.

A similar rationale can be employed for the conception of a circular polarizer. As shown in Fig. 4(a), a wideband $\pi/2-$ radians phase shift is now induced just by optimizing the LC-resonance. The resonance has now been delayed. The rest of circuit parameters have been left identical to the previous design. Fig. 4(b) corroborates the excellent linear-to-circular conversion via the axial ratio. Good circular-polarization purity is considered when $AR \leq 3$ dB. A fractional bandwidth of 58% is obtained.

III. Unit Cells for Rotator and Polarizer Designs

As was aforementioned, circuit models are good substitutes for real unit-cells thanks to the reduction of the complexity in the analysis. The goal is now the opposite: find a real implementation with metasurfaces departing from the circuital results. A good unit-cell candidate is the one shown in Fig. 5(a), consisting on a metallic strip rotated 45^o with respect the cell axis. This cell is quite simple but satisfies the circuital requirements. Assuming the incidence of a vertically-polarized plane wave, the electric field is decomposed into v- and u-components with the same amplitude and phase. The strip is

resonant for v-component, and practically transparent for u-component. This is manifested in Fig. 5(b) where the phase response of both components are similar to those in the previous section. This particular example has been optimized to conceive a rotator covering the K/Ka bands, as shown in Fig. 5(c). The optimization has been carried out with an equivalent circuit and the corresponding unit cell parameters have been estimated via the models published in [17]. The cell implementation and final numerical simulations have been done in the full-wave solver CST. This particular example exhibits a bandwidth of 80% for normal incidence (labelled as 0^o). Furthermore the performance is still kept for oblique incidence at 30^o, both TM and TE, which coincide. Notice that the dielectric width is $d = 1.52$mm, approximately 0.152λ at the center frequency of the band.

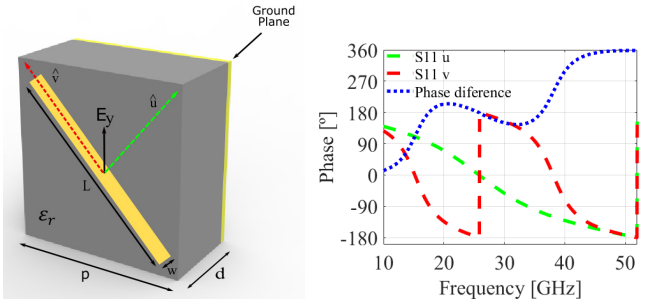

(a) (b)

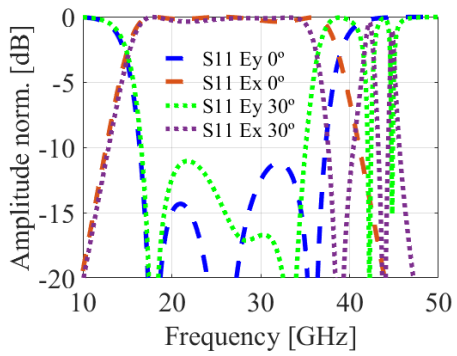

(c)

Fig. 5: (a) Unit cell for the rotator. Structure parameters: $p = 3.4$mm, $d = 1.52$mm, $w = 0.2$mm, $L = 4$mm, $\varepsilon_r = 3.6$. (b) Phase of v- and u-components obtained via CST. (c) Reflection coefficient for the co-polar (y-component) and cross-polar (x-component) for normal (0^o) and oblique (30^o) incidence, also obtained via CST.

A similar unit cell can be employed for the design of a polarizer in the same frequency band. Fig. 6(a) depicts the same cell, with a different patch length L. As can be inferred from the previous section, the modification of the LC-resonance is enough to switch the rotator-functionality into a polarizer. Thus with an optimized length $L = 2.75$mm, the red curve in Fig. 6(b) is displaced towards higher frequencies, inducing the required $\pi/2$-radians phase shift between both components. A fractional bandwidth of 55% has been attained, which is reduced down to 50% for oblique incidence at 30^o

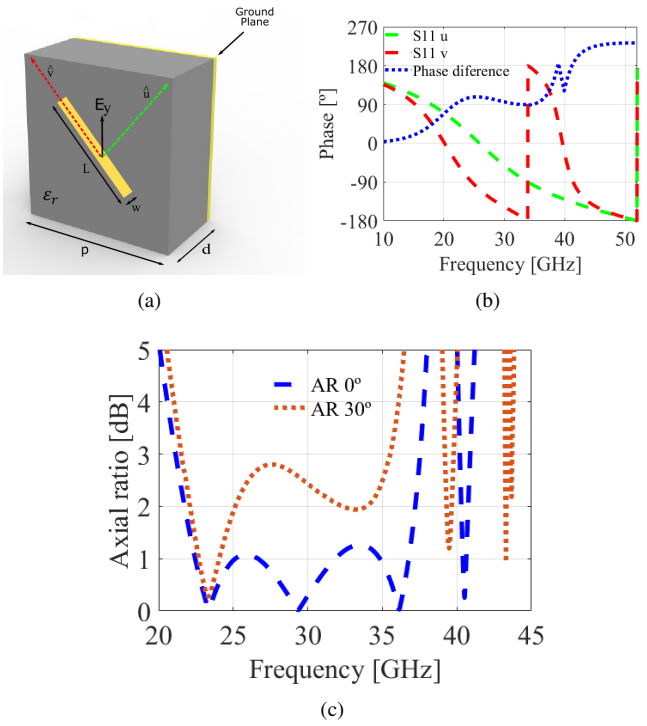

(a) (b)

(c)

Fig. 6: (a) Unit cell for the polarizer. Structure parameters: Same as in Fig. 5 excepting for $L = 4$mm. (b) Phase of v- and u-components obtained via CST. (c) Axial ratio for normal (0^o) and oblique (30^o) incidence obtained via CST.

in both TM/TE polarization.

It is worth remarking that the above results lead us to think on a dual-mode metasurface with (electronic or manual) reconfigurability. The switch from rotator to polarizer and vice versa is just a matter of varying the strip length. This task is left for future work. Addionally, the theoretical analysis of Sect. II has been carried out in the simplest way. The introduction of additional resonances for v- and u-components would increase the operational bandwidth, as well as it could induce multi-band operation if required.

A. *Experimental prototype*

In order to check the validity of the theoretical results, two prototypes have been fabricated. In spite of the existence of critical parameters for the fabrication tolerances, the metasurface has been successfully manufactured, both for rotator and polarizer functionalities. Fig. 7 shows photographs of preliminary prototypes, which have been fabricated using a mechanical milling machine (LPKF S103 from LPKF Laser & Electronics, stationed at Garbsen, Germany). They have not been experimentally tested yet but we expect to do it in the near future. As was mentioned above, the success of these measurements would lead us to conceive the reconfigurability of the proposed design.

IV. Conclusion

Wideband polarization converters have been achieved basing on metasurfaces with diagonal symmetry. A theoretical

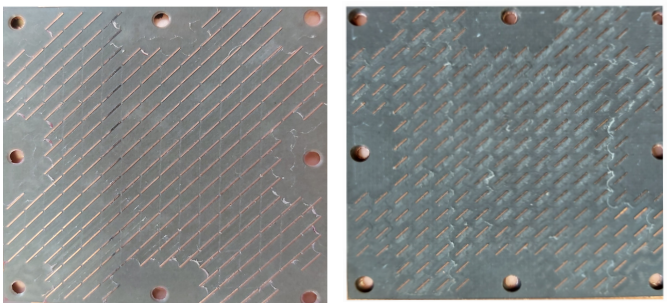

(a) (b)

Fig. 7: Photographs of the: (a) rotator prototype and, (b) polarizer prototype.

study has been carried out in terms of circuit models, where the problem is decoupled into two individual subproblems. The theoretical study leads to a design of wideband polarizers by using very simple metasurfaces cells, avoiding complex for the fabrication. A set of measurements is scheduled to be launched in a few weeks in order to test the manufactured prototypes and corroborate the validity of the approach.

ACKNOWLEDGMENT

This work was supported in part by the Spanish Government under Project PID2020-112545RB-C54, Project RTI2018-102002-A-I00 and Project TIN2016-75097-P, in part by "Junta de Andalucía" under Project B-TIC-402-UGR18, A-TIC-608-UGR20 and Project P18.RT.4830, in part by the Predoctoral Grant FPU18/01965, in part by FEDER/ Ministry of Science and Innovation / Agencia Estatal de Investigación / grant PID2020-116739GB-I00, in part by "BBVA" under the program Leonardo Grants 2021 for researchers and cultural creators. Jose L. Medrán del Río acknowledges financial support of a research scholarship of the Spanish Ministry of Education (ref. PRE2018-085677).

REFERENCES

[1] K. Singarajah, "Should one focus on ka-band or look beyond ka-band?," in *IET Seminar on Beyond Ka-Band: Meeting the Communication Bandwidth Requirements of the Future*, 2011, pp. 1-25.

[2] S. Mener, R. Gillard and L. Roy, "A Dual-Band Dual-Circular-Polarization Antenna for Ka-Band Satellite Communications," *IEEE Antennas Wireless Propag. Lett.*, vol. 16, pp. 274-277, 2017.

[3] H. L. Zhu, S. W. Cheung, K. L. Chung and T. I. Yuk, "Linear-to-Circular Polarization Conversion Using Metasurface," *IEEE Trans. Antennas Propag.*, vol. 61, no. 9, pp. 4615-4623, Sept. 2013.

[4] B. A. Munk, *Frequency Selective Surfaces: Theory and Design*. New York, NY, USA: Wiley, 2000.

[5] S. M. A. Momeni Hasan Abadi and N. Behdad, "Wideband Linear-to-Circular Polarization Converters Based on Miniaturized-Element Frequency Selective Surfaces," *IEEE Trans. Antennas Propag.*, vol. 64, no. 2, pp. 525-534, Feb. 2016.

[6] H. B. Wang, Y. J. Cheng and Z. N. Chen, "Wideband and Wide-Angle Single-Layered-Substrate Linear-to-Circular Polarization Metasurface Converter," *IEEE Trans. Antennas Propag.*, vol. 68, no. 2, pp. 1186-1191, Feb. 2020.

[7] M. S. Jalali Moghadam, M. Akbari, F. Samadi and A. Sebak, "Wideband Cross Polarization Rotation Based on Reflective Anisotropic Surfaces," *IEEE Access*, vol. 6, pp. 15919-15925, 2018.

[8] Y. Jia, Y. Liu, Y. J. Guo, K. Li and S. Gong, "Broadband Polarization Rotation Reflective Surfaces and Their Applications to RCS Reduction," *IEEE Trans. Antennas Propag.*, vol. 64, no. 1, pp. 179-188, Jan. 2016

[9] Babar Kamal, Jingdong Chen, Ying Yingzeng, Jian Ren, Sadiq Ullah, and Wasi Ur Rehman Khan, "High efficiency and ultra-wideband polariza, tion converter based on an L-shaped metasurface," *Opt. Mater. Express* vol. 11, no. 5, p. 1343, May 2021.

[10] Y. N. Jiang, L. Wang, J. Wang, C. N. Akwuruoha, and W. P. Cao, "Ultra-wideband high-efficiency reflective linear-to-circular polarization converter based on metasurface at terahertz frequencies," *Opt. Express*, vol. 25, no. 22, p. 27616, Oct. 2017.

[11] C. Yang *et al.*, "Wideband tunable mid-infrared cross polarization converter using rectangle-shape perforated graphene," *Opt. Express*, vol. 24, no. 15, pp. 16913–16922, Jul. 2016.

[12] X. Gao, X. Han, W. Cao, H. O. Li, H. F. Ma and T. J. Cui, "Ultrawideband and High-Efficiency Linear Polarization Converter Based on Double V-Shaped Metasurface," *IEEE Trans. Antennas Propag.*, vol. 63, no. 8, pp. 3522-3530, Aug. 2015.

[13] M. Karamirad, C. Ghobadi and J. Nourinia, "Metasurfaces for Wideband and Efficient Polarization Rotation," *IEEE Trans. Antennas Propag.*, vol. 69, no. 3, pp. 1799-1804, March 2021.

[14] Y. Khanna, and Y. K. Awasthi, "A Single Layer Wideband Metasurface absorber for Electromagnetic Interference Minimization in Ku-band Applications," *Int. Journal Microw. Wireless Techn.*, pp. 1-7, June 2021, DOI: https://doi.org/10.1017/S1759078721000970

[15] F. Medina, F. Mesa and R. Marques, "Extraordinary Transmission Through Arrays of Electrically Small Holes From a Circuit Theory Perspective," *IEEE Trans. Microw. Theory Techn.*, vol. 56, no. 12, pp. 3108-3120, Dec. 2008.

[16] Jin Xu, Rongqiang Li, Shenyun Wang, and Tiancheng Han, "Ultra-broadband linear polarization converter based on anisotropic metasurface," *Opt. Express*, vol. 26, no. 20, pp. 26235-26241, Oct. 2018.

[17] C. Molero, A. Alex-Amor, F. Mesa, Á. Palomares-Caballero and P. Padilla, "Cross-Polarization Control in FSSs by Means of an Equivalent Circuit Approach," *IEEE Access*, vol. 9, pp. 99513-99525, 2021.

2.1.3 Analytical Equivalent Circuits for Three-Dimensional Metamaterials and Metagratings

This paper presents a theoretical method for designing full-metal 3D metamaterials with spatial periodicity in their cross-sectional components. Taking advantage of Floquet-Bloch series, a closed-form circuit is proposed to extract the electromagnetic response of these metadevices. Unlike the heuristic or semi-analytical methods found in the literature, this manuscript proposes a complete analytical framework for simulating structures based on waveguide regions with slots perforated on the walls. This approach allows much shorter simulation times compared to full-wave software for both normal and oblique incidence, while providing valuable physical insights into the problem. Furthermore, the inclusion of the longitudinal dimension introduces a new degree of freedom, which in this work has enabled the independent resonant tailoring of orthogonal components for polarization control. To the best of our knowledge, this is one of the first fully analytical circuit methods that analyze a three-dimensional structure. As a result, a full-metal 3D polarizer operating in reflection is designed, showing excellent agreement with results obtained from full-wave simulation tools such as CST, and significantly improving simulation time performance.

THIS IS A POSTPRINT VERSION OF THE PAPER:

A. Alex-Amor, S. Moreno-Rodríguez, P. Padilla, J. F. Valenzuela-Valdés and C. Molero, "Analytical equivalent circuits for three-dimensional metamaterials and metagratings," *Physical Review Applied*, vol. 20, p. 044010, Oct 2023.

- Journal Impact Factor (JIF) in JCR 2023: 3.8
- Category: PHYSICS, APPLIED. JIF Rank: 54/179 (Q2).

Disclaimer:
This work has been published in Physical Review Applied.
DOI: 10.1103/PhysRevApplied.20.044010

Analytical Equivalent Circuits for Three-dimensional Metamaterials and Metagratings

Antonio Alex-Amor*
Department of Information Technology, Universidad San Pablo-CEU, CEU Universities, Campus Montepríncipe, 28668 Boadilla del Monte (Madrid), Spain *

Salvador Moreno-Rodríguez, Pablo Padilla, Juan F. Valenzuela-Valdés, Carlos Molero
Department of Signal Theory, Telematics and Communications, Research Centre for Information and Communication Technologies (CITIC-UGR), University of Granada, Granada, Spain

In recent times, three-dimensional (3D) metamaterials have undergone a revolution driven mainly by the popularization of 3D-printing techniques, which has enabled the implementation of modern microwave and photonic devices with advanced functionalities. However, the analysis of 3D metamaterials is complex and computationally costly in comparison to their 1D and 2D counterparts due to the intricate geometries involved. In this paper, we present a fully-analytical framework based on Floquet-Bloch modal expansions of the electromagnetic fields and integral-equation methods for the analysis of 3D metamaterials and metagratings. Concretely, we focus on 3D configurations formed by periodic arrangements of rectangular waveguides with longitudinal slot insertions. The analytical framework is computationally efficient compared to full-wave solutions and also works under oblique incidence conditions. Furthermore, it comes associated with an equivalent circuit that allows to gain physical insight into the scattering and diffraction phenomena. The analytical equivalent circuit is tested against full-wave simulations in commercial software CST. Simulation results show that the proposed 3D structures provide independent polarization control of the two orthogonal polarization states. This key property is of potential interest for the production of full-metal polarizers, such as the one illustrated here.

I. INTRODUCTION

Modern analog microwave and photonic devices, such as frequency selective surfaces (FSS), waveguide devices, filters, absorbers, antennas or polarizers, are based on the use of metamaterials [1–8]. Metamaterials are human-made artificially-engineered devices that allow arbitrary control and manipulation of the propagation of electromagnetic waves [9, 10]. Traditionally, metamaterials have rested on periodic or quasi-periodic arrangements of subwavelength insertions, that is, structures whose constituent elements repeat periodically in space [11], time [12] or space-time [13, 14]. Historically, scientific and engineering communities have paid special attention to one-dimensional (1D) and two-dimensional (2D) metamaterial configurations due to the simplicity related to their analysis, design and manufacturing [15]. Nonetheless, 1D and 2D metamaterials present fundamental limitations inherent to their geometry, such as independent orthogonal polarization control [16]. These limitations are mainly due to the fact that 1D and 2D configurations do not exploit the degrees of freedom associated to the longitudinal direction, the spatial direction in which the wave actually propagates. In that sense, 3D metamaterials are called to overcome the limitations of 1D and 2D configurations [17], leading to a new era in the metamaterial field from which wireless communication systems can benefit.

The popularization of 3D metamaterials is recent. At the cost of increasing the cell thickness, a new degree of freedom is introduced, which can be used to improve the performance of the device. This is associated to the exploitation of the longitudinal direction (z direction) in design. The different homogeneous longitudinal sections, i.e. waveguide regions, can be modified with the insertion of longitudinal slots. The inclusion of longitudinal slots allow us to tune the electromagnetic response of the 3D device in an effective manner, with potential application in reflectarray and transmitarray technology and other microwave and photonic devices [16, 17]. For instance, this inclusion often increases angular stability, allows dual-band frequency responses, enhances the operational bandwidth and provides structural robustness. This should be considered a valuable asset not present in flat 2D metasurfaces or in stacks of 2D devices (2.5D metastructures).

For the aforementioned reasons, 3D metamaterials are starting to be applied in microwave and photonics engineering for the realization of advanced polarizers [18], absorbers [19], beamforming systems [20], wide-angle impedance matching layers [21] and to control orthogonal linear polarizations in reflectarray/transmitarray cells [22]. This has been made possible thanks to the evolution of 3D-printing techniques and the impressive increase in computational resources in the last years [16, 17, 23–25]. Nonetheless, 3D metamaterials are bulkier than flat devices and, usually, more difficult to be analyzed due to their complex geometry. Robust and generalist full-wave tools, such as the finite elements method (FEM) or finite-difference time-domain (FDTD) tech-

* Corresponding author: antonio.alexamor@ceu.es

niques [26], can be employed for the analysis of 3D metamaterials. Normally, the use of the previously mentioned methods comes at the price of great computational resources and a lack of physical insight into the electromagnetic behavior of the structure. Some more efficient and physically-insightful alternatives to full-wave methods were discussed in [16], among which homogenization theory [27, 28], modal analysis [29, 30], ray optics [31, 32], transfer-matrix analysis [33, 34], circuit models [35, 36] or some specific combination of these can be found.

Among the methods mentioned above, circuit models are of particular interest. Complex physical phenomena can be described in a straightforward manner with the use of equivalent circuits ruled by basic circuit theory and its main components: voltage/current sources, impedances, admittances and transmission lines [37, 38]. Furthermore, circuit models are remarkably more computationally efficient than other numerical techniques. Without loss of generality, we can classify equivalent circuits into two main types: (i) heuristic and (ii) analytical. Heuristic approaches need of the support of an external method or simulator, such as CST Studio or Ansys HFSS, to calculate the value of their circuit components. There exist many examples in the literature where heuristic equivalent circuits are utilized to model and characterize complex electromagnetic phenomena in metamaterials and FSS structures [39–43]. On the other hand, analytical circuit approaches do not need of external support, i.e., they are fully operational by themselves [44–48]. This fact constitutes a major difference between heuristic and analytical equivalent circuits. Nevertheless, analytical circuit models are often restricted to canonical geometries since complex geometries may not be easily modeled with analytical mathematical expressions.

In this paper, we propose a rigorous and systematic analytical framework based on integral-equation techniques and Floquet-Bloch series expansions of the electromagnetic fields to analyze 3D metamaterials and metagratings. Related formulations have been successfully applied for the analysis of 1D [49–52] and 2D [44, 53–56] metamaterial structures in the past and, more recently, to time-varying systems [57–59]. Similarly to previous approaches, the analytical formulation is connected to an *analytical equivalent circuit* that models the 3D structure.

In all cases, we are dealing with thick (nonflat) metamaterials with a 3D profile, formed by 2D-periodic arrangements of slotted waveguides. The insertion of longitudinal slots modify the electromagnetic response of the 3D metastructure, allowing us to control and manipulate the transmission and reflection of electromagnetic waves. The proposed 3D metastructures are fundamentally based on metallic waveguide geometries. Thus, their interior is essentially hollow, filled with air. This causes the weight of the structure to be reduced, since the volume of metal or metallized material is small compared to the total volume of the metadevice.

The equivalent circuit is constituted by lumped elements that describe higher-order wave coupling between the different waveguide sections, and transmission lines that characterize the wave propagation in the different regions. To the best of our knowledge, this is one the first times that a rigorous fully-analytical equivalent circuit is proposed to model a 3D metamaterial. Some of the previous approaches found in the literature show pure heuristic [21, 35, 60] or quasi-heuristic (mixture of heuristic and analytical) [61] rationales, but none is purely analytical. Fully-analytical schemes are preferred over heuristic or quasi-heuristic ones, as they are independent of external full-wave simulations. Thus, the present analytical equivalent circuit can be used as an efficient surrogate model and be combined with artificial intelligence or conventional optimization techniques for the design of 3D devices.

All the considered structures are of fully-metallic nature. Nonetheless, the inclusion of dielectrics in the hollow waveguide sections can be easily treated from an analytical perspective with the circuit approach, if necessary. There are plenty of commercial applications where fully-metallic structures are preferred over dielectric ones. For instance, the use of dielectrics is not recommended in space applications, as the thermal expansion coefficients of dielectrics differ from those of metals, resulting in an uneven, non-uniform volume expansion, which can lead to structure failure. In general, fully-metallic structures fit very well in scenarios where systems are subjected to large thermal variations, both in space and on Earth. Additionally, the use of fully-metallic configurations, such as the ones presented in this work, is beneficial for operation at high frequencies. This is motivated by two main reasons. Firstly, dielectrics increase structure losses significantly as frequency increases. Fully-metallic structures are much more robust to losses, as ohmic losses are much easier to control provided that proper fabrication processes are applied. Secondly, fully-metallic designs can be easily scaled in frequency compared to mixed metallo-dielectric or fully-dielectric designs.

The paper is organized as follows. Section II presents the derivation of the analytical equivalent circuit that models 3D metamaterials. Then, some numerical computations are performed in order to check the correct operation of the circuit approach, including reflective and transmitting structures. Section III shows a relation between the original 3D metagrating and related configurations. It is shown that, under certain circumstances, related advanced configurations can be also analyzed with the present approach. Section IV details the utilization of the present circuit model for the efficient design of polarizer devices. Finally, Section V presents some general conclusions extracted from the work.

II. THEORETICAL FRAMEWORK & RESULTS

The original metamaterial under consideration is illustrated in Figure 1(a). It is a thick 3D metastructure

formed by a 2D-periodic arrangement (periodicities p_{x} and p_{y} along the x and y directions, respectively) of metallic waveguides with slot insertions placed along the longitudinal direction z. The unit cell of the 3D metamaterial is highlighted in blue and the main geometrical parameters are also remarked. The corresponding unit cell is bounded by periodic boundary conditions (PBCs) in the x and y directions.

The 3D metagrating (with 2D periodicity) shown in Figure 1 share some similarities with multilayer devices formed by stacks of 2D metasurfaces (commonly named as 2.5D structures), especially from an analytical perspective. In 2.5D structures, each (meta)layer that form the stack is homogenized and modeled as a shunt impedance/admittance, while the connecting homogeneous media between layers (typically air or generic dielectrics) is modeled as transmission lines [55, 56]. A similar approach is followed here for the analysis of the proposed 3D metadevice. The transitions between different waveguide sections are modeled with shunt admittances, while the connecting media (homogeneous waveguides) with transmission lines. Although the applied rationale could seem to be rather similar in both 2.5D and 3D cases, the homogeneous waveguide sections discussed here are significantly more complex to be analytically described, as well as the transitions between them. More importantly, the main difference between a 2.5D device (multilayer stack) and the proposed 3D device lies in the fact that, in a multilayer stack, the longitudinal direction cannot be exploited from a design perspective. This is not the case in the 3D device shown here, where the homogeneous waveguide sections can be modified with the insertion of longitudinal slots, which allows us to control and manipulate in a more efficient manner the transmission and reflection of electromagnetic waves.

Thus, the longitudinal structure of the cell can be split in several homogeneous regions. On the one hand, regions where there are no perforations, emulating conventional metallic rectangular waveguides (RWG) with dimensions $w_{\mathrm{x}} \times w_{\mathrm{y}}$. On the other hand, regions where perforations exist, emulating homogeneous *hard waveguides* (HWGs) with dimensions $p_{\mathrm{x}} \times h_{1,2}$, and where the TEM mode can propagate. As the cross-sectional view in Figure 1(b) shows, HWG regions are stretched along the y axis. In general, HWGs can be regarded as parallel-plate waveguides whose lateral walls are periodic boundary conditions. When normal incidence is considered, the symmetry of the cell with respect the principal planes reduces the periodic boundary conditions on the walls to perfect magnetic/electric conductors (PMC or PEC) conditions. For an incident electric-field vector polarized along $\hat{\mathbf{y}}$ (according to the frame of coordinates in Figure 1), PBCs in the YZ plane become PMCs. This situation is the most interesting since slot resonators may exhibit their resonant conditions. We will henceforth focus on this scenario.

The equivalent circuit that describes the physical phenomenology associated to the 3D metagrating is illustrated in Figure 1(c). Each discontinuity is modeled as a shunt equivalent admittance that takes into account all relevant information about higher-order coupling between evanescent modes/harmonics. For the present 3D structure, we have three main discontinuities, labeled as I, II, III. Discontinuity I models the transition between the input media (typically considered here to be air) and the RWG. Discontinuity II models the transition between the RWG and the lowest hard waveguide (WG–HWG transition). Discontinuity III models the transition between the lowest and the highest hard waveguides (HWG–HWG transition). Discontinuities IV, V and VI are of the same type than discontinuities III, II and I, respectively. This will be discussed later in more detail. Finally, each waveguide section (rectangular and hard) is circuitally modeled as a transmission line of length d_i, with specific values of the characteristic admittance and propagation constant (they depend on the waveguide nature). It is always assumed that the propagation is carried out by the fundamental mode/harmonic of each of the regions. Input (in) and output (out) media are semi-infinite spaces characterized by semi-infinite transmission lines with characteristic admittance $Y_{00}^{(\mathrm{in})}$ and $Y_{00}^{(\mathrm{out})}$, respectively.

Circuit parameters will be dependent on the geometry of the 3D structure. As will be explained below, the admittances associated with the rest of transmission lines (and other shunt admittances taking part in the equivalent circuit in Figure 1) are multiplied by a factor α_i, denoting the degree of coupling at the discontinuity planes. This factor is circuitally interpreted as transformer with turn ratio $1 : \sqrt{\alpha_i}$, as explicitly shown in [52, 62], among others. The current circuit version sketched in Figure 1(c) is equally valid and has now been selected in order to reduce the matrix-formalism complexity when cascading different transmission line sections (see Appendix A).

As was reported in [18, 61], slots in the YZ plane are easily excitable by $\hat{\mathbf{y}}$-polarized waves, and exhibit no effects for the opposite polarization. An identical rationale can be employed for resonators on the XZ plane and $\hat{x}$-polarized incident waves. We henceforth focus on cells with resonators on the YZ-plane and fed by $\hat{\mathbf{y}}$-polarized plane waves. The conclusions extracted are valid for the resonators on the XZ-plane fed by $\hat{\mathbf{x}}$-polarized incident electric fields.

A. Input Media – Waveguide Discontinuity (I)

For the derivation of the circuit parameters, we will consider the incident of a plane wave having the transverse electric-field vector oriented towards $\hat{\mathbf{y}}$. This scenario can be covered by TM (E_y, E_z, H_x) and TE (E_y, H_x, H_z) polarized plane waves impinging obliquely (angle θ), as illustrated in Figure 1(a). Time-harmonic variation ($\mathrm{e}^{\mathrm{j}\omega t}$) is present in all the considered electromagnetic fields and thus suppressed from now onwards.

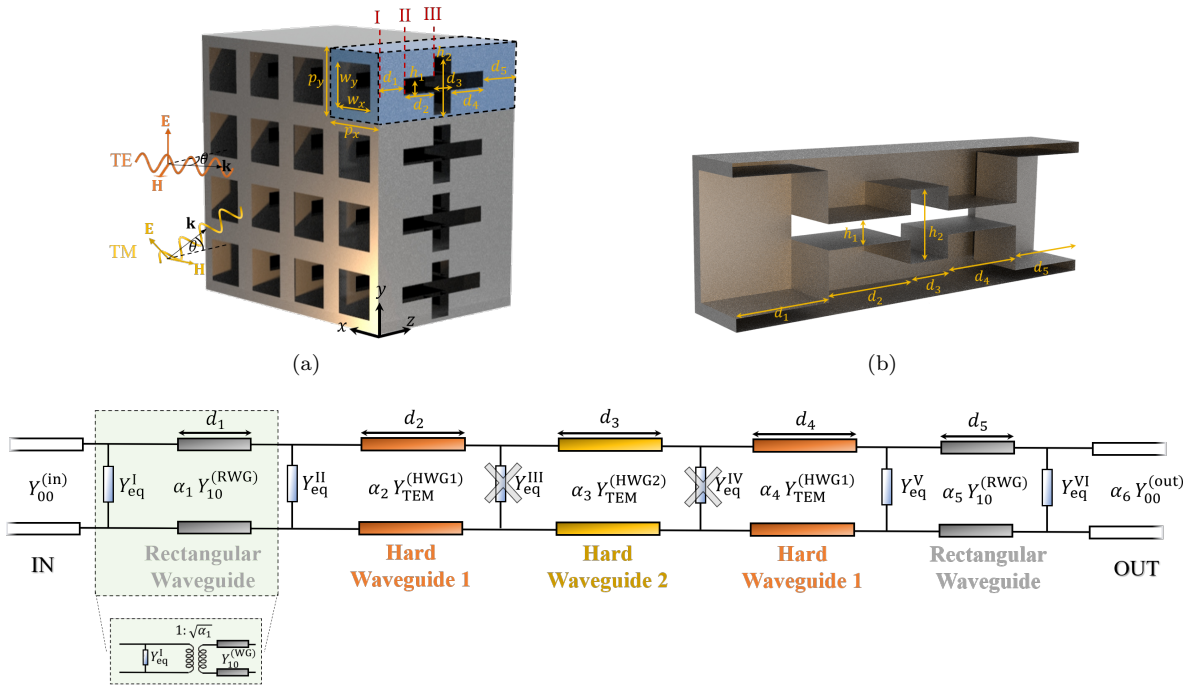

Figure 1. (a) 3D metamaterial formed by periodic repetitions of rectangular waveguides with longitudinal cross-shaped slot insertions. The unit cell of the 3D structure is highlighted in blue. (b) Cross-sectional view of a unit cell. (c) Analytical Floquet equivalent circuit.

The characterization of the discontinuity departs from the knowledge, a priori, of the electromagnetic field expansion at both sides of the discontinuity. In the input region, referenced by the superscript (in), the transverse electric field can be expressed by a Floquet series of harmonics. Each of these harmonics is excited after the interaction of the incident wave and the discontinuity.

Assuming TM incidence, the field expansion in the air-region can be written at the discontinuity plane ($z = 0$) as follows [53, 55]:

$$\begin{aligned}\mathbf{E}^{(\mathrm{in})}(x,y) &= \frac{1}{\sqrt{p_\mathrm{x}p_\mathrm{y}}}(1+E_{00}^{\mathrm{TM},(\mathrm{in})})\mathrm{e}^{-\mathrm{j}k_\mathrm{t}y}\hat{\mathbf{y}} \\ &+ \frac{1}{\sqrt{p_\mathrm{x}p_\mathrm{y}}}\sum_{\forall n,m\neq 0,0} E_{nm}^{\mathrm{TE},(\mathrm{in})}\frac{k_m\hat{\mathbf{x}}-k_n\hat{\mathbf{y}}}{k_{nm}}\mathrm{e}^{-\mathrm{j}(k_nx+k_my)} \\ &+ \frac{1}{\sqrt{p_\mathrm{x}p_\mathrm{y}}}\sum_{\forall n,m\neq 0,0} E_{nm}^{\mathrm{TM},(\mathrm{in})}\frac{k_n\hat{\mathbf{x}}+k_m\hat{\mathbf{y}}}{k_{nm}}\mathrm{e}^{-\mathrm{j}(k_nx+k_my)} \end{aligned} \quad (1)$$

with the unity being the normalized amplitude of the incident wave and $E_{00}^{\mathrm{TM},(\mathrm{in})}$ the unknown reflection coefficient. The coefficients $E_{nm}^{\mathrm{TE/TM},(\mathrm{in})}$ are the unknown amplitudes associated with TE/TM nm-harmonics. The transverse wavevector of a nm-th harmonic is referred as k_{nm}, defined as

$$k_{nm} = \sqrt{k_n^2 + k_m^2} \quad (2)$$

with

$$k_n = \frac{2\pi n}{p_\mathrm{x}} \quad (3)$$

$$k_m = \frac{2\pi m}{p_\mathrm{y}} + k_\mathrm{t}\,. \quad (4)$$

The longitudinal component of the wavevector of a nm-harmonic is denoted by β_{nm}

$$\beta_{nm} = \sqrt{k_0^2 - k_{nm}^2}\,. \quad (5)$$

with $k_0 = \omega/c$.

Similarly, the magnetic field expansion admits to be expressed as follows [53, 55]:

$$\begin{aligned}\mathbf{H}^{(\mathrm{in})}(x,y) &= -\frac{Y_{00}^{\mathrm{TM},(\mathrm{in})}}{\sqrt{p_\mathrm{x}p_\mathrm{y}}}(1-E_{00}^{\mathrm{TM},(\mathrm{in})})\mathrm{e}^{-\mathrm{j}k_\mathrm{t}y}\hat{\mathbf{y}} \\ &- \frac{1}{\sqrt{p_\mathrm{x}p_\mathrm{y}}}\sum_{\forall n,m\neq 0,0} Y_{nm}^{\mathrm{TE},(\mathrm{in})}E_{nm}^{\mathrm{TE},(\mathrm{in})}\frac{k_m\hat{\mathbf{y}}+k_n\hat{\mathbf{x}}}{k_{nm}}\mathrm{e}^{-\mathrm{j}(k_nx+k_my)} \\ &- \frac{1}{\sqrt{p_\mathrm{x}p_\mathrm{y}}}\sum_{\forall n,m\neq 0,0} Y_{nm}^{\mathrm{TM},(\mathrm{in})}E_{nm}^{\mathrm{TM},(\mathrm{in})}\frac{k_n\hat{\mathbf{y}}-k_m\hat{\mathbf{x}}}{k_{nm}}\mathrm{e}^{-\mathrm{j}(k_nx+k_my)} \end{aligned} \quad (6)$$

with

$$Y_{nm}^{\mathrm{TE,(in)}} = \frac{\beta_{nm}^{(\mathrm{in})}}{\eta_0 k_0} \tag{7}$$

$$Y_{nm}^{\mathrm{TM,(in)}} = \frac{k_0}{\eta_0 \beta_{nm}^{(\mathrm{in})}} \tag{8}$$

being the nmth-order TE and TM admittances, respectively, and η_0 is the free-space impedance..

In the RWG region, the field expansion is written in terms of the modal solutions of the RWG. However, at frequency ranges far below the excitation of higher-order modes, the electromagnetic field description inside the RWG admits to be represented in terms of a single mode, say the fundamental TE_{10} mode:

$$\mathbf{E}^{(\mathrm{RWG})}(x,y) = E_{10}^{\mathrm{TE,(RWG)}} \frac{2}{\sqrt{2}} \frac{1}{\sqrt{w_{\mathrm{x}} w_{\mathrm{y}}}} \cos(k_{10}^{(\mathrm{RWG})} x)\hat{\mathbf{y}} \tag{9}$$

$$\mathbf{H}^{(\mathrm{RWG})}(x,y) = Y_{10}^{\mathrm{TE,(RWG)}} [\mathbf{E}^{(\mathrm{RWG})}(x,y) \cdot \hat{\mathbf{y}}]\hat{\mathbf{x}} \tag{10}$$

with $E_{10}^{\mathrm{TE,(RWG)}}$ the unknown amplitude of the TE_{10} mode, $k_{10}^{(\mathrm{RWG})} = \pi/w_{\mathrm{x}}$ and $Y_{10}^{\mathrm{TE,\ (RWG)}} = \dfrac{\beta_{10}^{(\mathrm{RWG})}}{\eta_0 k_0}$. The propagation constant $\beta_{10}^{(\mathrm{RWG})}$ is similarly obtained as in (5), substituting k_{nm} by $k_{10}^{(\mathrm{RWG})}$.

The analytical derivation of the equivalent circuit demands an *a priori* estimation of the field profile at the discontinuity. Given the geometry taken into account, the field profile (spatial distribution) is expected to be similar to the fundamental or TE_{10} mode at lower frequencies. Thus, the field at the discontinuity admits to be described as

$$\mathbf{E}_{\mathrm{dis}} = A \cos\left(\frac{\pi}{w_{\mathrm{x}}} x\right) \hat{\mathbf{y}}\,, \tag{11}$$

where A is frequency-dependent constant to be determined. This estimation is good enough for frequencies below the onset of higher-order modes inside the RWG. For normal incidence, the second mode excitable is the TE_{30}, whose cutoff frequency $f_{30} = 3f_{10}$, with $f_{10} = c\,k_{10}^{(\mathrm{RWG})}/2\pi$ being the cutoff frequency of the TE_{10} mode.

The analytical expressions for the unknown amplitudes of each of the modes/harmonics in both regions are obtained after imposing the following conditions at the discontinuity:

$$\mathbf{E}^{(\mathrm{in})}(x,y) = \mathbf{E}_{\mathrm{dis}} \tag{12}$$

$$\mathbf{E}^{(\mathrm{RWG})}(x,y) = \mathbf{E}_{\mathrm{dis}} \tag{13}$$

$$\mathbf{E}_{\mathrm{dis}} \times [\mathbf{H}^{(\mathrm{in})}(x,y)]^* = \mathbf{E}_{\mathrm{dis}} \times [\mathbf{H}^{(\mathrm{RWG})}(x,y)]^* \tag{14}$$

where (12) and (13) refer to the continuity of the electric field and (14) describes the continuity of the Poyinting vector.

By developing the above equations after introducing the harmonic/modal expansion inside, and after several mathematical calculations, we achieve the following expression for the reflection coefficient $E_{00}^{\mathrm{TM,\ (in)}}$:

$$E_{00}^{\mathrm{TM,(in)}} = \frac{Y_{00}^{(\mathrm{in})} - \alpha_{10}^{\mathrm{TE,\ (RWG)}} Y_{10}^{\mathrm{TE,(RWG)}} - Y_{\mathrm{eq}}^{\mathrm{I}}}{Y_{00}^{(\mathrm{in})} + \alpha_{10}^{\mathrm{TE,\ (RWG)}} Y_{10}^{\mathrm{TE,(RWG)}} + Y_{\mathrm{eq}}^{\mathrm{I}}} \tag{15}$$

with

$$Y_{\mathrm{eq}}^{\mathrm{I}} = \sum_{\forall n,m \neq 0,0} \left[\alpha_{nm}^{\mathrm{TE,\ (in)}} Y_{nm}^{\mathrm{TE,(in)}} + \alpha_{nm}^{\mathrm{TM,\ (in)}} Y_{nm}^{\mathrm{TM,(in)}}\right]. \tag{16}$$

The factors $\alpha_{nm}^{\mathrm{TE/TM,\ (in)}}$ and $\alpha_{10}^{\mathrm{TE,\ RWG}}$ represent the coupling among all the harmonics/modes and $\mathbf{E}_{\mathrm{dis}}$, whose expressions are given by:

$$\alpha_{nm}^{\mathrm{TE,(in)}} = \left[\pi^2 \frac{k_n}{k_{nm}} \frac{\cos(k_n w_{\mathrm{x}}/2)}{(k_n w_{\mathrm{x}})^2 - \pi^2} \frac{\sin(k_m w_{\mathrm{y}}/2)}{\sin(k_{\mathrm{t}} w_{\mathrm{y}}/2)} \frac{k_{\mathrm{t}}}{k_m}\right]^2 \tag{17}$$

$$\alpha_{nm}^{\mathrm{TM,(in)}} = \frac{k_m^2}{k_n^2} \alpha_{nm}^{\mathrm{TE,(in)}} \tag{18}$$

$$\alpha_{10}^{\mathrm{TE,\ (RWG)}} = \frac{\pi^2}{8} \frac{p_{\mathrm{x}} p_{\mathrm{y}}}{w_{\mathrm{x}} w_{\mathrm{y}}} \left[\frac{k_{\mathrm{t}} w_{\mathrm{y}}/2}{\sin(k_{\mathrm{t}} w_{\mathrm{y}}/2)}\right]^2. \tag{19}$$

The above expressions and the reflection-coefficient equation in (15) leads to the identification of a transmission-line model where Y_{00}^{in} and $\alpha_{10}^{\mathrm{RWG}} Y_{10}^{\mathrm{TE,RWG}}$ are the characteristic admittances of the input and output transmission lines in discontinuity I respectively. They are formally the transmission lines in white and grey in the equivalent circuit in Figure 1. Henceforth, the parameter multiplying the admittance of the TE_{10} mode is redefined as follows:

$$\alpha_1 = \alpha_{10}^{\mathrm{TE,\ (RWG)}} \tag{20}$$

The admittance $Y_{\mathrm{eq}}^{\mathrm{I}}$ is the shunt admittance connecting both transmission lines.

A similar derivation can be done for TE incidence. In this case the transverse electric-field vector points towards $\hat{\mathbf{y}}$ (this plane wave is completed by magnetic field components pointing towards $\hat{\mathbf{x}}$ and $\hat{\mathbf{z}}$). The rationale employed is identical, but some of the expressions must now be redefined. Now, (21) and (22) are rewritten as follows

$$k_n = \frac{2\pi n}{p_{\mathrm{x}}} + k_{\mathrm{t}} \tag{21}$$

$$k_m = \frac{2\pi m}{p_{\mathrm{y}}} \tag{22}$$

since the transverse component of the wavevector is leading towards $\hat{\mathbf{x}}$, as mentioned above.

Furthermore, by applying the same methodology we achieve the following expressions for the factors multi-

plying the TE/TM admittances in Y_{eq}^{I}

$$\alpha_{nm}^{\text{TE,(in)}} = \left[\frac{k_n}{k_{nm}}\frac{\cos(k_n w_\text{x}/2)}{\cos(k_\text{t} w_\text{x}/2)}\frac{(k_\text{t} w_\text{x})^2-\pi^2}{(k_n w_\text{x})^2-\pi^2}\frac{\sin(k_m w_\text{y}/2)}{k_m w_\text{y}/2}\right]^2 \tag{23}$$

$$\alpha_{nm}^{\text{TM,(in)}} = \frac{k_m^2}{k_n^2}\alpha_{nm}^{\text{TE,(in)}} \tag{24}$$

$$\alpha_{10}^{\text{TE, (RWG)}} = \frac{1}{8\pi^2}\frac{p_\text{x} p_\text{y}}{w_\text{x} w_\text{x}}\left[\frac{(k_\text{t} w_\text{x})^2-\pi^2}{\cos(k_\text{t} w_\text{x}/2)}\right]^2 . \tag{25}$$

which contribute to redefine the admittances taking place on the equivalent circuit. The factor associated with the TE_{10} mode, α_1, keeps being the one in (20).

B. Rectangular Waveguide – Hard Waveguide Discontinuity (II)

In order to model discontinuity II, we assume the RWG as the input media, and the HWG with dimensions $p_\text{x}\times h_1$ as the output one. That is, the *feeding port* is set on the RWG side. In Sec. II A, it was assumed that the TE_{10}-mode was the dominant field inside the RWG (both in evanescent or propagative state). This approximation is valid for frequencies below and above the cutoff frequency of this mode, and it will also be applied in this section. Thus, the *incident field* is now the TE_{10} mode of the RWG.

The interaction of this mode with the discontinuity excites all the possible modal solutions in both waveguides. In the RWG region, the TE_{10} mode is highly dominant thus the modal expansion is exactly the same as that in (9) and (10). In the HWG, the excitable modal solutions *under the incidence* of the TE_{10} are those which respect the same symmetrical conditions imposed by this last mode. After some mathematical and physical analysis, it can be concluded that modal solutions with even orders n and m can only be excited at the discontinuity. The electric-field expansion in the HWG region therefore admits to be described as:

$$\begin{aligned}\mathbf{E}^{(\text{HWG})}(x,y) = {}& \frac{1}{\sqrt{p_\text{x} w_\text{y}}}E_{00}^{(\text{HWG})}\hat{\mathbf{y}} \\ & + \Bigg[\sum_{\substack{\forall n>0\\ \forall m\geq 0}}\gamma_{nm}^{(\text{HWG})}E_{nm}^{\text{TE, (HWG)}}k_n^{(\text{HWG})} \\ & \times\cos(k_n^{(\text{HWG})}x)\cos(k_m^{(\text{HWG})}y)\Bigg]\hat{\mathbf{y}} \\ & - \Bigg[\sum_{\substack{\forall n\geq 0\\ \forall m>0}}\gamma_{nm}^{(\text{HWG})}E_{nm}^{\text{TM, (HWG)}}k_m^{(\text{HWG})} \\ & \times\cos(k_n^{(\text{HWG})}x)\cos(k_m^{(\text{HWG})}y)\Bigg]\hat{\mathbf{y}}\end{aligned} \tag{26}$$

for n, m even numbers, and with

$$\gamma_{n0}^{(\text{HWG})} = \frac{2}{\sqrt{2}}\frac{1}{k_n^{(\text{HWG})}}\frac{1}{\sqrt{p_\text{x} w_\text{y}}} \tag{27}$$

$$\gamma_{0m}^{(\text{HWG})} = \frac{2}{\sqrt{2}}\frac{1}{k_m^{(\text{HWG})}}\frac{1}{\sqrt{p_\text{x} w_\text{y}}} \tag{28}$$

$$\gamma_{nm}^{(\text{HWG})} = \frac{1}{2}\frac{1}{k_{nm}^{(\text{HWG})}}\frac{1}{\sqrt{p_\text{x} w_\text{y}}} . \tag{29}$$

$$k_n^{(\text{HWG})} = \frac{n\pi}{p_\text{x}} \quad \forall n \text{ even} \tag{30}$$

$$k_m^{(\text{HWG})} = \frac{m\pi}{h_1} \quad \forall m \text{ even} \tag{31}$$

The field profile at the discontinuity is that used in Sect. II A, specified in (11). Taking this into account, and imposing the continuity equations in (12), (13) and (14), we obtain expression of an equivalent admittance for discontinuity II which includes the effect of all the higher order harmonics in the HWG:

$$\begin{aligned}Y_{\text{eq}}^{\text{II}} = {}& \sum_{\substack{\forall n>0\\ \forall m\geq 0}}\alpha_{nm}^{\text{TE, (HWG)}}Y_{nm}^{\text{TE, (HWG)}} \\ & + \sum_{\substack{\forall n\geq 0\\ \forall m>0}}\alpha_{nm}^{\text{TM, (HWG)}}Y_{nm}^{\text{TM, (HWG)}}\end{aligned} \tag{32}$$

where the factors α can be defined as follows

$$\alpha_1\alpha_{n0}^{\text{TE, HWG}} = 32\pi^2\frac{w_\text{x} w_\text{y}}{p_\text{x} h_1}\left[\frac{\cos(k_n^{(\text{HWG})}w_\text{x}/2)}{(k_n^{(\text{HWG})}w_\text{x})^2-\pi^2}\right]^2 \tag{33}$$

$$\begin{aligned}&\alpha_1\alpha_{nm}^{\text{TE, (HWG)}} = 64\pi^2\frac{w_\text{x} w_\text{y}}{p_\text{x} h_1}\times \\ &\left[\frac{k_n^{(\text{HWG})}}{k_{nm}^{(\text{HWG})}}\frac{\cos(k_n^{(\text{HWG})}w_\text{x}/2)}{(k_n^{(\text{HWG})}w_\text{x})^2-\pi^2}\frac{\sin(k_m^{(\text{HWG})}w_\text{y}/2)}{k_m^{(\text{HWG})}w_\text{y}/2}\right]^2\end{aligned} \tag{34}$$

$$\alpha_1\alpha_{0m}^{\text{TM, (HWG)}} = \frac{32}{\pi^2}\frac{w_\text{x} w_\text{y}}{p_\text{x} h_1}\left[\frac{\sin(k_m^{(\text{HWG})}w_\text{y}/2)}{k_m^{(\text{HWG})}w_\text{y}/2}\right]^2 \tag{35}$$

$$\alpha_{nm}^{\text{TM, (HWG)}} = \left[\frac{k_m^{(\text{HWG})}}{k_{nm}^{(\text{HWG})}}\right]^2\alpha_{nm}^{\text{TE, (HWG)}} . \tag{36}$$

The parameter α_1 is the one defined in (20). The admittance $Y_{\text{eq}}^{\text{II}}$ is connected to the input and output transmission lines in grey and orange colors in Figure 1. They are the input and output lines of this discontinuity, corresponding to the TE_{10} and TEM modes respectively. The characteristic admittances are given by $\alpha_1 Y_{10}^{\text{TE, (RWG)}}$ and $\alpha_2 Y_{\text{TEM}}^{(\text{HWG1})}$ with

$$\alpha_1\alpha_2 = \frac{16}{\pi^2}\frac{w_\text{x} w_\text{y}}{p_\text{x} h_1} . \tag{37}$$

and $Y_{\text{TEM}}^{(\text{HWG1})} = 1/\eta_0$.

C. Hard Waveguide – Hard Waveguide Discontinuity (III)

In order to model this kind of discontinuity, we take into account the previous conclusions extracted from the rest of discontinuity types. Now, two different HWGs are in contact at the discontinuity. The input HWG, being the output region in the previous section, has dimensions $p_x \times h_1$. The output HWG has dimensions $p_x \times h_2$. The feeding mode is now the TEM mode coming from the input HWG. At the discontinuity, the field at both sides is expressed as in (26), but employing the correct dimensions (p_x and h_1 for the input region; and p_x and h_2 for the output region) in the wavenumbers k_n and k_m.

The field profile at the discontinuity is proportional to the TEM-mode in the lowest-height HWG:

$$\mathbf{E}_d = A\hat{\mathbf{y}} \tag{38}$$

Assuming $h_1 < h_2$, and applying again the boundary conditions in (12), (13) and (14) we obtain:

$$E_{nm}^{\text{TE/TM, (HWG1/HWG2)}} = 0 \quad \text{if } n \neq 0 \text{ or } m \neq 0\,, \tag{39}$$

indicating that no higher-order modes are considered under this approximation. This approximation works well up to the excitation any of the first higher-order mode. Therefore, the fundamental modes (TEM) of each of the waveguides are represented by transmission lines with characteristic admittances $Y_{\text{TEM}}^{(\text{HWG1})} = Y_{\text{TEM}}^{(\text{HWG2})} = 1/\eta_0$, being those in orange and yellow in Figure 1 respectively. The parameter α_3 is defined as follows:

$$\alpha_1\alpha_2\alpha_3 = \frac{h_1}{h_2}\,. \tag{40}$$

It is worth remarking that, in case that $h_1 > h_2$, equation (40) becomes:

$$\alpha_1\alpha_2\alpha_3 = \frac{h_2}{h_1}\,. \tag{41}$$

In a first approach, the shunt admittance connecting both transmission lines can be neglected, $Y_{\text{eq}}^{\text{III}} = 0$, since it is formally formed by all the higher modes $E_{nm}^{\text{TE/TM, (HWG1) / (HWG2)}}$, non-excited under the conditions imposed at the discontinuity according to (39). This constitutes an approximation, expected to work well up to the excitation of the higher-order modes in any of the HWGs.

D. Numerical Examples: Reflective Structures

Now, we present some numerical results to validate and test the capabilities of the analytical equivalent circuit. We initially consider the 3D metamaterial structure included as an inset in Figure 2(a), with its associated circuit shown in Figure 2(d). It is a fully-metallic device, short circuited at its end, that operates as a reflective structure. From the circuit point of view, the input admittance seen from discontinuity III through the short-circuited line can be represented as

$$Y_{\text{in}}^{(\text{HWG2})} = -\text{j}\alpha_3 Y_{\text{TEM}}^{(\text{HWG2})} \cot(k_0 d_3)\,. \tag{42}$$

The longitudinal cross-shaped slots and the associated waveguide stretches allow to control the phase of the reflected wave in an efficient manner.

Figure 2(a) illustrates a comparison between results obtained by our approach (solid lines) and the full-wave simulator (circles) CST Microwave Studio. The parameters computed are the phase (black) and amplitude (red) of the reflection coefficient R. As observed, there is a good agreement between analytical and full-wave results in a wide range of frequencies. For the dimensions of the unit cell ($6 \times 6\,\text{mm}^2$), the onset frequency of the first higher-order harmonic is 50 GHz for normal incidence. Naturally, the computation time for the analytical circuit (order of seconds) is much less than that of commercial software CST (order of minutes or hours could be needed). For 1001 frequency points, the circuit approach took less than 2 seconds in giving the solution while CST took more than 400 seconds in the simplest case.

The square-waveguide section is under cutoff below 30 GHz for the selected dimensions ($5 \times 5\,\text{mm}^2$). This implies that only evanescent modes are excited inside the 3D metagrating below 30 GHz. Nonetheless, in cases where the RWG length is short enough, modes of evanescent nature in the RWG (e.g. $\text{TE}_{10}^{(\text{RWG})}$) may couple to the HWG section. This is due to the *slow* decay rate of the amplitude of the TE_{10} mode along the short RWG section. The HWG is therefore excited by the evanescent TE_{10} mode, manifested by the propagation of its fundamental mode, now identified as a propagating TEM mode. This excitation via evanescent waveguides is analogous to the well-known tunnel effect in quantum physics [63], and is particularly relevant to design transmitting structures via opaque waveguides. Such is the case described in Sec II E.

The spectral evolution of the reflection coefficient plotted in Figure 2(a) exhibits a rich phenomenology, specially for frequencies higher than 30 GHz. However, a sudden resonance jump appears around 22 GHz, identified as a sudden $\lambda/2$-resonance given in the HWG regions. The total length of the two HWG sections (transmission-line sections) sums up $D = d_2 + d_3 = 4.5\,\text{mm}$. The corresponding $\lambda/2$ resonance would be expected at 33.3 GHz in a case where the HWGs were isolated. However the HWGs sections are coupled to a RWG section, whose common discontinuity junction is modeled by the admittance $Y_{\text{eq}}^{\text{II}}$, predominantly capacitive. The presence of this capacitance is the responsible of the resonance shifting to lower frequencies. In this case down to 22 GHz. The rest of RWG section contributes as an inductive load though its influence over the rest of the structure is not quite relevant. The phase evolution starts to vary faster in

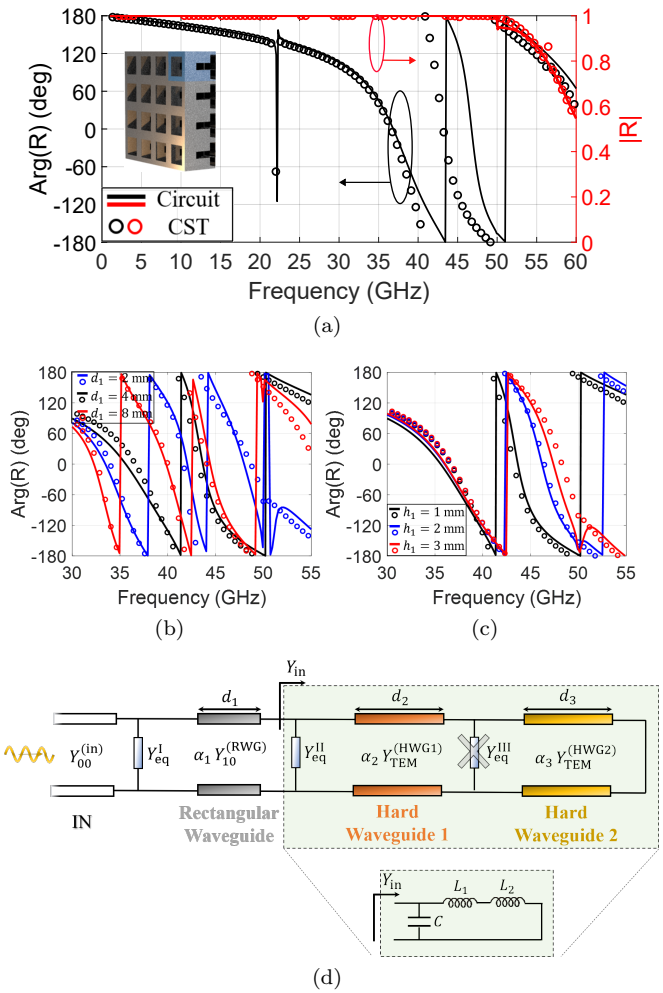

Figure 2. Reflection coefficient R of a reflective 3D structure for $d_1 = 4\,\text{mm}$ and $h_1 = 1\,\text{mm}$. (a) Phase and amplitude. (b) Effect of varying d_1. (c) Effect of varying h_1. In all cases, colored solid lines and circles correspond to the analytical and full-wave results, respectively. (d) Analytical circuit model. Geometrical parameters: $p_x = p_y = 6$ mm, $w_x = w_y = 5\,\text{mm}$, $d_2 = 4\,\text{mm}$, $d_3 = 0.5\,\text{mm}$, and $h_2 = 3\,\text{mm}$. Normal incidence.

frequency beyond 30 GHz, frequency at which the TE_{10}-mode becomes propagative. Both the $\lambda/4$ peak as well as this fast evolution of the phase at higher frequencies is well caught by the equivalent circuit, since it predicts all this phenomenology.

The red curve and circles show the amplitude evolution of the reflection coefficient in Figure 2(a). As expected, the reflective character of the cell invokes full reflection up to 50 GHz. Above 50 GHz, the first higher-order harmonic in the air region becomes propagative, thus the reflected power is split in two: part is carried by the incident wave and part by the higher-order harmonic. This is the reason why the reflection coefficient represented in the figure is no longer one beyond 50 GHz. Again, this phenomenon is well captured by the equivalent circuit.

Figures 2(b) and (c) illustrate the spectral evolution of the reflection phase when some geometrical parameters of the structure are modified. As expected, the increase of the lengths of the RWG and HWG sections has a direct impact on the phase response of the system. Figure 2(b) shows the phase modification when the length of the RWG section d_1 is varied. A comparison is made between the analytical-circuit results (solid lines) and CST (circles), showing a very good agreement in all cases. Slight differences can be appreciated at high frequencies, due to the complexity of the structure. Moreover, the model seems to be more accurate for higher values of d_1. For $d_1 = 2\,\text{mm}$, differences between CST and the circuit approach can be appreciated at lower frequencies in comparison with cases assuming higher values of d_1. The reason behind this disagreement is related to the lack of information associated with higher-order modes inside the RWG. The model assumes the excitation of the TE_{10}-mode (both in evanescent and propagative nature), and does avoid the excitation of the rest of higher-order modes. When d_1 is a large value, and the TE_{10}-mode is evanescent (under 30 GHz), its amplitude decays along the RWG and does not reach the end of the RWG. As d_1 decreases, this amplitude may not decay along the RWG length and the modal field can reach the end of the waveguide, coupling to the next waveguide (HWG). For $d_1 \ll \lambda$, the TE_{10}-mode does arrive to the end, but also some of the higher-order modes that have not been taken into account. When the frequency is higher than 30 GHz, the TE_{10}-mode becomes propagative and its amplitude stops decaying. The model captures well this fact. However the presence of the rest of higher-order modes is not considered in the circuit model, thus a lack of accuracy is expected when $d_1 \ll \lambda$. As it can be appreciated in Fig. 2(b), this disagreement from 30 GHz is not visible for $d_1 = 4$ and $d_1 = 8\,\text{mm}$.

Figure 2(c) shows the phase variation when h_1 is modified. The lower the value of h_1 is, the greater the observed phase shift is. Physical insight into this phenomenon can be achieved by means of the analytical circuit model. For HWG with short lengths ($d_2, d_3 \ll \lambda$), the short-circuited HWG sections contribute to the circuit model with a pure inductive term $L = L_1 + L_2$. In addition, the equivalent admittance that models the RWG-HWG discontinuity, $Y_{\text{eq}}^{\text{II}}$, contributes with a pure capacitive term C at frequencies above the RWG cutoff. Thus, the RWG-HWG-short section, whose input admittance is Y_{in} [see Figure 2(d)], can be simply described as a LC tank. The fact of decreasing the height of the HWG provokes that its lower and upper metallic plates are now closer. As a consequence, the associated capacitance C increases, shifting down in frequency the position of the the curves in Figure 2(c). Note that this effect is not appreciable near the cutoff of the square waveguide (30 GHz for the selected geometry), as the capacitive term C is not dominant yet.

Finally, results considering oblique incidence have been plotted in Figure 3. TE and TM incidences have been included, manifested by the

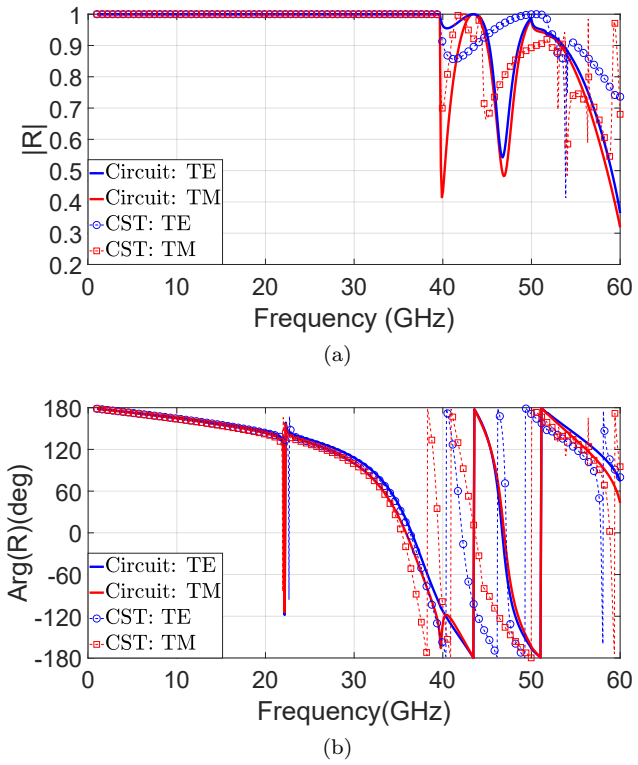

Figure 3. Reflection coefficient R of a reflective 3D structure under oblique incidence conditions ($\theta = 15$ deg). (a) Amplitude. (b) Phase. Geometrical parameters: $p_x = p_y = 6\,\text{mm}$, $w_x = w_y = 5\,\text{mm}$, $d_1 = d_2 = 4\,\text{mm}$, $d_3 = 0.5\,\text{mm}$, $h_1 = 1\,\text{mm}$ and $h_2 = 3\,\text{mm}$.

incidence of a plane wave with incidence angle $\theta = 15$ deg. The results provided by the circuit model fit well with those obtained by CST up to 40 GHz approximately. Beyond this frequency the agreement notably deteriorates, due to the excitation of additional modes that are no included in the mathematical circuit derivation. Specially, higher-order modes inside the RWG are now determinant, as the TE_{11}, with cutoff frequency $f_{11} = 42.43\,\text{GHz}$. Since this mode is excluded from the circuit derivation, it is expected the degradation manifested in Figure 3 near and beyond f_{11}. Though it constitutes an important limitation of our approach, the model is still wideband, exhibiting good performance for cell dimensions larger than $\lambda/2$. It is worth remarking that all the physical phenomena below f_{11} are well caught, as the resonance in the reflection phase around 22 GHz.

E. Numerical Examples: Transmitting Structures

The proposed 3D metastructure can operate in reflection and transmission modes. By minor modifications of the geometry of the waveguides that form the 3D metastructure, a design initially proposed for reflection operation can be converted into one with transmission operation. From a practical point of view, this is an interesting feature of the proposed 3D structures. When we normally consider other types of structures, specific designs are made for reflection and transmission, which can sometimes be very different from each other. In transmission mode, the 3D device can control both amplitude and phase of the scattered waves by properly adjusting the geometrical parameters of rectangular and hard waveguides.

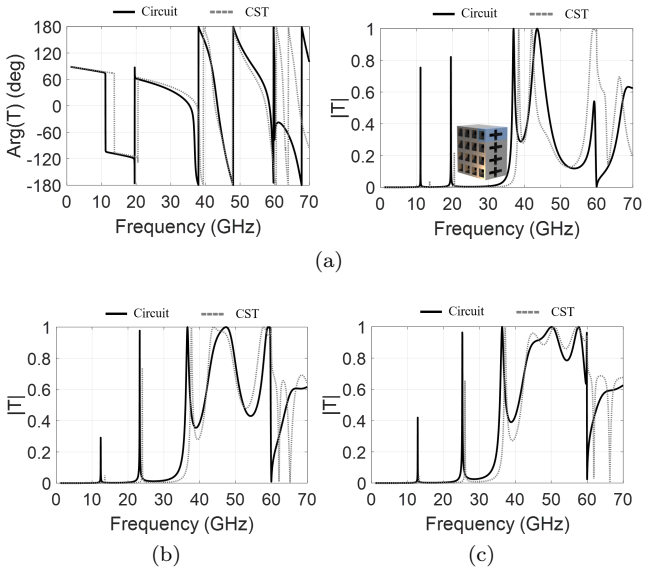

Figure 4. (a) Transmission coefficient T (phase and amplitude) of a transmitting 3D structure ($h_1 = 1\,\text{mm}$). (b) $|T|$ for $h_1 = 2\,\text{mm}$. (c) $|T|$ for $h_1 = 3\,\text{mm}$. The analytical circuit model corresponds to that shown in Figure 1(c). Geometrical parameters: $p_x = p_y = 5\,\text{mm}$, $w_x = w_y = 4\,\text{mm}$, $d_1 = 4\,\text{mm}$, $d_2 = 4\,\text{mm}$, $d_3 = 1\,\text{mm}$, $d_4 = 4\,\text{mm}$, $d_5 = 4\,\text{mm}$, and $h_2 = 3\,\text{mm}$. Normal incidence is assumed.

Figure 4 shows the transmission coefficient T (phase and amplitude) in the 3D transmitting structure. The performance of the analytical equivalent circuit is tested against full-wave results extracted from CST. A good agreement is generally observed in a wideband range. For the calculation of 5001 frequency points, the circuit approach lasted less than 4 seconds while CST took more than 10 minutes. Time-domain full-wave solvers such as CST are highly dependent on the size of the structure under analysis. Transmitting structures are longer than reflective structures, so computation times notably increase. Remarkably, our circuit approach is, for all practical purposes, independent from the considered size. In fact, even-odd excitation techniques [45, 62] can be considered for the analysis of longitudinally-symmetric transmitting structures such as the one considered here (symmetric with respect to the plane $D = d_1 + d_2/2$), approximately halving the computation time.

In Figure 4, two resonant transmission peaks appear below the cutoff frequency of the RWG (37.5 GHz for

the selected geometry). As previously discussed, evanescent waves travel along the RWG and, at some particular frequencies, may couple to the HWG sections led by the fundamental TEM mode. Thus, narrowband transmission does occur below the cutoff of the RWG. The two narrowband transmission peaks are caused by $\lambda/2$ and λ resonances in the HWG sections. Ideally, for the selected length of the HWG sections (9 mm in total), the $\lambda/2$ resonance would be located at 16.67 GHz if the HWG sections were isolated from the RWG and uniform in height. In practice, Figures 4(a), (b), (c) show that the $\lambda/2$ resonance is located at 11.2 GHz, 12.4 GHz and 13 GHz, respectively, for an increasing height h_1. As the height of the HWG increases, the simulated resonance approaches the theoretical estimation, as the capacitive contribution of $Y_{\text{eq}}^{\text{II}}$ and Y_{eq}^{V} (RWG–HWG transitions) is less prominent. Same rationale holds for the λ resonance created by the HWG.

The circuit approach stops being accurate beyond 60 GHz. This coincides with the onset of the first higher harmonic in the HWG, at 60 GHz (larger dimension/periodicity $p_{\text{x}} = 5\,\text{mm}$). In any case, the accuracy of the model is quite good below this frequency, covering an actually large bandwidth.

F. Independent Polarization Control

Another interesting property of the proposed 3D metamaterial is the independent polarization control of its two orthogonal linear states (X and Y polarizations). This is a key feature that can be exploited for the efficient design of polarizer devices. Independent polarization control is possible thanks to the use of the longitudinal direction as an additional degree of freedom. As was already shown in [18, 61], resonators perforated on the waveguide walls in the XZ-plane controls X polarization and are opaque for Y polarization. The opposite situation is achieved when the resonators are perforated on the YZ wall. It is true that specific 2D metasurface designs may achieve a certain degree of polarization independence [64, 65]. However this independence is highly sensitive to the scatterer shape and geometry. In 3D architectures, the resonator shapes do not break the polarization-independence property. Focusing on the structure under consideration in the present paper, independent polarization control can be easily achieved by placing an additional perpendicular HWG section. Thus, the HWG section in the 3D structure is now stretched along the x and y directions, as the insets in Figure 5 illustrate.

In Figure 5, the orthogonal polarization independence is tested in a reflective structure (short-circuited at its end). Figure 5 shows the amplitude of the reflection coefficient R for two perpendicular polarizations at normal incidence. In the legend, E_{ij} $(i, j = \{x, y\})$ states for the electric field associated to input $i-$polarized (horizontal) and output j-polarized (vertical) waves. Thus, subindexes ii and jj represent the co-polarization (co-pol) terms while ij and ji represent the cross-polarization (cross-pol) terms. The cross-pol level is under -40 dB in a wideband range. Therefore, a great polarization independence can be claimed for the horizontal and vertical polarizations. Note that, from 50 GHz onwards, the single-mode behaviour of the structure ceases as the second mode of the HWG becomes propagative, as well as the first-orders harmonics in the air region.

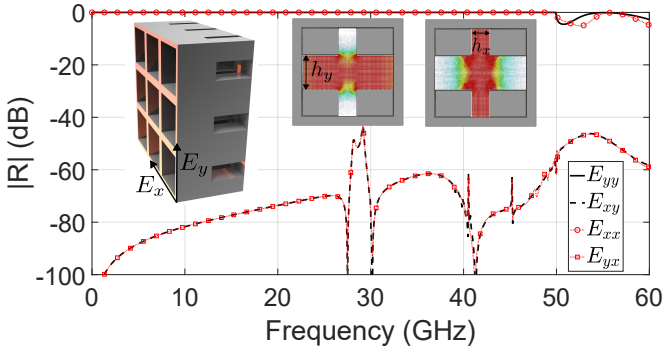

Figure 5. Amplitude of the reflection coefficient of a reflective 3D structure. Co-pol (E_{xx}, E_{yy}) and cross-pol (E_{xy}, E_{yx}) terms are plotted. Geometrical parameters: $p_{\text{x}} = p_{\text{y}} = 6\,\text{mm}$, $w_{\text{x}} = w_{\text{y}} = 5\,\text{mm}$, $d_1 = 4\,\text{mm}$, $d_2 = 6\,\text{mm}$, $h_{\text{x}} = 1\,\text{mm}$, $h_{\text{y}} = 2\,\text{mm}$.

For a visual representation, the inset in Figure 5 depicts the electric field profile of the fundamental mode for the horizontal and vertical polarizations. The electric field profile has been extracted with full-wave simulations in the commercial software. When the incident wave is polarized along the y axis, the entire electric field is confined within the horizontal HWG. Cutting the structure at the center part does not significantly affect the electric-field pattern, which still shows a TEM-like profile. This fact leads to the low cross-pol coupling level evidenced in Figure 5. The scenario is identical for a x-polarized incident wave. Most of the electric field is confined in the vertical HWG, also leading to a TEM-like profile. Polarization independence can be advantageously used for the design of polarizer devices, by simply tuning the length of the vertical and horizontal slots. Thus, a 0^{o}-phase or 180^{o}-phase resonances can be achieved when the length of the short-circuited slot is $\lambda/4$ or $\lambda/2$, respectively [60]. In addition, the polarization independence is also advantageous from the circuital point of view, since and individual and independent circuit approach can be employed for the control of each of the polarizations (x and y). The global problem, involving both polarizations, is split in two independent subproblems (one for the x component, one for the y component).

III. RELATED 3D STRUCTURES

In this section, we show that the proposed analytical circuit approach can be used not only for the analysis of

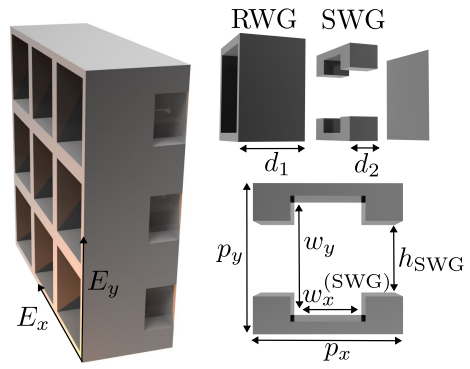

Figure 6. "Alternative" 3D metamaterial formed by RWG and SWG sections. Note that its internal structure differs from the "original" 3D metamaterial (RWG and HWG sections) shown in Figure 1(a). Geometrical parameters: $p_{\mathrm{x}} = p_{\mathrm{y}} = 6$ mm, $w_{\mathrm{x}} = w_{\mathrm{y}} = 5\,\mathrm{mm}$, $w_{\mathrm{x}}^{(\mathrm{SWG})} = 3\,\mathrm{mm}$, $d_1 = 4\,\mathrm{mm}$, $d_2 = 6\,\mathrm{mm}$. The parameter w_{y} is identical for the RWG and SWG regions.

the original 3D device shown in Figure 1, but also for the characterization of related 3D metastructures and metagratings. As it will be shown, under some circumstances, related 3D structures present similar electromagnetic behavior to the originally proposed 3D metamaterial, thus the analytical equivalent circuit is still applicable.

Specifically, we focus on the alternative version of the original 3D metamaterial shown in Figure 6. The alternative structure is similar in all aspects to the original one, except for the waveguide sections where the longitudinal slots are inserted. In the alternative 3D structure (Figure 6), the upper and lower metallic walls are not stretched along the y direction in the slotted waveguide (SWG) region. This leads to a different field excitation in the SWG [66].

In general, electromagnetic fields within the SWG region are different and of more complex nature than of a HWG. Note that a HWG is bounded with perfect electric conditions at the upper and lower walls and magnetic conditions at the lateral walls, which simply excites a TEM mode at low frequencies. The situation is different in a SWG section, where the electric field profile shows a TEM-like profile within the slotted region but does not vanish outside this region. However, under certain circumstances, it can be demonstrated that the SWG can behave effectively as a HWG, i.e., $\mathbf{E}^{(\mathrm{HWG})} \approx \mathbf{E}^{(\mathrm{SWG})}$. In those cases, the original and alternative 3D metastructures will show similar electromagnetic responses and, therefore, both can be analyzed with the analytical equivalent circuit. This scenario is illustrated in Figure 7. The reflection coefficient R is plotted for the original (solid lines) and alternative (dashed lines) 3D structures when varying the height of the longitudinal slots.

Figures 7(a) and (b) present scenarios where wide and narrow longitudinal slots are considered, respectively. Results suggest that wide slots in the SWG ($h_{\mathrm{SWG}} \gtrsim 0.6w_{\mathrm{y}}$) lead to similar electromagnetic responses between the original and alternative 3D metastructures. This is observed in a wide range of frequencies. On the other hand, the frequency range where the original and alternative 3D structures show a similar electromagnetic behavior significantly reduces when inserting narrow slots ($h_{\mathrm{SWG}} \lesssim 0.6w_{\mathrm{y}}$). This can be qualitatively explained by looking at the electric field profiles of the HWG and SWG shown in Figure 7. The electric field must vanish at the upper and lower metallic walls in the SWG region. In the extreme case $h_{\mathrm{SWG}} = w_{\mathrm{y}}$, the SWG section transforms into an actual HWG governed by the fundamental TEM mode. For this extreme case, the electromagnetic response of both original and alternative 3D structures is indistinguishable.

As the slot gets progressively narrower (h_{SWG} decreases), differences between both configurations start to appear, mainly at high frequencies. In cases where the slot is wide [Figure 7(a)], the electric field in the SWG is mainly of TEM nature, as the edge of the slot is close to the upper and lower metallic walls. From a practical perspective, the complex SWG can be reduced to an equivalent HWG section in order to operate. The equivalent HWG would be of same width (p_{x}) than the SWG and effective height h_{eff}. The concept of *effective height* is heuristically introduced after inspecting the excited fields in the SWG. It can be observed that the electric field is fundamentally confined in the slot (h_{SWG}) plus a tiny vertical region Δh_{SWG}, thus $h_{\mathrm{eff}} = h_{\mathrm{SWG}} + \Delta h_{\mathrm{SWG}}$. By analyzing the SWG in the alternative 3D structure as an equivalent HWG, the circuit models is able to provide accurate results on the scattering phenomena, as Figure 7(a) illustrates.

The situation is not that simple when considering narrow SWG slot insertions ($h_{\mathrm{SWG}} \lesssim 0.6w_{\mathrm{y}}$). In this case, as Figure 7(b) illustrates, the excited fields in the SWG departs from the TEM profile seen in the HWG. This fact becomes especially noticeable at high frequencies, where the original (solid lines) and alternative (dashed lines) 3D structures no longer show similar electromagnetic responses. Consequently, as discussed at the end of subsection II E, the results obtained with the circuit (circles) and CST (solid line) slightly differ from each other when considering narrow slots. This is due to the intense capacitive effects introduced by $Y_{\mathrm{eq}}^{\mathrm{II}}$ in the HWG, thus leading to a resonant frequency extracted by CST (38.16 GHz) to be somewhat lower than that calculated by the circuit (39.26 GHz). Distance between the top and bottom walls at the center of the SWG region (set by w_{y}) provokes the capacitance of the SWG to be smaller than of the HWG.

In order to estimate the values for the effective height h_{eff}, Figure 8 depicts the line impedance at 30 GHz of both HWG and SWG structures. Note that the line impedance is plotted as a function of the height of the slot (h parameter). These results have been extracted from port information in commercial software CST (v2022). It is worth noting that Z is the impedance associated with the propagative TEM mode through the uniform line.

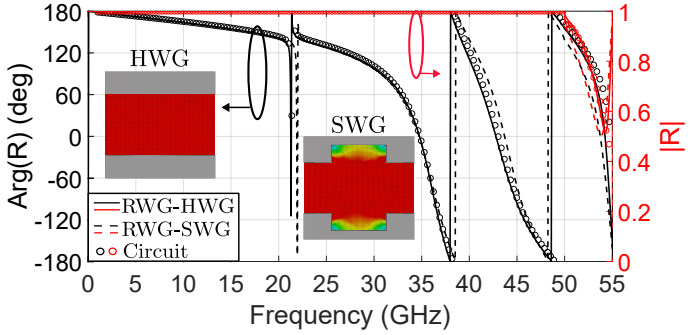

(a)

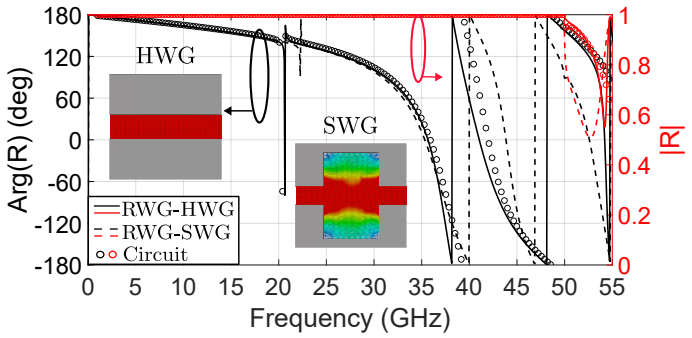

(b)

Figure 7. Comparison of the phase of the reflection coefficient for two different reflective metastructures: original (RWG and HWG sections) and alternative (RWG and SWG sections). Colored solid and dashed lines correspond to full-wave results while colored circles correspond to analytical results. The height of the slotted regions is varied. (a) $h_{\mathrm{SWG}} = 3\,\mathrm{mm}$, $h_{\mathrm{HWG}} = 3.42\,\mathrm{mm}$. (b) $h_{\mathrm{SWG}} = 1\,\mathrm{mm}$, $h_{\mathrm{HWG}} = 1.375\,\mathrm{mm}$. The original and alternative 3D structures show similar electromagnetic responses when the slot height is large [panel (a)]. Geometrical parameters: $p_{\mathrm{x}} = p_{\mathrm{y}} = 6\,\mathrm{mm}$, $w_{\mathrm{x}} = 5\,\mathrm{mm}$, $w_{\mathrm{y}} = 5\,\mathrm{mm}$, $w_{\mathrm{x}}^{(\mathrm{SWG})} = 3\,\mathrm{mm}$, $d_1 = 4\,\mathrm{mm}$, $d_2 = 6\,\mathrm{mm}$.

In the SWG, these curves has been extracted for three different values of w_{y}: $w_{\mathrm{y}} = 3$ mm (dashed green line), $w_{\mathrm{y}} = 4$ mm (dashed blue line) and $w_{\mathrm{y}} = 5$ mm (dashed red line).

Naturally, when the values of w_{y} and h are identical in the SWG structure, the extracted impedance coincides with that of the HWG. As a result, the impedance curves cross each other. However, the impedance values that are of particular interest in this work are those above the HWG curve (black solid line). In these cases, the original and alternative 3D structures are expected to show similar electromagnetic responses and, therefore, both can be analyzed with the present analytical circuit approach. Thus, it can be seen that for any selected height of SWG, there is another (greater) effective height of the HWG where their impedances coincide. As an example, a SWG region with $h = 3$ mm and $w_{\mathrm{y}} = 5$ mm will present the same line impedance (at 30 GHz) than a HWG region with $h_{\mathrm{eff}} = 3.42$ mm.

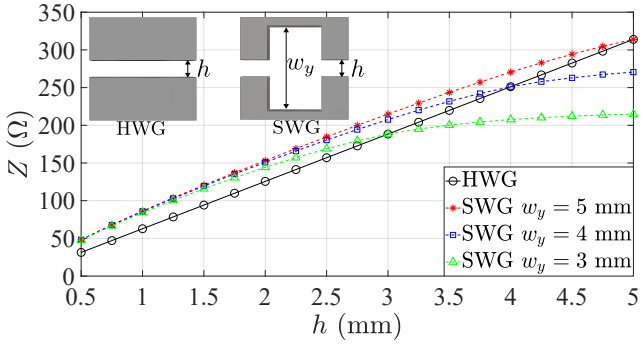

Figure 8. Line impedance in the the SWG and HWG as a function of the height h. Geometrical parameters: $p_{\mathrm{x}} = p_{\mathrm{y}} = 6\,\mathrm{mm}$, $w_{\mathrm{x}}^{(\mathrm{SWG})} = 3\,\mathrm{mm}$. Results extracted with CST Studio.

IV. APPLICATIONS: FULL-METAL POLARIZER

One of the main advantages of the proposed 3D metamaterials is the independent control of the two orthogonal polarization states. This fact has become evident after evaluating the results obtained in Figures 5 and 7. Independent polarization control is a remarkable feature, rarely found in 1D and 2D implementations, that can be advantageously exploited for the design and prototyping of full-metal polarizers.

As an example, the proposed analytical approach is applied for the design of a reflective polarizer that operates from 35 GHz to 43.2 GHz. The proposed 3D device rotates the polarization plane of the reflected wave 90 degrees in the selected frequency range. Consequently, the direction of rotation of a circularly polarized incident wave would also change. This is one of the main applications in which the analytical circuit study can be used from an engineering perspective. It is worth noting that the purpose of this section is not to design a state-of-the-art polarizer, but to show the applicability of the circuit approach in real-world scenarios.

Figure 9(a) sketches the fully-metallic 3D reflective polarizer. As it can be appreciated, the 3D polarizer is composed of all the regions depicted above: RWG, SWG and HWG. Note that, with this configuration it is possible to achieve slots of different lengths in the vertical and horizontal walls, thus the resonances can be tuned by modifying parameters d_2 and d_3.

Reflective fully-metallic 3D structures allow simple but efficient polarizer designs due to the low ohmic losses involved. As the polarizers are short-circuited at the end of the structures, only the phase shift between the orthogonal components of the incident electric field needs to be set for the design of polarizers of different nature. In order to polarize an incoming wave whose electric field vibrates along $\hat{\mathbf{u}}$-direction [shown in Figure 9(a)], it is sufficient to set the phases separately from the reflection coefficient R of its main components E_{x} and E_{y}. Therefore,

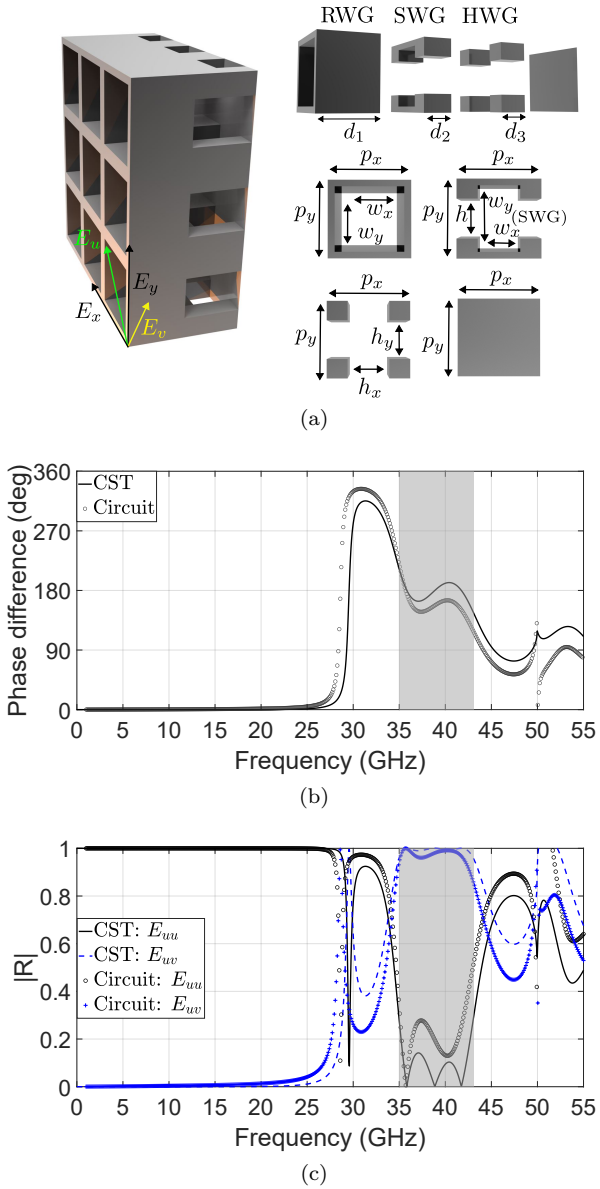

Figure 9. (a) Illustration of a 3D reflective polarization rotator. (b) Phase difference between the reflection coefficient of the vertical co-polarization (E_{yy}) and the reflection coefficient of the horizontal co-polarization (E_{xx}). (c) Amplitude of the reflection coefficient R, showing the co-pol. (black) and cross-pol. (blue) components for E_u and E_v. The shadowed region (in grey) indicates the operative range of the polarization rotator. Solid and dashed lines correspond to full-wave results, while circles and crosses to analytical ones. Geometrical parameters: $p_x = p_y = 6\,\text{mm}$, $w_x = w_y = 5\,\text{mm}$, $w_x^{(SWG)} = 3\,\text{mm}$, $d_1 = 4\,\text{mm}$, $d_2 = d_3 = 2\,\text{mm}$, $h = 3\,\text{mm}$, $h_x = h_y = 3\,\text{mm}$.

if the reflection coefficient of E_x and E_y in their co-polar direction (E_{xx} and E_{yy}) present a phase shift of 180 deg, a rotator is achieved. From a design perspective, it is common to assume a maximum error of $180\,\text{deg} \pm 37\,\text{deg}$ [67, 68]. This error band fixes the operation bandwidth of the polarization rotator.

The operation of the polarizator rotator is as follows. In both E_{xx} and E_{yy} components, the incident wave impinges in the RWG section whose dimensions prevent the propagation of the fundamental mode below 30 GHz. Subsequently, the propagative $TE_{10}^{(RWG)}$ mode is guided from 30 GHz to 50 GHz by the SWG and the short-circuited HWG as a TEM-like and TEM mode respectively. Thus, single-mode operation is guaranteed from 30 GHz to 50 GHz. Above 50 GHz, the amplitude decays as the second propagative mode is excited. A center frequency of 37.4 GHz is assumed as a starting design point. At this frequency, the shorter vertical slot insertion (SWG-HWG-short section) creates a $\lambda/4$ resonance, while the larger horizontal slot insertion (HWG-short section) creates a $\lambda/2$ resonance. Both $\lambda/4$ and $\lambda/2$ resonances produce a relative phase shift of 180 deg between the horizontal and vertical components, which leads to a rotation of the polarization plane for the reflected wave. The study realized in section III has made it possible to simulate the SWG region as a HWG with parameters that approximate their electromagnetic responses.

Figure 9(b) illustrates the phase difference of the reflection coefficient R of the two orthogonal components E_{xx} and E_{yy}. The shadowed region indicates the simulated bandwidth where the 3D polarization rotator is operative. In Figure 9(c), the rotation on the electric field is directly visualized. It shows the amplitude of the reflection coefficient R for an incident wave whose electric field vibrates according to E_u. The shadowed region sets the previous bandwidth where the co-polarization reflection is below to -10 dB in logarithmic scale. Consequently, the power is transmitted to the orthogonal component E_v. As can be seen, the bandwidth obtained by the circuit model is slightly lower than the simulated bandwidth. Despite this, a good agreement is observed between full-wave numerical results in CST and the analytical circuit taking into account the variations from the original structure shown in Figure 1. Naturally, it is important to remark the difference in computational times between CST and the circuit in the design stage, beyond the physical insight that the circuit may also provide. For the extraction of the two orthogonal components, CST took approximately 10 minutes and the analytical circuit only 2 seconds.

It is interesting to highlight the reduced weight of the 3D polarizer. As the polarizer is based on the use of periodic waveguides (RWG, HWG, SWG), the interior of the structure is essentially hollow and filled with air. This causes the weight of the structure to be much less than originally suspected, since the volume of metal (or metallized material) is small compared to the total volume. Of the total volume of the polarizer, approximately 63% is air while only 37% is metal. This leads to a reduced weight for the polarizer, as well as for the others 3D metastructures presented in this work, which is of great interest for potential commercial applications.

Additionally, the size of the proposed 3D polarizer is

smaller than one may initially think. The dimensions of its unit cell are $0.75\lambda \times 0.75\lambda \times \lambda$ (width $\times$ height $\times$ thickness), considering a central frequency of 37.5 GHz. A fabricated functional polarizer would require, at least, of a structure formed by 10×10 unit cells so the real-world finite implementation can be approached as periodic and analyzed with the present mathematical framework. Thus, the dimensions of the fabricated finite structure would be $7.5\lambda \times 7.5\lambda \times \lambda$. If we compare these dimensions with those required in a lens-type antenna or with other reflectarrays/transmitarrays based on 2D configurations, we see that the 3D polarizer has a relatively compact size. A compact size is a great practical advantage when fabricating and using the 3D metastructures, e.g. for integration into mobile communication platforms.

V. CONCLUSION

Analytical modeling of complex 3D metastructures has been elusive due to the intricate geometries involved. In this paper, we have derived an analytical framework for the analysis of 3D metamaterials formed by periodic arrangements of rectangular waveguides with longitudinal slot insertions. The proposed approach comes with an associated analytical equivalent circuit. The analytical circuit model is constituted by transmission lines that model wave propagation through the different homogeneous waveguide sections and shunt equivalent admittances that model higher-order harmonic excitation at the discontinuities. It is shown that the slotted waveguide sections can be modeled as a general waveguide with periodic boundary conditions (PBC). For the selected input excitation, and especially for normal incidence, PBC conditions can be relaxed to perfect magnetic conductor (PMC) conditions. Thus, slotted waveguides sections can be modeled as "hard waveguides" (HWG). We have tested the analytical framework against full-wave numerical results. A good agreement is observed in all cases, when considering reflective (short circuited) and transmitting (open) 3D configurations in normal and oblique incidence conditions. In the 3D metagrating, narrowband transmission is observed at frequencies below the cut-off. In cases where the rectangular waveguide (RWG) is short, evanescent waves may couple to the HWG (led by its fundamental TEM mode) and transmit without losses along the 3D structure. The analytical circuit model has proven to be a powerful tool to gain physical insight into complex scattering and diffraction phenomena, such as this one. Additionally, results show that the proposed 3D metamaterial is suitable for the efficient design of full-metal polarizer devices with advanced or complex functionalities. This is attributed to the reliable independent polarization control of the two orthogonal states that the 3D metamaterial exhibits. An example is the polarization rotator shown in the work, which operates from 35 to 44 GHz approximately. The good agreement exhibited by full-wave and circuit results makes the circuit approach to become a rapid design tool. We hope that the analytical methodology developed in this work will be a step forward in the analysis and design of more advanced and, surely, more attractive 3D metastructures.

ACKNOWLEDGMENTS

This work has been supported by grant PID2020-112545RB-C54 funded by MCIN/AEI/10.13039/501100011033 and by the European Union NextGenerationEU/PRTR. It has also been supported by grants PDC2022-133900-I00, TED2021-129938B-I00 and TED2021-131699B-I00.

A. TRANSMISSION MATRICES

In the way that the analytical circuit model is defined in Figure 1(c), the computation of the scattering parameters is based on the usage of transmission (ABCD) matrices. Shunt equivalent admittances Y_{eq} can be modeled with the following ABCD matrix [69]

$$\left[\mathbf{T}_Y(Y_{\text{eq}})\right] = \begin{bmatrix} 1 & 0 \\ Y_{\text{eq}} & 1 \end{bmatrix}. \tag{43}$$

Note that a short circuit in reflective structures can be modeled with the previous expression by simpling selecting $Y_{\text{eq}} \to \infty$. Waveguide sections (RWG and HWG) are modeled as lossless transmission lines according to [69]

$$\left[\mathbf{T}_L(Y_0, \beta, d)\right] = \begin{bmatrix} \cos(\beta d) & \mathrm{j}\frac{1}{Y_0}\sin(\beta d) \\ \mathrm{j}Y_0 \sin(\beta d) & \cos(\beta d) \end{bmatrix}, \tag{44}$$

where Y_0, β and d are the characteristic admittance, propagation constant and length of the transmission line.

The global transmission matrix $\left[\mathbf{T}\right]$ is computed by cascading (multiplying) the individual transmission matrices that form the complete circuit. Then, the global scattering matrix $\left[\mathbf{S}\right]$ is extracted from $\left[\mathbf{T}\right]$ by using the formulas detailed in [70], which take into consideration that the input and output media (impedance/admittance of the reference ports) could be different.

[1] N. Marcuvitz, *Waveguide Handbook* (Institution of Electrical Engineers, GBR, 1986).

[2] A. Vengsarkar, P. Lemaire, J. Judkins, V. Bhatia, T. Erdogan, and J. Sipe, Long-period fiber gratings as band-rejection filters, Journal of Lightwave Technology **14**, 58 (1996).

[3] P.-S. Kildal, E. Alfonso, A. Valero-Nogueira, and E. Rajo-Iglesias, Local metamaterial-based waveguides in gaps between parallel metal plates, IEEE Antennas and Wireless Propagation Letters **8**, 84 (2009).

[4] Y. Zhao, M. A. Belkin, and A. Alú, Twisted optical metamaterials for planarized ultrathin broadband circular polarizers, Nat. Comm **3**, 870 (2012).

[5] Y. Cui, K. H. Fung, J. Xu, H. Ma, Y. Jin, S. He, and N. X. Fang, Ultrabroadband light absorption by a sawtooth anisotropic metamaterial slab, Nano Letters **12**, 1443 (2012), pMID: 22309161.

[6] G. Minatti, M. Faenzi, E. Martini, F. Caminita, P. De Vita, D. González-Ovejero, M. Sabbadini, and S. Maci, Modulated metasurface antennas for space: Synthesis, analysis and realizations, IEEE Transactions on Antennas and Propagation **63**, 1288 (2015).

[7] A. Palomares-Caballero, A. Alex-Amor, P. Padilla, and J. F. Valenzuela-Valdés, Dispersion and filtering properties of rectangular waveguides loaded with holey structures, IEEE Transactions on Microwave Theory and Techniques **68**, 5132 (2020).

[8] O. Quevedo-Teruel, M. Ebrahimpouri, and M. Ng Mou Kehn, Ultrawideband metasurface lenses based on off-shifted opposite layers, IEEE Antennas and Wireless Propagation Letters **15**, 484 (2016).

[9] N. Engheta and R. Ziolkowski, *Metamaterials: Physics and Engineering Explorations* (Wiley-IEEE Press: Hoboken, NJ, USA, 2006).

[10] F. Capolino, *Theory and Phenomena of Metamaterials* (CRC Press, 2009).

[11] D. Smith, J. B. Pendry, and M. C. K. Wiltshire, Metamaterials and negative refractive index, Science **305**, 5685 (2004).

[12] E. Galiffi, R. Tirole, S. Yin, H. Li, S. Vezzoli, P. A. Huidobro, M. G. Silveirinha, R. Sapienza, A. Alù, and J. B. Pendry, Photonics of time-varying media, Advanced Photonics **4**, 014002 (2022).

[13] C. Caloz and Z.-L. Deck-Léger, Spacetime metamaterials—part i: General concepts, IEEE Transactions on Antennas and Propagation **68**, 1569 (2020).

[14] S. Taravati and G. V. Eleftheriades, Generalized space-time-periodic diffraction gratings: Theory and applications, Phys. Rev. Applied **12**, 024026 (2019).

[15] O. Quevedo-Teruel, H. Chen, A. Díaz-Rubio, G. Gok, A. Grbic, G. Minatti, E. Martini, S. Maci, G. V. Eleftheriades, M. Chen, and et al., Roadmap on metasurfaces, Journal of Optics **21**, 073002 (2019).

[16] A. Alex-Amor, A. Palomares-Caballero, and C. Molero, 3-D metamaterials: Trends on applied designs, computational methods and fabrication techniques, Electronics **11**, 410 (2022).

[17] M. Kadic, G. Milton, M. van Hecke, and M. Wegener, 3D metamaterials, Nat. Rev. Phys. **1**, 98–210 (2019).

[18] C. Molero Jimenez, E. Menargues, and M. García-Vigueras, All-metal 3-D frequency-selective surface with versatile dual-band polarization conversion, IEEE Transactions on Antennas and Propagation **68**, 5431 (2020).

[19] O. Tsilipakos, A. Xomalis, G. Kenanakis, M. Farsari, C. M. Soukoulis, E. N. Economou, and M. Kafesaki, Split-cube-resonator-based metamaterials for polarization-selective asymmetric perfect absorption, Sci. Rep **10**, 17653 (2020).

[20] C. Molero, A. Palomares-Caballero, A. Alex-Amor, I. Parellada-Serrano, F. Gamiz, P. Padilla, and J. F. Valenzuela-Valdés, Metamaterial-based reconfigurable intelligent surface: 3D meta-atoms controlled by graphene structures, IEEE Communications Magazine **59**, 42 (2021).

[21] D. Bermúdez-Martín, R. Gillard, C. Molero, H. Legay, and M. García-Vigueras, Methodology for improving scanning performance loading an array element with a 3D all-metal waim, Electronics **11** (2022).

[22] A. Palomares-Caballero, C. Molero, P. Padilla, M. García-Vigueras, and R. Gillard, Wideband 3-D-printed metal-only reflectarray for controlling orthogonal linear polarizations, IEEE Transactions on Antennas and Propagation **71**, 2247 (2023).

[23] H. Y. Jeong, E. Lee, S.-C. An, Y. Lim, and Y. C. Jun, 3D and 4D printing for optics and metaphotonics, Nanophotonics **9**, 1139 (2020).

[24] P. Sanchez-Olivares, M. Ferreras, E. Garcia-Marin, L. Polo-López, A. Tamayo-Domínguez, J. Córcoles, J. M. Fernández-González, J. L. Masa-Campos, J. R. Montejo-Garai, J. M. Rebollar-Machain, and et al., Manufacturing guidelines for W-band full-metal waveguide devices: Selecting the most appropriate technology, IEEE Antennas and Propagation Magazine , 2 (2022).

[25] M. García-Vigueras, L. Polo-Lopez, C. Stoumpos, A. Dorlé, C. Molero, and R. Gillard, *Hybrid Planar*, edited by M. D. Fernandez, J. A. Ballesteros, H. Esteban, and Ángel Belenguer (IntechOpen, Rijeka, 2022) Chap. 6.

[26] T. Itoh, *Numerical Techniques for Microwave and Millimeter-Wave Passive Structures* (Wiley, 1989).

[27] J. Blanchard, E. Newman, and M. Peters, Integral equation analysis of artificial media, IEEE Transactions on Antennas and Propagation **42**, 727 (1994).

[28] M. Silveirinha and C. Fernandes, Homogenization of 3-D-connected and nonconnected wire metamaterials, IEEE Transactions on Microwave Theory and Techniques **53**, 1418 (2005).

[29] O. Rabinovich and A. Epstein, Dual-polarized all-metallic metagratings for perfect anomalous reflection, Phys. Rev. Appl. **14**, 064028 (2020).

[30] N. Kari, D. Seetharamdoo, J.-M. Laheurte, and F. Sarrazin, Modal analysis of chiral metamaterial using characteristic mode analysis and eigenmode expansion method, IEEE Journal on Multiscale and Multiphysics Computational Techniques **5**, 37 (2020).

[31] G. Deschamps, Ray techniques in electromagnetics, Proceedings of the IEEE **60**, 1022 (1972).

[32] Q. Liao, N. J. G. Fonseca, M. Camacho, A. Palomares-Caballero, F. Mesa, and O. Quevedo-Teruel, Ray-tracing model for generalized geodesic-lens multiple-beam antennas, IEEE Transactions on Antennas and Propagation **71**, 2640 (2023).

[33] Z.-Y. Li and L.-L. Lin, Photonic band structures solved by a plane-wave-based transfer-matrix method, Phys. Rev. E **67**, 046607 (2003).

[34] F. Giusti, Q. Chen, F. Mesa, M. Albani, and O. Quevedo-Teruel, Efficient Bloch analysis of general periodic structures with a linearized multimodal transfer-matrix approach, IEEE Transactions on Antennas and Propagation **70**, 5555 (2022).

[35] A. Grbic and G. V. Eleftheriades, An isotropic three-dimensional negative-refractive-index transmission-line metamaterial, Journal of Applied Physics **98** (2005).

[36] M. Zedler, C. Caloz, and P. Russer, A 3-D isotropic left-handed metamaterial based on the rotated transmission-

line matrix (TLM) scheme, IEEE Transactions on Microwave Theory and Techniques **55**, 2930 (2007).
[37] F. Mesa, R. Rodriguez-Berral, and F. Medina, Unlocking complexity using the ECA: The equivalent circuit model as an efficient and physically insightful tool for microwave engineering, IEEE Microwave Magazine **19**, 44 (2018).
[38] F. Costa, A. Monorchio, and G. Manara, Efficient analysis of frequency-selective surfaces by a simple equivalent-circuit model, IEEE Antennas and Propagation Magazine **54**, 35 (2012).
[39] M. Kafesaki, I. Tsiapa, N. Katsarakis, T. Koschny, C. M. Soukoulis, and E. N. Economou, Left-handed metamaterials: The fishnet structure and its variations, Phys. Rev. B **75**, 235114 (2007).
[40] J. Carbonell, C. Croënne, F. Garet, E. Lheurette, J. L. Coutaz, and D. Lippens, Lumped elements circuit of terahertz fishnet-like arrays with composite dispersion, Journal of Applied Physics **108**, 014907 (2010).
[41] G. Perez-Palomino, J. E. Page, M. Arrebola, and J. A. Encinar, A design technique based on equivalent circuit and coupler theory for broadband linear to circular polarization converters in reflection or transmission mode, IEEE Transactions on Antennas and Propagation **66**, 2428 (2018).
[42] M. Borgese and F. Costa, A simple equivalent circuit approach for anisotropic frequency-selective surfaces and metasurfaces, IEEE Transactions on Antennas and Propagation **68**, 7088 (2020).
[43] A. Hernández-Escobar, E. Abdo-Sánchez, P. Mateos-Ruiz, J. Esteban, T. María Martín-Guerrero, and C. Camacho-Peñalosa, An equivalent-circuit topology for lossy non-symmetric reciprocal two-ports, IEEE Journal of Microwaves **1**, 810 (2021).
[44] R. Dubrovka, J. Vazquez, C. Parini, and D. Moore, Equivalent circuit method for analysis and synthesis of frequency selective surfaces, Proc. Inst. Elect. Eng.—Microw., Antennas Propag **153**, 213–220 (2006).
[45] V. Torres, F. Mesa, M. Navarro-Cía, R. Rodríguez-Berral, M. Beruete, and F. Medina, Accurate circuit modeling of fishnet structures for negative-index-medium applications, IEEE Transactions on Microwave Theory and Techniques **64**, 15 (2016).
[46] A. Khavasi and B. Rejaei, Analytical modeling of graphene ribbons as optical circuit elements, IEEE Journal of Quantum Electronics **50**, 397 (2014).
[47] F. Mesa, R. Rodríguez-Berral, M. García-Vigueras, F. Medina, and J. R. Mosig, Simplified modal expansion to analyze frequency-selective surfaces: An equivalent circuit approach, IEEE Transactions on Antennas and Propagation **64**, 1106 (2016).
[48] S. Barzegar-Parizi, B. Rejaei, and A. Khavasi, Analytical circuit model for periodic arrays of graphene disks, IEEE Journal of Quantum Electronics **51**, 1 (2015).
[49] R. Rodriguez-Berral, F. Medina, F. Mesa, and M. Garcia-Vigueras, Quasi-analytical modeling of transmission/reflection in strip/slit gratings loaded with dielectric slabs, IEEE Transactions on Microwave Theory and Techniques **60**, 405 (2012).
[50] R. Rodríguez-Berral, C. Molero, F. Medina, and F. Mesa, Analytical wideband model for strip/slit gratings loaded with dielectric slabs, IEEE Trans. Microw. Theory Techn **60**, 3908 (2012).
[51] C. Molero, R. Rodríguez-Berral, F. Mesa, and F. Medina, Analytical circuit model for 1-D periodic T-shaped corrugated surfaces, IEEE Trans. Antennas Propag **62**, 794 (2014).
[52] C. Molero, R. Rodríguez-Berral, F. Mesa, and F. Medina, Wideband analytical equivalent circuit for coupled asymmetrical nonaligned slit arrays, Phys. Rev. E **95**, 023303 (2017).
[53] R. Rodríguez-Berral, F. Mesa, and F. Medina, Analytical multimodal network approach for 2-D arrays of planar patches/apertures embedded in a layered medium, IEEE Transactions on Antennas and Propagation **63**, 1969 (2015).
[54] C. Molero, M. García-Vigueras, R. Rodríguez-Berral, F. Mesa, and N. Llombart, Equivalent circuit approach for practical applications of meander-line gratings, IEEE Antennas Wirel. Propag. Lett **16**, 3088 (2017).
[55] A. Alex-Amor, F. Mesa, A. Palomares-Caballero, C. Molero, and P. Padilla, Exploring the potential of the multi-modal equivalent circuit approach for stacks of 2-D aperture arrays, IEEE Transactions on Antennas and Propagation **69**, 6453 (2021).
[56] C. Molero, A. Alex-Amor, F. Mesa, A. Palomares-Caballero, and P. Padilla, Cross-polarization control in FSSs by means of an equivalent circuit approach, IEEE Access **9**, 99513 (2021).
[57] A. Alex-Amor, S. Moreno-Rodríguez, P. Padilla, J. F. Valenzuela-Valdés, and C. Molero, Diffraction phenomena in time-varying metal-based metasurfaces, Phys. Rev. Appl. **19**, 044014 (2023).
[58] S. Moreno-Rodríguez, A. Alex-Amor, P. Padilla, J. F. Valenzuela-Valdés, and C. Molero, Time-periodic metallic metamaterials defined by floquet circuits, Arxiv Preprint, doi: 2211.13271 (2023).
[59] A. Alex-Amor, C. Molero, and M. G. Silveirinha, Analysis of metallic space-time gratings using Lorentz transformations, Phys. Rev. Appl. **20**, 014063 (2023).
[60] M. A. Balmaseda-Márquez, S. Moreno-Rodríguez, P. H. Zapata, C. Molero, and J. F. Valenzuela-Valdés, Fully-metallic 3D cells for wideband applications, IEEE Transactions on Antennas and Propagation **71**, 4588 (2023).
[61] C. Molero and M. García-Vigueras, Circuit modeling of 3-D cells to design versatile full-metal polarizers, IEEE Trans. Microw. Theory Techn. **67**, 1357 (2019).
[62] C. Molero, R. Rodríguez-Berral, F. Mesa, F. Medina, and A. B. Yakovlev, Wideband analytical equivalent circuit for one-dimensional periodic stacked arrays, Phys. Rev. E **93**, 013306 (2016).
[63] D. Griffiths, *Introduction to Quantum Mechanics* (Prentice Hall, 1995).
[64] S. Mercader-Pellicer, W. Tang, D. Bresciani, H. Legay, N. J. G. Fonseca, and G. Goussetis, Angularly stable linear-to-circular polarizing reflectors for multiple beam antennas, IEEE Transactions on Antennas and Propagation **69**, 4380 (2021).
[65] A. A. Omar, Z. Shen, and S. Y. Ho, Multiband and wideband 90° polarization rotators, IEEE Antennas and Wireless Propagation Letters **17**, 1822 (2018).
[66] C. Molero, H. Legay, T. Pierré, and M. García-Vigueras, Broadband 3D-printed polarizer based on metallic transverse electro-magnetic unit-cells, IEEE Transactions on Antennas and Propagation **70**, 4632 (2022).
[67] W. Chen, C. A. Balanis, and C. R. Birtcher, Checkerboard EBG surfaces for wideband radar cross section reduction, IEEE Transactions on Antennas and Propagation **63**, 2636 (2015).

[68] Z. Zhang, J. Wang, X. Fu, Y. Jia, H. Chen, M. Feng, R. Zhu, and S. Qu, Single-layer metasurface for ultra-wideband polarization conversion: bandwidth extension via fano resonance, Sci. Rep. **11**, 585 (2021).

[69] D. M. Pozar, *Microwave Enginnering*, 3rd ed. (Wiley, Hoboken, NJ, USA, 2005).

[70] D. Frickey, Conversions between S, Z, Y, H, ABCD, and T parameters which are valid for complex source and load impedances, IEEE Transactions on Microwave Theory and Techniques **42**, 205 (1994).

2.1.4 Analytical Framework to Model Reconfigurable Metasurfaces including Lumped Elements

In this paper, we present a potential tool for simulating spatially-modulated metamaterials with the inclusion of lumped elements. The periodic arrangement of lumped elements in the spatial structure with a 1D periodic modulation transforms the original problem into a 2D periodically-modulated structure. The proposed analytical framework has been tested with lumped Resistor-Inductor-Capacitor (RLC) tanks, even under oblique incidence, showing excellent agreement with commercial full-wave software. A realistic design of a dual-band absorber has been developed and simulated, demonstrating significant potential for the design of devices based on more complex circuit models, including diodes and transistors. This work could be very useful for the simulation of reconfigurable or time-varying metamaterials.

THIS IS A POSTPRINT VERSION OF THE PAPER:

Mario Perez Escribano, S. Moreno-Rodríguez, C. Molero , J. F. Valenzuela-Valdés, P. Padilla and Antonio Alex-Amor, "Analytical Framework to Model Reconfigurable Metasurfaces including Lumped Elements," *IEEE Transactions on Circuits and Systems II: Express Briefs*, vol. 71, no. 4, pp. 1784-1788, April 2024.

- Journal Impact Factor (JIF) in JCR 2023: 4.0
- Category: ENGINEERING, ELECTRICAL & ELECTRONIC. JIF Rank: 100/352 (Q2).

Disclaimer:
This work has been published on IEEE Transactions on Circuits and Systems II: Express Briefs.
DOI: 10.1109/TCSII.2023.3330318

Analytical Framework to Model Reconfigurable Metasurfaces including Lumped Elements

Mario Pérez-Escribano, Salvador Moreno-Rodríguez, Carlos Molero, *Member, IEEE,*
Juan F. Valenzuela-Valdés, Pablo Padilla, Antonio Alex-Amor

***Abstract*—This manuscript introduces an analytical framework for the design of reconfigurable metasurfaces rooted in 2D periodic structures. Incorporating lumped elements into the model streamlines the design process for such devices, offering significantly improved efficiency compared to designs reliant on full-wave software. The theoretical framework, founded on Floquet modal expansions, also guarantees robust performance even under oblique incidence conditions, far beyond the onset of the first grating lobe. In practical applications, an absorber has been devised by integrating a resistor into the model. Nevertheless, circuit analysis extends the possibilities for crafting more intricate structures utilizing diodes or tunable varactors, enabling the design of phase shifters, polarizers, and reconfigurable intelligent surfaces (RIS).**

***Index Terms*—Analytical framework, lumped elements, metasurfaces, Floquet expansion, oblique incidence, reconfigurable.**

I. Introduction

LUMPED elements are, by definition, circuit elements (resistors, inductors, capacitors, diodes, transistors, etc.) of much smaller size compared to the operating wavelength [1]. The design and application of lumped elements have been an intense research object in the radiofrequency (RF) and microwave communities in the last decades [2]. Lumped elements have been traditionally combined with distributed elements, e.g., transmission lines, in integrated and planar technologies for the realization of passive and active microwave circuits such as filters, absorbers, 3-dB quadrature hybrids, impedance transformers, amplifiers, rectifiers or time-modulated antennas [1]–[6]. Recently, with the appearance of metamaterials, artificial composites that can go beyond the conventional properties of materials in nature, novel and sophisticated lumped-element-based microwave and mm-wave devices have seen the light. Examples of lumped-element-based metastructures, such as periodically-loaded phase shifters or diode-tunable absorbers, reflectarray/transmitarray cells, and intelligent metasurfaces, can be found in [7]–[9].

The study of microwave devices and metamaterials, including the presence of lumped elements, is a nontrivial task. The interaction and electromagnetic coupling between the lumped and distributed elements considerably hinder the analysis. Most of the state-of-art numerical approaches are based on full-wave schemes, such as the finite-difference time-domain (FDTD) [10], [11] and the finite element method (FEM) [12]. Iterative techniques [13] and the transmission line method (TLM) [14] have also proven to be practical solutions. More recently, homogenization techniques have been applied to analyze metastructures using time-modulated lumped elements [15].

In general, precise analytical or quasi-analytical methods are preferred over numerical ones due to their simplicity and computational efficiency in resolving the problem [16]. This paper proposes an alternative fully analytical approach based on Floquet-Bloch series expansions and equivalent circuits to analyze 2D metamaterials loaded with generic lumped elements. The analytical approach is computationally efficient and gives physical insight into the scattering phenomena via the related equivalent circuit. Furthermore, it works under oblique-incidence conditions in a wideband range, even for frequency regions above the diffraction regime.

The paper is organized as follows. Section II describes the analytical framework, as well as the advantages and limitations of the method. Section III illustrates some numerical examples to validate the approach. Section IV shows the utilization of the analytical approach to design a dual wideband absorber. Finally, conclusions are drawn in Section V.

II. Circuit Topology and Theoretical Framework

A. Circuit Topology

The structure under consideration consists of a metasurface fed by the incidence of an oblique (angle θ) plane wave. The transverse electric-field vector is directed along the perpendicular direction of the strips to excite a richer phenomenology. It corresponds to a TE ($\phi = 0^{\text{o}}$) or a TM ($\phi = 90^{\text{o}}$) polarization, as shown in Fig. 1. Rows of lumped elements, such as networks based on resistors, inductors, and capacitors, will be placed periodically at the slit aperture connecting two consecutive strips. This makes the 1D grating a two-dimensional structure, as shown in Fig. 1. The distance

This work has been supported by grant PID2020-112545RB-C54 funded by MCIN/AEI/10.13039/501100011033 and by the European Union NextGeneration EU/PRTR. It has also been supported by grants PDC2022-133900-I00, TED2021-129938B-I00, and TED2021-131699B-I00, and by Ministerio de Universidades and the European Union NextGenerationEU, under Programa Margarita Salas, and by MCIN/AEI/10.13039/501100011033 and the European Union NextGenerationEU/PRTR under grant IJC2020-043599-I.

(Corresponding author: Antonio Alex-Amor)

Mario Pérez-Escribano is with the Telecommunication Research Institute (TELMA), Universidad de Málaga, E.T.S. Ingeniería de Telecomunicación, 29010 Málaga, Spain.

Mario Pérez-Escribano, Salvador Moreno-Rodríguez, Carlos Molero, Juan F. Valenzuela-Valdés, and Pablo Padilla are with the Department of Signal Theory, Telematics and Communications, Research Centre for Information and Communication Technologies (CITIC-UGR), Universidad de Granada, 18071 Granada, Spain.

Antonio Alex-Amor is with the Department of Information Technologies, Universidad San Pablo-CEU, CEU Universities, Campus Montepríncipe, 28668 Boadilla del Monte (Madrid), Spain.

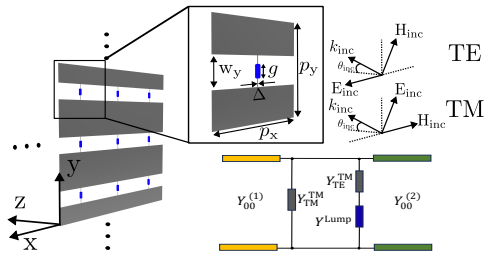

Figure 1. Sketch of the 2D metasurface loaded with lumped elements.

between adjacent strips determines periodicity along the y direction, whereas periodicity along the x direction is defined by the distance between two consecutive lumped elements. In Fig. 1, p_x and p_y are the periods of the 2D grating along the x and y directions, $w_x = p_x - \Delta$ and w_y are the slit widths, Δ is the thickness of the strip, and g is the gap in which the lumped element is placed.

In [17], a broadband analytical circuit model was proposed for the 1D grating without lumped elements. Unlike most previous models, the circuit approach captured the phenomenology associated with grating-lobe excitation. Simply, for TM incidence, the grating-discontinuity effect was represented by a shunt capacitor $C_{\text{eq}}^{\text{TM}}$. This element turned into an inductor $L_{\text{eq}}^{\text{TE}}$ for TE incidence. To validate this first approximation, which is the baseline for the proposed approach, a simulation of the structure in Fig. 1 is carried out in the full-wave simulator CST Studio Suite, with $p_x = p_y = 10$ mm, $w_y = 3$ mm, considering 2 Floquet modes in each port (one for TM incidence and one for TE). The results of the simulation, in terms of S-parameters, are depicted in Fig. 2(a) and (b). The evaluation of the lumped element has been carried out by assuming normal incidence, $\theta = 0^{\text{o}}$, in both cases. In addition, the results of the equivalent circuit obtained from a Keysight Advanced Design System (ADS) fitting are shown. The values obtained for the capacitor and inductor are $C_{\text{eq}}^{\text{TM}} = 47\,\text{fF}$ and $L_{\text{eq}}^{\text{TE}} = 230\,\text{pH}$, respectively.

Once the results for the first approximation have been obtained, the next step is to perform a simulation in which a tiny wire is added, joining the two extremes of the slit in the unit cell. Again, normal incidence is assumed. This case could be interpreted as a lumped element (an ideal 0 Ω resistor or short-circuit, without inductive behavior) that has been added to the structure. Results for TM and TE incidences are depicted in Fig. 2(c) and 2(d). As seen, a resonance has appeared for the TM incidence case. This resonance admits being modeled in the equivalent circuit as a shunt inductor, $L_{\text{eq}}^{\text{TM}}$, whose value can be obtained through the simulation as

$$L_{\text{eq}}^{\text{TM}} = \frac{1}{C_{\text{eq}}^{\text{TM}}(2\pi f_r)^2}, \tag{1}$$

being f_r the frequency where the resonance appears. In this case, the achieved value is $L_{\text{eq}}^{\text{TM}} = 5.08\,\text{nH}$. The result obtained from the equivalent circuit corresponds to the electromagnetic simulation performed. This is an important detail since it is shown that adding a lumped element between the slits causes them to no longer have the pure capacitive behavior expected

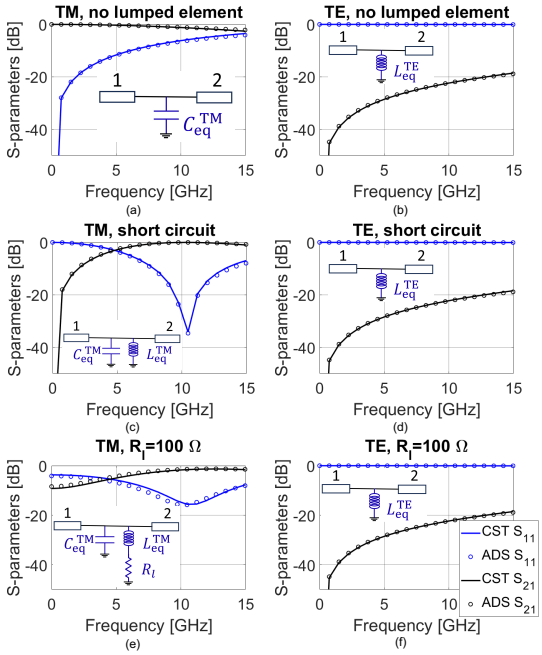

Figure 2. S-parameters of the CST simulation and the proposed equivalent model for (a)-(b) an open, (c)-(d) a short-circuited, and (e)-(f) a resistor-loaded metasurface. Parameters: $p_x = p_y = 10$ mm, $w_y = 3$ mm, $C_{\text{eq}}^{\text{TM}} = 47$ fF, $L_{\text{eq}}^{\text{TE}} = 230$ pH, $L_{\text{eq}}^{\text{TM}} = 5.08$ nH, $R_l = 100\ \Omega$.

for an isolated 1D grating illuminated by a TM wave [17]. An inductive contribution appears as a consequence of the system's evolution from a 1D to a 2D periodic distribution. On the other hand, it can be seen that adding the infinitesimal wire when there is a TE incidence does not imply a change in the behavior of the grating. This is because the electric field is the same at both ends of the wire, so the electric currents will have the same value and direction at both ends, making the lumped element irrelevant to the circuit's behavior.

To validate the conclusions obtained, the last simulated case consists of placing a 100 Ω resistor, R_{l}, in the slit. In this case, the resistor will replace the short circuit previously imposed for the TM incidence case, connecting it in series with the inductor, $L_{\text{eq}}^{\text{TM}}$. As seen in Fig. 2(e), the equivalent circuit fits perfectly the CST simulation, in which the resistor is placed as a lumped element. The incident plane wave is normally oriented, as in the previous cases. As anticipated, the TE incidence (Fig. 2(f)) is not affected by the resistor. This case is, therefore, discarded for the rest of the work, focusing only on TM incidence.

B. Isolated Metasurface

As detailed in Sec. II.A, the circuit topology shown in Fig. 1 captures perfectly the phenomenology associated with wave scattering in a metasurface loaded with a generic lumped element. Interestingly, both the capacitive term ($C_{\text{eq}}^{\text{TM}}$) and the inductive term ($L_{\text{eq}}^{\text{TM}}$), can be computed in a purely analytical form, by isolating the metasurface from the lumped element.

The rationale for the analysis of the isolated metasurface is based on previous works that describe wave scattering in 1D and 2D metagratings [17]–[20], and, more recently, 3D

[21], [22] metagratings. According to [18], the TM and TE admittances associated with the *isolated* 2D metasurface can be computed as

$$Y_{\text{TM}}^{\text{TM}} = \sum_{\forall n,m\neq 0,0} N_{nm}^{\text{TM}} \left(Y_{nm}^{\text{TM},(1)} + Y_{nm}^{\text{TM},(2)} \right) , \quad (2)$$

$$Y_{\text{TE}}^{\text{TM}} = \sum_{\forall n,m\neq 0,0} N_{nm}^{\text{TE}} \left(Y_{nm}^{\text{TE},(1)} + Y_{nm}^{\text{TE},(2)} \right) , \quad (3)$$

where the superindex TM in $Y_{\text{TE}}^{\text{TM}}$ and $Y_{\text{TM}}^{\text{TM}}$ denotes the type of incidence, and the subindexes TE/TM denotes the nature of the Floquet harmonics taking place on the expression. We can clearly indentify $Y_{\text{TM}}^{\text{TM}}$ with $C_{\text{eq}}^{\text{TM}}$ and $Y_{\text{TE}}^{\text{TM}}$ with $L_{\text{eq}}^{\text{TM}}$. Notice that the terms with $n = m = 0$ are excluded from the summation. This harmonic is the incident one, and it is always propagative. The rest of the harmonics are generally evanescent (reactive). This allows us to separate both kinds of harmonics in the circuit.

The elements $N_{nm}^{\text{TM/TE}}$ are terms that identify the complex transformers of the nm-th TM/TE Floquet mode, which take the value

$$N_{nm}^{\text{TM}} = \frac{k_{ym}^2}{k_{xn}^2 + k_{ym}^2} \left| \frac{\tilde{E}_a\left(k_{xn}, k_{ym}\right)}{\widetilde{E}_a(0,0)} \right|^2 , \quad (4)$$

$$N_{nm}^{\text{TE}} = \frac{k_{xn}^2}{k_{xn}^2 + k_{ym}^2} \left| \frac{\tilde{E}_a\left(k_{xn}, k_{ym}\right)}{\widetilde{E}_a(0,0)} \right|^2 , \quad (5)$$

with

$$\widetilde{E}_a(k_{xn}, k_{ym}) = \Big[J_0\left(\frac{w_x}{2}\left|k_{xn} + \pi/w_x\right|\right) + J_0\left(\frac{w_x}{2}\left|k_{xn} - \pi/w_x\right|\right)\Big] \times \frac{\sin\left(\frac{w_y}{2}k_{ym}\right)}{k_{ym}} , \quad (6)$$

describing the Fourier transform of a suitable spatial profile (basis function) for a rectangular aperture of dimensions $w_x \times w_y$ under oblique TM illumination [23].

The admittances of the nm-th harmonic are computed as

$$Y_{nm}^{\text{TM},(i)} = \frac{k_0\sqrt{\varepsilon_r^{(i)}}}{\eta^{(i)}\beta_{nm}^{(i)}} , \quad (7)$$

$$Y_{nm}^{\text{TE},(i)} = \frac{\beta_{nm}^{(i)}}{\eta^{(i)}k_0\sqrt{\varepsilon_r^{(i)}}} , \quad (8)$$

with $\eta^{(i)}$ being the impedance of the input ($i = 1$) and output ($i = 2$) media and $k_0 = \omega/c$. The propagation constant $\beta_{nm}^{(i)}$ reads

$$\beta_{nm}^{(i)} = \sqrt{\varepsilon_r^{(i)}k_0^2 - k_{nm}^2} , \quad (9)$$

where $k_{nm} = \sqrt{k_{xn}^2 + k_{ym}^2}$ with $k_{xn} = k_{x0} + 2\pi n/p_x$, $k_{ym} = k_{y0} + 2\pi m/p_y$, $k_{x0} = k_0 \sin\theta\cos\phi$, and $k_{y0} = k_0 \sin\theta \sin\phi$.

C. Analytical Circuit Model including Lumped Elements

According to the circuit model shown in Fig. 1, the reflection coefficient of the 2D grating loaded with a lumped element with admittance Y^{Lump} is

$$R = \frac{Y_{00}^{(1)} - Y_{00}^{(2)} - Y_{\text{tot}}}{Y_{00}^{(1)} + Y_{00}^{(2)} + Y_{\text{tot}}} \quad (10)$$

where $Y_{00}^{(1)/(2)}$ are the input/output transmission lines corresponding to the incident harmonic. Since TM incidence is considered,

$$Y_{00}^{(1/2)} = \frac{\sqrt{\varepsilon_{\text{r}}^{(i)}}}{\eta^{(i)}\cos(\theta)} \qquad i = 1, 2 . \quad (11)$$

The transmission coefficient is calculated as $T = 1 + R$. In (10), Y_{tot} represents the equivalent admittance of the 2D grating loaded with lumped elements, whose expression is extracted from the circuit model (Fig. 1) and takes the form

$$Y_{\text{tot}} = Y_{\text{TM}}^{\text{TM}} + \frac{1}{1/Y_{\text{TE}}^{\text{TM}} + 1/Y^{\text{Lump}}} . \quad (12)$$

Interestingly, the present analytical methodology can account for losses in the metamaterial [17]. Moreover, plasmonic metagrarings, such as graphene-based ones, could also be considered with modifications of the present approach [24].

III. Numerical Results & Validation

This section shows some numerical examples to validate the analytical approach. Results are tested with full-wave simulations in commercial software CST Studio Suite.

A. Lumped RLC Tank. Oblique Incidence

The first numerical example, schematized in Fig. 3(a), includes a 2D metasurface loaded with a lumped RLC tank of values R_l, C_l and L_l. This example is of general and complex nature, as oblique incidence ($\theta \neq 0$) is also tested. In the case of considering an RLC tank, the admittance of the lumped element to insert in eq. (12) is $Y^{\text{Lump}} = 1/R_{\text{l}} + 1/(j\omega L_{\text{l}}) + j\omega C_{\text{l}}$.

Figs. 3(b) and 3(c) present the amplitude of the reflection (blue curves) and transmission (black curves) coefficients for the oblique-incident angles $\theta = 20^{\text{o}}$ and $\theta = 40^{\text{o}}$, respectively. There is a good agreement between the analytical and CST results. As observed, the analytical circuit perfectly captures the frequency displacement of the grating lobe as the incident angle increases. The onset of the grating-lobe diffraction regime is given by the expression $f = c/(p[1 + \sin\theta])$, which moves to 22.35 GHz for $\theta = 20^{\text{o}}$ and to 18.26 GHz for $\theta = 40^{\text{o}}$. Notice that the onset frequency of grating lobes varies with the incidence angle, as accounted for in the above formula. This is due to the dependence on the angle of the transverse wavelength (wavelength associated with the transverse wavevector of the incidence wave) [17]. A new grating lobe is excited when the transverse wavelength is an integer factor of the periodicity of the grating. For a given angle, there exists just a given onset frequency. As the angle of incidence varies, this onset frequency must also change. Far beyond the onset of the diffraction regime, the analytical approach still provides accurate results, even for narrowband resonances above 30 GHz. The resonance below 2 GHz, well captured by the circuit is created by the lumped RLC tank.

The computation time of the analytical model is much lower than that of CST, as previously discussed. In fact, oblique incident scenarios notably increase computation times in CST while remaining somewhat similar whether normal or oblique incidence is considered in our analytical approach.

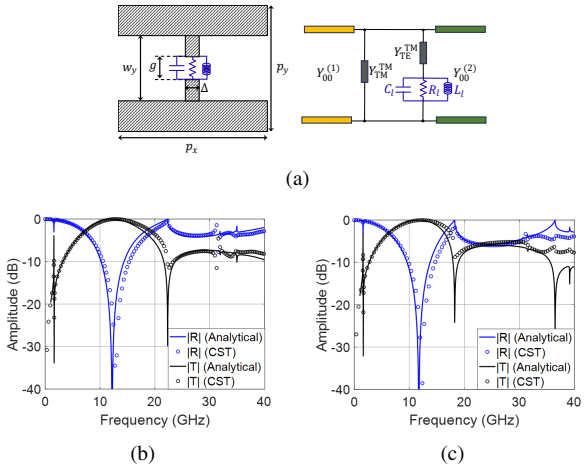

Figure 3. (a) Schematic of 2D grating loaded with a lumped RLC tank. Amplitude of the reflection and transmission coefficient under TM oblique incidence: (b) $\theta = 20^{\text{o}}$, (c) $\theta = 40^{\text{o}}$. Parameters: $R_{\text{l}} = 1000\,\Omega$, $C_{\text{l}} = 100$ pF, $L_{\text{l}} = 100$ pH, $\Delta = 0.1$ mm, $w_y = 3$ mm, $p_x = p_y = 10$ mm.

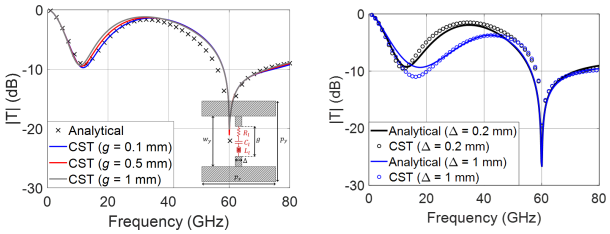

Figure 4. Transmission coefficient $|T|$ in a 2D grating loaded with a lumped series RLC resonator. (a) The gap size g ($\Delta = 0.1$ mm), and (b) the thickness of the strip Δ ($g = 0.1$ mm) are varied. Parameters: $R_{\text{l}} = 100\,\Omega$, $C_{\text{l}} = 0.1$ pF, $L_{\text{l}} = 0.1$ nH, $w_y = 2$ mm, $p_x = p_y = 5$ mm. TM normal incidence.

B. Lumped Series RLC Resonator. Effect of Δ and g

Fig. 4 illustrates the following numerical example as an inset. A different 2D metasurface is loaded with a lumped series RLC resonator of values R_{l}, C_{l}, and L_{l}. In the case of considering a series RLC resonator, the admittance of the lumped element is $Y^{\text{Lump}} = [(R_{\text{l}} + j\omega L_{\text{l}} + 1/(j\omega C_{\text{l}})]^{-1}$.

In this case, we perform a parametric study to see the effect of the thickness of the strip Δ and its gap size g on the method's accuracy. Results are illustrated in Fig. 4. Only the transmission coefficient is plotted in this case to ease the visualization. Technically, the formulation developed in Sec. II assumes that the length of the gap is $g = 0$. However, as Fig. 4(a) illustrates, increasing the gap size does not significantly affect the method's accuracy. Gap sizes of 0.5 mm and 1 mm are realistic values where a microwave lumped element (varactor, PIN diode, etc.) may be soldered.

Then, Fig. 4(b) shows the effect of varying the strip thickness Δ. The circuit's topology in Fig. 1 ideally assumes that $\Delta \ll p_x$. Fig. 4(b) shows how the method's accuracy slightly deteriorates as the thickness Δ increases. However, good agreement is still observed with the commercial software. Note that, from a practical point of view, thicknesses $\Delta \geq 0.1$ mm are easily manufacturable in microstrip or similar technologies. The combined effect of increasing the gap g and the strip thickness Δ might deteriorate the analytical approach results.

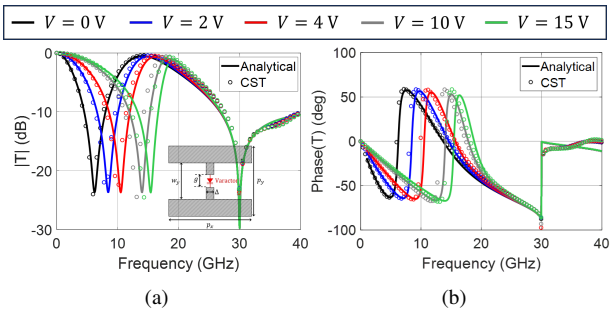

Figure 5. Transmission in a metasurface loaded with a varactor: (a) amplitude, (b) phase. Parameters: $w_y = 3$ mm, $p_x = p_y = 10$ mm. TM incidence.

C. Lumped Varactor Diode

Now, we consider the case where the metasurface is loaded with a varactor diode [see Fig. 5(a)]. This is a common scenario, highly interesting and useful in the design of reconfigurable devices, such as reflectarrays/transmitarrays and time-modulated modules, which have been gaining attention lately [6], [8], [9], [15]. We consider the commercial microwave varactor MAVR-011020-1411 for this example. At low frequencies, the varactor diode can be modeled as a series RC circuit, with $R_{\text{l}} = 13.2\,\Omega$ and a varying capacitor C_l controlled by a bias voltage V. The relation between the applied V and the obtained C_{l} is as follows: $V = \{0, 2, 4, 10, 15\}$ V $\leftrightarrow C_{\text{l}} = \{0.233, 0.125, 0.080, 0.0439, 0.0357\}$ pF.

Figs. 5(b) and 5(c) illustrate the amplitude and phase terms of the transmission coefficient, respectively. As observed, there is a good correspondence between the analytical results and those obtained by CST in a wideband range of frequencies, even above the diffraction regime (30 GHz). An increase in the reverse bias voltage V, is translated into a decrease in the series capacitance C_{l} and, subsequently, a decrease in the lumped admittance $Y^{\text{Lump}} = [(R_{\text{l}} + 1/(j\omega C_{\text{l}})]^{-1}$. Therefore, lower current flows through the varactor branch so that the TM (capacitive) term clearly predominates over the TE (inductive) one, increasing the transmission level at the low frequencies (near DC). In other words, the zero-transmission peak shifts to higher frequencies as the bias voltage increases and C_{l} is smaller. This example highlights the physical insight that the analytical model provides about the scattering phenomenon.

IV. Realistic Design

The analytical model can also be used as an efficient and physically insightful *design* tool. As an example, we apply the analytical framework for the design of a dual-band absorber. Fig. 6(a) illustrates the proposed device, based on a metasurface loaded with a lumped resistor R_{l}. To achieve a higher absorption ratio, the resistor-loaded metasurface is backed by a metallic plate, separated by a distance, d. The medium separating the two is air, although other dielectric materials could be chosen. The analytical formulation stays identical, except for the term $Y_{nm}^{\text{TM/TE},(2)}$ used in Eqs. (2), (3) and (10), that should be replaced by $Y_{\text{in},nm}^{\text{TM/TE},(2)} = -jY_{nm}^{\text{TM/TE},(2)}\cot(\beta_{nm}^{(2)}d)$.

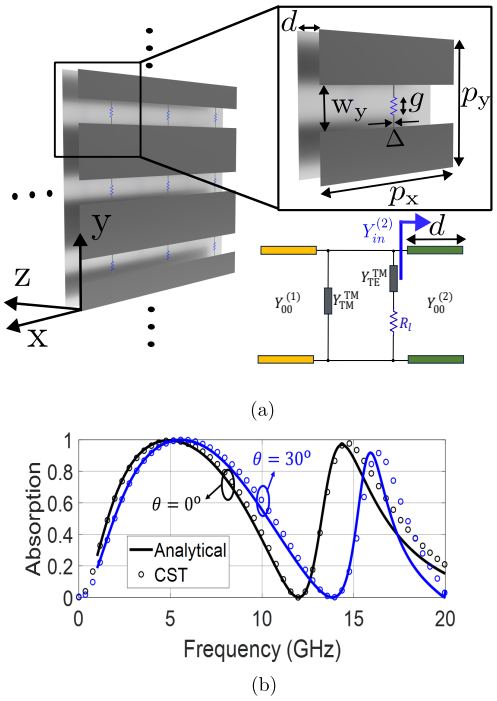

Figure 6. (a) Sketch of a resistor-based meta-absorber. (b) Absorption under TM normal (black) and oblique (blue) incidence. Solid lines and circles represent the analytical and CST results. Parameters: $R_l = 310\,\Omega$, $\Delta = 0.1$ mm, $g = 0.5$ mm, $w_y = 3$ mm, $p_x = p_y = 10$ mm, $d = 12.5$ mm.

Fig. 6(b) presents the absorption parameter. A greater absorption rate is obtained near the $\lambda/4$ and $3\lambda/4$ resonances (around 6 GHz and 18 GHz). Under normal TM incidence, a fractional bandwidth (FBW) of 72.8% is achieved in the first band (from 3.28 GHz to 7.04 GHz), assuming an absorption of more than 90%. A second absorption band appears from 14.08 GHz to 15.38 GHz, giving a FBW of 8.8%. This second band can still be used, as the first grating lobe is excited at 30 GHz. Under oblique TM incidence ($\theta = 30^o$), the first grating lobe appears around 20 GHz. Even so, the first absorption bandwidth obtains a FBW = 68% (from 3.84 GHz to 7.8 GHz), showing robustness under oblique-incidence conditions. In this case, CST took 1 and more than 8 minutes when normal and oblique incidence were considered, respectively. The analytical approach took less than 1 second in both cases.

V. Conclusion

In this paper, we have proposed a self-consistent model for analyzing metasurfaces loaded with lumped elements. The present approach is fully analytical; thus, physical insight is given into complex scattering phenomena. Moreover, it notably reduces the computation time. In normal and oblique incidence, the analytical framework works in a wide range of frequencies, even far beyond the onset of the grating-lobe regime. Finally, the analytical approach has been tested against full-wave numerical results in CST. Accurate results are obtained even for oblique incidences of $\theta = 40^o$.

Acknowledgments

We would like to thank Francisco J. García-Ruiz for using his Keysight Advanced Design System (ADS) license.

References

[1] I. Bahl, *Lumped Elements for RF and Microwave Circuits*, 2003.
[2] M. Caulton, B. Hershenov, S. Knight, and R. DeBrecht, "Status of lumped elements in microwave integrated circuits - present and future," *IEEE Trans. Microw. Theory Tech.*, vol. 19, no. 7, pp. 588–599, 1971.
[3] D. Daly, S. Knight, M. Caulton, and R. Ekholdt, "Lumped elements in microwave integrated circuits," *IEEE Trans. Microw. Theory Tech.*, vol. 15, no. 12, pp. 713–721, 1967.
[4] M. Caulton, S. Knight, and D. Daly, "Hybrid integrated lumped-element microwave amplifiers," *IEEE Trans. Microw. Theory Tech.*, vol. 16, no. 7, pp. 397–404, 1968.
[5] A. Alex-Amor, J. Moreno-Núñez, J. M. Fernández-González, P. Padilla, and J. Esteban, "Parasitics impact on the performance of rectifier circuits in sensing RF energy harvesting," *Sensors*, vol. 19, no. 22, p. 4939, 2019.
[6] J. Zang, A. Alvarez-Melcon, and J. Gomez-Diaz, "Nonreciprocal phased-array antennas," *Phys. Rev. Appl.*, vol. 12, p. 054008, Nov 2019.
[7] M. Antoniades and G. Eleftheriades, "Compact linear lead/lag metamaterial phase shifters for broadband applications," *IEEE Antennas Wireless Propag. Lett.*, vol. 2, pp. 103–106, 2003.
[8] P. Padilla, A. Muñoz-Acevedo, M. Sierra-Castañer, and M. Sierra-Pérez, "Electronically reconfigurable transmitarray at ku band for microwave applications," *IEEE Trans. Antennas Propag.*, vol. 58, p. 2571, 2010.
[9] F. Liu and *et al.*, "Intelligent metasurfaces with continuously tunable local surface impedance for multiple reconfigurable functions," *Phys. Rev. Appl.*, vol. 11, p. 044024, Apr 2019.
[10] W. Sui, D. Christensen, and C. Durney, "Extending the two-dimensional FDTD method to hybrid electromagnetic systems with active and passive lumped elements," *IEEE Trans. Microw. Theory Tech.*, vol. 40, no. 4, pp. 724–730, 1992.
[11] Y.-D. Kong, X.-L. Chen, and Q.-X. Chu, "Numerical stability and dispersion analysis of the two-dimensional FDTD method including lumped elements," *IEEE Trans. Antennas Propag.*, pp. 1–1, 2023.
[12] K. Guillouard, M.-F. Wong, V. Hanna, and J. Citerne, "A new global finite element analysis of microwave circuits including lumped elements," *IEEE Trans. Microw. Theory Tech.*, vol. 44, no. 12, pp. 2587–2594, 1996.
[13] H. Trabelsi, A. Gharsallah, and H. Baudrand, "Analysis of microwave circuits including lumped elements based on the iterative method," *International Journal of RF and Microwave Computer-Aided Engineering*, vol. 13, no. 4, pp. 269–275, 2003.
[14] P. Russer, P. So, and W. Hoefer, "Modeling of nonlinear active regions in TLM (distributed circuits)," *IEEE Microw. Guided Wave Lett.*, vol. 1, no. 1, pp. 10–13, 1991.
[15] Z. Wu, C. Scarborough, and A. Grbic, "Space-time-modulated metasurfaces with spatial discretization: Free-space N-path systems," *Phys. Rev. Applied*, vol. 14, p. 064060, Dec 2020.
[16] O. Luukkonen, C. R. Simovski, A. V. Raisanen, and S. A. Tretyakov, "An efficient and simple analytical model for analysis of propagation properties in impedance waveguides," *IEEE Trans. Microw. Theory Tech.*, vol. 56, no. 7, pp. 1624–1632, 2008.
[17] R. Rodríguez-Berral, C. Molero, F. Medina, and F. Mesa, "Analytical wideband model for strip/slit gratings loaded with dielectric slabs," *IEEE Trans. Microw. Theory Techn*, vol. 60, no. 12, pp. 3908–3918, 2012.
[18] R. Rodríguez-Berral, F. Mesa, and F. Medina, "Analytical multimodal network approach for 2-D arrays of planar patches/apertures embedded in a layered medium," *IEEE Trans. Antennas Propag.*, vol. 63, no. 5, pp. 1969–1984, 2015.
[19] F. Mesa, M. García-Vigueras, F. Medina, R. Rodríguez-Berral, and J. R. Mosig, "Circuit-model analysis of frequency selective surfaces with scatterers of arbitrary geometry," *IEEE Antennas Wireless Propag. Lett.*, vol. 14, pp. 135–138, 2015.
[20] A. Alex-Amor, F. Mesa, A. Palomares-Caballero, C. Molero, and P. Padilla, "Exploring the potential of the multi-modal equivalent circuit approach for stacks of 2-D aperture arrays," *IEEE Trans. Antennas Propag.*, vol. 69, no. 10, pp. 6453–6467, 2021.
[21] C. Molero and M. García-Vigueras, "Circuit modeling of 3-D cells to design versatile full-metal polarizers," *IEEE Trans. Microw. Theory Techn.*, vol. 67, no. 4, pp. 1357–1369, 2019.
[22] A. Alex-Amor, S. Moreno-Rodríguez, P. Padilla, J. Valenzuela-Valdés, and C. Molero, "Analytical equivalent circuits for three-dimensional metamaterials and metagratings," *Phys. Rev. Appl.*, vol. 20, 2023.
[23] S. Rengarajan, "Choice of basis functions for accurate characterization of infinite array of microstrip reflectarray elements," *IEEE Antennas Wireless Propag. Lett.*, vol. 4, pp. 47–50, 2005.
[24] A. Khavasi and B. Rejaei, "Analytical modeling of graphene ribbons as optical circuit elements," *IEEE J. Quantum Electron.*, vol. 50, pp. 397–403, 2014.

2.2 Time Modulation

2.2.1 Diffraction Phenomena in Time-Varying Metal-Based Metasurfaces

In this work, we develop a circuital analysis for simulating time-varying metallic metamaterials. A nondispersive metasurface that alternates its properties over time is assumed, presenting two states: metal (full reflection) and air (full transmission). The previous experience in circuital modeling for spatially-modulated metamaterials has been applied to time-varying systems. Through the use of the proposed analytical method, users gain physical insight into the diffraction pattern (diffraction angles, scattering parameters, nature of the temporal harmonics) and the frequency conversion phenomena typical of these structures.

Due to the lack of commercial tools capable of efficiently simulating such time-varying structures, a self-implemented FDTD method has been developed to compare the electromagnetic response. The results reveal that this metasurface is spacetime nondispersive and that the higher-order modes are resistive (propagative), whereas in spatially-modulated systems, these higher-order harmonics are usually capacitive/inductive (evanescent). Moreover, the values obtained through the circuit-based approach show good agreement with FDTD simulations, drastically reducing computation times. Therefore, the performance of these time-varying metasurfaces positions them as strong candidates for beamforming and frequency mixing applications.

THIS IS A POSTPRINT VERSION OF THE PAPER:

A. Alex-Amor, S. Moreno-Rodríguez, P. Padilla, J. F. Valenzuela-Valdés and C. Molero, "Diffraction phenomena in time-varying metal-based metasurfaces," *Physical Review Applied*, vol. 19, p. 044014, Apr 2023.

- Journal Impact Factor (JIF) in JCR 2023: 3.8
- Category: PHYSICS, APPLIED. JIF Rank: 54/179 (Q2).

Disclaimer:
This work has been published in Physical Review Applied.
DOI: 10.1103/PhysRevApplied.19.044014

Accepted for publication in Physical Review Applied. doi: https://doi.org/10.1103/PhysRevApplied.19.044014

Diffraction Phenomena in Time-varying Metal-based Metasurfaces

Antonio Alex-Amor*
Department of Information Technology, Universidad San Pablo-CEU, CEU Universities, Campus Montepríncipe, 28668 Boadilla del Monte (Madrid), Spain

Salvador Moreno-Rodríguez, Pablo Padilla, Juan F. Valenzuela-Valdés, Carlos Molero
Department of Signal Theory, Telematics and Communications, Universidad de Granada, 18071 Granada, Spain

This paper presents an analytical framework for the analysis of time-varying metal-based metamaterials. Concretely, we particularize the study to time-modulated metal-air interfaces embedded between two different semi-infinite media that are illuminated by monochromatic plane waves of frequency ω_0. The formulation is based on a Floquet-Bloch modal expansion, which takes into account the time periodicity of the structure ($T_s = 2\pi/\omega_s$), and integral-equation techniques. It allows to extract the reflection/transmission coefficients as well as to derive nontrivial features about the dynamic response and dispersion curves of time-modulated metal-based screens. In addition, the proposed formulation has an associated analytical equivalent circuit that gives physical insight to the diffraction phenomenon. Similarities and differences between space- and time-modulated metamaterials are discussed via the proposed circuit model. Finally, some analytical results are presented to validate the present framework. A good agreement is observed with numerical computations provided by a self-implemented finite-difference time-domain (FDTD) method. Interestingly, the present results suggest that time-modulated metal-based screens can be used as pulsed sources (when $\omega_s \ll \omega_0$), beamformers ($\omega_s \sim \omega_0$) to redirect energy in specific regions of space, and analog samplers ($\omega_s \gg \omega_0$).

I. INTRODUCTION

The propagation properties of electromagnetic waves through time-varying media is a topic that has classically been studied to understand effective modulations produced by interaction of two waves [1, 2]. In the last years the topic has been revisited due to the potential applications of time-varying systems in communications. Exotic properties related to the inherent non-reciprocity [3, 4] or beam-steering capabilities [5] attracted the interest of many researchers. At the same time, the theoretical background associated with time-varying systems has benefited a fruitful development. This is the case of the generalization of Kramer-Kronig relations to temporal scenarios [6], dual behaviors in spacially- and temporally-varying systems [7], or the discovery of promising scenarios based on moving gratings [8]. A complete compilation of spacetime media is reported in [9, 10], exposing the general concepts and examining theoretical implications and promising application fields.

Modern time-varying systems are based on periodic-structure and metasurface configurations, whose architecture can approximately be interpreted as periodic or quasi-periodic distributions of individual emitters or meta atoms [11, 12]. Following this line of argument, further definitions are discussed for temporal systems in [13]. An original concept arises by mixing classical metamaterials and metasurfaces with time modulation. The fundamental advantage of this conception is the long tradition of metamaterials/metasurfaces in the microwave and photonics communities, and the vast knowledge accumulated in the last 20 years from both the experimental and manufacturing point of view [14–16]. Time modulation can individually be incorporated on the meta atoms by reconfigurable elements, such as mechanical, electrical or optical, among others [17].

These spatiotemporal metamaterials/metasurfaces have succeeded in performing non-reciprocal systems. Non-reciprocity, in this context, is given when the metastructure receives radiation from a given direction and reflects it along a second direction, but the opposite situation is not given. In other words, time reversal symmetry is broken [18]. Plethora of works have been published remarking this property [19, 20]. Other works benefits from this property to derive some applications, such as [21, 22]. Some other applications use temporal systems to tailor frequency modulation, as those in [5, 23, 24] for wavefront control, the one in [25] for direction-of-arrival (DOE) estimation, or [26] for multiplexing.

The analysis and design of temporal and spatiotemporal models lacks from the existence of commercial tools. Generally, a home-made numerical code based on Finite-Differences Time Domain (FDTD) [28] provides good physical insight, especially to simulate the time evolution of systems. However it lacks from providing specific parameters such as reflection and transmission coefficients, and most refined techniques are commonly needed. For example, for time-varying dielectric slabs, [29] employs a classical mode matching technique whereas [30] solves

the eigenvalue problem of the dispersion equation. Mode matching technique is also applied in [3] for a spacetime periodic grating. Some other techniques depart from a Floquet analysis, implementing the SD-TW modulation [11], or modelling a Huygens metasurface with Lorentzian dispersion models [31]. In [32], the solution of the system is found thanks to the implementation of a Method-of-Moments (MoM). Circuit-model interpretations have also been reported based on shunt topologies derived from admittance matrices [33, 34]. In most cases, direct comparisons with results provided by FDTD are needed to validate the models [35, 36].

State-of-art works in the literature have traditionally focused on the study of dielectric-like systems with spatiotemporal variations. This work discusses on time-varying systems of metallic nature, consisting of infinitely extended metallic screens that appear and vanish periodically. This situation emulates systems in microwave, millimeter and low-THz regions, where metals behave as good conductors. A plane wave impinges on the structure, interacting with the time-modulated screen. Despite the simplicity of the scenario, it is prone to pose the problem in terms of Floquet and a subsequent circuit analysis. The derivation of simple expressions for the circuit elements allows the reader to acquire substantial physical insight. The methodology is motivated by previous analysis reported in the literature, as in [37–39] for 1-D structures and [40–43] for 2-D structures modulated in space. The structure considered in this manuscript is a kind of analogous but in time. The conclusions extracted from this work can easily be extended to other higher-dimensional structures modulated in both time and spaces.

The time-periodic system presented here is formed by a screen that periodically alternates between "metal" and "air" states. To recreate this system in a real-world implementation, we would require the use of materials, of metallic/semiconductor nature, that can be electronically reconfigured. 2-D materials such as graphene, molibdenum disulfide (MoS2) and hexagonal boron nitride (hBN) could be an interesting option to consider [44–46]. For instance, it is well known that graphene can act as a metal (good conductor) when it is electrically biased. Moreover, the sheet resistance of graphene can be reconfigured depending on the bias [47–49]. Thus, graphene can act as a good conductor (metal state), as a bad conductor, as an absorber and as a transparent layer that is perfectly matched to the surrounding media [50, 51]. Transparent-like responses would lead to the realization of the air state. Naturally, a periodic tuning of the graphene's sheet resistance to achieve metal and air states would require appropriate and specific control electronics. Alternatively, up to microwave frequencies, the use of conventional electronically-reconfigurable schemes based on PIN and varactor diodes could be considered. To recreate "air" and "metal" states in our time-periodic system, we would require of the realization of a reconfigurable planar frequency selective surface (FSS). When properly designed, the reconfigurable FSS would allow full transmission (air state) and full reflection (metal state) of the incident electromagnetic waves [52]. In a metallic FSS, full transmission and reflection can be achieved by means of resonances in a particular range of frequencies.

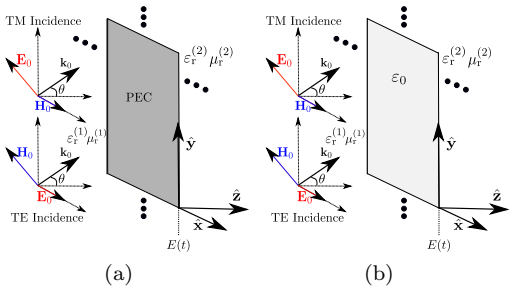

Figure 1. Sketch of the scenario. The time interface is found at position $z = 0$. (a) Time interval when the interface is a PEC sheet ("metal" state). (b) Time interval when the interface vanishes ("air" state).

The paper is organized as follows: Section II is left for the exposition of the theoretical background, analysis of the dynamic and dispersion response, and circuit derivation. Section III is used to evaluate and validate the proposal. The conclusions of the work are found at the end of the paper.

II. THEORETICAL FORMALISM

The scenario to evaluate a time-varying metallic structure is depicted in Figure 1. An infinitely-extended time-varying interface is placed in between of two semi-infinite media ($i = 1$ for input, $i = 2$ for output). The interface (or discontinuity) is a perfect-electric conductor (PEC) sheet that appears and vanishes periodically with period T_s and angular frequency $\omega_\mathrm{s} = 2\pi/T_\mathrm{s}$. A plane wave vibrating with period of T_0 and angular frequency $\omega_0 = 2\pi/T_0$ illuminates the discontinuity. A real implementation of a system of this kind can be, for example, a graphene sheet switching between conductor and non-conductor states, controlled by an external bias voltage [47–49].

Let us define an arbitrary plane wave impinging on such a discontinuity. Assuming TE incidence, the fields associated to this plane wave are expressed as

$$\mathbf{E}_0 = \mathrm{e}^{\mathrm{j}\omega_0 t - \mathrm{j}k_t y - \mathrm{j}\beta_0^{(1)} z}\,\hat{\mathbf{x}} \tag{1}$$

$$\mathbf{H}_0 = Y_0^{(1)}\,\mathrm{e}^{\mathrm{j}\omega_0 t - \mathrm{j}k_t y - \mathrm{j}\beta_0^{(1)} z}\,[\hat{\mathbf{y}}\cos(\theta) - \hat{\mathbf{z}}\sin(\theta)] \tag{2}$$

where we have assumed electric-field amplitude unity. The parameter $Y_0^{(1)}$ is the wave admittance in the incidence region (1) ($z < 0$), and the vectors $k_t = \sqrt{\varepsilon_r^{(1)}\mu_r^{(1)}}\,k_0\sin(\theta)$ and $\beta_0^{(1)} = \sqrt{\varepsilon_r^{(1)}\mu_r^{(1)}}\,k_0\cos(\theta)$ refer to the transverse and longitudinal components of the incident wavevector, respectively. The angle θ corre-

sponds to the incidence angle. In the case of TM incidence, the fields of the incident plane wave are expressed as

$$\mathbf{E}_0 = \mathrm{e}^{\mathrm{j}\omega_0 t - \mathrm{j}k_t y - \mathrm{j}\beta_0^{(1)} z}\,[\hat{\mathbf{y}}\cos(\theta) - \hat{\mathbf{z}}\sin(\theta)] \tag{3}$$

$$\mathbf{H}_0 = Y_0^{(1)}\,\mathrm{e}^{\mathrm{j}\omega_0 t - \mathrm{j}k_t y - \mathrm{j}\beta_0^{(1)} z}\,\hat{\mathbf{x}} \tag{4}$$

A. Floquet-Bloch Expansion

Due to the existence of the time-varying interface and its interaction with the incidence wave, the global transverse electromagnetic field in region (1) admits to be represented in terms of a Floquet series:

$$\mathbf{E}_{\mathrm{t}}^{(1)}(y,z,t) = \Bigg[\mathrm{e}^{\mathrm{j}\omega_0 t - \mathrm{j}k_t y - \mathrm{j}\beta_0^{(1)} z} + R\mathrm{e}^{\mathrm{j}\omega_0 t - \mathrm{j}k_t y + \mathrm{j}\beta_0^{(1)} z} + \sum_{\forall n\neq 0} E_n^{(1)}\mathrm{e}^{\mathrm{j}\omega_n t - \mathrm{j}k_t y + \mathrm{j}\beta_n^{(1)} z}\Bigg]\hat{\mathbf{x}} \tag{5}$$

$$\mathbf{H}_{\mathrm{t}}^{(1)}(y,z,t) = \Bigg[Y_0^{(1)}\mathrm{e}^{\mathrm{j}\omega_0 t - \mathrm{j}k_t y - \mathrm{j}\beta_0^{(1)} z} - RY_0^{(1)}\mathrm{e}^{\mathrm{j}\omega_0 t - \mathrm{j}k_t y + \mathrm{j}\beta_0^{(1)} z} - \sum_{\forall n\neq 0} Y_n^{(1)} E_n^{(1)}\mathrm{e}^{\mathrm{j}\omega_n t - \mathrm{j}k_t y + \mathrm{j}\beta_n^{(1)} z}\Bigg]\hat{\mathbf{y}} \tag{6}$$

where $E_n^{(1)}$ is the amplitude of the nth harmonic, R is the reflection coefficient caused by the time-varying interface, and ω_n is the angular frequency associated with the nth-order harmonic:

$$\omega_n = \omega_0 + n\omega_{\mathrm{s}}\,. \tag{7}$$

As it can be appreciated in eqs. (5)-(7), Floquet harmonics include a dependence not only on the angular rate of change ω_s, related to the time-varying metallic screen, but also on the angular frequency of the incident plane wave, ω_0. The additional phase factor that ω_0 brings to the series provokes that the problem cannot be reduced to a conventional Fourier series.

In a similar way, we define the transverse electromagnetic field at the region (2) ($z > 0$),

$$\mathbf{E}_{\mathrm{t}}^{(2)}(y,z,t) = \Bigg[T\mathrm{e}^{\mathrm{j}\omega_0 t - \mathrm{j}k_t y - \mathrm{j}\beta_0^{(2)} z} + \sum_{\forall n\neq 0} E_n^{(2)}\mathrm{e}^{\mathrm{j}\omega_n t - \mathrm{j}k_t y - \mathrm{j}\beta_n^{(2)} z}\Bigg]\hat{\mathbf{x}} \tag{8}$$

$$\mathbf{H}_{\mathrm{t}}^{(2)}(y,z,t) = \Bigg[TY_0^{(2)}\mathrm{e}^{\mathrm{j}\omega_0 t - \mathrm{j}k_t y - \mathrm{j}\beta_0^{(2)} z} + \sum_{\forall n\neq 0} Y_n^{(2)} E_n^{(2)}\mathrm{e}^{\mathrm{j}\omega_n t - \mathrm{j}k_t y - \mathrm{j}\beta_n^{(2)} z}\Bigg]\hat{\mathbf{y}} \tag{9}$$

where T denotes the transmission coefficient and $E_n^{(2)}$ the amplitude associated to a nth-order Floquet harmonic.

In the former expressions, $Y_n^{(i)}$ is the admittance of the i-th medium ($i = 1$ for input, $i = 2$ for output) associated with the nth-order harmonic:

$$Y_n^{(i)} = \frac{\varepsilon_r^{(i)}\varepsilon_0\,\omega_n}{\beta_n^{(i)}} \quad \text{TM incidence} \tag{10}$$

$$Y_n^{(i)} = \frac{\beta_n^{(i)}}{\mu_r^{(i)}\mu_0\,\omega_n} \quad \text{TE incidence} \tag{11}$$

with

$$\beta_n^{(i)} = \sqrt{\left[k_n^{(i)}\right]^2 - k_t^2} \tag{12}$$

$$k_n^{(i)} = \sqrt{\varepsilon_r^{(i)}\mu_r^{(i)}}\,\frac{\omega_n}{c}\,. \tag{13}$$

The parameter $k_n^{(i)}$ is the nth-order wavenumber and $\beta_n^{(i)}$ its corresponding propagation constant, both in region (i). For TE incidence, just TE admittances in (11) take part in (6) and (9). Similarly, for TM incidence (6) and (9) do use TM admittances only.

B. Dispersion Properties

Figure 2 illustrates the dispersion relation $\omega(k)$ for the time-modulated metallic screen. Dispersion curves are linear (non dispersive) for all the considered harmonics n and are separated from each other by ω_s. Moreover, no stopband region is observed. This is due to the infinitesimal thickness of the time-modulated screen. Actually, this situation is expected to hold as long as the thickness of the screen is much smaller compared to the incident wavelength. This is a remarkable difference compared to time-modulated dielectrics slabs $\varepsilon(t)$ [29, 30], which are typically dispersive and present forbidden bands. Another fact to remark is the existence of negative frequencies and wavenumbers. This means that the corresponding nth-order wavenumber is negative, referring to a mode travelling backward [3].

Additionally, by looking at eqs. (12), (13), it can be readily inferred that most of the diffraction orders created by time-varying metallic screen are purely propagative. It can be demonstrated that only a few negative integer orders n are evanescent (β_n should be imaginary for evanescent waves). These orders would be restricted to

$$-\frac{\omega_0}{\omega_s}\left[1+\sin(\theta)\right] < n < -\frac{\omega_0}{\omega_s}\left[1-\sin(\theta)\right],\ \text{Eva. waves}, \tag{14}$$

when the considered background is air. In fact, in case of normal incidence ($\theta = 0$), there are no evanescent waves. Conversely, larger ratios ω_0/ω_s in combination with large incident angles θ provoke that a greater number of modes are evanescent.

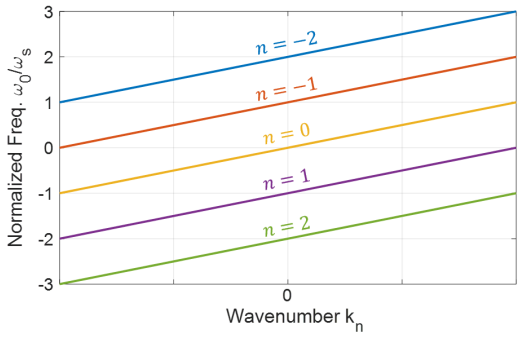

Figure 2. Dispersion curves for the time-modulated metallic screen.

C. Time-varying E-field at the Discontinuity. Equivalent-circuit interpretation

In order to proceed, we will assume the a priori knowledge of the time-dependent field profile at the discontinuity. Without loss of generality, it can be described by a function depending on time $\mathbf{E}(t)$. This assumption allows us to apply and adapt the models presented in [37, 38] for a time periodic problem.

Thus, we first begin by imposing the continuity of the electric field at the interface $z = 0$,

$$\mathbf{E}^{(1)}(y,0,t) = \mathbf{E}^{(2)}(y,0,t) = \mathbf{E}(t)\,, \tag{15}$$

where both $\mathbf{E}^{(1)}(y,0,t)$ and $\mathbf{E}^{(2)}(y,0,t)$ have the field profile at the discontinuity $\mathbf{E}(t)$. This equality allows us to apply standard Fourier analysis, where we reach the following expressions:

$$(1+R) = T = \frac{1}{T_\mathrm{s}}\int_{-T_\mathrm{s}/2}^{T_\mathrm{s}/2} E(t)\mathrm{e}^{-\mathrm{j}\omega_0 t}\mathrm{d}t \tag{16}$$

$$E_n^{(1)} = E_n^{(2)} = \frac{1}{T_\mathrm{s}}\int_{-T_\mathrm{s}/2}^{T_\mathrm{s}/2} E(t)\mathrm{e}^{-\mathrm{j}\omega_n t}\mathrm{d}t\,. \tag{17}$$

From eq.(16) and eq.(17) we get the following relationship:

$$E_n^{(1)} = E_n^{(2)} = (1+R)N(\omega_n) \tag{18}$$

where

$$N(\omega_n) = \frac{\displaystyle\int_{-T_\mathrm{s}/2}^{T_\mathrm{s}/2} E(t)\mathrm{e}^{-\mathrm{j}\omega_n t}\mathrm{d}t}{\displaystyle\int_{-T_\mathrm{s}/2}^{T_\mathrm{s}/2} E(t)\mathrm{e}^{-\mathrm{j}\omega_0 t}\mathrm{d}t} \tag{19}$$

accounts for the coupling between the incident wave and the corresponding nth-order harmonic.

Now, the continuity of the instantaneous Poynting vector at the interface is imposed. The power passing through the interface is evaluated over a period T_s,

$$\int_{-T_\mathrm{s}/2}^{T_\mathrm{s}/2} \mathbf{E}(t)\times\mathbf{H}^{(1)}(y,0,t)\mathrm{d}t = \int_{-T_\mathrm{s}/2}^{T_\mathrm{s}/2} \mathbf{E}(t)\times\mathbf{H}^{(2)}(y,0,t)\mathrm{d}t \tag{20}$$

leading to

$$\begin{aligned}(1-R)Y_0^{(1)}&\int_{-T_\mathrm{s}/2}^{T_\mathrm{s}/2} E(t)\mathrm{e}^{\mathrm{j}\omega_0 t}\mathrm{d}t \\ &- (1+R)\sum_{\forall n\neq 0} N(\omega_n)Y_n^{(1)}\int_{-T_\mathrm{s}/2}^{T_\mathrm{s}/2} E(t)\mathrm{e}^{\mathrm{j}\omega_n t}\mathrm{d}t \\ &= (1+R)Y_0^{(2)}\int_{-T_\mathrm{s}/2}^{T_\mathrm{s}/2} E(t)\mathrm{e}^{\mathrm{j}\omega_0 t}\mathrm{d}t \\ &+ (1+R)\sum_{\forall n\neq 0} N(\omega_n)Y_n^{(2)}\int_{-T_\mathrm{s}/2}^{T_\mathrm{s}/2} E(t)\mathrm{e}^{\mathrm{j}\omega_n t}\mathrm{d}t\,. \end{aligned} \tag{21}$$

The former expression is valid as long as the input and output media are identical. Comparing the integrals in eq.(21) and rearranging terms, the reflection coefficient is finally expressed in the following way,

$$R = \frac{Y_0^{(1)} - Y_0^{(2)} - \displaystyle\sum_{\forall n\neq 0}|N(\omega_n)|^2(Y_n^{(1)}+Y_n^{(2)})}{Y_0^{(1)} + Y_0^{(2)} + \displaystyle\sum_{\forall n\neq 0}|N(\omega_n)|^2(Y_n^{(1)}+Y_n^{(2)})}\,, \tag{22}$$

where we can identify each of the admittances taking part on the expression as individual transmission lines with characteristic admittance $Y_n^{(i)}$ and propagation constant $\beta_n^{(i)}$. Similarly as in [37, 43], eq.(22) is circuitally interpreted by the topology shown in Figure 3. Each of the parameters $N(\omega_n)$ is interpreted as a complex transformer (it transforms both amplitude and phase). Moreover, the infinite sum in (22) groups all relevant information about the diffracted waves created by the time-modulated screen. From a circuit standpoint, this term can be interpreted as an equivalent admittance Y_eq that reads

$$Y_\mathrm{eq} = \sum_{\forall n\neq 0}|N(\omega_n)|^2(Y_n^{(1)}+Y_n^{(2)}) \tag{23}$$

Thus, the reflection coefficient can be rewritten as

$$R = \frac{Y_0^{(1)} - Y_0^{(2)} - Y_\mathrm{eq}}{Y_0^{(1)} + Y_0^{(2)} + Y_\mathrm{eq}} \tag{24}$$

Close inspection of eqs. (12) and (13) reveals that higher-order harmonics are *propagative* in the present time-modulated screen (see Appendix A for further details). This can be appreciated by looking at the wave admittances of the n-th higher-order mode,

$$Y_n^{(i),\mathrm{TM}} = Y_n^{(i),\mathrm{TE}} \approx \sqrt{\frac{\varepsilon_r^{(i)}\varepsilon_0}{\mu_r^{(i)}\mu_0}} = Y_0^{(i)}, \quad |n|\gg 1\,, \tag{25}$$

which are real-valued (in lossless media), independent from index n, and identical for both TM and TE polarizations. This provokes that higher-order modes contribute

with a purely resistive term $R_{\rm eq}^{\rm hi}$ that can be modeled as a resistor [see Figure 3(b)]

$$\frac{1}{R_{\rm eq}^{\rm hi}} = (Y_0^{(1)} + Y_0^{(2)}) \sum_{|n|>N_{\rm lo}}^{\infty} |N(\omega_n)|^2 \qquad (26)$$

The minimum nth order associated with a mode participating in (26), $N_{\rm lo}$ would be calculated by just considering $|\beta_n| \gg k_{\rm t}$. Thus the summation in (26) can be calculated once and stored, since it will keep invariant for any incidence angle. The former discussion shows a conceptual change with respect to spatially-modulated gratings, where higher-order harmonics are normally evanescent and carry reactive power (capacitive and inductive for TM and TE modes, respectively) [37, 38, 43].

The situation is different when considering low-order harmonics, whose associated wave impedance/admittance is a function, among other parameters, of the incident angle θ. Thus, the *complex* low-order contribution of the equivalent admittance present in Figure 3(b) can be computed as

$$Y_{\rm eq}^{\rm lo} = \sum_{\substack{n=-N_{\rm lo} \\ n\neq 0}}^{n=N_{\rm lo}} |N(\omega_n)|^2 (Y_n^{(1)} + Y_n^{(2)})\,. \qquad (27)$$

At this point, it is important to remark that a n-*th* TE and TM low-order harmonic do now differ. Unlike higher-order harmonics, which behaves almost identically regardless of their TM or TE nature (see (25) for instance), admittances associated with lower-order harmonics are governed by the expressions in (10) and (11), which exhibit clear differences between them. The global lower-order admittance $Y_{\rm eq}^{\rm lo}$ in (27) varies according to the TE- or TM-incidence scenario, influencing both the reflection coefficient R and the amplitude associated with the lower-order harmonics in both semi-spaces $E_n^{(1/2)}$. Thus, the resulting electromagnetic response of the whole system therefore differs with a TE- or a TM-case in a general oblique-incidence scenario. However, the behavior of the time-varying system is indistinguishable under TE or TM excitation when the incidence is normal to the discontinuity plane ($\hat{\mathbf{z}}$-direction according to the frame of coordinates in Figure 1). TE incidence will just excite TE higher-order harmonics and TM incidence will only excite TM higher-order harmonics. This is typical in 1D problems when the transverse components of the incident wave coincide with $\hat{\mathbf{x}}$ and $\hat{\mathbf{y}}$.

D. Diffraction Angles

The reflection/transmission angle of each nth-order harmonic is described by

$$\theta_n^{(i)} = \arctan\left(\frac{k_t}{\sqrt{\varepsilon_r^{(i)}\mu_r^{(i)}[\frac{\omega_0+n\omega_s}{c}]^2 - k_t^2}}\right). \qquad (28)$$

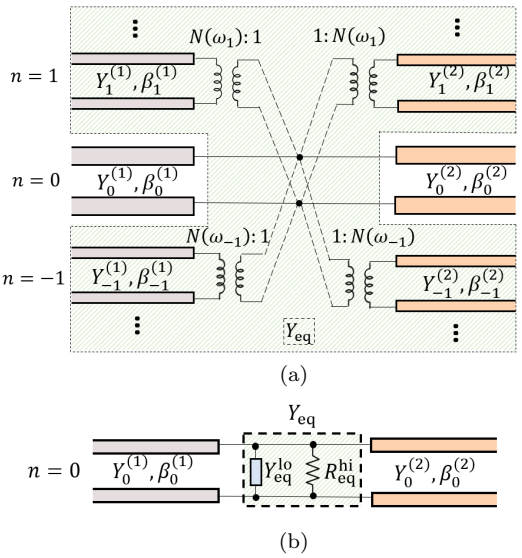

Figure 3. (a) Equivalent circuit that models the time-modulated metallic screen. It consists of a infinite parallel connection of transmission lines, each representing a different harmonic. (b) Compact equivalent circuit. The equivalent admittance $Y_{\rm eq}$, which contains all relevant information about the time-varying screen, can be subdivided into low-order (lo) and higher-order (hi) contributions.

Notice that the fundamental harmonic ($n = 0$) is not affected by the time modulation. This implies that the fundamental harmonic simply obeys conventional Snell's law of refraction,

$$\frac{\sin(\theta)}{\sin\left(\theta_0^{(i)}\right)} = \frac{\sqrt{\varepsilon_r^{(i)}\mu_r^{(i)}}}{\sqrt{\varepsilon_r^{(1)}\mu_r^{(1)}}}\,, \qquad (29)$$

thus propagates in the same direction of incidence when the considered input and output media are air ($\theta_0^{(i)} = \theta$).

It can be inferred from eq.(28) that, for the case of normal incidence $\theta_n^{(i)} = 0$, $\forall n$. Moreover, the diffraction angle is expected to change inside the dielectric media as $\beta_n^{(i)}$ does. By looking at the expression for $\theta_n^{(i)}$, it can be appreciated that the denser the medium under consideration is, the closer the diffracted angles are to the normal (when the input media is considered to be air). This would be similar to a conventional refraction between two media. This phenomenon is even more accentuated if the time-modulated screen commutes fast between its two states; namely, if ω_s is large, the diffraction angle for higher-order harmonics goes progressively to zero as $|n|$ increases.

The application of eq.(28) has important implications from an engineering perspective. Figure 4(a) illustrates a 4D representation of the (normalized) diffraction angle θ_n, assuming that the time-varying screen is surrounded by air. This angle is evaluated as a function of the incident angle θ, integer index n, and normalized modulation frequency ω_s/ω_0; namely, $\theta_n = \theta_n(\theta, n, \omega_s/\omega_0)$. Only

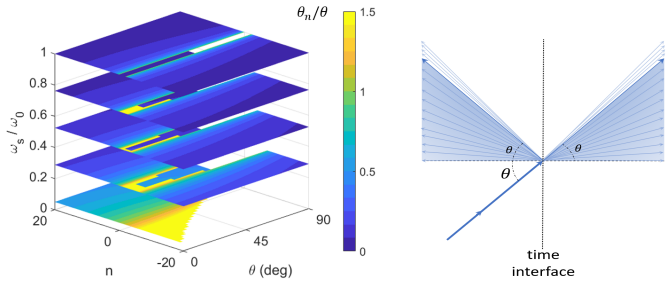

(a) (b)

Figure 4. (a) Normalized diffraction angle (θ_n/θ) as a function of the incident angle θ, harmonic index n, and normalized modulation frequency ω_s/ω_0. Only propagative angles are plotted. Evanescent regions are identified by blank spaces in the figure. (b) Sketch of the diffraction created by the time-modulated interface.

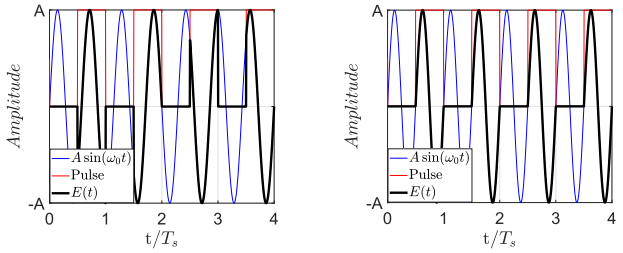

(a) (b)

Figure 5. Field profile $E(t)$ in cases where the time modulation ω_s is slower than the vibration of the incident wave ω_0. (a) $w_0/w_s = 1.75$ and (b) $w_0/w_s = 2$.

propagative difraction orders are considered in the figure, while evanescent orders are displayed as blank spaces. Note that in the vast majority of scenarios, the normalized diffraction angle is less than the unity, thus θ_n is generally less than θ. Only in cases where $\omega_s \ll \omega_0$, the diffraction angle θ_n is larger than the incident angle θ. Nonetheless, note that if $\omega_s \ll \omega_0$ in eq.(28), θ_n would be larger than θ but certainly close to it. On the other hand, the minimum angle at which propagative waves can diffract is $\theta_n = 0$. This is the case for higher-order harmonics ($|n \gg 1|$). Therefore, the range of diffraction angles is limited, in practice, to $\theta_n \approx [0, \theta]$. This situation is conceptually sketched in Figure 4(b) for an obliquely incident plane wave that impinges the time-varying interface.

E. Basis Function Choice

The choice of the basis function $E(t)$ is crucial to validate the above approach. At this point, it is important to remark that the time period related to appearance/disappearance of the electric wall T_s does not necessarily coincide with the period associated with $E(t)$. In order to make both periods to coincide, there must be a particular relationship between ω_s and ω_0. It can be demonstrated that this relationship must satisfy $\omega_0/\omega_\mathrm{s} = p$, with $p \in \mathbb{N}$. Figure 5 illustrates this statement in a visual way. Figure 5(a) represents $E(t)$ for $\omega_0/\omega_\mathrm{s} = 1.75$. We observe that $E(t)$ does not repeat within intervals separated by T_s, but by $4T_\mathrm{s}$. This situation is not given when $\omega_0/\omega_\mathrm{s} = 2$, where the periodicity is exactly T_s as shown in Figure 5(b). This last is the situation taken into account in this paper. It is worth remarking that the situation in Figure 5(a) could also be addressed by considering some additional aspects, but is out of the scope of this work.

The basis function will therefore be expressed as follows:

$$\mathbf{E}(t) = \hat{\mathbf{y}} \times \begin{cases} 0 & -T_\mathrm{s}/2 \leq t < 0 \\ A\sin(\omega_0 t) & 0 \leq t < T_\mathrm{s}/2 \end{cases} . \tag{30}$$

When the time-varying screen turns into a *metal* ($-T_\mathrm{s}/2 \leq t < 0$), the tangential electric field should vanish if a perfect electric conductor (PEC) is assumed. When the time-varying screen is in *air state* ($0 \leq t \leq T_s/2$), the tangential field has the shape of the incident time-harmonic excitation; namely, a sinusoidal wave. Furthermore, the continuity of the electric/magnetic displacement fields $\mathbf{D}$ and $\mathbf{B}$ is guaranteed at $t = 0\,\mathrm{s}$, what is strictly mandatory to satisfy the boundary conditions [9].

Computing the Fourier transform to the basis function, we reach the following expression for the transformers (19),

$$N(\omega_n) = -\frac{4\omega_0}{\omega_n^2 - \omega_0^2} \times \frac{\mathrm{e}^{-\mathrm{j}\omega_n T_\mathrm{s}/2}\left[\mathrm{j}\omega_n \sin(\omega_0 T_\mathrm{s}/2) + \omega_0 \cos(\omega_0 T_\mathrm{s}/2)\right] - \omega_0}{\mathrm{j}\omega_0 T_\mathrm{s} + \mathrm{e}^{-\mathrm{j}\omega_0 T_\mathrm{s}} - 1} . \tag{31}$$

The expressions for the transformers $N(w_n)$ will give the relative weight of the harmonics [eq. (18)]. Note that eq. (31) indicates that the transformers, and so the Floquet harmonics, have a decay $N(w_n) \sim 1/n$. This weight is one of the parameters that can be compared to those extracted by FDTD.

Under the above assumption ($\omega_0/\omega_\mathrm{s} = p$, with $p \in \mathbb{N}$), it can be appreciated that the reflection and transmission ($T = 1 + R$) coefficients do not depend on time. Both coefficients are the result of the average obtained over the period T_s [see eqs. (16)-(17)]. In general, this situation is expected to hold as long as the ratio ω_0/ω_s is a rational number. Nonetheless, it should be stated that rational ratios ω_0/ω_s would contain M cycles to form a macroperiod $T = MT_\mathrm{s}$, unlike purely integer ratios ω_0/ω_s whose periodic response is self-contained in a single period T_s.

Up to this point, we have only considered scenarios where the time modulation is either slower or identical

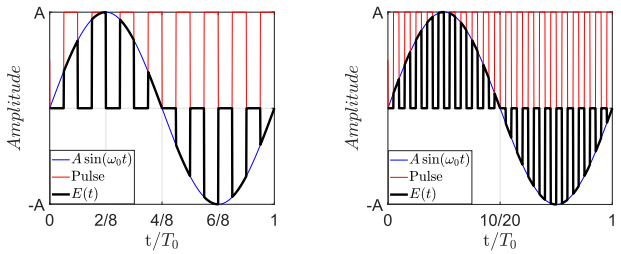

Figure 6. Field profile $E(t)$ in cases where the time modulation ω_s is faster than the vibration of the incident wave ω_0. (a) $w_0/w_s = 0.125$ and (b) $w_0/w_s = 0.05$.

to the vibration of the incident wave ($\omega_s \leq \omega_0$). Now, Figure 6 presents some cases where the time modulation is faster than the vibration of the incident wave; namely, $\omega_s > \omega_0$. This scenario is a bit different from previous ones. It can be demonstrated that the time needed to achieve a complete period is now T_0 instead of T_s, as visualized in Figures 6(a) and 6(b). This is due to the fact that the period of the incident wave (T_0) is larger than the period of the modulation (T_s) in cases where $\omega_s > \omega_0$. Therefore, a sampling-like phenomena arises for the basis function $E(t)$ (black curve), caused by the rapid variation of the screen.

F. Dielectric and Magnetic Losses

Losses in dielectrics can be accounted in a straightforward manner. Simply replace the real-valued dielectric constant $\varepsilon_r^{(i)}$ by the complex term [53]

$$\varepsilon_r^{(i)} \rightarrow \varepsilon_r^{(i)}(1 - \mathrm{j}\tan\delta^{(\mathrm{i})}) \tag{32}$$

where $\tan\delta^{(\mathrm{i})}$ is the loss tangent term. A similar rationale can be applied for magnetic losses, where the relative permeability would also be defined by a complex-valued expression. Dielectric and magnetic losses can be incorporated in both models.

III. RESULTS, VALIDATION & APPLICATIONS

In order to validate the former approach, some results are presented here. We initially consider the scenario depicted in Figure 1: a time-modulated metallic screen that periodically vanishes (PEC: $-T_s/2 \leq t \leq 0$; air: $0 \leq t \leq T_s/2$). Initially, both input and output media are considered to be air ($\varepsilon_r^{(1)} = \mu_r^{(1)} = \varepsilon_r^{(2)} = \mu_r^{(2)} = 1$). Nonetheless, we should remark that the former approach can be further extended to more complex scenarios involving dielectrics and modulations in both space and time.

Figure 7 illustrates the normalized Floquet coefficients $|E_n|$ extracted with the present approach and a self-implemented FDTD formulation (see Appendix B for specific details related to the FDTD) for the case of a time-modulated screen with different modulation angular frequencies ω_s. Normal TE incidence is assumed. As an indication, the selected basis function $E(t)$ is also included as an inset in Figures 7(a)-(c). An excellent agreement is observed between the results extracted from the Floquet-Bloch approach and the FDTD.

Some conclusions can be extracted by looking at Figure 7. When the time modulation ω_s is slow compared to the frequency of the incident wave ($\omega_\mathrm{s} \ll \omega_0$), the modal separation between the two harmonics that carry the main power contribution is large. This can be appreciated in Figure 7(a). Conversely, when the time modulation is of the order of the frequency of the incident wave ($\omega_\mathrm{s} \sim \omega_0$), then the modal separation between two main harmonics that carry the main power contribution narrows. This is observed in Figures 7(b)-(c). Additionally, it is of interest to note that, in the case $\omega_\mathrm{s} = \omega_0$, the harmonic with the highest power contribution is is $n = -1$ [see Figure 7(c)]. This means that great amount of power could be transferred from the incident wave to (-1)-th harmonic, fact that is of potential interest to be exploited in engineering for beamforming purposes and the creation of analog mixers [35]. Furthermore, the symmetry of the considered tangential field $E(t)$ causes that higher-order even harmonics are null, fact that is corroborated by the FDTD simulation. It is expected that higher-order even harmonics are no longer null if the time that the screen is in the air state and in the metal state is not the same; that is, if the change occurs at an instant different from $T_\mathrm{s}/2$. Finally, Figure 7(d) illustrates the amplitude of Floquet harmonics when $\omega_\mathrm{s} = 4\omega_0$. Cases where the time modulation is notably faster than the vibration of the incident wave ($\omega_\mathrm{s} \gg \omega_0$) provoke that most of the diffracted power transfer to the fundamental ($n = 0$) and $n = -2$ harmonics. According to eq.(28), both harmonics have diffraction angles in the same direction of incidence $\theta_0 = \theta_{-2} = \theta$. Moreover, when the screen commutes fast, it is expected that a significant amount of power is transferred to angles close to the normal. This that will be verified in further FDTD simulations.

Figure 8 illustrates a FDTD simulation showing the electric field distribution when different time modulations ω_s are considered. In this case, oblique TE incidence ($\theta = 30^\mathrm{o}$) is assumed. For a better visualization of the diffraction phenomena, only transmitted waves are plotted in this case. Black arrows indicate the theoretical propagation direction of the Floquet harmonics that carry most of the diffracted power. By looking at Figure 8(a), it can observed that, in those cases where ω_s is much less compared to the frequency of the incident wave ($\omega_\mathrm{s} \ll \omega_0$), higher-order harmonics diffract with angles very close to that of the fundamental harmonic $n = 0$. As a consequence, they appear to overlap. This is in agreement with the theoretical expression for the angles of the transmitted waves (28). In this scenario, the system acts

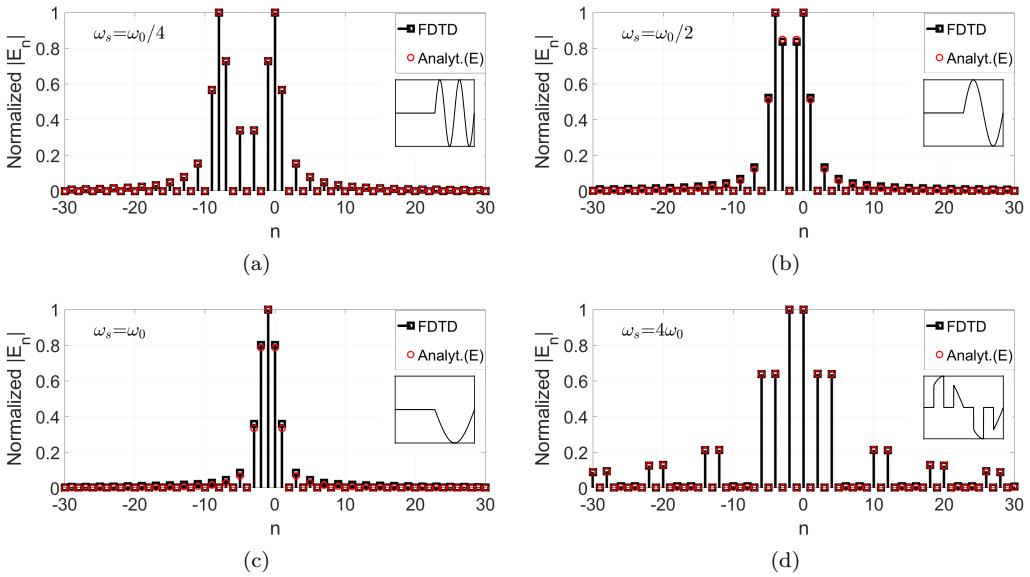

Figure 7. Normalized Floquet coefficients $|E_n|$ when a TE-polarized plane wave impinges the time-modulated interface. Normal incidence is assumed. (a) $\omega_s = \omega_0/4$, (b) $\omega_s = \omega_0/2$, (c) $\omega_s = \omega_0$, (d) $\omega_s = 4\omega_0$. Analytical results are compared to the FDTD method.

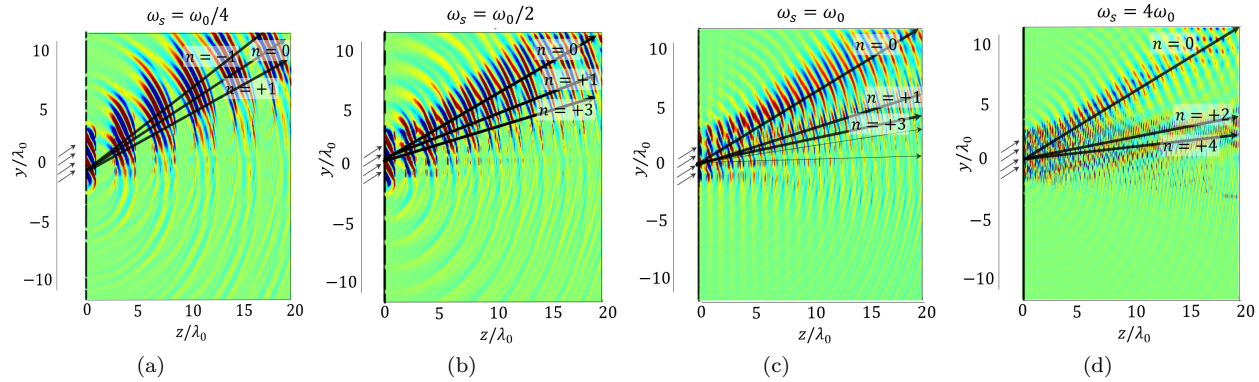

Figure 8. FDTD simulation (electric field) showing transmission through a time-modulated metallic screen when a TE-polarized oblique wave ($\theta = 30^o$) impinges the structure. (a) $\omega_s = \omega_0/4$, (b) $\omega_s = \omega_0/2$, (c) $\omega_s = \omega_0$, (d) $\omega_s = 4\omega_0$.

as a pulsed source of angular frequency ω_s.

Cases where $\omega_s \ll \omega_0$ are not desirable in order to control the steering angle. However, the situation is different when $\omega_s \sim \omega_0$. The fact that the modulation frequency is comparable to the frequency of the incident wave causes that the angle of reflection/transmission of higher-order modes broadens. This is illustrated in Figures 8(b)-(c). Concretely, let us focus on Figure 8(c), where the time modulation is identical to the frequency of the incident wave. The angle of the transmitted higher-order waves θ_n can be calculated analytically according to eq.(28). The resulting theoretical values are $\theta_0 = 30^o$, $\theta_1 = 14.48^o$, $\theta_2 = 9.59^o$, and $\theta_3 = 7.18^o$. These values are in agreement with the FDTD simulation: $\theta_0^{\text{FDTD}} = \arctan(11.5/20) = 29.89^o, \theta_1^{\text{FDTD}} = \arctan(5.1/20) = 14.31^o, \theta_2^{\text{FDTD}} = \arctan(3.4/20) = 9.65^o, \theta_3^{\text{FDTD}} = \arctan(2.6/20) = 7.41^o$.

As discussed previously, cases $\omega_s \gg \omega_0$ are expected to locate most of the diffracted energy in the direction of incidence ($\theta = 30^o$) or relatively close to it. This can be appreciated in the FDTD simulation shown in Figure 8(d). This can be understood by looking at the sampling that the time-varying screen causes to the incident wave [see Figures 6(a) and 6(b)]. As the sampling is finer (ω_s increases), the original incident wave is reproduced in a better way. Therefore, the basis function (field profile) $E(t)$ turns progressively into a discrete version of $\sin(\omega_0 t)$, sampled at integer multiples of T_s. Thus the most of power is carried by the harmonics $n = 0$ and $n = -2$, which are electromagnetically identical ($|k_0| = |k_{-2}|$). The rest of diffraction orders transmits and reflects at angles close to the normal and with lower (generally much lower) amplitudes. Comparison between analytical and FDTD diffracted angles in Figure 8(d)

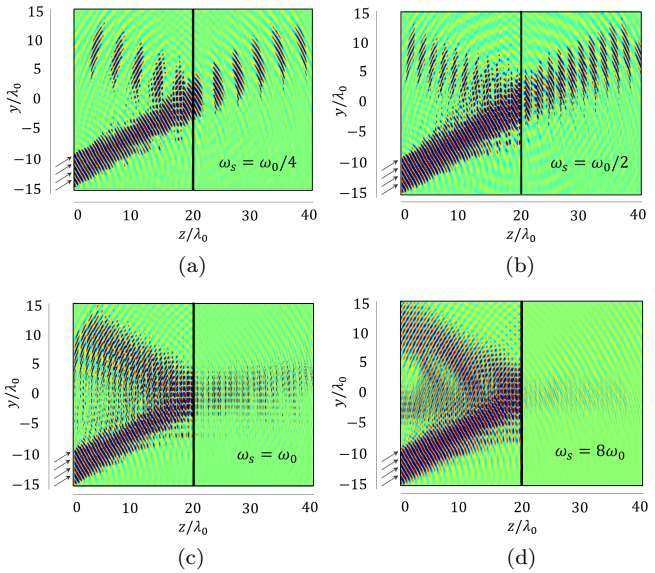

Figure 9. FDTD simulation (electric field) showing reflection and transmission through a time-modulated metallic screen when a TE-polarized oblique wave ($\theta = 30^{\rm o}$) impinges the structure. Cases: (a) $\omega_s = \omega_0/4$, (b) $\omega_s = \omega_0$, (c) $\omega_s = \omega_0$, (d) $\omega_s = 8\omega_0$.

show a good agreement. Analytical values are $\theta_0 = 30^{\rm o}$, $\theta_2 = 9.59^{\rm o}$ and $\theta_4 = 5.74^{\rm o}$, while values obtain by FDTD are $\theta_0^{\rm FDTD} = \arctan(11.3/20) = 29.46^{\rm o}, \theta_2^{\rm FDTD} = \arctan(3.5/20) = 9.93^{\rm o}, \theta_4^{\rm FDTD} = \arctan(2/20) = 5.71^{\rm o}$. In addition, little transmission observed at angles below $0^{\rm o}$ is due to numerical noise and should not be confused with waves actually propagating.

Now, Figure 9 presents a more general FDTD scenario involving reflected and transmitted waves. In this case, the time-varying screen is located at position $z = 20\lambda_0$ and the incident angle is $\theta = 30^{\rm o}$. Following the previous discussion, slow time modulations ($\omega_{\rm s} \ll \omega_0$) provoke that the time-varying screen acts as a pulsed source, both in reflection and transmission, with practically null diffraction. This is sketched in Figures 9(a) and 9(b). Naturally, the separation between consecutive wavefronts is related to the ratio $\omega_0/\omega_{\rm s}$. Modulations of the kind $\omega_{\rm s} \sim \omega_0$ [see Figure 9(c)] show the richest pattern in terms of diffraction, while fast time modulations ($\omega_{\rm s} \gg \omega_0$) mainly diffract waves in the specular-reflection and direct-transmission angles as well as in regions near the normal [see Figure 9(d)]. Apparently, it is seen in Figures 9(a)-(d) that the amplitude of the reflected waves increases (transmission decreases) as $\omega_0/\omega_{\rm s}$ is smaller.

A. Dielectric Media

Figure 10 illustrates a FDTD simulation showing the electric field distribution for a structure formed by a time-varying screen backed by a semi-infinite medium of relative permittivity $\varepsilon_r^{(2)}$. Input medium is considered to

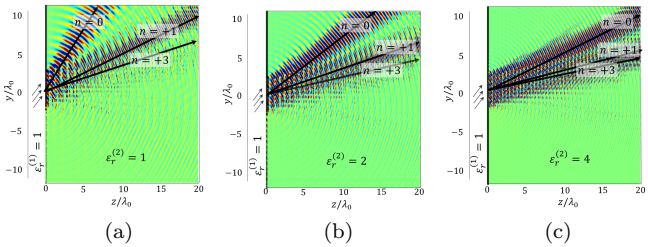

Figure 10. FDTD simulation (electric field) showing transmission through a time-modulated metallic screen loaded with a semi-infinite dielectric ε_r when a TE-polarized oblique wave ($\theta = 60^{\rm o}$) impinges the structure. Cases: (a) $\varepsilon_r^{(2)} = 1$, (b) $\varepsilon_r^{(2)} = 2$, (c) $\varepsilon_r^{(2)} = 4$. Parameters: $\omega_{\rm s} = \omega_0$.

TABLE I. Diffraction angle θ_n (deg) for the nth-harmonic in a structure formed by a time-varying screen backed by a semi-infinite medium of relative permittivity $\varepsilon_r^{(2)}$. Parameters: $\omega_{\rm s} = \omega_0$, $\varepsilon_r^{(1)} = \mu_r^{(1)} = \mu_r^{(2)} = 1$, $\theta = 60^{\rm o}$.

Diffraction Angle (deg)	θ_0	θ_1	θ_2	θ_3
Theory $\left(\varepsilon_r^{(2)} = 1\right)$	60	25.66	16.78	12.50
FDTD $\left(\varepsilon_r^{(2)} = 1\right)$	59.40	25.87	16.69	-
Theory $\left(\varepsilon_r^{(2)} = 2\right)$	37.76	17.83	11.78	8.81
FDTD $\left(\varepsilon_r^{(2)} = 2\right)$	37.48	18.00	11.31	-
Theory $\left(\varepsilon_r^{(2)} = 4\right)$	25.66	12.50	8.30	6.21
FDTD $\left(\varepsilon_r^{(2)} = 4\right)$	26.10	12.68	8.53	-

be air and $\omega_s = \omega_0$ to enhance the spacing between angles of different diffraction orders. Then, the angle of transmission of the n-th diffracted wave, θ_n, is calculated analytically according to eq. (28) and compared to numerical FDTD simulations in Table I. Results show a good agreement between theory and numerical computations. As already predicted in Sec. II.D, large values of $\varepsilon_r^{(2)}$ provoke that the diffracted waves approach to the normal ($\theta = 0$). If the output medium is dense, higher-order harmonics concentrate on a small angular region close to the normal, which makes them very difficult to visualize in a field chart. As a consequence, diffraction orders $n \geq 3$ are not compared to the FDTD in Table I.

B. Applications

At the light of the present results, the applications of the proposed time-periodic metallic screen are directly linked to its diffractive and pulsed-source behavior. In general, diffraction gratings (space-only, time-only or spacetime-modulated) are commonly used as filters, monochromators, spectrometers, lasers, wavelength division multiplexing devices, holographers, polarizers, beamformers, direction-of-arrival (DoA) estimators, and in many other microwave, photonic and optical applica-

tions. Naturally, gratings can be of reflective or transmissive types, depending on the intended operation. The main advantages of time gratings compared to traditional space gratings are related to the inherent capabilities of time-periodic structures to mix frequencies. This is an inherent property related to the time periodicity, $\omega_n = \omega_0 + n\omega_s$. This fact is a valuable asset that can be exploited in engineering for the design of analog FSS-based mixers.

Furthermore, combining time and space periodicities could directly lead to nonreciprocal responses for the considered devices. The search of nonreciprocity has become a hot topic in electromagnetism in the last years, especially if it is achieved by avoiding bulky magnets or, in general, magnetic materials. Next-generation networks based on beamforming can take advantage of the nonreciprocal response of spacetime-modulated metamaterials. In fact, the present time-varying screen can efficiently act as a beamformer by simply adjusting the frequency modulation ω_s.

On the other hand, pulsed sources are demanded in many fields of physics, engineering and medicine. For instance, pulsed electromagnetic field therapy (PEMF) uses electromagnetic fields to heal non-union fractures and other injuries [54]. Spectrometry and spectroscopy are traditional applications of pulsed waves [55]. More exotic applications of pulsed sources can be found in agriculture, where pulsed electromagnetic fields stimulate biological effects of chemically active species in the plasma [56]. Actually, time-modulated metamaterials are currently being investigated as a feasible and alternative source of pulsed waves [57]. In fact, the proposed time-varying metamaterial can act as a pulsed source if the modulation frequency is small compared to the vibration of the incident wave ($\omega_s \ll \omega_0$). The waveform of the generated pulses will coincide with the waveform of the incident wave. In this case, the incident wave is a plane wave of sinusoidal nature, so the pulses are of sinusoidal nature too.

In addition, the proposed structure can act as an analog sampler when the modulation frequency is much greater than the vibration of the incident wave ($\omega_s \gg \omega_0$). This phenomenon can be visualized in Figure 6. The modulation frequency ω_s of the time-periodic screen would control the sampling rate.

IV. CONCLUSION

Previous state-of-art works have mainly focused on the study of dielectric-based metamaterials with spatiotemporal variations. In this work, we have presented an analytical framework that serves as a basis for the study of time-modulated metal-based metamaterials. The time periodicity of the problem allows us to expand the electromagnetic fields in terms of a Floquet-Bloch series. By imposing the continuity of the electric field and the instantaneous Poynting vector across the time interface, the Floquet coefficients, dispersion curves, diffraction angles as well as the reflection/transmission coefficients are derived. The present approach comes with an associated equivalent circuit, formed by two input and output transmission lines and an equivalent admittance that models the time-varying screen. This equivalent admittance groups an infinitely set of parallel transformers and transmission lines (one per each harmonic). By checking the dispersion curves of the system, we have seen the linearity (non-dispersion) of the modes and the absence of stopbands. In addition, we have shown that higher-order harmonics are propagative, which is a notable difference compared to spatially-modulated diffraction gratings where higher-order modes are typically evanescent and carry reactive power. Some analytical and numerical (self-implemented FDTD) results are provided in order to validate the approach. Results show that time-modulated metallic screens can act either as pulsed sources (when $\omega_s \ll \omega_0$) or as beamformers (when $\omega_s \sim \omega_0$) to redirect power. Moreover, cases where the time modulation is notably faster compared to the frequency of the incident wave ($\omega_s \gg \omega_0$) provoke that most of the diffracted power redirect to the fundamental harmonic and to angles close to the normal. These are interesting features that can be considered for the manipulation and reconfiguration of electromagnetic waves in future wireless communications systems.

ACKNOWLEDGMENTS

This work was supported in part by the Spanish Government under Project PID2020-112545RB-C54 and Project RTI2018-102002-A-I00, in part by "Junta de Andalucía" under Project B-TIC-402-UGR18, Project A-TIC-608-UGR20, Project PYC20-RE-012-UGR and Project P18.RT.4830, and and in part by a Leonardo Grant of the BBVA foundation. The authors acknowledge the support of the BBVA foundation for the funds associated to a project belonging to the program Leonardo Grants 2021 for researchers and cultural creators from the BBVA foundation.

Appendix A: Higher-order Propagative Waves

The propagation constant in medium (i) reads

$$\beta_n^{(i)} = \sqrt{\varepsilon_r^{(i)}\mu_r^{(i)}}\sqrt{\left[k_0 + n\frac{\omega_s}{c}\right]^2 - \left[k_0\sin(\theta)\right]^2} \quad \text{(A1)}$$

In the case of dealing with higher-order waves ($|n| \gg 1$), $[k_0 + n\omega_s/c]^2 \gg [k_0\sin(\theta)]^2$ and $|n\omega_s/c| \gg k_0$. As a consequence, (A1) can be simplified to

$$\beta_n^{(i)} \approx \frac{\sqrt{\varepsilon_r^{(i)}\mu_r^{(i)}}}{c}\, n\omega_s, \quad |n| \gg 1\ . \quad \text{(A2)}$$

By inserting eq. (A2) into eqs. (10), (11) and noticing that $|n\omega_s| \gg \omega_0$ when $|n| \gg 1$, we would reach the expression for the wave admittances of higher-order waves:

$$Y_n^{(i),\mathrm{TM}} = Y_n^{(i),\mathrm{TE}} \approx \sqrt{\frac{\varepsilon_r^{(i)}\varepsilon_0}{\mu_r^{(i)}\mu_0}} = Y_0^{(i)}, \quad |n| \gg 1\ . \quad \text{(A3)}$$

As it can be appreciated, TM and TE admittances are identical, real-valued (in lossless media) and independent from n in the case of considering higher-order waves.

Appendix B: FDTD Simulations

Numerical simulations are performed with a self-implemented finite-difference time-domain (FDTD) method programmed in Matlab. Our FDTD approach is directly derived from Maxwell's equations by assuming media free of charges, and then particularized to 2-D cases where the incident plane wave is TE polarized (E_x, H_y, H_z). We have worked with a staggered FDTD scheme; namely, $\mathbf{H}^{(\Delta t\cdot n)}$ and $\mathbf{E}^{(\Delta t\cdot n/2)}$, where $\Delta t = C\Delta y/c$ is the time step, n is an integer and C is a dimensionless parameter associated to the CFL stability condition. To suppress numerical reflections, second-order Engquist-Majda absorbing boundary conditions have been employed. For the simulations, we have considered a uniform square grid with spatial resolution $\Delta_y = \Delta_z = \lambda_0/35$, and $C = 0.4$ (for stability: $C < 1/\sqrt{2}$ if $\Delta_y = \Delta_z$). Furthermore, our FDTD approach can include both static [$\varepsilon \equiv$ ctt] and time-modulated dielectrics [$\varepsilon = \varepsilon(t)$]. However, the time-varying metallic screen, located at $z = z_{\mathrm{pos}}$, is directly modelled in our case as a time-dependent boundary condition for the electric field [$E_x(y, z_{\mathrm{pos}}, t) = 0$, for $-T_{\mathrm{s}}/2 \leq t < 0$, $\forall y$]. Additionally, Floquet coefficients can be extracted from the FDTD as a part of a post-processing step. To do so, the tangential electric field $E(t)$, evaluated along the time period at the screen's interface z_{pos}, should be stored and numerically integrated [see eq. (17)].

[1] T. Tamir, H. C. Wang and A. A. Oliner, Wave propagation in sinusoidally stratified dielectric media, IEEE Trans. Microw. Theory Techn. **12**, 323-335 (1964).

[2] C. Elachi, "Electromagnetic wave propagation and source radiation in space-time periodic media," Ph. D Thesis, Caltech, 1971.

[3] S. Taravati, and G. V. Eleftheriades, Generlized space-time periodic diffraction gratings: theory and applications, Phys. Rev. Appl. **12**, 024026 (2019).

[4] A. M. Shaltout, A. Kildishev, and V. Shalaev, Time-varying metasurfaces and Lorentz on-reciprocity, Optics Express **5**, 246293 (2015).

[5] L. Zhang, Z. Q. Chen, S. Liu, Q. Zhang, J. Zhao, J. Y. Dai, G. D. Bai, X. Wan, Q. Cheng, G. Castaldi, V. Galdi, and T. J. Cui, Space-time coding digital metasurfaces, Nat. Comm. **9**, 4334 (2018).

[6] D. M. Solís, and N. Engheta, Functional analysis of the polarization response in linear-time varying media: a generalization of Kramer-Kronig relations, Phys. Rev. B **103**, 144303 (2018).

[7] V. Pacheco-Peña, and N. Engheta, Temporal equivalence of Brewster angles, Phys. Rev. B **104**, 214308 (2021).

[8] J. Pendry, P. Huidobro, M. Silveirinha, and E. Galiffi, Crossing the light line, Nanophotonics **11**, 161-167, (2022).

[9] C. Caloz and Z. Deck-Léger, Spacetime metamaterials—Part I: General concepts, IEEE Trans. Antennas Propag. **68** 1569-1582 (2020).

[10] C. Caloz and Z. Deck-Léger, Spacetime metamaterials—Part II: Theory and applications, IEEE Trans. Antennas Propag. **68**, 1583-1598, (2020).

[11] V. Tiukuvaara, T. J. Smy and S. Gupta, Floquet analysis of space-time modulated metasurfaces with Lorentz dispersion, IEEE Trans. Antennas Propag. **69**, 7667-7678 (2021).

[12] G. Ptitcyn, M. S. Mirmoosa, and S. A. Tretyakov, Time-modulated meta-atoms, Phys. Rev. Research **1**, 023014 (2019).

[13] S. Yin, E. Gaffili and A. Alu, Floquet metamaterials, eLight **1**, 1-13 (2022).

[14] R. Marqués, F. Martín and M. Sorolla, Metamaterials with negative parameters: theory, design and microwave applications, Jonh Wiley & Sons, 2008.

[15] B. A. Munk, Metamaterials: critique and alternatives, Jonh Wiley & Sons, 2009.

[16] A. Alex-Amor, A, Palomares-Caballero, C. Molero, 3-D metamaterials: Trends on applied designs, computational methods and fabrication techniques, Electronics **11**, 410 (2022).

[17] A. M. Shaltout, V. M. Shalaev, and M. L. Brongersma, Spaciotemporal light control with active metasurfaces, Science **364**, 648 (2019).

[18] Y. Hadad, D. L. Sounas and A. Alu, Space-time-gradient metasurfaces, Phys. Rev. B **92**, 100304, (2015).

[19] Y. Hadad, J. C. Solic, and A. Alu, Breaking temporal frequencies for emission and absorption, Proc. National Academy Science (PNAS) **113**, 3471-3475 (2016).

[20] D. L. Sounas, and A. Alu, Non-reciprocal photonics based on time modulation, Nature Photonics **11**, 774-783 (2017).

[21] S. Yin, and A. Alu, Efficient phase conjugation in space-time leaky waveguide, ACS Photonics **9**, 979-974 (2022).

[22] N. Chamanara, S. Taravati, Z.-L. Deck-Léger, and C. Caloz, Optical isolation based on space-time engineered asymmetric photonic band gaps, Phys. Rev. B **96**, 1554092017 (2017).

[23] M. M. Salary, S. Jafar-Zangani, and A. Mosallaei, Electrically tunable harmonics in time-modulated metasurfaces for wavefront engineering, New Journal of Physics **20**, 123023 (2018).

[24] Y. Shi, and S. Fang, Dynamic non-reciprocal metasurfaces with arbitrary phase reconfigurability based on photonics transitions in meta-atoms, App. Phys. Lett. **108**, 021110 (2016).

[25] X. Fang, M. Li, and J. Hang, Accurate direction-of-arrival estimation method based on space-time modulated metasurfaces, TechRxiv Preprint, https://doi.org/10.36227/techrxiv.17698181.v2 (2022).

[26] X. Wang, and C. Caloz, Spacetime-modulated metasurface for spacial multiplexing communications, 13*th* International congress on artificial materials for novel wave phenomena - metamaterials 2019, Rome, Italy, 465-467 (2019).

[27] N. Tiukuvaara, Y. Vahabzadeh and C. Caloz, Simultaneous control of the spacial and temporal spectra of light with space-time varying metasurfaces, IEEE Trans. Antennas Propag. **67**, 2430-2441 (2019).

[28] T. Itoh, Numerical techniques for microwave and millimeter-wave passive structures, John Wiley & Sons, 1989.

[29] J. R. Zurita-Sánchez, P. Halevi and J. C, Cervantes-González, Reflection and transmission of a wave incident on a slab with a time-periodic dielectric function $\epsilon(t)$, Phys. Rev. A **79**, 053821 (2021).

[30] A. Sotoodehfar, M. S. Mirmoosa and S. A. Tretyakov, Waves in Linear Time-Varying Dielectric Media, 2022 16th European Conference on Antennas and Propagation (EuCAP), Madrid, Spain, 1-5 (2022).

[31] Z. Wu, C. Scarborough and A. Grbic, Space-time modulated metasurfaces with spatial discretization: free-space N-path systems, Phys. Rev. Appl. **14**, 064060 (2020).

[32] S. F. Bass, A. M. Palmer, K. R. Schab, K. C. Kerby-Patel and J. E. Ruyle, Conversion matrix method of moments for time-varying electromagnetic analysis, IEEE Trans. Antennas Propag. **70**, 6763-6774 (2022).

[33] X. Wang, A. Díaz-Rubio, H. Li, S. A. Tretyakov, and A. Alu, Theory and design of multifunctional space-time metasurfaces, Phys. Rev. Appl. **13**, 044040 (2020).

[34] M. H. Mostafa, A. Díaz-Rubio, M. S. Mirmoosa, and S. A. Tretyakov, Coherently time-varying metasurfaces, Phys. Rev. Applied **17**, 064048 (2022).

[35] S. Taravati, and G. V. Eleftheriades, Microwave space-time-modulated metasurfaces, ACS Photonics **9**, 305-318 (2022).

[36] Y. Vahabzadeh, N. Chamanara and C. Caloz, Generalized sheet transition condition FDTD simulation of metasurface, IEEE Trans. Antennas Propag. **66**, 271-280 (2018).

[37] R. Rodriguez-Berral, C. Molero, F. Medina and F. Mesa, Analytical wideband model for strip/slit gratings loaded With dielectric slabs, IEEE Trans. Microw. Theory Tech. **60**, 3908-3918 (2012).

[38] R. Rodriguez-Berral, F. Medina, F. Mesa and M. Garcia-Vigueras, Quasi-analytical modeling of transmission/reflection in strip/slit gratings loaded With dielectric slabs, IEEE Trans. Microw. Theory Tech. **60**, 405-418 (2012).

[39] C. Molero, R. Rodríguez-Berral, F. Mesa, F. Medina, Wideband analytical equivalent circuit for coupled asymmetrical nonaligned slit arrays, Phys. Rev. E **95**, 023303 (2017).

[40] R. Dubrovka, J. Vazquez, C. Parini, and D. Moore, Equivalent circuit method for analysis and synthesis of frequency selective surfaces, IEE Proceedings - Microw., Antennas Propag. **153**, 213-220 (2006).

[41] R. Rodríguez-Berral, F. Mesa and F. Medina, Analytical multimodal network approach for 2-D arrays of planar patches/apertures embedded in a layered medium, IEEE Trans. Antennas Propag. **63**, 1969-1984 (2015).

[42] C. Molero, M. García-Vigueras, R. Rodríguez-Berral, F. Mesa and N. Llombart, Equivalent circuit approach for practical applications of meander-line gratings, IEEE Antennas Wireless Propag. Lett. **16**, 3088-3091 (2017).

[43] A. Alex-Amor, F. Mesa, Á. Palomares-Caballero, C. Molero and P. Padilla, Exploring the potential of the multi-modal equivalent circuit approach for stacks of 2-D aperture arrays, IEEE Trans. Antennas Propag. **69**, 6453-6467 (2021)

[44] W. Yu, L. Sisi, Y. Haiyan, L. Jie, Progress in the functional modification of graphene/graphene oxide: a review, RSC Adv. **10**, 15328-15345 (2020).

[45] X. Li, H. Zhu, Two-dimensional MoS2: Properties, preparation, and applications, Journal of Materiomics **1**, 33-44 (2015).

[46] A. Laturia, M.L. Van de Put, W.G. Vandenberghe, Dielectric properties of hexagonal boron nitride and transition metal dichalcogenides: from monolayer to bulk, npj 2D Mater Appl., **2**, 6 (2018).

[47] N. Salazar, C. Marquez, and F. Gamiz, Synthesis of graphene and other two-dimensional materials, *Nanophotonics, 2D Materials for Nanophotonics,* Elsevier, 1-79 (2021).

[48] N. Mishra, J. Boeckl, N. Motta, and F. Iacopi, Graphene growth on silicon carbide: A review, Phys. Status Solidi A **213**, 2277–2289 (2016)

[49] C. Molero et al., Metamaterial-based reconfigurable intelligent surface: 3D meta-Atoms controlled by graphene structures, IEEE Communications Magazine **59**, 42-48 (2021)

[50] M.J. Allen, V.C. Tung, R.B. Kaner, Honeycomb carbon: A review of graphene, Chemical Reviews **110**, 132-145 (2010).

[51] S.-E. Zhu, S. Yuan G. C. A. M. Janssen, Optical transmittance of multilayer graphene, Europhysics Letters **108**, 17007 (2014).

[52] Q. Hu et al., An intelligent programmable omni-metasurface, Laser Photon. Rev. **16**, 2100718 (2022).

[53] C. Molero, A. Alex-Amor, F. Mesa, Á. Palomares-Caballero and P. Padilla, Cross-polarization control in FSSs by means of an equivalent circuit approach, IEEE Access **9**, 99513-99525 (2021).

[54] M.S. Markov, Expanding use of pulsed electromagnetic field therapies, Electromagn. Biol. Med. **26**, 257-74 (2007).

[55] A. Dolla, Pulsed and continuous-wave magnetic resonance spectroscopy using a low-cost software-defined radio, AIP Advances **9**, 115110 (2019).

[56] K. Takaki, K. Takahashi, N. Hayashi, D. Wang, T. Ohshima, Pulsed power applications for agriculture and food processing, Rev. Mod. Plasma Phys. **5**, 12 (2021).

[57] C. Rizza, G. Castaldi, and V. Galdi, Short-pulsed metamaterials, Phys. Rev. Lett. **128**, 257402 (2022).

2.2.2 Time-Periodic Metallic Metamaterials defined by Floquet Circuits

This paper explores the performance of a previously developed time-varying metallic metasurface by including new temporal parameters. We extend the applicability of the 1D metamaterial presented in "Diffraction Phenomena in Time-Varying Metal-Based Metasurfaces" by introducing variables such as duty cycles and macroperiods. The duty cycle breaks the time symmetry of the temporal periods, altering the temporal profile of the fields, exciting new harmonics, and modifying the reflection/transmission coefficients.

On the other hand, the imposition of macroperiods allows for the simulation of the structure when the ratio between the modulation frequency and the operational frequency is a rational number. This results in the emergence of new temporal harmonics with different frequencies, thereby increasing the frequency conversion options. Additionally, these new variables enhance the beamforming capabilities of the discretized spectrum compared to the previous version. The obtained results for diffraction angles and transmission coefficients show excellent agreement with FDTD simulations.

THIS IS A POSTPRINT VERSION OF THE PAPER:

S. Moreno-Rodríguez, A. Alex-Amor, P. Padilla, J. F. Valenzuela-Valdés and C. Molero, "Time-Periodic Metallic Metamaterials defined by Floquet Circuits," *IEEE Access*, vol. 11, pp. 116 665–116 673, 2023.

- Journal Impact Factor (JIF) in JCR 2023: 3.4
- Category: COMPUTER SCIENCE, INFORMATION SYSTEMS. JIF Rank: 87/249 (Q2).
- Category: ENGINEERING, ELECTRICAL & ELECTRONIC. JIF Rank: 122/352 (Q2).
- Category: TELECOMMUNICATIONS. JIF Rank: 47/119 (Q2).

Disclaimer:
This work has been published on IEEE Access.
DOI: 10.1109/ACCESS.2023.3325909

IEEE Access
Multidisciplinary ⋮ Rapid Review ⋮ Open Access Journal

Received 19 September 2023, accepted 16 October 2023, date of publication 19 October 2023, date of current version 26 October 2023.

Digital Object Identifier 10.1109/ACCESS.2023.3325909

RESEARCH ARTICLE

Time-Periodic Metallic Metamaterials Defined by Floquet Circuits

SALVADOR MORENO-RODRÍGUEZ[1], ANTONIO ALEX-AMOR[2], PABLO PADILLA[1], JUAN F. VALENZUELA-VALDÉS[1], AND CARLOS MOLERO[1], (Member, IEEE)

[1]Department of Signal Theory, Telematics and Communications, Research Centre for Information and Communication Technologies (CITIC-UGR), University of Granada, 18071 Granada, Spain
[2]Department of Information Technology, Universidad CEU San Pablo, 28003 Madrid, Spain

Corresponding author: Salvador Moreno-Rodríguez (salvamr96@ugr.es)

This work has been supported by grant IJC2020-043599 /AEI/10.13039/501100011033 and by the European Union NextGenerationEU/PRTR. It has also been supported by grants TED2021-129938B-I00, PDC2022-133900-I00, PID2020-112545RB-C54 and TED2021-131699B-I00.

ABSTRACT In this paper, we study the scattering and diffraction phenomena in time-modulated metamaterials of metallic nature by means of Floquet equivalent circuits. Concretely, we focus on a time-periodic screen that alternates between ''metal'' and ''air'' states. We generalize our previous approaches by introducing the concepts of ''macroperiod'' and ''duty cycle'' to the time modulation. This allows to analyze time-periodic metallic metamaterials whose modulation ratios are, in general, rational numbers. Furthermore, with the introduction of the duty cycle, perfect temporal symmetry is broken within the time modulation as the time screen could remain a different amount of time in metal and air states. Previous statements lead to an enrichment of the diffraction phenomenon and to additional degrees of freedom that can be exploited in engineering to control the reflection and transmission of electromagnetic waves. Finally, we present some analytical results that are validated with a self-implemented finite-difference time-domain (FDTD) approach. Results show that the scattering level and diffraction modes can be controlled independently by means of the duty cycle and the modulation ratio, respectively, leading to an efficient design of time-based pulsed sources and beamformers.

INDEX TERMS Floquet circuit, FDTD, modulation ratio, macroperiod, duty cycle.

I. INTRODUCTION

The resolution of electromagnetic problems based on periodic structures has classically benefited from systematic simplifications thanks to the use of Floquet's theorem [1], [2]. That is, the reduction of the complexity of the whole structure to a waveguide problem [3]. Circuit models have proven to be very efficient tools to emulate waveguide environments [4], [5], [6]. Simple models avoid the *dynamic* behavior of the structure, combining transmission lines and quasi-static elements [7]. More sophisticated proposals include the contribution of higher-order modes/harmonics [8], [9], [10]. This implies the validity of the models for scenarios where higher-order harmonics have a leading role [11]. This scenario is, for instance, quite common in time-varying systems, or in a more general context, in spacetime structures [12].

Spacetime systems introduce time, generally in the form of a periodic modulation, adding non-linearities that are widely used in RF systems such as frequency dividers [13] and modulators [14]. Time implies an additional degree of freedom [15], [16], [17], [18], [19]. Though pioneering studies were theoretically reported in the middle of last century [20], [21], [22], they have regained interest in the recent years, especially when non-reciprocity [23], [24], [25] was sought as a substitute of magnetic materials for insulators [26]. Some other impressive properties have since then been reported, as temporal mechanisms for amplification [27], subharmonic mixing [28], giant bianosotropy [29], negative refraction [30], metamirrors [31] or an equivalent of the Brewster angle [32].

The associate editor coordinating the review of this manuscript and approving it for publication was Ladislau Matekovits.

Interesting applications, just to name a few, are proposed in the propagation domain focused on DOA estimation [33], imaging [34], digital processing [35].

Transmission-line and ABCD-parameter models have already been employed in electromagnetic systems with instantaneous temporal interfaces [36], [37]. Such are the cases reported in [38] and [39] and more recently in [40]. The equivalent circuit aids for a better understanding of the situations there described. However, in most cases, no periodic modulation exists and there is no excitation of higher-order harmonics. The work in [41] considers a system formed by a metallic screen suffering a periodic modulation. The system is fed by an external plane wave, exciting an infinite number of periodic Floquet harmonics. The paper reports the derivation of the circuit model but no many situations are evaluated. The present work is intended to exploit the model possibilities, increasing the number of modulation ratios, introducing the concepts of *macroperiod* and *duty cycle* to the time modulation, with the objective of enriching the diffraction phenomenon. Furthermore, it has been shown that breaking the temporal symmetry allows the suppression of non-desired harmonics [42]. The scattering parameters are quantitatively evaluated, constituting an additional contribution with respect previous works in the literature. It is worth remarking that, though the paper intention is to describe a temporal system from the theoretical point of view, the experimental time-varying scenario could be motivated by switching metasurfaces as those previously reported [43], [44], [45], [46], [47], [48], [49], [50]. Our particular case would demand a specific metasurface with periodic modulation alternating fully-transparent and fully-reflecting states.

The paper is organized as follows: Section II is left for the exposition of the time-varying scenario, explanation of the variables involved and their implications on diffraction phenomenon. Section III focuses on applying this method for reconfigurability of the propagation of electromagnetic waves. The conclusions of the work are found at the end of the paper.

II. THEORETICAL ANALYSIS

The structure under consideration is sketched in Fig. 1. A monochromatic plane wave of frequency ω_0 illuminates a time metamaterial that periodically alternates between ''air'' and ''metal'' (perfect electric conductor, PEC) states, as represented in Fig. 1(a). This can be realized by alternating two resonant states of the metamaterial, invoking fully transparency or fully reflectivity via tunable biased diodes, as can be read in [47]. Future alternatives coming from electronic materials such as graphene [51] or Vanadium oxide [52] could be promising for this purpose.

The time screen is considered to be infinitesimally thin along the propagation direction (z axis) and very large in x and y directions [see Fig. 1(b)]. Transverse magnetic, TM (E_x, E_z, H_y), or transverse electric, TE (E_y, H_x, H_z), polarizations for the oblique-incident waves are considered.

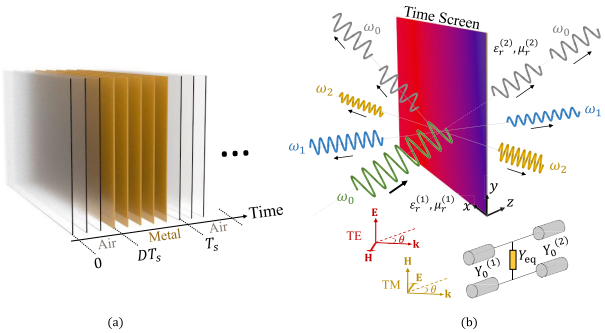

FIGURE 1. (a) Time evolution of the proposed configuration. The screen periodically alternates between "air" and "metal" states. (b) Illustration of the spacetime diffraction caused by the time-periodic screen and its equivalent circuit for both TE and TM incidence.

The time periodicity of the varying screen is $T_s = 2\pi/\omega_s$, from which the whole cycle repeats. In the more general scenario, the time screen could remain in air state (DT_s) for a different time than it remains in metal state ($[1 - D]T_s$). Here, $D \in [0, 1]$ is the *duty cycle* of the time modulation. Extreme cases $D = 0$ and $D = 1$ would imply that the time screen remains invariant in metal and air states the whole time, respectively. The fact of varying the duty cycle D and its implications were not discussed in our previous work [41], since a fixed value of $D = 0.5$ was implicitly assumed. As it will be detailed later, modifying the duty cycle enriches the diffraction phenomenon, since half-period temporal symmetry is broken and this leads to asymmetries in harmonic excitation. The *modulation ratio* $F = \omega_0/\omega_s = T_s/T_0$ constitutes a second factor to be discussed. The nature of the reflected and transmitted fields across the discontinuity directly depends on this parameter, and as it will be discussed below, it may govern the power transfer between different harmonics.

The time-periodic tangential fields are expanded in terms of Floquet-Bloch series:

$$E_t^{(1)}(x,z,t) = e^{-jk_t x}\left[e^{j\omega_0 t - j\beta_0^{(1)} z} + Re^{j\omega_0 t + j\beta_0^{(1)} z} + \sum_{\forall n\neq 0} E_n^{(1)} e^{j\omega_n t + j\beta_n^{(1)} z}\right] \quad (1)$$

$$H_t^{(1)}(x,z,t) = e^{-jk_t x}\left[Y_0^{(1)} e^{j\omega_0 t - j\beta_0^{(1)} z} - RY_0^{(1)} e^{j\omega_0 t + j\beta_0^{(1)} z} - \sum_{\forall n\neq 0} Y_n^{(1)} E_n^{(1)} e^{j\omega_n t + j\beta_n^{(1)} z}\right] \quad (2)$$

$$E_t^{(2)}(x,z,t) = e^{-jk_t x}\left[Te^{j\omega_0 t - j\beta_0^{(2)} z} + \sum_{\forall n\neq 0} E_n^{(2)} e^{j\omega_n t - j\beta_n^{(2)} z}\right] \quad (3)$$

$$H_t^{(2)}(x,z,t) = e^{-jk_t x}\left[TY_0^{(2)} e^{j\omega_0 t - j\beta_0^{(2)} z} + \sum_{\forall n\neq 0} Y_n^{(2)} E_n^{(2)} e^{j\omega_n t - j\beta_n^{(2)} z}\right] \quad (4)$$

where k_t is the transverse component of the wavevector, β_n ($n \in \mathbb{Z}$) is the nth-order longitudinal component of the wavevector associated with a nth-order harmonic, and $\omega_n = \omega_0 + n2\pi/T_m$ is the angular frequency associated to the n-th Floquet harmonic. For the sake of simplicity, the amplitude of the electric field associated with the incident wave is unity (harmonic of order $n = 0$) and its contribution is out from the summation in (1)-(4). The admittance values Y_n are expressed as

$$Y_n^{(i)} = \frac{\varepsilon_r^{(i)} \varepsilon_0 \, \omega_n}{\beta_n^{(i)}} \quad \text{TM admittances} \tag{5}$$

$$Y_n^{(i)} = \frac{\beta_n^{(i)}}{\mu_r^{(i)} \mu_0 \, \omega_n} \quad \text{TE admittances} \tag{6}$$

where the use of TE/TM admittances depends on the polarization of the incident wave, and $i = 1, 2$ accounts for the input and output media, respectively. It is worth remarking that the fields expanded in (1)-(4) are vectors. The vector notation have been removed for simplicity. For TM incidence the electric fields in (1) and (3) are directed along x whereas the magnetic fields in (2) and (4) points towards y. For TE incidence, the fields directions are exactly the opposite.

The higher-order Floquet coefficients $E_n^{(1/2)}$ and the reflection (R)/transmission (T) terms related to the fundamental harmonic are extracted by applying integral-equation methods on a field profile $\mathbf{E}(x, t)$ that models the dynamical behavior of the time-periodic metallic metamaterial. This methodology was previously employed in [53] and [54]. The propagation of the incident and reflected waves, and the transmitted one are represented by transmission lines with $Y_0^{(1)}$ and $Y_0^{(2)}$ characteristic admittances, respectively. In general, Floquet coefficients E_n are computed as

$$E_n^{(1)} = E_n^{(2)} = (1 + R)N(\omega_n). \tag{7}$$

The coupling between harmonics, described in terms of transformers with turn ratio $N(\omega_n)$ [see eq. (8)], demands a previous knowledge of the field profile at the discontinuity along a time period.

$$N(\omega_n) = \frac{\int_0^{T_m} E(x, t) e^{-j\omega_n t} dt}{\int_0^{T_m} E(x, t) e^{-j\omega_0 t} dt} \tag{8}$$

When the time interface is in air state, the metallic metamaterial "appears to vanish", so $\mathbf{E}(x, t)$ follows the sinusoidal shape of the incident plane wave. When the time interface is in metal state, the tangential field profile $\mathbf{E}(x, t)$ is assumed to be zero.

Moreover, R and T, can directly be estimated from the circuit model as

$$R = \frac{Y_0^{(1)} - Y_0^{(2)} - Y_{eq}}{Y_0^{(1)} + Y_0^{(2)} + Y_{eq}}, \tag{9}$$

$$T = 1 + R. \tag{10}$$

where the equivalent admittance Y_{eq} accounts for the effect of the *time discontinuity*, including the effect of all the higher-order harmonics E_n.

The equivalent admittance that models the time-periodic screen is computed as

$$Y_{eq} = \sum_{\forall n \neq 0} |N(\omega_n)|^2 (Y_n^{(1)} + Y_n^{(2)}) \tag{11}$$

Close inspection of (11) reveals that Y_{eq} is actually formed by parallel-connected transmission lines loaded with complex transformers, one for each Floquet harmonic. This allows us to expand the simplified equivalent circuit illustrated in Fig. 1(b) into the more complex, but also more physically insightful, version shown in [41]. In that sense, the admittance of the present temporal problem shares some similarities with the admittance extracted in purely spatial structures [6]. However, as discussed in our previous work [41], there also exist major differences between them. The most significant one is the fact that higher-order harmonics are propagative (of resistive nature) in the time-periodic problem while these are evanescent (of capacitive/inductive nature) in the purely spatial counterparts. Higher-order harmonics in mixed space-time scenarios are expected to contribute with both resistive and capacitive/inductive terms to the equivalent circuit.

A. MACROPERIODS

Our previous work is focused on integer time-modulation ratios F, assuming $\omega_s \leq \omega_0$ in most cases. This is a very restricted situation. The extension from integer to rational (not irrational) modulation ratios is here taken into account, modifying the way to get $\mathbf{E}(x, t)$. Now, $\mathbf{E}(x, t)$ is influenced by D and F, leading to the definition of the term *macroperiod*. A macroperiod T_m is defined as the minimum time periodicity where both the incident-wave vibration (ω_0) and the screen variation (ω_s) complete a full cycle simultaneously. Mathematically, every *rational* modulation ratio F can be approximated by a fraction of two integers, F_N and F_D, according to $F = F_N/F_D$. Since F was previously defined as $F = T_s/T_0$, the temporal macroperiod T_m must follow the condition

$$T_m = F_N T_0 = F_D T_s. \tag{12}$$

Thus, a macroperiod is completed after F_N and F_D cycles for the incident wave (T_0) and the time modulation (T_s), respectively. Please note that an *irrational* modulation ratio F cannot be described in terms of a fraction of two integers, leading to an infinite set of decimals. As a consequence, the macroperiod of an irrational modulation ratio would be infinite and the formulation proposed here would not be applicable since time periodicity is lost. Thus, the field profile is therefore defined along a macroperiod, ensuring a stationary situation. It can be mathematically described as

$$\mathbf{E}(x, t) = A(x) \sin(\omega_0 t) P(t) \hat{\mathbf{y}}, \quad t \in [0, T_m], \tag{13}$$

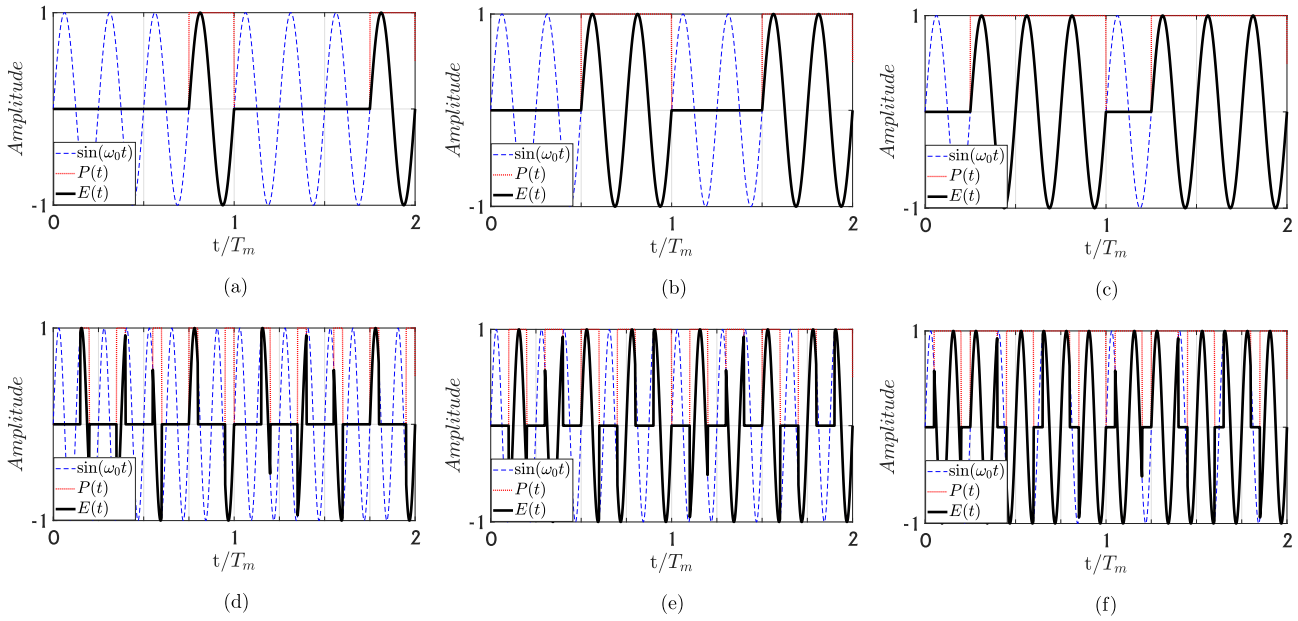

FIGURE 2. Two macroperiods of $E(t)$ when: (a) $F = 4$, $D = 0.25$, (b) $F = 4$, $D = 0.5$, (c) $F = 4$, $D = 0.75$, (d) $F = 1.6$, $D = 0.25$, (e) $F = 1.6$, $D = 0.5$, (f) $F = 1.6$, $D = 0.75$. A monochromatic incident wave of $\omega_0 = 2\pi \cdot 30$ GHz is assumed.

where $P(t)$ is a pulse train of period T_s, unit amplitude and duty cycle D, and $A(x)$ a function including the spatial dependence.

It is worth remarking that the pulse train invokes *instantaneous* switching between air/metal. Of course this is ideal. In practice this switching is not instantaneous, there exist a small (or not so small) transient time between both states. Experimental prototypes to come must neglect transient effects as much as possible. Possible solutions are based on metasurfaces with pin-diodes incorporated in the cells [55]. In addition, the frequency associated with the time-varying screen ω_s may sometimes be much slower than ω_0 (orders of few MHz Vs GHz), thus transient times, of the order of few *ns* can directly be neglected. Such is the case reported, for instance, in [35] and [43].

For the sake of simplicity, the incident wave considered in the following results has $\omega_0 = 2 \cdot \pi \cdot 30$ GHz, corresponding to a wavelenght of 10 mm. The same conclusions can be extracted at any other frequency as long as F and D remain identical. Figs. 2(a)-(c) depict the evolution of $E(t) = |\mathbf{E}(0, t)|$, when the modulation ratio is fixed to $F = 4$ ($F = F_N/F_D = 4/1$), for duty cycles $D = 0.25, 0.5, 0.75$, respectively. Notice that, given the homogeneity of the discontinuity along x, identical conclusions would be inferred when the field is evaluated at $x \neq 0$, $E(t) = E(x \neq 0, t)$. Thus $x = 0$ have been chosen for the sake of simplicity. In addition, all the field profiles $E(t)$ represented in Figs. 2 have been normalized to unity. In these cases, the value of the *macroperiod* T_m coincides with T_s (or $4T_0$). A second case regarding F as a rational number is exhibited in Figs. 2(d)-(f), where it can be appreciated how the shape of $E(t)$ becomes more complex. Now $F = 1.6 = 8/5$, increasing the macroperiod up to $T_m = 5T_s$ or, analogously, $T_m = 8T_0$. In all these figures $E(t)$ is drawn in a time interval defined by two consecutive macroperiods, in order to appreciate the existing periodicity. As will be explained below, the variation of D has direct implications on the amplitude provided by each Floquet harmonic.

B. DUTY CYCLES

A correct definition of $E(t)$ is crucial to guarantee accurate predictions by the circuit model. A first test of the validity of the circuit approach is shown in Fig. 3. It illustrates the normalized spectral response of the transmitted field in the cases reported in Fig. 2, with an inset showing the field profile $E(t)$. A TM-polarized plane wave impinging normally has been assumed for the computation. As expected, the spectrum is split in discrete harmonics, whose amplitudes vary for each case. Together with the results provided by the equivalent circuit, numerical results extracted by self-implemented finite-different time-domain (FDTD) are included. FDTD methods [56], [57] have proven to be interesting numerical alternatives to validate analytical results due to the absence of specific commercial electromagnetic solvers oriented to deal with spacetime metamaterials. It is also worthy to emphasise that due to assumption of normal incidence, all the harmonics are propagative (there is no harmonics with evanescent nature) and moreover, they leave the air-metal interface at the incidence direction ($\theta_n = 0^o$). This result comes from Eq. [28] in [41]

$$\theta_n^{(i)} = \arctan\left(\frac{k_t}{\sqrt{\varepsilon_r^{(i)}\mu_r^{(i)}\left[\frac{\omega_0 + 2\pi n/T_m}{c}\right]^2 - k_t^2}}\right) \tag{14}$$

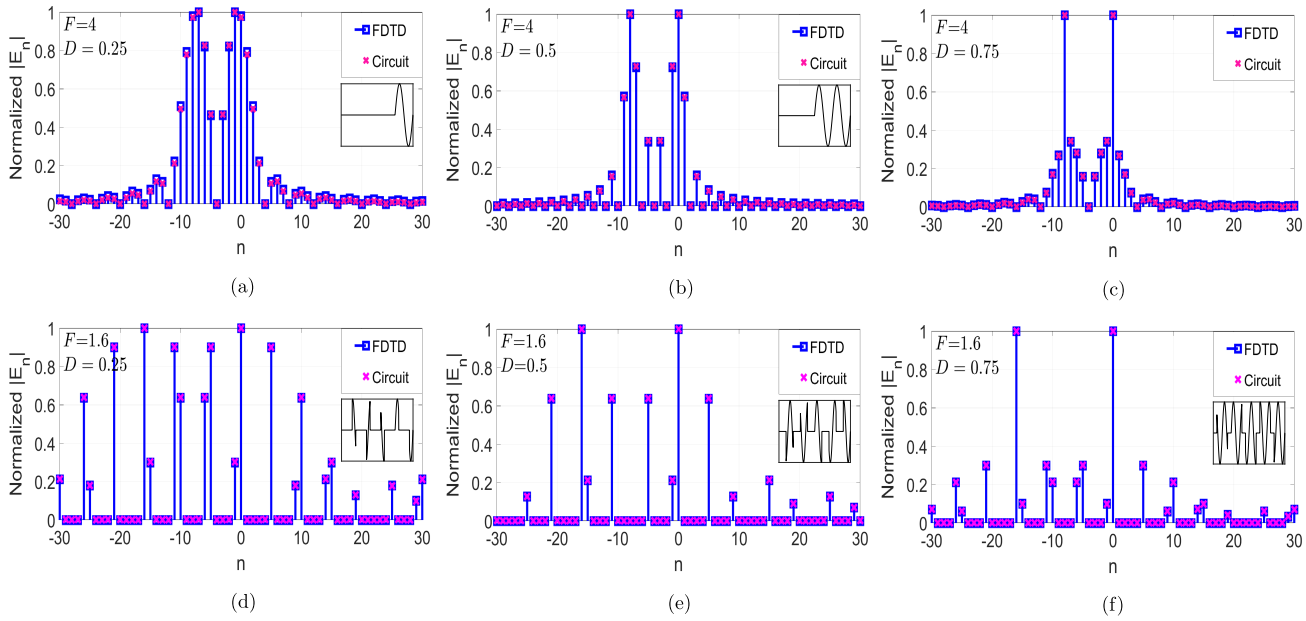

FIGURE 3. Normalized amplitude of the Floquet coefficients in the cases: (a) $F = 4$, $D = 0.25$, (b) $F = 4$, $D = 0.5$, (c) $F = 4$, $D = 0.75$, (d) $F = 1.6$, $D = 0.25$, (e) $F = 1.6$, $D = 0.5$, (f) $F = 1.6$, $D = 0.75$. A monochromatic incident wave of $\omega_0 = 2\pi \cdot 30$ GHz under normal incidence is assumed.

when imposing $k_t = 0$ with k_t being the transverse wavevector of the incident wave, and $i = 1, 2$ being the index indicating the leftmost/ rightmost medium respectively.

As visualized in Figs. 3(a)-(c) for $F = 4$, the value of D modifies the amplitude of the harmonics. For instance, when the wave encounters free-space in a longer time interval than metal at the interface, $D = 0.75$, the biggest amplitude values are carried by the fundamental harmonic ($n = 0$) and that with order $n = -8$ [see Fig. 3(c)]. When this interval decreases to $D = 0.25$, the amplitude of these predominant harmonics reduces with respect the rest of diffracted harmonics [see Fig. 3(a)]. This tendency seems to be progressive if we check Figs. 3(a)-(c) from left to right. If the modulation ratio is varied down to $F = 1.6$, as illustrated in the spectra shown in Figs. 3(d)-(f), it can be noticed that the modal distance between harmonics have changed. This fact can be appreciated since those carrying more energy are now the fundamental one ($n = 0$) and the one with order $n = -16$. In general, increasing the duty cycle D provokes that the time screen remains in "air" state a greater amount of time. Thus, the field profile $\mathbf{E}(t)$ progressively turns into the original incident plane wave as D approaches the unit. Therefore, the spectrum of the system resembles the spectrum of a conventional sine function, predominated by two delta functions at frequencies $\pm\omega_0$, with the rest of harmonics being significantly attenuated. This phenomenon is observed in Figs. 3(a)-(c) and Figs. 3(d)-(f) as D is increased. Note that breaking the perfect temporal symmetry of the modulation ($D \neq 0.5$) causes that harmonics of even and odd nature excite indistinctly. The situation was different in our previous work [41], where the duty cycle was fixed to $D = 0.5$. In that case, perfect temporal symmetry provoked that higher-order even harmonics became null, fact that can be also appreciated in Figs. 3(b) and (e). Therefore, the introduction of the duty cycle to the time modulation enriches the diffraction spectrum, which is of potential interest for the development of time-based beamformers.

III. DIFFRACTION RECONFIGURABILITY

To understand the effect of the reconfigurability in this time-periodic metamaterial, Fig. 4 shows configurations with different modulation ratios F while keeping the same duty cycle fixed to $D = 0.5$. This situation is well captured by the circuit model, after a previous definition of $E(t)$. The temporal evolution of $E(t)$ along a macroperiod is included as an inset of the figures. Now, TE oblique incidence is assumed under an angle of incidence $\theta_{\text{inc}} = 30^{\text{o}}$. The transverse wavevector is no longer null ($k_t \neq 0$), opening the possibility to excite evanescent harmonics according to (14). Fig. 4(a) depicts a first case governed by $F = 2.5$. For this configuration, some evanescent harmonics have non-zero amplitude values, as those with orders $n = -6, -4$. The rest of harmonics with non-zero amplitude are propagative. As F changes, the amplitude distribution get modified. In case illustrated in Fig. 4(b) the modulation ratio is $F = 1.6$, and now the evanescent harmonics with significant amplitude are those with orders $n = -11, -5$. For $F = 0.8$, reported in Fig. 4(c), they become the ones with orders $n = -5, -3$.

The harmonics with propagative nature appearing in Fig. 4 now scatters in different directions. The diffraction angles of each propagating harmonic have been calculated using (14). They have been compared with the angles obtained by FDTD in TABLE 1 under two different incident angles: $\theta_{inc} = 30^{\text{o}}$ and $\theta_{inc} = 50^{\text{o}}$. As observed, there is a good agreement between both analytical (Floquet circuit) and numerical results. Naturally, one point to note is

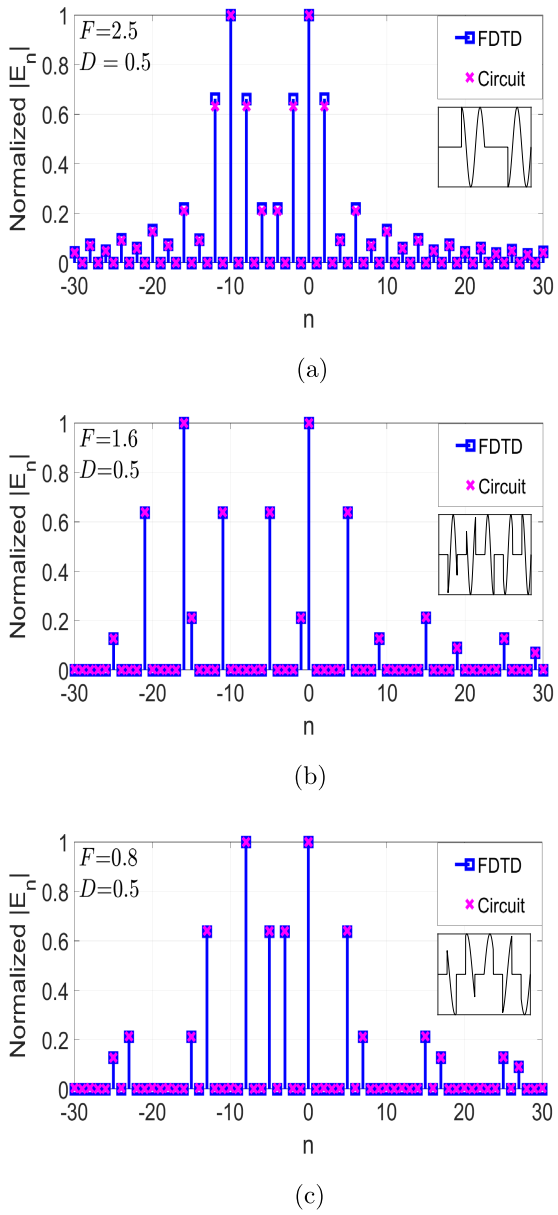

FIGURE 4. Normalized amplitude of the Floquet coefficients in the cases: (a) $F = 2.5$, $D = 0.5$, (b) $F = 1.6$, $D = 0.5$, (c) $F = 0.8$, $D = 0.5$. A monochromatic incident wave of $\omega_0 = 2\pi \cdot 30$ GHz under oblique incidence is assumed: $\theta_{inc} = 30^o$.

TABLE 1. Diffraction angle θ_n of the main Floquet harmonics for different modulation ratios F. A monochromatic incident wave with $\omega_0 = 2\pi \cdot 30 \cdot 10^9\ s^{-1}$ under oblique incidences is considered. Incidence angles: $\theta_{inc} = 30^o$ and $\theta_{inc} = 50^o$. The duty cycle of the time-periodic screen is $D = 0.5$.

	θ_{inc}	θ_n	Circuit	FDTD
$F = 2.5$	30^o	$\theta_{-2}(^o)$	56.44	56.49
		$\theta_0(^o)$	30.00	29.97
		$\theta_2(^o)$	20.92	20.93
		$\theta_4(^o)$	16.12	16.17
		$\theta_6(^o)$	13.13	13.17
	50^o	$\theta_{-2}(^o)$	eva.	eva.
		$\theta_0(^o)$	50.00	49.96
		$\theta_2(^o)$	33.17	33.18
		$\theta_4(^o)$	25.18	25.17
		$\theta_6(^o)$	20.37	20.30
$F = 1.6$	30^o	$\theta_0(^o)$	30.00	29.98
		$\theta_5(^o)$	17.92	17.95
		$\theta_9(^o)$	13.60	13.63
		$\theta_{15}(^o)$	10.01	10.03
	50^o	$\theta_0(^o)$	50.00	49.96
		$\theta_5(^o)$	28.12	28.10
		$\theta_9(^o)$	21.13	21.15
		$\theta_{15}(^o)$	15.45	15.48
$F = 0.8$	30^o	$\theta_0(^o)$	30.00	29.98
		$\theta_5(^o)$	12.83	12.87
		$\theta_7(^o)$	10.47	10.50
		$\theta_{15}(^o)$	6.04	6.02
	50^o	$\theta_0(^o)$	50.00	50.02
		$\theta_5(^o)$	19.90	19.92
		$\theta_7(^o)$	16.17	16.17
		$\theta_{15}(^o)$	9.28	9.31

the difference in simulation times for each solution. The analytical Floquet solution reduces notably the computational complexity compared to the FDTD. Concretely, the circuit model requires a simulation time of the order of seconds, while the FDTD takes minutes to simulate the scenario. This becomes more evident as the macroperiod of the time-modulated metamaterial is larger.

Subsequently, Fig. 5 illustrates the electric field distribution in the transmission region ($z > 0$) for the cases reported in TABLE 1. The simulation space takes $40\lambda_0 \times 20\lambda_0$. For simplicity, in all cases it has been assumed a fixed duty cycle of $D = 0.5$. These diffraction patterns obtained by FDTD allows for a clear identification of the direction of some harmonics. Some other harmonics taking place in the whole field expansion do not appear for the following reasons: their amplitude is not significant; they have an evanescent nature; they propagate backwards ($\beta_n^{(2)} < 0$). Thus, Fig. 5(a) and Fig. 5(d) show the diffraction pattern for a fixed modulation ratio $F = 2.5$ under the incident angles: $\theta_{inc} = 30^o$ and $\theta_{inc} = 50^o$, respectively. Please, note that the increase of the incident angle does not modify the excitation of the Floquet modes, but some of them are converted from propagative to evanescent nature. For this reason, the harmonic with order $n = -2$ does not appear when the incident angle rises up to 50^o. In Fig. 5(b) and Fig. 5(e), the modulation ratio has been fixed to $F = 1.6$. As it is expected according to Fig. 4, the index of the excited harmonics and, consequently, their frequencies are modified. As F decreases, it can be noticed that the diffraction angle of higher-order harmonics separate from that of the fundamental harmonic ($\theta_0 = 30^o$ for Fig. 5(b) and $\theta_0 = 50^o$ for Fig. 5(e)), approaching the

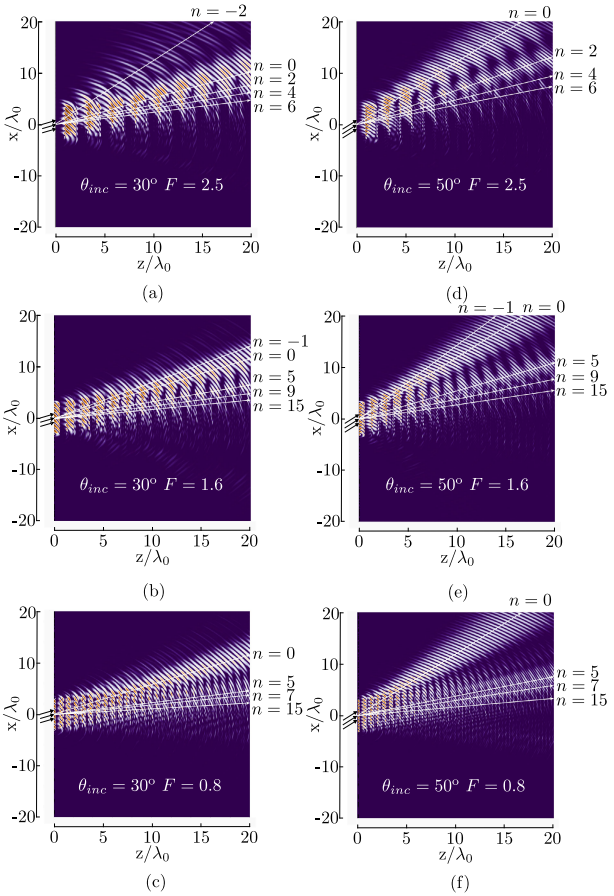

FIGURE 5. Electric field distribution obtained by means of FDTD method for the cases: (a) $F = 2.5$, $\theta_{inc} = 30^{o}$, (b) $F = 1.6$, $\theta_{inc} = 30^{o}$, (c) $F = 0.8$, $\theta_{inc} = 30^{o}$, (d) $F = 2.5$, $\theta_{inc} = 50^{o}$, (e) $F = 1.6$, $\theta_{inc} = 50^{o}$, (f) $F = 0.8$, $\theta_{inc} = 50^{o}$. Duty cycle has been fixed to $D = 0.5$ in all cases. A monochromatic incident wave of $\omega_0 = 2\pi \cdot 30$ GHz is assumed.

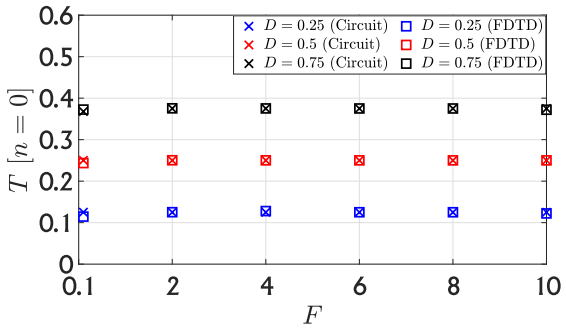

FIGURE 6. Transmission coefficient T as a function of the modulation ratio F for different duty cycles D.

normal direction ($\theta_n \approx 0^{o}$). This is accurately predicted by (14). This phenomenon becomes even more pronounced in Fig. 5(c) and Fig. 5(f), where the modulation ratio is $F = 0.8$. The identification of higher harmonics becomes significantly more challenging in this scenario.

Finally, Fig. 6 shows the transmission coefficient T, related to the fundamental harmonic ($n = 0$), for several values of the modulation ratio F and duty cycle D. Normal incidence is now considered, though oblique incidence can straightforwardly be computed. A comparison is illustrated between the results extracted from the Floquet circuit and the FDTD method, showing an good agreement. It can be appreciated that, for a fixed duty cycle, the transmission coefficient remains constant regardless of the value of the modulation ratio. Conversely, the transmission coefficient increases as the duty cycle does. This is due to the fact that the time-periodic screen remains a greater amount of time in the "air" state than in the "metal" state, allowing the incident waves to pass through it more easily in average.

IV. CONCLUSION

To conclude, in this Manuscript, we have studied the diffraction of electromagnetic fields produced by an incident plane wave with TE/TM polarization impinging on a time-periodic metallic screen. The proposed time-modulated metamaterial periodically alternates between "air" and "metal" states, leading to the excitation of diffraction orders that can be exploited to manipulate the propagation of electromagnetic waves. We have carried out the analysis by means of two tools: an analytical Floquet circuit and a numerical FDTD method. By introducing the concepts of "macroperiod" (T_{m}) and "duty cycle" (D) to the time modulation, we have extended the beamforming capabilities of the temporal structure shown in our previous works. The reconfigurability of higher-order modes has been discussed as a function of changes in the modulation ratio F and the duty cycle D. These results open up the possibility to simulate time-varying structures in a much more faster and efficient way than other full-wave electromagnetic tools, with the aim of designing modern time-based microwave and photonic devices.

REFERENCES

[1] C. Elachi, "Waves in active and passive periodic structures: A review," *Proc. IEEE*, vol. 64, no. 12, pp. 1666–1698, Dec. 1976.

[2] A. Alex-Amor, Á. Palomares-Caballero, and C. Molero, "3-D metamaterials: Trends on applied designs, computational methods and fabrication techniques," *Electronics*, vol. 11, no. 3, p. 410, Jan. 2022.

[3] J. E. Varela and J. Esteban, "Characterization of waveguides with a combination of conductor and periodic boundary contours: Application to the analysis of bi-periodic structures," *IEEE Trans. Microw. Theory Techn.*, vol. 60, no. 3, pp. 419–430, Mar. 2012.

[4] N. Marcuvitz, *Waveguide Handbook*, no. 21. IET, 1986.

[5] F. Costa, A. Monorchio, and G. Manara, "Efficient analysis of frequency-selective surfaces by a simple equivalent-circuit model," *IEEE Antennas Propag. Mag.*, vol. 54, no. 4, pp. 35–48, Aug. 2012.

[6] F. Mesa, R. Rodriguez-Berral, and F. Medina, "Unlocking complexity using the ECA: The equivalent circuit model as an efficient and physically insightful tool for microwave engineering," *IEEE Microw. Mag.*, vol. 19, no. 4, pp. 44–65, Jun. 2018.

[7] O. Luukkonen, C. Simovski, G. Granet, G. Goussetis, D. Lioubtchenko, A. V. Raisanen, and S. A. Tretyakov, "Simple and accurate analytical model of planar grids and high-impedance surfaces comprising metal strips or patches," *IEEE Trans. Antennas Propag.*, vol. 56, no. 6, pp. 1624–1632, Jun. 2008.

[8] R. Rodríguez-Berral, F. Mesa, and F. Medina, "Analytical multimodal network approach for 2-D arrays of planar patches/apertures embedded in a layered medium," *IEEE Trans. Antennas Propag.*, vol. 63, no. 5, pp. 1969–1984, May 2015.

[9] A. Alex-Amor, F. Mesa, Á. Palomares-Caballero, C. Molero, and P. Padilla, "Exploring the potential of the multi-modal equivalent circuit approach for stacks of 2-D aperture arrays," *IEEE Trans. Antennas Propag.*, vol. 69, no. 10, pp. 6453–6467, Oct. 2021.

[10] C. Molero, A. Alex-Amor, F. Mesa, Á. Palomares-Caballero, and P. Padilla, "Cross-polarization control in FSSs by means of an equivalent circuit approach," *IEEE Access*, vol. 9, pp. 99513–99525, 2021.

[11] C. Molero, R. Rodríguez-Berral, F. Mesa, F. Medina, M. Memarian, and T. Itoh, "Planar resonant blazed gratings from a circuit model standpoint," *IEEE Trans. Antennas Propag.*, vol. 68, no. 4, pp. 2765–2778, Apr. 2020.

[12] S. Taravati and G. V. Eleftheriades, "Generalized space-time-periodic diffraction gratings: Theory and applications," *Phys. Rev. Appl.*, vol. 12, Aug. 2019, Art. no. 024026, doi: 10.1103/PhysRevApplied.12.024026.

[13] H. Chen, M. Liu, A. Li, and E. H. W. Chan, "Microwave frequency dividers with reconfigurable fractional 2/N and 3/N division ratios," *IEEE Access*, vol. 11, pp. 29128–29137, 2023.

[14] S. Sugiura, T. Ishihara, and M. Nakao, "State-of-the-art design of index modulation in the space, time, and frequency domains: Benefits and fundamental limitations," *IEEE Access*, vol. 5, pp. 21774–21790, 2017.

[15] V. Pacheco-Peña, D. M. Solís, and N. Engheta, "Time-varying electromagnetic media: Opinion," *Opt. Mater. Exp.*, vol. 12, no. 10, pp. 3829–3836, Oct. 2022. [Online]. Available: https://opg.optica.org/ome/abstract.cfm?URI=ome-12-10-3829

[16] C. Caloz and Z.-L. Deck-Léger, "Spacetime metamaterials—Part I: General concepts," *IEEE Trans. Antennas Propag.*, vol. 68, no. 3, pp. 1569–1582, Mar. 2020.

[17] C. Caloz and Z.-L. Deck-Léger, "Spacetime metamaterials—Part II: Theory and applications," *IEEE Trans. Antennas Propag.*, vol. 68, no. 3, pp. 1583–1598, Mar. 2020.

[18] K. J. Deshmukh and G. W. Milton, "An energy conserving mechanism for temporal metasurfaces," *Appl. Phys. Lett.*, vol. 121, no. 4, Jul. 2022, Art. no. 041702.

[19] E. Galiffi, R. Tirole, S. Yin, H. Li, S. Vezzoli, P. A. Huidobro, M. G. Silveirinha, R. Sapienza, A. Alù, and J. B. Pendry, "Photonics of time-varying media," *Adv. Photon.*, vol. 4, no. 1, Feb. 2022, Art. no. 014002, doi: 10.1117/1.AP.4.1.014002.

[20] M. Moshinsky, "Diffraction in time," *Phys. Rev.*, vol. 88, pp. 625–631, Nov. 1952.

[21] F. R. Morgenthaler, "Velocity modulation of electromagnetic waves," *IEEE Trans. Microw. Theory Techn.*, vol. MTT-6, no. 2, pp. 167–172, Apr. 1958.

[22] T. Tamir, H. C. Wang, and A. A. Oliner, "Wave propagation in sinusoidally stratified dielectric media," *IEEE Trans. Microw. Theory Techn.*, vol. MTT-12, no. 3, pp. 323–335, May 1964.

[23] J. W. Zang, D. Correas-Serrano, J. T. S. Do, X. Liu, A. Alvarez-Melcon, and J. S. Gomez-Diaz, "Nonreciprocal wavefront engineering with time-modulated gradient metasurfaces," *Phys. Rev. Appl.*, vol. 11, no. 5, May 2019, Art. no. 054054.

[24] D. L. Sounas and A. Alù, "Non-reciprocal photonics based on time modulation," *Nature Photon.*, vol. 11, no. 12, pp. 774–783, Dec. 2017.

[25] A. Alex-Amor, C. Molero, and M. G. Silveirinha, "Analysis of metallic space-time gratings using Lorentz transformations," *Phys. Rev. Appl.*, vol. 20, no. 1, Jul. 2023, Art. no. 014063.

[26] S. Taravati, N. Chamanara, and C. Caloz, "Nonreciprocal electromagnetic scattering from a periodically space-time modulated slab and application to a quasisonic isolator," *Phys. Rev. B, Condens. Matter*, vol. 96, no. 16, Oct. 2017, Art. no. 165144. [Online]. Available: https://link.aps.org/doi/10.1103/PhysRevB.96.165144

[27] J. B. Pendry, E. Galiffi, and P. A. Huidobro, "Gain in time-dependent media—A new mechanism," *J. Opt. Soc. Amer. B, Opt. Phys.*, vol. 38, no. 11, pp. 3360–3366, Nov. 2021. [Online]. Available: https://opg.optica.org/josab/abstract.cfm?URI=josab-38-11-3360

[28] Z. Wu, C. Scarborough, and A. Grbic, "Space-time-modulated metasurfaces with spatial discretization: Free-space N-path systems," *Phys. Rev. Appl.*, vol. 14, no. 6, Dec. 2020, Art. no. 064060.

[29] P. A. Huidobro, M. G. Silveirinha, E. Galiffi, and J. B. Pendry, "Homogenization theory of space-time metamaterials," *Phys. Rev. Appl.*, vol. 16, no. 1, Jul. 2021, Art. no. 014044, doi: 10.1103/PhysRevApplied.16.014044.

[30] V. Bruno, C. DeVault, S. Vezzoli, Z. Kudyshev, T. Huq, S. Mignuzzi, A. Jacassi, S. Saha, Y. D. Shah, S. A. Maier, D. R. S. Cumming, A. Boltasseva, M. Ferrera, M. Clerici, D. Faccio, R. Sapienza, and V. M. Shalaev, "Negative refraction in time-varying strongly coupled plasmonic-antenna-epsilon-near-zero systems," *Phys. Rev. Lett.*, vol. 124, no. 4, Jan. 2020, Art. no. 043902.

[31] R. Tirole, E. Galiffi, J. Dranczewski, T. Attavar, B. Tilmann, Y.-T. Wang, P. A. Huidobro, A. Alù, J. B. Pendry, S. A. Maier, S. Vezzoli, and R. Sapienza, "Saturable time-varying mirror based on an epsilon-near-zero material," *Phys. Rev. Appl.*, vol. 18, no. 5, Nov. 2022, Art. no. 054067.

[32] V. Pacheco-Peña and N. Engheta, "Temporal equivalent of the Brewster angle," *Phys. Rev. B, Condens. Matter*, vol. 104, no. 21, Dec. 2021, Art. no. 214308, doi: 10.1103/PhysRevB.104.214308.

[33] X. Fang, M. Li, J. Han, D. Ramaccia, A. Toscano, F. Bilotti, and D. Ding, "Low-complexity DoA estimation method based on space-time modulated metasurfaces," in *Proc. IEEE Int. Symp. Antennas Propag. USNC-URSI Radio Sci. Meeting (AP-S/URSI)*, Jul. 2022, pp. 1282–1283.

[34] B. H. Kolner, "Space-time imaging, magnification, and time reversal of matter waves," *Appl. Phys. Lett.*, vol. 117, no. 12, Sep. 2020, Art. no. 124001.

[35] L. Li, H. Zhao, C. Liu, L. Li, and T. J. Cui, "Intelligent metasurfaces: Control, communication and computing," *eLight*, vol. 2, no. 1, p. 7, May 2022.

[36] Y. Xiao, D. N. Maywar, and G. P. Agrawal, "Reflection and transmission of electromagnetic waves at a temporal boundary," *Opt. Lett.*, vol. 39, no. 3, pp. 574–577, Feb. 2014. [Online]. Available: https://opg.optica.org/ol/abstract.cfm?URI=ol-39-3-574

[37] S. Y. Elnaggar and G. N. Milford, "Modeling space–time periodic structures with arbitrary unit cells using time periodic circuit theory," *IEEE Trans. Antennas Propag.*, vol. 68, no. 9, pp. 6636–6645, Sep. 2020.

[38] D. Ramaccia, A. Toscano, and F. Bilotti, "Light propagation through metamaterial temporal slabs: Reflection, refraction, and special cases," *Opt. Lett.*, vol. 45, no. 20, pp. 5836–5839, Oct. 2020. [Online]. Available: https://opg.optica.org/ol/abstract.cfm?URI=ol-45-20-5836

[39] D. Ramaccia, A. Alù, A. Toscano, and F. Bilotti, "Temporal multilayer structures for designing higher-order transfer functions using time-varying metamaterials," *Appl. Phys. Lett.*, vol. 118, no. 10, Mar. 2021, Art. no. 101901.

[40] L. Stefanini, S. Yin, D. Ramaccia, A. Alù, A. Toscano, and F. Bilotti, "Temporal interfaces by instantaneously varying boundary conditions," *Phys. Rev. B, Condens. Matter*, vol. 106, no. 9, Sep. 2022, Art. no. 094312, doi: 10.1103/PhysRevB.106.094312.

[41] A. Alex-Amor, S. Moreno-Rodríguez, P. Padilla, J. F. Valenzuela-Valdés, and C. Molero, "Diffraction phenomena in time-varying metal-based metasurfaces," *Phys. Rev. Appl.*, vol. 19, Apr. 2023, Art. no. 044014, doi: 10.1103/PhysRevApplied.19.044014.

[42] A. Gebhard, S. Sadjina, S. Tertinek, K. Dufrene, H. Pretl, and M. Huemer, "A harmonic rejection strategy for 25% duty-cycle IQ-mixers using digital-to-time converters," *IEEE Trans. Circuits Syst. II, Exp. Briefs*, vol. 67, no. 7, pp. 1229–1233, Jul. 2020.

[43] S. Taravati and G. V. Eleftheriades, "Microwave space-time-modulated metasurfaces," *ACS Photon.*, vol. 9, no. 2, pp. 305–318, Feb. 2022.

[44] Y. Liu, Y. Wang, X. Fu, L. Shi, F. Yang, J. Luo, Q. Y. Zhou, Y. Fu, Q. Chen, J. Y. Dai, L. Zhang, Q. Cheng, and T. J. Cui, "Toward sub-terahertz: Space–time coding metasurface transmitter for wideband wireless communications," *Adv. Sci.*, Aug. 2023, Art. no. 2304278, doi: 10.1002/advs.202304278.

[45] V. Kozlov, D. Vovchuk, and P. Ginzburg, "Broadband radar invisibility with time-dependent metasurfaces," *Sci. Rep.*, vol. 11, no. 1, p. 14187, Jul. 2021. [Online]. Available: https://api.semanticscholar.org/CorpusID:233324557

[46] X. Fang, M. Li, D. Ramaccia, A. Toscano, F. Bilotti, and D. Ding, "Self-adaptive retro-reflective Doppler cloak based on planar space-time modulated metasurfaces," *Appl. Phys. Lett.*, vol. 122, no. 2, Jan. 2023, Art. no. 021702, doi: 10.1063/5.0132125.

[47] L. Zhang, X. Q. Chen, S. Liu, Q. Zhang, J. Zhao, J. Y. Dai, G. D. Bai, X. Wan, Q. Cheng, G. Castaldi, V. Galdi, and T. J. Cui, "Space-time-coding digital metasurfaces," *Nature Commun.*, vol. 9, no. 1, p. 4334, Oct. 2018.

[48] J. Zhang, P. Li, R. C. C. Cheung, A. M. H. Wong, and J. Li, "Generation of time-varying orbital angular momentum beams with space-time-coding digital metasurface," *Adv. Photon.*, vol. 5, no. 3, Apr. 2023, Art. no. 036001, doi: 10.1117/1.AP.5.3.036001.

[49] Y. Zhu, X. Fang, Z. Lai, M. Li, and D. Ding, "Low complexity design methods of the space-time modulated metasurface: Theory and experiments," in *Proc. 17th Eur. Conf. Antennas Propag. (EuCAP)*, Mar. 2023, pp. 1–4.

[50] Z. Xu, X. Kong, J. Chang, D. F. Sievenpiper, and T. J. Cui, "Topological flat bands in self-complementary plasmonic metasurfaces," *Phys. Rev. Lett.*, vol. 129, no. 25, Dec. 2022, Art. no. 253001, doi: 10.1103/PhysRevLett.129.253001.
[51] C. Huang, J. Liao, C. Ji, J. Peng, L. Yuan, and X. Luo, "Graphene-integrated reconfigurable metasurface for independent manipulation of reflection magnitude and phase," *Adv. Opt. Mater.*, vol. 9, no. 7, Apr. 2021, Art. no. 2001950, doi: 10.1002/adom.202001950.
[52] C. V. S. Kumar, F. Maury, and N. Bahlawane, "Vanadium oxide as a key constituent in reconfigurable metamaterials," in *Metamaterials and Metasurfaces*. IntechOpen, 2018.
[53] R. Rodriguez-Berral, C. Molero, F. Medina, and F. Mesa, "Analytical wideband model for strip/slit gratings loaded with dielectric slabs," *IEEE Trans. Microw. Theory Techn.*, vol. 60, no. 12, pp. 3908–3918, Dec. 2012.
[54] F. Mesa, M. García-Vigueras, F. Medina, R. Rodríguez-Berral, and J. R. Mosig, "Circuit-model analysis of frequency selective surfaces with scatterers of arbitrary geometry," *IEEE Antennas Wireless Propag. Lett.*, vol. 14, pp. 135–138, 2015.
[55] (Oct. 2023). *SMP1320-Series*. [Online]. Available: https://www.skyworksinc.com/en/Products/Diodes/SMP1320-Series
[56] S. A. Stewart, Tom. J. Smy, and S. Gupta, "Finite-difference time-domain modeling of space–time-modulated metasurfaces," *IEEE Trans. Antennas Propag.*, vol. 66, no. 1, pp. 281–292, Jan. 2018.
[57] Y. Vahabzadeh, N. Chamanara, and C. Caloz, "Generalized sheet transition condition FDTD simulation of metasurface," *IEEE Trans. Antennas Propag.*, vol. 66, no. 1, pp. 271–280, Jan. 2018.

SALVADOR MORENO-RODRÍGUEZ received the B.Sc. and M.Sc. degrees in telecommunication engineering from the University of Granada (UGR), Spain, in 2019 and 2021, respectively, where he is currently pursuing the Ph.D. degree. Since 2021, he has been with the Department of Signal Theory, Telematics and Communications, Research Centre for Information and Communication Technologies (CITIC-UGR). His current research interests include polarizers, metamaterials, and applied electromagnetism.

ANTONIO ALEX-AMOR received the B.Sc. degree in telecommunication engineering from the University of Granada (UGR), Granada, Spain, in 2016, and the M.Sc. and Ph.D. degrees in telecommunication engineering from Universidad Politécnica de Madrid (UPM) in 2018 and 2021, respectively. From 2016 to 2021, he was with the Radiation Group, Department of Signal, Systems and Radiocommunications, UPM. From 2018 to 2019, he was with the Department of Language and Computer Science, Universidad de Málaga. From 2020 to 2021, he was with the Departamento de Teoría de la Señal, Telemática y Telecomunicaciones, UGR. He is currently an Assistant Professor with Universidad CEU San Pablo, Madrid, Spain. He was a Visiting Student with the KTH Royal Institute of Technology in 2019 for four months and conducted a Short Postdoctoral Mission with Universidade de Lisboa, Lisbon, Portugal, in 2021. His current research interests include the analysis and design of metamaterial structures and antennas, and wireless communication systems. In 2020, he received the Best Electromagnetics Paper Award at the 14th European Conference on Antennas and Propagation (EuCAP 2020). He is also an active science communicator in blogs and social media.

PABLO PADILLA was born in Jaén, Spain, in 1982. He received the degree in telecommunication engineering and the Ph.D. degree from the Radiation Group, Department of Signal, Systems and Radiocommunications, Technical University of Madrid (UPM), Spain, in 2005 and 2009, respectively. In 2007, he was an invited Ph.D. Student with the Laboratory of Electromagnetism and Acoustics, École Polytechnique Fédérale de Lausanne, Lausanne, Switzerland. In 2009, he carried out a postdoctoral position with the Helsinki University of Technology (AALTO, formerly TKK). In 2009, he became an Assistant Professor with the Department of Signal Theory, Telematics and Communications, University of Granada, where he has been an Associate Professor, since 2012. In 2017, he was an invited Visiting Professor with the Royal Institute of Technology of Stockholm. He has authored more than 65 high-impact journal contributions and more than 60 contributions to international symposia. His research interests include a variety of topics related mainly to electromagnetism and communication issues (radiofrequency devices, antennas, and propagation).

JUAN F. VALENZUELA-VALDÉS was born in Marbella, Spain. He received the degree in telecommunication engineering from Universidad de Málaga, Málaga, Spain, in 2003, and the Ph.D. degree from Universidad Politécnica de Cartagena, Cartagena, Spain, in 2008. In 2004, he joined the Department of Information Technologies and Communications, Universidad Politécnica de Cartagena. In 2007, he joined EMITE Ing., Murcia, Spain, as the Head of Research. In 2011, he joined Universidad de Extremadura, Mérida, Spain. In 2015, he joined Universidad de Granada, Granada, Spain, where he is currently a Full Professor, the Head of the SWAT Research Group, and the Co-Head of the Singular Laboratory of electromagnetic characterization of microwave and millimeter devices and antennas. His publication record comprised of more than 100 publications, including 50 Journal Citation Reports (JCR) indexed articles and seven book chapters. He holds several national and international patents. His current research interests include wireless communications, radio frequency devices, antennas, and propagation. He received several prizes, including the National Prize for the Best Ph.D. in mobile communications by Vodafone.

CARLOS MOLERO (Member, IEEE) was born in Seville, Spain, in April 1987. He received the Licenciado and Ph.D. degrees in physics from Universidad de Sevilla, Seville, in 2011 and 2017, respectively. From 2017 to 2020, he held a postdoctoral position with INSA Rennes, Rennes, France. Since 2020, he has been a Postdoctoral Researcher with the University of Granada. His research interests include the study of periodic structures, both in planar and 3-D architectures, circuit models, full-metal devices, a new conception of polarizers based on 3-D printable self-supported cells, and space-time metasurfaces. He was a recipient of some prizes, such as the Best Engineer Prize from the European Microwave Conference of 2015, Paris, France.

2.3 Space-Time Modulation

2.3.1 Space-Time Metallic Metasurfaces for Frequency Conversion and beam forming

In this paper (selected by the journal as an Editor's Suggestion), we analyze the electromagnetic response of a spacetime-modulated metagrating. This involves a zero-thickness metasurface that can alternate between three states: full transparency, full reflection, and an indefinitely-extended grating. The inclusion of spatial modulation into the previously time-only-varying metasurfaces introduces a new degree of freedom, which generates new spacetime harmonics throughout the entire space, thereby enhancing beamforming capabilities. Moreover, the variation of temporal parameters in the structure enables the beamformers to operate in either reflection or transmission mode. Additionally, we detail the design of frequency mixers by leveraging the intrinsic properties of the spacetime-varying metasurfaces. This manuscript thus explains and provides physical insight into the diffraction phenomena, the evanescent or propagative nature of each spacetime harmonic, and the scattering parameters using a circuit-based approach.

THIS IS A POSTPRINT VERSION OF THE PAPER:

S. Moreno-Rodríguez, A. Alex-Amor, P. Padilla, J. F. Valenzuela-Valdés, and C. Molero, "Space-time metallic metasurfaces for frequency conversion and beam forming," *Physical Review Applied*, vol. 21, p. 064018, Jun. 2024.

- Journal Impact Factor (JIF) in JCR 2023: 3.8
- Category: PHYSICS, APPLIED. JIF Rank: 54/179 (Q2).

Disclaimer:
This work has been published in Physical Review Applied.
DOI: 10.1103/PhysRevApplied.21.064018

Space-time Metallic Metasurfaces for Frequency Conversion and Beamforming

Salvador Moreno-Rodríguez[1,*]
[1] *Department of Signal Theory, Telematics and Communications, Research Centre for Information and Communication Technologies (CITIC-UGR), Universidad de Granada, 18071 Granada, Spain**

Antonio Alex-Amor,[2] Pablo Padilla,[1] Juan F. Valenzuela-Valdés[1] and Carlos Molero[1]
[2] *University of Pennsylvania, Department of Electrical and Systems Engineering, Philadelphia, Pennsylvania 19104, United States*

This paper details a class of metal-based space-time metasurfaces for application in wireless communications scenarios. Concretely, we describe space-time metasurfaces that periodically alternate their properties in time between three spatial states: "air", "conductor" and "grating". We analyze the physics of these metastructures via a computationally-efficient analytical technique based on the use of Floquet-Bloch series, integral equations and circuit models. By doing so, we reveal important features of these spatiotemporal metasurfaces: scattering parameters, field profiles, diffraction angles and nature of the space-time harmonics. The results, corroborated with a self-implemented numerical FDTD approach, show the potential application of these space-time metasurfaces as beamformers acting in reflection, in transmission or both. The amplitude and direction of the diffracted orders can be electronically controlled with the paramaters of the metasurface. Moreover, the intrinsic ability of time-modulated diffractive metasurfaces to mix and multiply frequencies is tested. We show how two different modulations can lead to the same diffraction angle but with different mixed output frequencies.

I. INTRODUCTION

Metamaterials have been conceived as artificially engineered devices with the property of manipulating electromagnetic waves. The term metamaterial originally referred to structures exhibiting negative permittivity and permeability simultaneously [1]. However, in the subsequent years this conception has experimented different evolutions, remarking the emergence of thinner/planar versions called metasurfaces [2].

A conventional metasurface can be physically described as a thin screen with planar geometry exhibiting spatial modulation [3]. Thanks to this modulation, metasurfaces become excellent terminals for a wide range of applications, such as microwave absorbers [4], beam shaping [5], or lenses [6], among others. Currently, researchers are paying close attention to a new evolution of metasurfaces, the so-called *space-time metasurfaces*, in which time is employed as an additional modulation to the existing purely spatial one [7, 8]. This introduces additional degrees of freedom as well as richer physics on the system [9–11]. Likewise, time modulation also enhances the capabilities of the active terminals [12], leading to promising concepts such as intelligent programmable metasurfaces [13] that could be combined and integrated into wireless communications and radars systems [14].

The recent development and fabrication of magnetic-free non-reciprocal devices [15–19] has been a key factor for the interest in space-time modulated devices [20, 21]. Thus, the number of theoretical studies of space-time varying structures in the microwave and optics range [9, 22, 23] have increased in the last few years favoring the emergence of novel theoretical applications, such as the use of temporal photonic crystals to achieve amplification [24], filtering and isolation [25], the utilization of travelling-wave modulations for power combining [26], the use of grounded slab for efficient phase conjugations [27], production of temporal chirping and lensing [28], or frequency mixing and multiplying [29].

Specifically, in the field of telecommunications, radar and wireless systems, frequency mixing and multiplying is of capital relevance [30, 31]. Traditionally, frequency mixing has been achieved via nonlinear circuit components such as Schottky diodes, GaAs FETs and CMOS transistors. Interestingly, frequency mixing is an intrinsic property of time-modulated diffractive systems, as the frequency of the diffracted waves is directly related to the frequency of the incident wave [32, 33]. Thus, spatiotemporal metasurfaces can complement the use of nonlinear components and even replace them in frequency ranges or scenarios where they are no longer functional. Time-modulated antennas have opened new alternatives in this regard as well [34, 35].

Furthermore, the versatility to simultaneously modify the momentum and frequency of waves has led space-time-modulated devices to be strong candidates for beamforming or beamsteering [36, 37]. Recently, it has been possible to test the beamsteering capabilities of these devices by modifying the phase constant associated to each unit cell with different temporal sequences [38]. It probes the potential of these metasurfaces as candidates for the future intelligent communications [28].

Unfortunately, the lack of available commercial so-

* Corresponding author: salvamr96@ugr.es

lutions to simulate complex behavior in space-time-modulated media hampers the analysis and design of these metadevices. At present, commercial simulator COMSOL Multiphysics is the only direct alternative for simulating spatiotemporal metamaterials. Nonetheless, it naturally presents the limitations inherent to a general-purpose electromagnetic simulator. As an in-house alternative, many of these applications are usually simulated using numerical techniques such as the finite-difference time-domain (FDTD) method [39]. However, the high computational costs and long simulation times that this code entails, have prompted the development of adaptive mesh-based solutions to enhance computational efficiency, such as the Discontinuous Galerkin Time-Domain (DGTD) method [40]. Others numerical solutions based on generalized sheet transition conditions (GSTCs) [41, 42], modal techniques [43] and integral-equation methods [44] show high performance when simulating time-varying metasurfaces. Nonetheless, many times the researchers also search approaches that can provide a deep physical insight of the studied problems. Thus, some alternatives based on analytical and semi-analytical techniques have already been reported [45–48].

In this work, we implement an analytical technique for the analysis of space-time metallic metasurfaces that can commute between three states: "air", "conductor" and "grating". As it will be show, a wise temporal combination of the three mentioned spatial states can produce a rich diffraction spectrum. Transmission and reflection levels can be tuned at convenience depending on the amount of time the metasurface is in these states. The air state favours transmission, while the conductor state favours reflection. The addition of the grating state adds richness and variety to the diffraction spectrum. The present space-time metasurface is of potential interest for related applications such as frequency conversion and beamforming.

Our analytical proposal is based on a Floquet-Bloch series expansion of the electromagnetic fields and integral-equation techniques that account for the space-time boundary conditions. The analytical formulation comes with an equivalent circuit that gives phyisical insight on spatiotemporal diffraction. Interestingly, the associated circuit model comes from first-principle computations; namely, the topology and elements of the circuit are not imposed by the designer, but arise as a consequence of the analytical formulation itself. Analytical circuits for spatially-modulated [49–51] and temporally-modulated [52–54] systems have been previously reported by the authors. The *analytical circuit* is a physically-insightful object that will give us information on the nature of the space-time harmonics, coupling between them, preferred diffraction directions and scattering parameters for both transverse magnetic (TM) and transverse electric (TE) polarizations. Moreover, computational times are minimal: a wideband range of frequencies can be simulated in less than a second.

The paper is organized as follows. Section II presents the space-time metasurface and depicts the analytical framework. We discuss on the physics of the diffraction spectrum, field profiles, nature of Floquet harmonics and scattering parameters via the associated equivalent circuit. Section III focuses on describing the feasibility of the spatiotemporal metasurface for use in wireless applications. Concretely, we focus on its beamforming and frequency-mixing capabilities, both studied via the analytical method and a supportive self-implemented FDTD approach. Finally, general conclusions are drawn in Section IV.

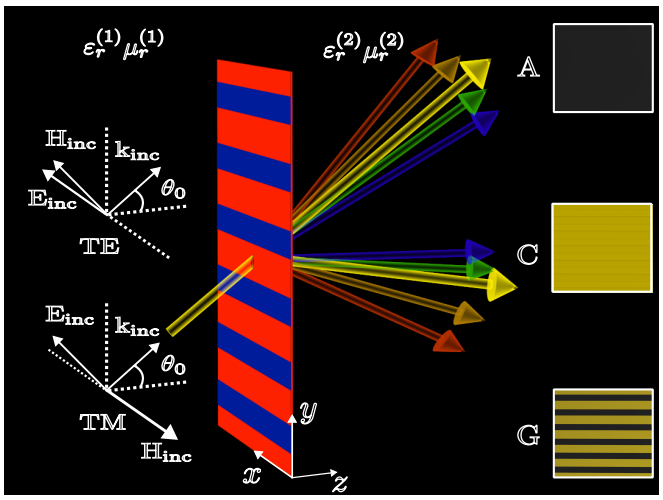

Figure 1. Sketch of the space-time-varying metasurface. The metasurface can alternate in time between three spatial states: air (A), conductor (C) and grating (G). By smartly combining the three states, a rich diffraction phenomenology can be created, from which wireless communications systems can take advantage.

II. ANALYTICAL FRAMEWORK

A. Space-Time Metasurface

Fig. 1 depicts the spatio-temporal system studied in this manuscript. The system is formed by a space-time-modulated diffractive metasurface that manipulates the incident transverse electric (TE) or transverse magnetic (TM) plane waves. The diffractive metasurface is based on different strips painted in red and blue that alternate their electromagnetic properties in time. Each strip can either become electromagnetically transparent or behave like a solid metal as it is assumed in [55].

Depending on the electromagnetic behavior of each of the strips, the space-time-modulated diffractive metasurface can operate in *three different states*: "air" (A), "conductor" (C) and "grating" (G). In the *air state*, all strips appear to vanish from an electromagnetic perspective, so full transmission of the incident wave is expected. In the *conductor state*, all strips behave as a solid metal achiev-

ing a solid metallic wall, so full reflection of the incident wave is expected. In the case of the *grating state*, the red strips behave as solid metals, and the blue strips become electromagnetically transparent, causing the space-time metasurface to operate as a spatially-modulated metallic diffraction grating.

The three states of the space-time metasurface can be realized by alternating between total transparency or total reflectivity, as recently achieved in [56]. Nonetheless, the implementation of the metasurface could also be inspired by several innovative prototypes in the microwave range [57]. Many of these devices are based on adjustable biased PIN diodes [58–60] and varactors [18, 19, 61], traditionally implemented in reflectarray and trasmittarray systems. Moreover, novel theoretical designs based on the use of electronically-reconfigurable materials such as graphene [62, 63] or transparent conductive oxides [64] open new alternatives for the millimeter-wave and terahertz regimes.

The geometrical parameters of the metasurface are the following. The space-time diffractive metasurface is placed along the XY plane, as Fig. 1 illustrates. In the time intervals in which the metasurface is in the grating state, it turns into a periodic arrangement of perfect electric conductor (PEC) strips (period P and slit width W) that are infinitely-extended along the x axis. The spatial periodicity of the grating state is along the y axis. In the conductor and air states, the metasurface can be modeled as infinitely-extended uniform thin PEC and air screens, respectively. The air state assumes electrical parameters $\varepsilon_r = \mu_r = 1$. In order to construct a proper analytical framework, we only need to enforce the temporal variation of the system to follow a *time-periodic* scheme, of period T_{M}.

By wisely combining the three states in time (A-G, C-G or A-C), a rich diffraction phenomenology can be created. From an engineering perspective, the diffraction pattern can be electrically tuned by setting the space-time parameters of the system. This enables an efficient beamforming platform that could be potentially applied in wide range of wireless communications scenarios. Remarkably, the space-time metasurface can act as a beamformer in reflection, transmission or both simultaneously by simply tuning its electrical parameters. This will be illustrated in detail in the next sections.

B. Floquet-Bloch Expansion

Since the diffractive metasurface behaves as space-time-periodic media, the transverse electric and magnetic fields in regions (1) and (2) can be expressed in terms of Floquet-Bloch series. Both media are electromagnetically defined by $\varepsilon_{\mathrm{r}}^{(i)}$ and $\mu_{\mathrm{r}}^{(i)}$. Thus, let us consider a space-time metasurface with spatial period P along the y-direction and temporal *macroperiod* T_{M} [53]. It receives a plane wave impinging obliquely with angular frequency ω_0 and TE polarization. The fields at both sides of the metasurface can be expressed in terms of a Floquet expansion of harmonics. In region (1) ($z < 0$):

$$\mathbf{E}_{\mathrm{t}}^{\mathrm{TE},(1)}(y,z,t) = \Bigg[\mathrm{e}^{\mathrm{j}(\omega_0 t - k_0 y - \beta_{00}^{(1)} z)} + R\mathrm{e}^{\mathrm{j}(\omega_0 t - k_0 y + \beta_{00}^{(1)} z)} + \sum_{\forall mn \neq 00} E_{mn}^{(1)} \mathrm{e}^{\mathrm{j}(\omega_n t - k_m y + \beta_{mn}^{(1)} z)} \Bigg] \hat{\mathbf{x}} \quad (1)$$

$$\mathbf{H}_{\mathrm{t}}^{\mathrm{TE},(1)}(y,z,t) = \Bigg[Y_{00}^{\mathrm{TE},(1)} \mathrm{e}^{\mathrm{j}(\omega_0 t - k_0 y - \beta_{00}^{(1)} z)} - RY_{00}^{\mathrm{TE},(1)} \mathrm{e}^{\mathrm{j}(\omega_0 t - k_0 y + \beta_{00}^{(1)} z)} - \sum_{\forall mn \neq 00} Y_{mn}^{\mathrm{TE},(1)} E_{mn}^{(1)} \mathrm{e}^{\mathrm{j}(\omega_n t - k_m y + \beta_{mn}^{(1)} z)} \Bigg] \hat{\mathbf{y}} \,. \quad (2)$$

In the former expressions, $E_{mn}^{(1)}$ is the amplitude of the (m,n)-th space-time harmonic operating in region (1), R is the reflection coefficient associated with the incident wave (00-th harmonic), ω_n is the angular frequency associated with the temporal n-th harmonic,

$$\omega_n = \omega_0 + n\frac{2\pi}{T_{\mathrm{M}}}, \quad (3)$$

and k_m is the transverse wavenumber linked to the spatial m-th harmonic:

$$k_m = k_t + m\frac{2\pi}{P} \quad (4)$$

with

$$k_t = \sqrt{\varepsilon_r^{(1)}\mu_r^{(1)}}\,\frac{\omega_0}{c}\sin(\theta_0) \quad (5)$$

and θ_0 being the incidence angle.

In a similar way, we define the tangential electromagnetic field via Floquet expansion in the region (2) ($z > 0$),

$$\mathbf{E}_{\mathrm{t}}^{\mathrm{TE},(2)}(y,z,t) = \Bigg[T\mathrm{e}^{\mathrm{j}(\omega_0 t - k_0 y - \beta_{00}^{(2)} z)} + \sum_{\forall mn \neq 00} E_{mn}^{(2)} \mathrm{e}^{\mathrm{j}(\omega_n t - k_m y - \beta_{mn}^{(2)} z)} \Bigg] \hat{\mathbf{x}} \quad (6)$$

$$\mathbf{H}_{\mathrm{t}}^{\mathrm{TE},(2)}(y,z,t) = \Bigg[TY_{00}^{\mathrm{TE},(2)} \mathrm{e}^{\mathrm{j}(\omega_0 t - k_0 y - \beta_{00}^{(2)} z)} + \sum_{\forall mn \neq 00} Y_{mn}^{\mathrm{TE},(2)} E_{mn}^{(2)} \mathrm{e}^{\mathrm{j}(\omega_n t - k_m y - \beta_{mn}^{(2)} z)} \Bigg] \hat{\mathbf{y}} \quad (7)$$

where T denotes the transmission coefficient and $E_{mn}^{(2)}$ the amplitude associated to the (m,n)-th Floquet harmonic. In the magnetic fields expansions in (2) and (7), $Y_{mn}^{(i)}$ denote the admittance of the the (m,n)-th Floquet

harmonic located at the i-th medium, defined for TE incidence as

$$Y_{mn}^{\mathrm{TE},(i)} = \frac{\beta_{mn}^{(i)}}{\mu_r^{(i)}\mu_0\,\omega_n}, \tag{8}$$

with

$$\beta_{mn}^{(i)} = \sqrt{\varepsilon_r^{(i)}\mu_r^{(i)}\left[\frac{\omega_n}{c}\right]^2 - [k_m]^2}\,. \tag{9}$$

being the propagation constant of the (m,n)-th harmonic in region (i).

The previous derivation can be easily adapted for TM incidence. In the TM case, the electric and magnetic field orientations are the opposite to the TE case, thus

$$\mathbf{E}_{\mathrm{t}}^{\mathrm{TM},(i)}(y,z,t) = [\hat{\mathbf{x}}\cdot\mathbf{E}_{\mathrm{t}}^{\mathrm{TE},(i)}(y,z,t)]\hat{\mathbf{y}} \tag{10}$$

$$\mathbf{H}_{\mathrm{t}}^{\mathrm{TM},(i)}(y,z,t) = [\hat{\mathbf{y}}\cdot\mathbf{H}_{\mathrm{t}}^{\mathrm{TE},(i)}(y,z,t)]\hat{\mathbf{x}}\,. \tag{11}$$

In addition, the admittance expressions must now be replaced to those related to TM harmonics,

$$Y_{mn}^{\mathrm{TM},(i)} = \frac{\varepsilon_r^{(i)}\varepsilon_0\,\omega_n}{\beta_{mn}^{(i)}}\,. \tag{12}$$

C. Nature of the Space-Time Harmonics

Real(imaginary) values of $\beta_{mn}^{(i)}$ imply that the nature of the (m,n)-th Floquet harmonic is propagative(evanescent). By using eq. (9), it can be shown that all evanescent space-time harmonics fulfill the general conditions

$$\frac{\sqrt{\varepsilon_r\mu_r}}{c}\left(\omega_0\sin(\theta_0) - \left|\omega_0 + n\frac{2\pi}{T_{\mathrm{M}}}\right|\right) + m\frac{2\pi}{P} > 0 \tag{13a}$$

$$\frac{\sqrt{\varepsilon_r\mu_r}}{c}\left(\omega_0\sin(\theta_0) + \left|\omega_0 + n\frac{2\pi}{T_{\mathrm{M}}}\right|\right) + m\frac{2\pi}{P} < 0 \tag{13b}$$

In a simpler scenario where the surrounding media are air ($\varepsilon_r = \mu_r = 1$) and the waves impinge normally ($\theta_0 = 0$) to the space-time metasurface, eq. (13) reduces to:

$$-\left|1 + n\frac{T_0}{T_{\mathrm{M}}}\right| + m\frac{\lambda_0}{P} > 0 \tag{14a}$$

$$+\left|1 + n\frac{T_0}{T_{\mathrm{M}}}\right| + m\frac{\lambda_0}{P} < 0 \tag{14b}$$

The former expressions show that, for a fixed temporal macroperiod T_{M}, there will be a greater number of evanescent space-time harmonics as the spatial periodicity P reduces. Likewise, for a fixed P, there will be a greater number of evanescent harmonics as T_{M} increases.

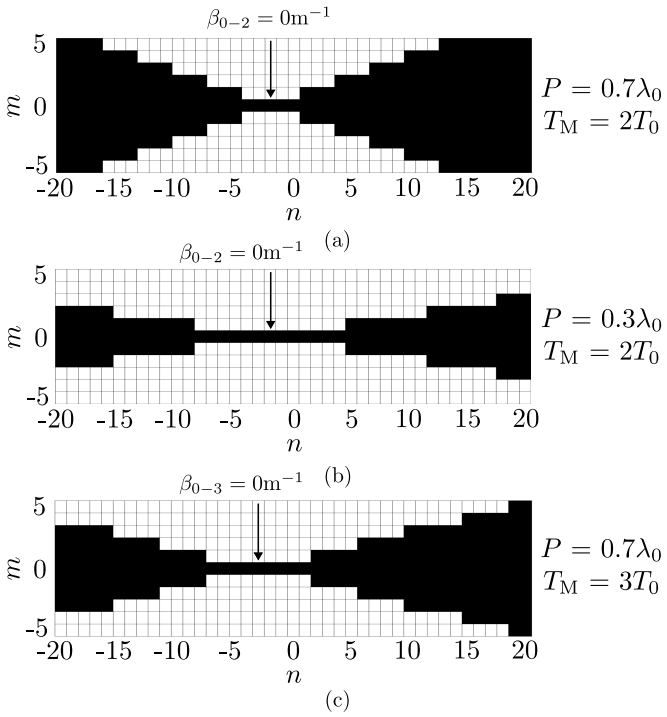

Figure 2. Propagative (black) and evanescent (white) nature of (m,n)-harmonics when an incident wave of angular frequency $\omega_0 = 2\pi\cdot 30$ GHz impinges on the space-time-varying metasurface with: (a) $P = 0.7\lambda_0$ and $T_{\mathrm{M}} = 2T_0$, (b) $P = 0.3\lambda_0$ and $T_{\mathrm{M}} = 2T_0$, (c) $P = 0.7\lambda_0$ and $T_{\mathrm{M}} = 3T_0$. Normal incidence and $\varepsilon_r = \mu_r = 1$ are assumed.

Moreover, all the $(0,n)$-th harmonics ($m = 0, \forall n$) are propagative under normal incidence. This is consistent with the results extracted in our previous work [52], as the $(0,n)$-th Floquet harmonics are only driven by the time modulation.

Fig. 2 summarizes all the aforementioned phenomenology related to the space-time harmonics. In the figure, the vertical axis represents the spatial (m-indexed) harmonics and the horizontal axis represents the temporal (n-indexed) harmonics. The evanescent harmonics are marked in white and the propagative ones in black. Upon analyzing Fig. 2, it is evident the existence of certain symmetry for both indexes. In the case of considering normal incidence, this symmetry appears around the null of the propagation constant in both the vertical and horizontal planes. Therefore, seeking the roots of eq. (9) under normal incidence, the (m,n)-th harmonic with $\beta_{mn} = 0$ emerges for $m = 0$ and $n = -\frac{T_{\mathrm{M}}}{T_0}$. It corresponds to a DC harmonic ($\omega_n = 0$) [42], which is present at $(m = 0, n = -2)$ in Fig. 2(a)-(b) and at $(m = 0, n = -3)$ in Fig. 2(c).

The phenomenology of the propagative and evanescent harmonics is much richer here than in the case considered in our previous works [52, 53]. In this work, we are considering a space-time modulation, where in [52, 53] we considered a time-only modulation. Time-only mod-

ulations led to scenarios where most of the harmonics are propagative, and only a few are evanescent. In fact, it was shown in [52] that all time harmonics are propagative under normal incidence conditions in the time-modulated metasurface. The situation is rather different and more interesting from a physics and engineering perspective when spatial and temporal modulations intervene together [54].

D. Diffraction Angles and Beamforming

The diffraction angle of the (m,n)-th Floquet harmonic can be computed using:

$$\theta_{mn}^{(i)} = \operatorname{asin}\left(\frac{k_m}{\sqrt{\varepsilon_r^{(i)}\mu_r^{(i)}}\left[\frac{\omega_n}{c}\right]}\right) = \operatorname{atan}\left(\frac{k_m}{\beta_{mn}}\right) \tag{15a}$$

$$\theta_{mn}^{(i)} = \operatorname{asin}\left(\frac{\sqrt{\varepsilon_r^{(1)}\mu_r^{(1)}}\sin(\theta_0) + m\frac{\lambda_0}{P}}{\sqrt{\varepsilon_r^{(i)}\mu_r^{(i)}}\left[1 + n\frac{T_0}{T_\mathrm{M}}\right]}\right) \tag{15b}$$

At a first sight, one can visualize in eq. (15a) that propagation below the XZ plane, i.e., negative angles $\theta_{mn}^{(i)}$, is allowed. A negative transverse wavenumber k_m (with real-valued $\beta_{mn}^{(i)}$) is easily achievable for some negative indexes m, which translates into a negative diffraction angle $\theta_{mn}^{(i)}$. This constitutes a major difference with respect to our previous works on time-only metasurfaces, where negatives diffraction angles were forbidden [52]. Additionally, eq. (15b) reveals that most of the diffraction harmonics tend to close to the normal ($\theta_{mn} \to 0$) when the temporal period T_M decreases or, analogously, when the time-modulation frequency ω_M increases, with the exception of the $(m,0)$-th harmonics that are not affected by the time modulation. Therefore, the diffraction pattern produced here is of a much richer nature. Thus, the beamforming capabilities of the present space-time metasurface are expected to significantly exceed those of the previous space-only and time-only configurations.

E. Reflection/Transmission Coefficients

The derivation of the scattering parameters, i.e., the reflection and transmission coefficients, require of *prior knowledge* of the electric-field profiles at the space-time discontinuity. Formally, the space-time profile, also referred to as *basis function* (bf), can be described by the function $\mathbf{E}_\mathrm{bf}(y,t)$ depending on space and time.

The application of the continuity of the electric fields through the space-time interface ($z=0$),

$$\mathbf{E}_t^{\mathrm{TE/TM},(1)}(y,0,t) = \mathbf{E}_\mathrm{bf}(y,t) = \mathbf{E}_t^{\mathrm{TE/TM},(2)}(y,0,t)\,, \tag{16}$$

leads to

$$1 + R = T \tag{17}$$

$$1 + R = \frac{\widetilde{E}_\mathrm{bf}(k_0,\omega_0)}{PT_\mathrm{M}} \tag{18}$$

$$E_{mn}^{(1)} = E_{mn}^{(2)} = \frac{\widetilde{E}_\mathrm{bf}(k_m,\omega_n)}{PT_\mathrm{M}}\,, \tag{19}$$

with

$$\widetilde{E}_\mathrm{bf}(k_m,\omega_n) = \int_{-\frac{P}{2}}^{\frac{P}{2}}\int_0^{T_\mathrm{M}} E_\mathrm{bf}(y,t)\,\mathrm{e}^{-\mathrm{j}(\omega_n t - k_m y)}\mathrm{d}y\,\mathrm{d}t\,. \tag{20}$$

The term $E_\mathrm{bf}(y,t)$ is simply the instantaneous amplitude of the vector $\mathbf{E}_\mathrm{bf}(y,t)$ representing the base function and $\widetilde{E}_\mathrm{bf}(k_m,\omega_n)$ is its Fourier transform.

The imposition of the boundary conditions in eq. (16) presents a fundamental difference with respect to other analytical methods that are also based on the use of Bloch-Floquet series [42]. Other methods, after expanding the fields in Bloch-Floquet series to the left (1) and right (2) sides of the space-time interface, directly impose continuity between them, i.e., $\mathbf{E}_t^{\mathrm{TE/TM},(1)} = \mathbf{E}_t^{\mathrm{TE/TM},(2)}$. Then, the fields are projected on each Floquet harmonic to reach a linear system of equations with complex values that gives the Floquet coefficients E_{mn}. This technique share similarities with mode-matching methods. In our case, the approach is different. We project separately the fields of the left and right sides of the space-time discontinuity onto a single basis function E_bf of our choice, i.e., $\mathbf{E}_t^{\mathrm{TE/TM},(1)} = \mathbf{E}_\mathrm{bf}$ and $\mathbf{E}_t^{\mathrm{TE/TM},(2)} = \mathbf{E}_\mathrm{bf}$. In this case, instead of reaching a complex-valued linear system of equations, we directly obtain the value of the Floquet coefficients E_{mn}. This approximation has been successfully applied in the past for the analysis of 1D-spatial [49, 65], 1D-time [52, 53], 2D-spatial [66–68] and 3D-spatial [51] periodic systems. It significantly reduces the computation time by avoiding solving the system of equations and allows to extract the associated equivalent circuit shown in Fig. 3(a).

We project separately the fields of the left and right sides of the space-time discontinuity onto a single basis function E_bf of our choice, i.e., $E^{(1)} = E_\mathrm{bf}$ and $E^{(2)} = E_\mathrm{bf}$ [see eq. (16)].

From eqs. (18) and (19), we may also obtain that

$$E_{mn}^{(1)} = E_{mn}^{(2)} = (1+R)N(k_m,\omega_n)\,, \tag{21}$$

where

$$N(k_m,\omega_n) = \frac{\widetilde{E}_\mathrm{bf}(k_m,\omega_n)}{\widetilde{E}_\mathrm{bf}(k_0,\omega_0)} \tag{22}$$

is a term that accounts for the coupling between the fundamental 00-th harmonic and the corresponding (m,n)-th space-time harmonic.

Now, the continuity of the instantaneous Poynting vector is imposed at the space-time interface ($z=0$). The

power passing through the interface is evaluated over a temporal period T_M and over a spatial period P. This leads to

$$\int_{-\frac{P}{2}}^{\frac{P}{2}}\int_{0}^{T_\mathrm{M}} \mathbf{E}_\mathrm{bf}(y,t)\times {\mathbf{H_t}}^{\mathrm{TE/TM},(1)}(y,0,t)\,\mathrm{d}y\,\mathrm{d}t = \int_{-\frac{P}{2}}^{\frac{P}{2}}\int_{0}^{T_\mathrm{M}} \mathbf{E}_\mathrm{bf}(y,t)\times {\mathbf{H_t}}^{\mathrm{TE/TM},(2)}(y,0,t)\,\mathrm{d}y\,\mathrm{d}t \quad (23)$$

By replacing the values of eqs. (2), (7) (TE incidence) or eq. (11) (TM incidence) and eq. (21) into eq. (23) and operating, we achieve:

$$(1-R)Y_{00}^{\mathrm{TE/TM},(1)} - (1+R)\sum_{mn\neq 00} Y_{mn}^{\mathrm{TE/TM},(1)}\,|N(k_m,\omega_n)|^2 = (1+R)Y_{00}^{\mathrm{TE/TM},(2)} + (1+R)\sum_{mn\neq 00} Y_{mn}^{\mathrm{TE/TM},(2)}|N(k_m,\omega_n)|^2 , \quad (24)$$

By manipulating (24), the reflection coefficient R admits to be expressed as

$$R = \frac{Y_{00}^{\mathrm{TE/TM},(1)} - Y_{00}^{\mathrm{TE/TM},(2)} - Y_\mathrm{eq}}{Y_{00}^{\mathrm{TE/TM},(1)} + Y_{00}^{\mathrm{TE/TM},(2)} + Y_\mathrm{eq}}\,. \quad (25)$$

The term Y_eq, which groups the double sums in eq. (24), is the *equivalent admittance* that models the space-time metasurface. It is computed as

$$Y_\mathrm{eq} = \sum_{\forall mn\neq 00} |N(k_m,\omega_n)|^2 \left(Y_{mn}^{\mathrm{TE/TM},(1)} + Y_{mn}^{\mathrm{TE/TM},(2)}\right). \quad (26)$$

F. Circuit Topology

Eqs. (25) and (26) are circuitally interpreted by the topology shown in Fig. 3. In general, eq. (25) reveals that the circuit model associated to the analytical framework consists of two semi-infinite transmission lines modeling the input (1) and output (2) media, and an equivalent admittance Y_eq that models the space-time metasurface [see Fig. 3(b)]. A deeper insight into eq. (26) shows that the equivalent admittance is internally formed by a sum of the admittances (parallel connections of semi-infinite transmission lines) associated to each space-time Floquet harmonic.

Each of the parameters $N(k_m,\omega_n)$ taking part in eq. (26) is interpreted as a complex transformer that takes into consideration the coupling between the (m,n)-th harmonic and the fundamental $(0,0)$th one. Each admittance of each Floquet harmonic is loaded with a complex transformer, except for the fundamental harmonic whose value is $N(k_0,\omega_0)=1$. This is sketched in Fig. 3(a). Note that, for the sake of visualization, only a few harmonics of the double infinite sum are represented in Fig. 3(a), and that the transmission lines of the fundamental harmonic are marked in blue.

At a first sight, the circuit topologies shown in Figs. 3(a) and 3(b) coincide with those shown in previous works on space-only [69] and time-only [52] metamaterial configurations. However, the value of the forming admittances and complex transformers, which rule the diffraction behavior of the metasurface, are completely different. In (three-dimensional) space-only systems, the complex transformers are a function of the transverse wavenumbers k_m, k_n and k_l. In time-only problems, those are a function of the angular frequency ω_n. In spatiotemporal systems, the complex transformers are a function of the transverse wavenumbers plus the angular frequency.

It was shown that higher-order harmonics in space-only and time-only metasurfaces described by the present topology are of evanescent and propagative nature, respectively. This causes that higher-order harmonics contribute with capacitive and/or inductive terms in space-only (patch-based and aperture-based) metasurfaces [69], while higher-order harmonics contribute with a purely resistive term in time-only configurations [52]. The scenario is rather more complex in the present space-time metasurface. Higher-order harmonics fulfilling $|n|\gg|m|$ are predominantly temporal. Their propagation constant is frequency-independent and real-valued. It can be approximated as

$$\beta_{mn}^{(i)}\big|_{|n|\gg|m|} \approx \left|\frac{2\pi n}{cT_\mathrm{M}}\right| \sqrt{\varepsilon_r^{(i)}\mu_r^{(i)}}\,. \quad (27)$$

By using eqs. (12) and (8), the admittances of the (m,n)-th harmonic read in this case:

$$Y_{mn}^{\mathrm{TM/TE},(i)}\big|_{|n|\gg|m|} \approx Y_{00}\sqrt{\frac{\varepsilon_r^{(i)}}{\mu_r^{(i)}}} \quad (28)$$

Therefore, all the space-time harmonics with $|n|\gg|m|$ contribute together with a pure resistive term.

On the other hand, higher-order harmonics fulfilling $|m|\gg|n|$ are predominantly spatial. Their propagation constant is frequency-independent and imaginary:

$$\beta_{mn}^{(i)}\big|_{|m|\gg|n|} \approx -\mathrm{j}\frac{2\pi}{P}\,|m|\,. \quad (29)$$

The associated admittances read:

$$Y_{mn}^{\mathrm{TM},(i)}\big|_{|m|\gg|n|} \approx \mathrm{j}(\omega_0+n\omega_\mathrm{M})\frac{\varepsilon_r^{(i)}\varepsilon_0 P}{2\pi|m|} \quad (30a)$$

$$Y_{mn}^{\mathrm{TE},(i)}\big|_{|m|\gg|n|} \approx \frac{1}{j(\omega_0+n\omega_\mathrm{M})}\frac{2\pi|m|}{\mu_r^{(i)}\mu_0 P} \quad (30b)$$

where $\omega_\mathrm{M}=2\pi/T_\mathrm{M}$ is simply the angular frequency of the time modulation.

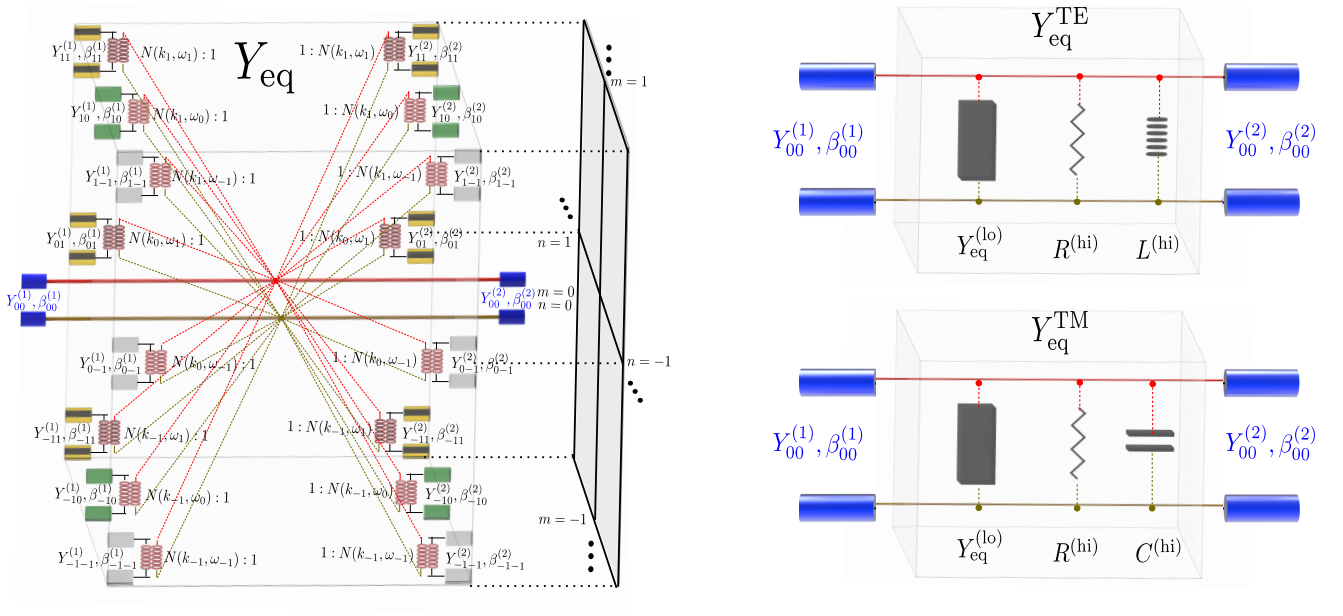

Figure 3. Circuit topology that describes the physics of the space-time-varying metasurface: (a) Complete equivalent circuit including the two-dimensional sum of infinite transmission lines representing each (m,n)-th harmonic. (b) Reduced equivalent circuit for TE and TM incidences.

From the former expressions, it can be identified that the (m,n)-th higher-order TM harmonic fulfilling $|m| \gg |n|$ contributes with *two parallel capacitors*. The first capacitor is dependent on the frequency of the incident wave ω_0 and second one on the time modulation of the space-time metasurface ω_{M}. When considering higher-order terms ($|n| \gg 1$), the latter capacitor is the dominant, being the time modulation of the metasurface truly relevant in this case. Similarly, the (m,n)-th higher-order TE harmonic fulfilling $|m| \gg |n|$ contributes with *two series inductors*, the one associated to the frequency ω_{M} being the dominant. Therefore, space-time harmonics with $|m| \gg |n|$ contribute jointly with a pure capacitive or inductive term, depending on the type of wave incidence.

The propagation constant of higher-order harmonics that fulfill $|m| \sim |n|$ ($|m|, |n| \gg 1$) is still frequency-independent, but cannot lead to a simple classification of the harmonic contributions into purely resistive or purely capacitive/inductive. Depending on the surrounding media (ε_r and μ_r) and electrical parameters of the space-time modulation (P and T_{M}), the propagation constant $\beta_{mn}^{(i)}$ will be real or imaginary and the (m,n)-th higher-order harmonic fulfilling $|m| \sim |n|$ will either contribute with a resistive or a capacitive/inductive term.

Conversely, low-order harmonics have associated a propagation constant that is frequency-dependent and a function of the incident angle θ_0, among other parameters. As a consequence, low-order terms cannot be decoupled into purely spatial or purely temporal. Thus, they cannot be directly associated to resistors, capacitors or inductors. To maintain the wideband behavior of the analytical approach, low-order harmonics should be analyzed directly with their *complex* admittances $Y_{mn}^{\mathrm{TE/TM},(i)}$. Therefore, the whole equivalent admittance Y_{eq} in eq. (26) can be divided into three main parallel contributions: a complex and frequency-dependent admittance $Y_{\mathrm{eq}}^{(\mathrm{lo})}$ describing the effect of low-order harmonics, a resistor $R^{(\mathrm{hi})}$ modeling predominantly-temporal higher-order TM/TE harmonics, and either a capacitor $C^{(\mathrm{hi})}$ (TM incidence) or an inductor $L^{(\mathrm{hi})}$ (TE incidence) modeling predominantly-spatial higher-order harmonics.

If needed, further approximations can be made in the quasi-static regime (low frequencies: $\omega_0 \ll 2\pi/T_{\mathrm{M}}$ and $\omega_0/c \ll 2\pi/P$) in order to neutralize the frequency-dependence of the complex low-order admittance $Y_{\mathrm{eq}}^{\mathrm{lo}}$. However, this comes at the expense of reducing the operation bandwidth of the wideband analytical model. In the quasi-static regime, the time modulation truly marks the behavior of the space-time harmonics, i.e., $\omega_n \approx n\omega_{\mathrm{M}}$ and $k_m \approx 2\pi m/P$. Thus, the admittance of the (m,n)-th harmonic under a quasi-static (qs) approximation is

$$Y_{mn}^{\mathrm{TM},(i),qs} \approx \frac{\varepsilon_r^{(i)}\varepsilon_0\, n\,\omega_{\mathrm{M}}}{\sqrt{\varepsilon_r^{(i)}\mu_r^{(i)}(n\,\omega_{\mathrm{M}})^2 - \left(\frac{2\pi m}{P}\right)^2}} \tag{31a}$$

$$Y_{mn}^{\mathrm{TE},(i),qs} \approx \frac{\sqrt{\varepsilon_r^{(i)}\mu_r^{(i)}(n\,\omega_{\mathrm{M}})^2 - \left(\frac{2\pi m}{P}\right)^2}}{\mu_r^{(i)}\mu_0\, n\,\omega_{\mathrm{M}}}, \tag{31b}$$

which can only be purely real or reactive depending on the selected (m,n)-th harmonic. As a consequence, the equivalent admittance in eq. (26) can be reduced in the quasi-static case to a parallel connection of a resistor

$R^{(\mathrm{hi}),\,\mathrm{qs}}$ and a capacitor $C^{(\mathrm{hi}),\,\mathrm{qs}}$ (TM incidence) or the resistor $R^{(\mathrm{hi}),\,\mathrm{qs}}$ and an inductor $L^{(\mathrm{hi}),\,\mathrm{qs}}$ (TE incidence).

G. Basis Functions

As detailed in Section II E, the knowledge of the tangential electric field profile (basis function) $\mathbf{E}_{\mathrm{bf}}(y,t)$ is crucial for the analysis of the space-time metasurface via the analytical method. We expect to obtain accurate results as long as the selected basis functions carry actual physical information of the electromagnetic fields taking place in the considered scenario. In this subsection, we describe the analytical expressions for the space-time base functions involving the three states under consideration: air (A), conductor (C) and grating (G).

1. Air state (A)

In the air state, the space-time metasurface *vanishes* from an electromagnetic perspective. Therefore, the base function that models the air state coincides with the electric profile of the incident plane wave; namely,

$$E_{\mathrm{bf}}(y,t) = A\sin(\omega_0 t),\ \forall y \in \left[-\frac{P}{2},\frac{P}{2}\right], t \in t_A, \quad (32)$$

where t_A is the time in which the space-time metasurface is in the air state.

2. Conductor state (C)

In the conductor state, the space-time metasurface turns into an infinitesimally-thin metallic sheet. If losses are neglected, the metallic sheet can be modeled with PEC conditions, so the tangential electric field must be zero at its surface. This leads to the base function

$$E_{\mathrm{bf}}(y,t) = 0,\ \forall y \in \left[-\frac{P}{2},\frac{P}{2}\right], t \in t_C, \quad (33)$$

where t_C is the time in which the metasurface is in the conductor state.

3. Grating (G)

The grating state can be modeled with the following base function

$$E_{\mathrm{bf}}(y,t) = A\sin(\omega_0 t)\begin{cases}\left[1-\left(\frac{2y}{W}\right)^2\right]^{\frac{1}{2}}, & \text{TE pol.}\\ \left[1-\left(\frac{2y}{W}\right)^2\right]^{-\frac{1}{2}}, & \text{TM pol.},\end{cases} \quad (34)$$

defined in the slit region ($-W/2 \le y \le W/2$) and the time interval $t \in t_G$, time in which the space-time metasurface is in the grating state. This base function relates the field excitation and charge distribution in a conventional one-dimensional diffraction grating illuminated by a sinusoidal plane wave of frequency ω_0.

As previously introduced, a wise combination (A-G, C-G) of the three states in a *time-periodic scheme* can lead to a rich diffraction phenomenology from which beamformers can benefit. Left side of Fig. 4(a) sketches the scenario where the space-time metasurface alternates between conductor and grating states (C-G case). As shown, the scheme is periodic in space and time, with periods P and T_{M}, respectively. Moreover, the terms t_C and t_G indicate the time in which the metasurface is in the conductor and grating states. Note that $T_{\mathrm{M}} = t_C + t_G$ in this case to retain time periodicity. The basis function that models the C-G scenario is plotted at the rigth side of Fig. 4(a) for TE and TM incident polarizations. Null regions indicate that the space-time metasurface is in the conductor state [eq. (33)], while $\cap$- and $\cup$-shaped regions [eq. (34)] are associated to the grating state under TE and TM incidences, respectively.

Similar rationale is applied to the air-conductor (A-G) case, sketched at left side of Fig. 4(b). The A-G configuration is periodic in space and time, with periods P and T_{M}, respectively. In this case, the time period is constituted by two addends, $T_{\mathrm{M}} = t_A + t_G$, related to the time in which the metasurface is in the air and grating states. The basis function of the A-G case is illustrated in the right side of Fig. 4(b). $\cap/\cup$-shaped regions indicate that the space-time metasurface is in grating state, while sinusoidal regions indicate that the metasurface is in the air state [eq. (32)].

The different states of the structure can also be invoked by regarding reconfigurable metasurfaces, which for this case would consist of a reconfigurable grating. Reconfiguration is realized via active elements such as diodes or varactors [58], or via electronic materials such as graphene [68] or $Ge_2Sb_2Te_2$ [70]. Their electronic effect over the grating is tuned to vary periodically, invoking periodic cycles in which the states of full transparency (A), full reflectivity (C), or the natural grating (G) interchange in the sense described above. This can be possible thanks to the excitation of resonant states in the grating through these elements. The existence of a transient regime when passing from one state to the other is neglected since we are assuming transient time to be temporarily short enough in comparison with the rest of times (t_C, t_A, t_G) taking part in a periodic cycle. Small transient times have negligible effects on the Fourier Transform of the electric field profile at the discontinuity [19].

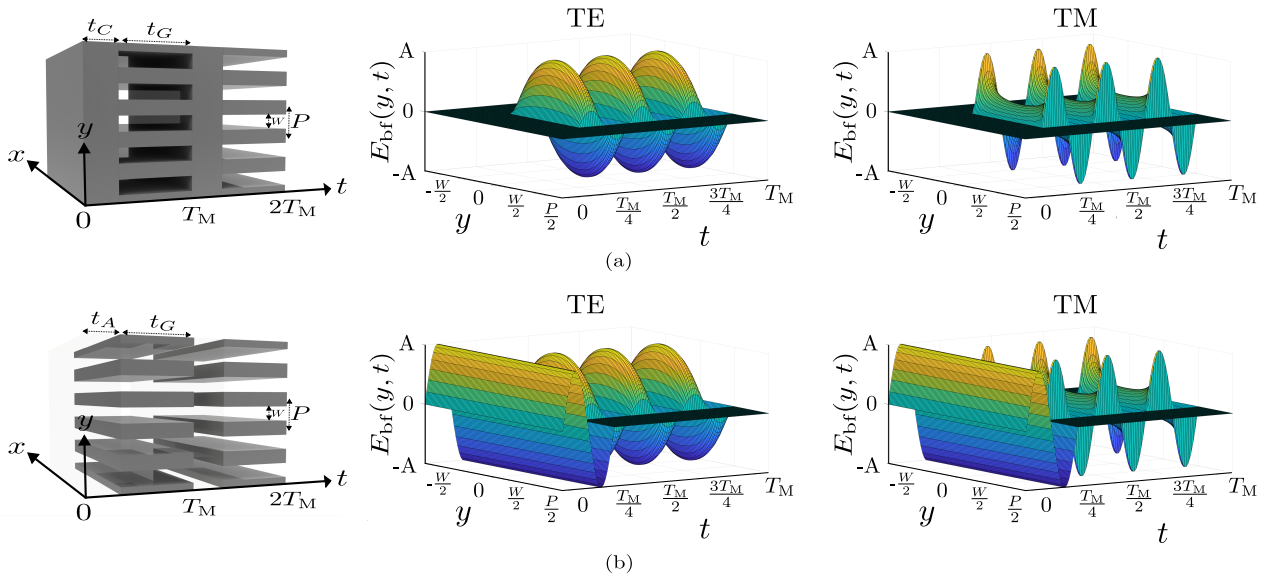

Figure 4. (a) Sketch of the C-G metasurface and the $\mathbf{E}_{\rm bf}(y,t)$ on a single space-time unit cell of the C-G configuration under TE/TM normal incidence. (b) Sketch of the A-G metasurface and the $\mathbf{E}_{\rm bf}(y,t)$ on a single space-time unit cell of the A-G configuration under TE/TM normal incidence. Parameters: $T_{\rm M} = 4T_0$, $t_C = t_A = [0,\ 0.25T_{\rm M}]$, $t_G = [0.25T_{\rm M},\ T_{\rm M}]$, $P = 0.7\lambda_0$ and $W = 0.5P$.

H. On the Limitations of the Analytical Approach

As we fundamentally work with air and metal states, we first have to define the properties of these elements. Without loss of generality, the air state is modeled as a dielectric of electrical properties $\varepsilon_r = \mu_r = 1$. A first approximation comes when defining the properties of metal-based states: conductor and grating. We consider here that metals are modeled as *perfect electric conductors* (PEC). The assumption of PEC is expected to give accurate results in radio, microwave and millimeter-wave frequencies, where good conducting metals such as copper, gold or silver behave essentially as PEC. When working with metasurfaces and frequency selective surfaces (FSS), it is a common practice in the literature to approximate the response of metals as perfect electric conductors in the aforementioned frequency ranges [49, 66, 71]. In fact, we expect that the PEC assumption give accurate results up to the low-THz regime (< 10 THz), as long as transients can be neglected in the system. However, the approximation of PEC to model metal-based states would cease to be physical, and therefore valid, in the optical range and at higher frequencies.

The considered basis functions also limit the frequency range of the analytical approach. Of the three states in which the space-time metasurface can be (air, conductor and grating), the grating state is the most limiting from an analytical perspective, but the richest one in terms of diffraction. In [71], it is reported that the maximum operating frequency to be covered with eq. (34) may go beyond to $f \sim 1.5c/P$. For instance, for two different spatial periods of $P = 3$ mm and $P = 3$ μm, the maximum frequencies in the grating state may not overpass 150 GHz and 150 THz, respectively. When oblique incidence is considered, this range could decrease to $f_{\rm max} \sim c/P$ (100 GHz and 100 THz in the former example). Moreover, the slit width should be less than $W \lesssim 0.7P$ to obtain accurate results [71]. Otherwise, it would be more convenient to directly work with currents instead of with electric field profiles [49]. As seen, the frequency range is wide, but naturally limited, when modeling the grating state.

The maximum operation frequency $f_{\rm max}$ of the analytical approach would be determined by the worst-case scenario of the two main approximations discussed above. If the maximum frequency is exceeded, the accuracy in the results is expected to degrade significantly. Above $f_{\rm max}$, the proposed basis functions could not be representative of the actual physical phenomena occurring in the spatiotemporal metastructure. Additionally, metals could stop being fully-reflective objects (PEC scenario) and start being semi-transparent from the incident wave's perspective. Therefore, the actual reflection and transmission coefficients can drastically change with respect to the theoretical estimations.

Moreover, above the maximum operation frequency $f_{\rm max}$ of the analytical circuit, frequency dispersion and transients could play an important role in the response of the metastructure. Transient effects, out of the scope of the present manuscript, can completely redefine the actual electromagnetic response of the space-time metasurface. Transients are expected to be non-negligible at frequencies close to the plasma frequency ω_p (Drude model). In good conductors such as copper, gold or silver, the plasma frequency is of the order of $\omega_p \sim 10^{16}$ rad/s, and the relaxation times are $\tau \sim 10^{-14}$ s. Thus, the effect

of transients should be appreciable around frequencies of the order of 10^{14} rad/s. Below this limit (radio, microwaves, millimeter-waves), transients may be neglected without significantly affecting the response of the system.

III. WIRELESS APPLICATIONS

In this section, we test the capabilities of the space-time metasurface for wireless applications. We show how the electrical tuning of the different space-time parameters can lead to a rich diffraction phenomenology, mixing frequencies, setting specific angular regions and favoring transmission or reflection. Furthermore, we validate the present analytical approach by comparing the results with full-wave simulations in a self-implemented finite-difference time-domain (FDTD) code.

A. Harmonic Distribution

We start by considering the case in which the space-time metasurface alternates between the conductor and grating states. The basis function that models the C-G case is mathematically described by a combination of eqs. (33) and (34). Fig. 5 depicts the obtained normalized amplitudes of the Floquet harmonics under normal TE and TM incidences. In all these simulations, the incidence of a monochromatic wave with a frequency of 30 GHz has been assumed. The results are obtained with the proposed analytical model and then compared with our FDTD code. The agreement between the analytical and FDTD results is good, thus validating the present approach.

The harmonic pattern shows similarities for TE and TM incidences. Note that two main lobes appear in Fig. 5 for $n = 0$ and $n = -16$. These indexes correspond to the frequencies $\omega_n = \pm\omega_0$, respectively. However, in the TM case, the amplitude of the spatial (m-indexed) harmonics show a slower decay; namely, a larger number of spatial modes are needed to accurately reconstruct the basis function. This is due to the singularity of the spatial profile present in the TM case that is not in the TE case. On the other hand, the harmonic pattern under TE incidence is mainly governed by the temporal n-indexed harmonics.

Fig. 5(b) presents the Floquet harmonic pattern in the case of reducing the time period from $T_\mathrm{M} = 8T_0$ to $T_\mathrm{M} = 2T_0$. The peaks are observed for the temporal harmonics $n = 0$ and $n = -4$. As illustrated, the two main lobes approach each other in the case of reducing the time period (increasing the switching frequency of the metasurface). The spatial and temporal harmonic dependencies are decoupled, as eqs. (32)-(34) impose and Fig. 5 confirms. Thus, the behaviour of the spatial modes for both incidences is not affected by modifying the time period.

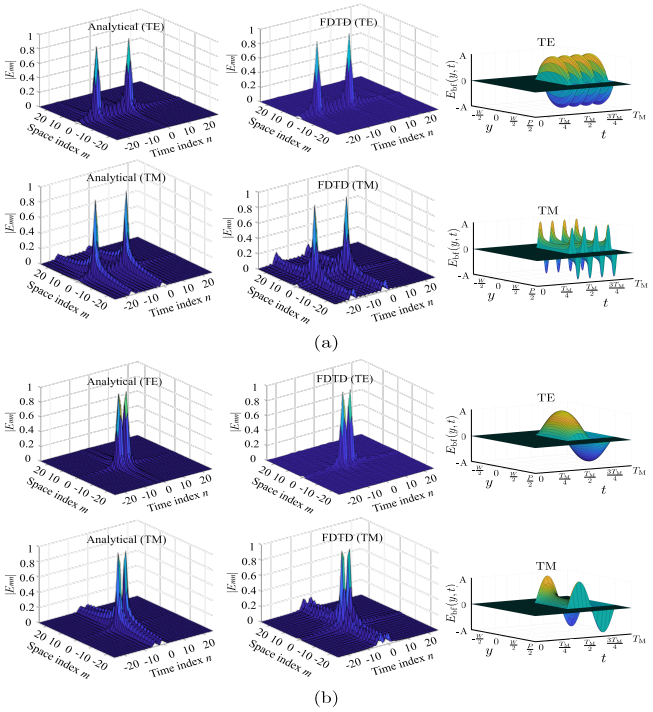

Figure 5. Normalized amplitude of the Floquet coefficients when varying the temporal period in a C-G scenario. Normal TM and TE incidences are considered. Cases: (a) $T_\mathrm{M} = 8T_0$ and (b) $T_\mathrm{M} = 2T_0$. The basis function $E_\mathrm{bf}(y,t)$ is plotted along the results. Parameters: $t_C = [0,\ 0.5T_\mathrm{M}]$, $t_G = [0.5T_\mathrm{M},\ T_\mathrm{M}]$, $P = 0.7\lambda_0$, $W = 0.5P$.

Another temporal parameter of interest is the *duty cycle* D [53]. The duty cycle is a dimensionless parameter that relates the amount of time that the space-time metasurface is in each of the three states. As it will be discussed later, the duty cycle plays an important role in controlling the amplitude of the diffracted, reflected and transmitted, waves. For the present C-G case, the metasurface keeps in conductor state a time given by DT_M, with T_M being the temporal macroperiod. Otherwise, it remains in the grating state $(1-D)T_\mathrm{M}$ seconds. First and second row of Fig. 6(a) show the harmonic pattern when the duty cycle is $D = 0.25$ and $D = 0.75$, respectively. Increasing the duty case in this case implies a greater presence of the grating state. Therefore, the width of the main lobes narrows along the temporal (n-indexed) axis as the spatiotemporal field profile (basis function) is more similar to that of a pure sine.

The last spatial parameter of interest is the relation between the slit width W and the spatial period P; namely, the dimensionless ratio W/P. Logically, decreasing the slit width in a grating implies an increase in the reflection through the structure. From a harmonic perspective [see the harmonic pattern in Fig. 6(b)], decreasing the ratio W/P provokes that the width of the main lobes widens. This is specially noticeable in the TM case, as the basis function includes the presence of two singularities at the

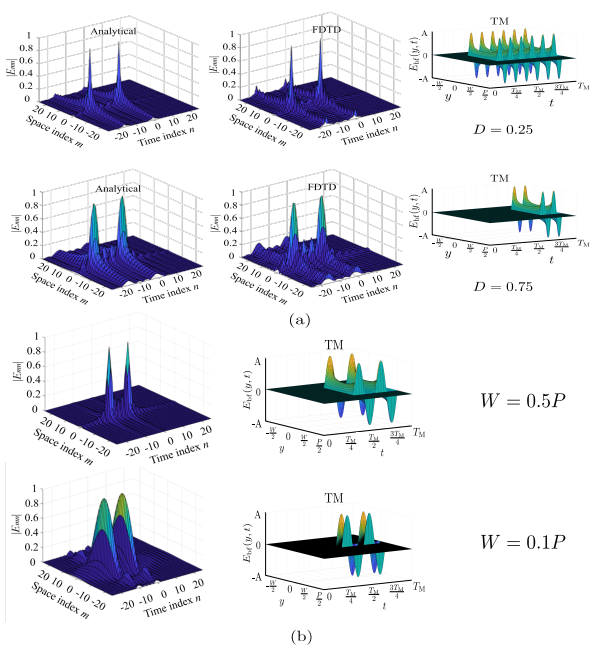

Figure 6. Normalized amplitude of the Floquet coefficients in a C-G scenario. Normal TM incidence is assumed and the basis function $E_{\rm bf}(y,t)$ is plotted along the results. (a) The duty cycle is varied. First row: $D = 0.25$. Second row: $D = 0.75$. Here, D and $1 - D$ indicates the amount of time that the metasurface is in the conductor and grating states, respectively. Parameters: $T_{\rm M} = 8T_0$, $P = 0.7\lambda_0$ and $W = 0.5P$. (b) The spatial ratio W/P is varied. First row: $W = 0.1P$. Second row: $W = 0.5P$. Parameters: $T_{\rm M} = 4T_0$, $P = 0.7\lambda_0$ and $D = 0.5$.

edge of the slits (positions $y = \pm W/2$ within the unit cell) in a ∪-shaped profile. The two singularities get closer as W/P reduces. As a consequence, more spatial modes are needed to reconstruct the tangential electric-field profile due to the rapid spatial variation of the basis function along y.

B. Diffracted Waves

To gain a more comprehensive understanding on the diffraction patterns of these metasurfaces, Fig. 7(a) and Fig. 7(b) illustrate the electric-field distributions of the A-G and C-G cases, respectively, extracted with the self-implemented FDTD code. The same duty cycle $D = 0.5$ is maintained in both configurations for a fair comparison.

In general, higher transmission is observed for TM polarization than for TE polarization. This is in line with the results obtained in previous works on spatially-modulated surfaces [49, 65]. However, when the metasurface alternates between air and grating states [A-G configuration in Fig. 7(a)], a high degree of transmission is generally seen. In contrast, when the metasurface switches between the conductor and grating states

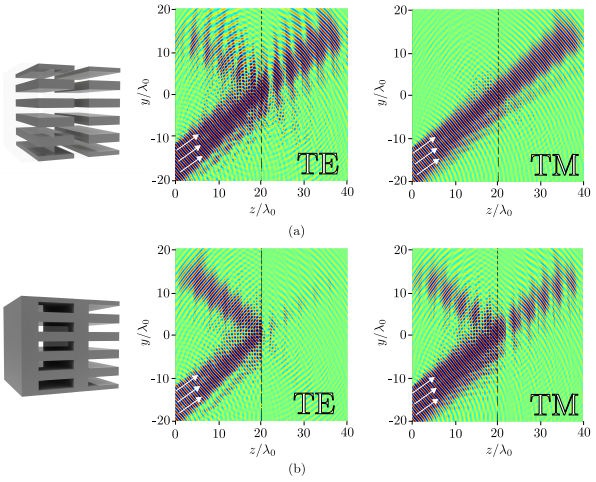

Figure 7. FDTD simulation of the diffracted electric fields for the (a) A-G and the (b) C-G configurations. The space-time metasurface is placed at $z/\lambda_0 = 20$. Oblique TE and TM incidences ($\theta_0 = 40^{\rm o}$) are analyzed. Parameters: $T_{\rm M} = 4T_0$, $t_C = t_A = [0,\ 0.5T_{\rm M}]$, $t_G = [0.5T_{\rm M},\ T_{\rm M}]$, $P = 0.7\lambda_0$, $W = 0.5P$.

[C-G configuration in Fig. 7(b)], high reflection is created. This is a somewhat expected but interesting feature from an engineering perspective, since the air and conductor states tend to favor transmission and reflection, respectively. This feature of the space-time metasurface, combined with the tuning of the duty cycle parameter, can be exploited in practice for the efficient design of reflection-based, transmission-based or mixed reflection-transmission-based beamformers.

From a physical perspective, it is noteworthy that the incorporation of spatial modulation by the grating leads to the emergence of spatial modes in the upper ($y \geq 0$) and lower ($y < 0$) half-spaces. This constitutes a major difference with respect to our previous works on time-only modulated metamaterials, where only diffraction in the upper half-space was permitted [52, 53]. Thus, the present space-time metasurface creates a richer diffraction pattern compared to time-only configurations.

C. Frequency Mixing

Frequency mixing is vital for some physics and engineering applications such as radio astronomy, telecommunications or radar systems. Traditionally, nonlinear components such as Schottky diodes, GaAs FETs and CMOS transistors are used for this purpose. In this regard, temporal and spatiotemporal metamaterials possess the inherent ability to mix frequencies [33]. This is essentially due to "temporal" diffraction and the production of higher-order Floquet harmonics ruled by the condition $\omega_n = \omega_0 + 2\pi n/T_{\rm M}$ [see eq. (3)]. Thus, the proposed space-time metasurface can produce new frequencies, ω_n, from the frequency of the incident wave,

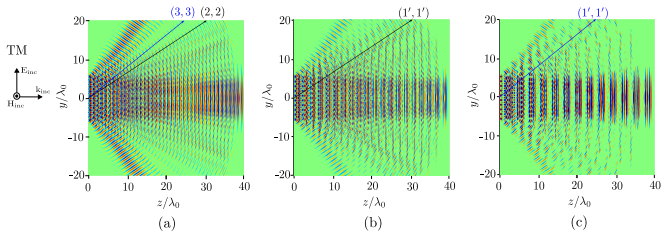

Figure 8. FDTD results for a C-G frequency mixer for an incident wave of frequency $\omega_0 = 2\pi\cdot 30$ GHz: (a) $T_{\rm M} = T_0$; (b) $T'_{\rm M} = 2T_0$; (c) $T'_{\rm M} = 3T_0$. Normal TM incidence is considered. Parameters: $t_C = [0,\ 0.25T_{\rm M}]$, $t_G = [0.25T_{\rm M},\ T_{\rm M}]$, $P = 1.2\lambda_0$, $W = 0.5P$.

ω_0.

Interestingly, eq. (15a) suggests that two different space-time modulations can lead to the same diffraction angle, but with different output frequencies, by simply tuning their space-time parameters. In order to show this frequency-mixing effect, let us consider the two following modulations. Modulation #1 is defined by the (unprimed) space-time parameters $\{m, n, P, T_{\rm M}\}$. Similarly, modulation #2 is defined by the (primed) parameters $\{m', n', P', T'_{\rm M}\}$. This leads to the diffraction angles θ_{mn} and $\theta_{m'n'}$ (associated to modulations #1 and #2, respectively), given by

$$\theta_{mn} = \text{asin}\left(\frac{k_t + \frac{2\pi m}{P}}{\frac{2\pi}{cT_0}\sqrt{\varepsilon_r^{(1)}\mu_r^{(1)}}\left(1 + n\frac{T_0}{T_{\rm M}}\right)}\right) \tag{35}$$

$$\theta_{m'n'} = \text{asin}\left(\frac{k_t + \frac{2\pi m'}{P'}}{\frac{2\pi}{cT_0}\sqrt{\varepsilon_r^{(1)}\mu_r^{(1)}}\left(1 + n'\frac{T_0}{T'_{\rm M}}\right)}\right) \tag{36}$$

Nonetheless, both configurations are expected to have the same spatial period ($P' = P$), since this parameter cannot be electronically reconfigured in practice like the duty cycle D or the time period $T_{\rm M}$. Under this assumption, by equating eqs. (35) and (36), we have

$$\frac{k_t + \frac{2\pi m}{P}}{\frac{2\pi}{cT_0}\sqrt{\varepsilon_r^{(1)}\mu_r^{(1)}}\left(1 + n\frac{T_0}{T_{\rm M}}\right)} = \frac{k_t + \frac{2\pi m'}{P}}{\frac{2\pi}{cT_0}\sqrt{\varepsilon_r^{(1)}\mu_r^{(1)}}\left(1 + n'\frac{T_0}{T'_{\rm M}}\right)} \tag{37}$$

The former equation reduces under normal incidence ($k_t = 0$) to

$$\frac{m}{m'} = \frac{1 + n\frac{T_0}{T_{\rm M}}}{1 + n'\frac{T_0}{T'_{\rm M}}} \tag{38}$$

Expressions (37) and (38) give us the design equations to produce frequency mixing between harmonics of different orders ($\{m, n\}$ and $\{m', n'\}$) while maintaining the same output diffraction angle. This can be done by simply adjusting the temporal periods of the two modulations, $T_{\rm M}$ and $T'_{\rm M}$.

Fig. 8 shows a practical example of frequency mixing. For simplicity, we have selected an scenario ruled by normally-incident waves. However, the previous discussion can be straightforwardly extended to the design of spatiotemporal frequency mixers that operate under oblique-incidence conditions by using eq. (37). In the figure, a monochromatic plane wave of frequency ω_0 impinges normally on a C-G space-time metasurface (located at $z/\lambda_0 = 0$). As seen, the metasurface creates a rich diffraction pattern, where only the transmitted diffracted fields are plotted for a better visualization of the results. With the design information given by eq. (38), the temporal periods of Figs. 8(a), 8(b), 8(c) have been carefully chosen. The underlying idea is to keep the same diffraction angle while varying the output frequencies in the three configurations that are shown. For instance, it can be seen that the diffraction orders $(m = 2, n = 2)$ and $(m' = 1, n' = 1)$ in Figs. 8(a) and 8(b) share the same diffraction angle ($\theta_{22} = \theta_{1'1'} = 33.72^{\rm o}$) while their output frequencies are different ($\omega_2 = 3\omega_0$, $\omega_{1'} = 1.5\omega_0$). The aforementioned diffraction orders are marked with a blue line in Figs. 8(a) and 8(b). Similarly, the diffraction orders $(m = 3, n = 3)$ and $(m' = 1, n' = 1)$, marked with a black line in Figs. 8(a) and 8(c), have the same diffraction angle ($\theta_{33} = \theta_{1'1'} = 38.65^{\rm o}$) while their output frequencies are $\omega_3 = 4\omega_0$ and $\omega_{1'} = 1.33\omega_0$, respectively. As this example seeks to illustrate, the capabilities of the present metal-based metasurface are promising for the production of frequency mixers and frequency multipliers based on space-time architectures that could be integrated in wireless communication systems.

D. Transmissive Beamformer

The main purpose of this section is to exploit the performance of these structures as transmission beamformers. Thus, we test the A-G configuration by changing the spatial and temporal periods. For a better visualization in the simulations, only the transmissive part of the diagrams is plotted. The A-G metasurface is placed at the beginning of the space simulation ($z/\lambda_0 = 0$). The most important diffraction orders have been marked with an arrow to facilitate their visualization. and their space and time indexes (m, n) have been included to know their nature.

Thus, Fig. 9(a) depicts the diffraction pattern of a monochromatic wave that impinges in the spatiotemporal metasurface under oblique TM incidence ($\theta_0 = 40^{\rm o}$). Note how, in the upper part of the transmission plane ($y/\lambda_0 > 0$), the diffraction angles must be similar to the time-only case since the $(m = 0, n)$-th harmonics are implied. However, in this manuscript, the beamformer capabilities have been increased since the arising of the new space-time harmonics in the lower part of the transmission diagram ($y/\lambda_0 < 0$). In these examples, it is noticeable the emerging of the $(-1, n)$-th harmonics.

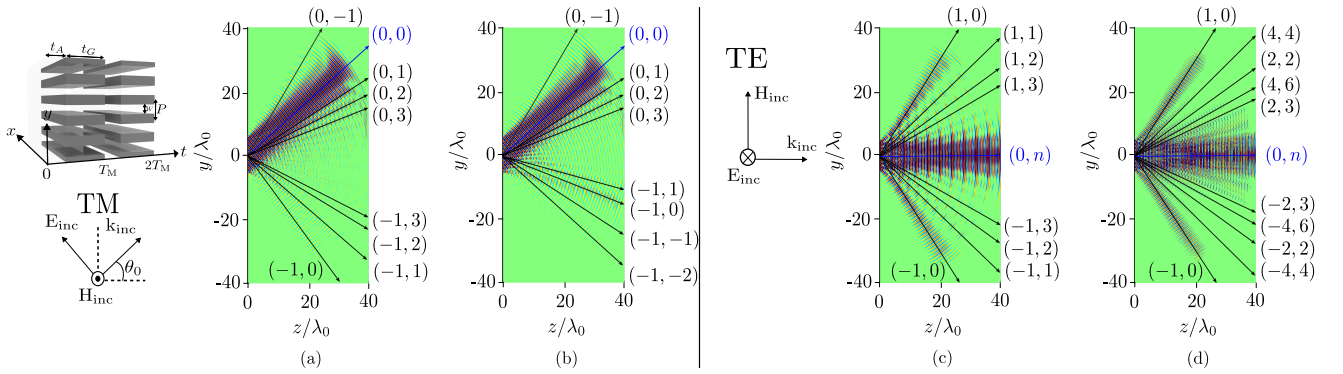

Figure 9. (a)-(b) Diffraction patterns of the A-G configuration under oblique TM incidence ($\theta_0 = 40^o$): (a) $T_M = 4T_0$ and $P = 0.7\lambda_0$. (b) Different spatial period: $P = \lambda_0$. Fixed parameters: $t_A = [0,\ 0.25T_M]$, $t_G = [0.25T_M,\ T_M]$, $W = 0.5P$. (c)-(d) Diffraction patterns of the A-G configuration under normal TE incidence: (c) $T_M = 4T_0$ and $P = 1.2\lambda_0$. (d) Different temporal period: $T_M = T_0$. Fixed parameters: $t_A = [0,\ 0.25T_M]$, $t_G = [0.25T_M,\ T_M]$, $W = 0.6P$.

Fig. 9(b) shows the same scenario but with a slight increase of spatial period (from $P = 0.7\lambda_0$ to $P = \lambda_0$). The rest of the parameters, $T_M = 4T_0$, $W = 0.5P$ and $D = 0.25$, are kept fixed. Fig. 9(b) illustrates how $(m = -1, n)$-th harmonics approach the normal as the spatial period P and the temporal index n increase. This is well predicted by eq. (15b). Moreover, notice how the temporal $(m = 0, n)$-th harmonics are not affected by a change in the spatial period, since the temporal period is the same in both Figs. 9(a) and 9(b).

In contrast, Figs. 9(c)-(d) depict the phenomenology when the temporal period is modified. For simplicity, TE normal incidence is assumed and slit width is increased to $W = 0.6P$ in order to achieve a higher transmission. Furthermore, a spatial period greater than the wavelength of the incident wave is imposed to enrich the diffraction diagram since the first (spatial) grating lobes are excited. Fig. 9(c) shows the diffraction pattern for the same time period as considered throughout the previous section of the manuscript ($T_M = 4T_0$). In this case, a symmetric pattern is appreciated where the temporal $(0, n)$-th harmonics are in the same direction ($\theta_{0n} = 0^o$). Moreover, all the $(0, n)$-th harmonics are propagative due to their temporal nature and the normal incidence conditions. However, since spatial modulation has been included, new spatiotemporal harmonics emerge symmetrically at both the upper and lower parts of the diagram. Finally, in Fig. 9(d), it is observed how the higher-order (m, n)-th harmonics approach to the normal when the temporal period is reduced (from $T_M = 4T_0$ to $T_M = T_0$), as it was predicted in Section II D.

Table I provides a comparison of the diffraction angles for the previous cases shown in Fig. 9. They have been extracted with the analytical approach [by means of eq. (15b)] and the FDTD method. A good agreement is appreciated between the analytical and numerical results.

Frequency-mixing phenomena can be appreciated in Figs. 9(c) and 9(d) as well. As discussed in Section III C, two different space-time modulations can lead to different output frequencies while maintaining the same diffraction angle. This is case for the diffraction orders ($m = 1$, $n = 1$) in Fig. 9(c) and ($m' = 4$, $n' = 4$) in Fig. 9(d). Both diffraction orders have associated the same diffraction angle ($\theta_{11} = \theta_{4'4'} = 41.77^o$) but different output frequencies ($\omega_{n=1} = 1.25\omega_0$, $\omega_{n'=4} = 5\omega_0$). In a general case, eqs. (37) and (38) can be applied in the design of frequency mixers under oblique and normal incidence, respectively, by simply tuning the space-time parameters of the modulation. The key parameter in design is the time period, as the spatial period cannot be easily reconfigured electronically in the current metastructure. Without loss of generality, with this scenario, achieving the demodulation of the same signal by users located in different positions would be possible, which is highly interesting for applications in mobile or satellite communications. The present discussion opens the way to the design of spatiotemporal frequency mixers based on aperiodic metallic structures, which are expected to provide more degrees of freedom in design and ease of control than purely-periodic metallic ones [33].

E. Reflective Beamformer

In this subsection we test the tunability of the reflection coefficient for the C-G beamformer. Fig. 10 depicts the analysis of the reflection coefficient as a function of the frequency of the incident wave when the temporal $T_M = 4T_0$ ($f_0 = 4f_M$) and spatial $P = 10$ mm periods are fixed. Note that, in the present scenario, frequency of the modulation increases as the frequency of the incident wave does. Thus, the ratio f_0/f_M is fixed to a value of four.

The main advantage that the analytical approach contributes is the faster extraction of the scattering parameter for different points in frequency. Note that, the simulations carried out by means of the FDTD method [assuming a monochromatic impinging wave] takes several minutes depending on the mesh and the simulation space. However, the circuital approach takes only a few seconds

TABLE I. Diffraction angles obtained for each (m, n)-th harmonic using the FDTD and analytical method for the cases shown in Fig. 9.

	Incidence	$\theta_{mn}(^\circ)$	Analytical	FDTD
$T_\mathrm{M}=4T_0$ $P=0.7\lambda_0$	$\theta_0^\mathrm{TM}=40^\circ$	θ_{0-1}	58.98	58.17
		θ_{00}	40.00	40.36
		θ_{01}	30.94	31.27
		θ_{02}	25.37	25.40
		θ_{03}	21.54	20.38
		θ_{-13}	−26.64	−25.98
		θ_{-12}	−31.54	−30.20
		θ_{-1-1}	−38.89	−39.43
		θ_{-10}	−51.70	−52.40
$T_\mathrm{M}=4T_0$ $P=\lambda_0$	$\theta_0^\mathrm{TM}=40^\circ$	θ_{0-1}	58.98	58.17
		θ_{00}	40.00	40.36
		θ_{01}	30.94	31.27
		θ_{02}	25.37	25.40
		θ_{03}	21.54	20.38
		θ_{-11}	−16.57	−15.28
		θ_{-10}	−20.88	−21.18
		θ_{-1-1}	−28.38	−31.38
		θ_{-1-2}	−45.48	−41.50
$T_\mathrm{M}=4T_0$ $P=1.2\lambda_0$	$\theta_0^\mathrm{TE}=0^\circ$	$\theta_{\pm10}$	±56.38	±56.37
		$\theta_{\pm11}$	±41.77	±42.61
		$\theta_{\pm12}$	±33.72	±34.41
		$\theta_{\pm13}$	±28.41	28.7
$T_\mathrm{M}=T_0$ $P=1.2\lambda_0$	$\theta_0^\mathrm{TE}=0^\circ$	$\theta_{\pm10}$	±56.38	±55.98
		$\theta_{\pm44}$	±41.77	±43.15
		$\theta_{\pm22}$	±33.72	±34.31
		$\theta_{\pm46}$	±28.41	27.99
		$\theta_{\pm23}$	±24.60	23.82

to simulate the whole frequency range.

Fig. 10(a) shows the curves obtained by the proposed analytical method for the reflection coefficient $|S_{11}|$ when varying the duty cycle D. In this case, DT_M represents the time in which the C-G metasurface is in the conductor state. FDTD simulations of the electric-field distributions are also included as insets. The black, blue and red solid lines are associated to the duty cycle $D = 0.75$, $D = 0.5$ and $D = 0.25$, respectively. It can be seen how the amplitude of the reflection coefficient decreases as the space-time metasurface remains less time in the conductor (fully reflective) state; namely, as D decreases. This is in line with the former theoretical discussion and with the FDTD results inserted in Fig. 10(a). Moreover, the oblique incident angle ($\theta_0 = 20^\circ$) leads to the emerging

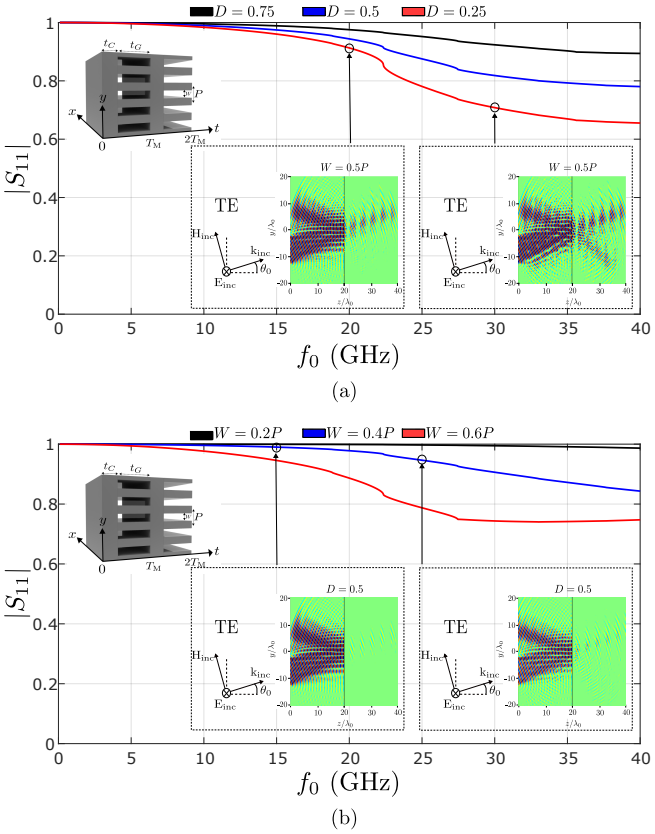

Figure 10. Reflection coefficient as a function of the frequency of the incident wave for the C-G configuration. (a) When varying the duty cycle. (b) When varying the spatial dimension ratio. TE oblique incidence ($\theta_0 = 20^\circ$) is considered. Fixed parameters: $P = 10$ mm, $T_\mathrm{M} = 4T_0$.

of the grating lobe approximately at 23 GHz. This phenomenology is well caught by the circuital approach. It can be also appreciated in the FDTD results, as the grating lobes make appearance at 30 GHz (see the lower half space) but do not show at 20 GHz, below the grating-lobe regime. Finally, Fig. 10(b) shows the amplitude of the reflection coefficient in the case of varying the spatial ratio W/P and fixing the duty cycle. In this case, less reflection is observed as the spatial ratio (slit width W) increases.

A crucial difference related to these two parameters should be noted. The modification of D and W is useful to adjust the reflection coefficient of the system, as explained in this section. However, as discussed in Section III A, the harmonic distribution of the diffraction pattern is also affected. Nevertheless, the majority of (m, n)-th harmonics that can attain significant amplitudes when varying W are of evanescent nature. This is not an issue from the beamforming perspective, since this parameter remains fixed in the grating state. On the other hand, when D is modified, many of these (m, n)-th harmonics that can attain significant amplitudes will be propagative. Thus, this property of the temporal param-

eters turns them into the best option for adjusting the beamsteering of the system. Therefore, the best choice for setting the reflection and transmission coefficients of the system is selecting the proper configuration (A-G or C-G), as expected. This feature is very interesting for future wireless communications where the communication at both sides of the device is desired [72].

Finally, the efficiency of the proposed analytical method is noteworthy. The computational times associated with our analytical (circuit-based) approach are much lower compared to other numerical techniques. Computation time is less than a second here, while FDTD and other numerical approaches normally take minutes to provide the solution. From a practical perspective, our approach is an efficient method that can be used as a surrogate model to be combined with external optimization or artificial intelligence techniques for an efficient design of future metal-based space-time metastructures.

Although the experimental part is beyond the scope of the paper, it is worth mentioning some of the challenges that a future implementation of the space-time metasurface will face. Naturally, an interesting alternative in the microwaves is the use of PIN and varactor diodes. Some alternatives of this kind can be found in the literature. Switching times and related transients between ON and OFF states in PIN diodes and varactors are indeed one of the main technological challenges. From the theoretical side, we are extending the analytical framework to include the complete circuit model of these active elements [73] (including parasitic effects at higher frequencies). In the low-THz regime, a more exotic alternative could be the use of graphene. Blue and red strips in Fig. 1 could be treated as biased elements at different voltages, thus giving the air and conductor responses. Optical pumping could be an alternative too [74, 75]. The performance of a future prototype will then be validated experimentally in an anechoic chamber and an optic table. The main task will be to check the beamsteering and frequency mixing capabilities of the space-time metasurface by measuring the transmission and reflection coefficients and the diffracted angles with any of the combinations of the three states: air, conductor and grating.

IV. CONCLUSIONS

In this manuscript, we have introduced a novel metal-based spatiotemporal metasurface for application in wireless communications systems. The metasurface can alternate its properties in time within three different states: "air" (fully transparent), "conductor" (fully reflective) and "grating" (partially transparent and reflective). By combining the three states in a time-periodic scheme, a rich diffraction pattern is created, which can be electronically reconfigured by setting the space-time parameters of the system.

The physics of the space-time metasurface is described by means of an analytical technique based on equivalent circuits, Floquet-Bloch expansions and integral equations. We have considered scenarios where the metasurface is illuminated by oblique TE and TM plane waves. The analytical technique has proven to be computationally efficient compared to general numerical approaches and the self-implemented FDTD code. Moreover, it provides physical insight on the diffraction spectrum, nature (evanescent/propagative) of the space-time Floquet harmonics, and scattering parameters.

The results of the work show that the present space-time metasurface offer clear advantages compared to our previous time-only configuration. Here, we have exploited the inherent ability of the space-time metasurface to mix and multiply frequencies. We have shown that two or more output frequencies can be engineered so their diffraction angles is the same. Finally, we have shown that efficient beamforming can be realized by tuning the space-time parameters of the system. Combinations of the conductor and grating states are prone to smartly reflect most of the diffracted power. Conversely, combinations of the air and grating states can enable effiecient beamforming in transmission.

ACKNOWLEDGMENTS

This work has been supported by grant TED2021-129938B-I00 funded by MCIN/AEI/10.13039/501100011033 and by the European Union NextGenerationEU/PRTR. It has also been supported by grants PID2020-112545RB-C54, PDC2022-133900-I00, and PDC2023-145862-I00, funded by MCIN/AEI/10.13039/501100011033 and by the European Union NextGenerationEU/PRTR. It is also part of the grant IJC2020-043599-I funded by MICIU/AEI/10.13039/501100011033 and by European Union NextGenerationEU/PRTR..

APPENDIX A

The analytical results have been compared with a self-implemented 2D finite-difference time-domain (FDTD) method based on a staggered grid scheme. Two independent codes have been programmed for TE and TM incidences. For an impinging TE-polarized wave (E_x, H_y, H_z), the space-time-varying boundary conditions in the metallic regions of the metasurface (placed in z_{pos}) are enforced as $E_x = 0$ in both conductor and grating states. For TM incidence (E_y, E_z, H_x), the space-time-varying boundary conditions in the metallic regions are enforced as $E_y = 0$. Second-order Engquist-Majda relations have been implemented as absorbing boundary conditions at the outer limits of the simulation box. The rest of parameters that are involved in the FDTD simulations are: uniform mesh grid with $\Delta y = \Delta z = \frac{\lambda_0}{35}$; time step of $\Delta t = C \cdot \frac{\Delta z}{c}$, with $C = 0.5$ being the CFL sta-

bility condition parameter. To model the zero-thickness metasurface, a homogeneous slab with a thickness less than $0.1\lambda_0$ has been considered.

[1] F. Falcone, T. Lopetegi, J. D. Baena, R. Marqués, F. Martín, and M. Sorolla, Effective negative-/spl epsiv/stopband microstrip lines based on complementary split ring resonators, IEEE microwave and wireless components letters **14**, 280 (2004).

[2] O. Quevedo-Teruel, H. Chen, A. Díaz-Rubio, G. Gok, A. Grbic, G. Minatti, E. Martini, S. Maci, G. V. Eleftheriades, M. Chen, *et al.*, Roadmap on metasurfaces, Journal of Optics **21**, 073002 (2019).

[3] E. Martini and S. Maci, Theory, analysis, and design of metasurfaces for smart radio environments, Proceedings of the IEEE **110**, 1227 (2022).

[4] Y. Ra'di, C. R. Simovski, and S. A. Tretyakov, Thin perfect absorbers for electromagnetic waves: theory, design, and realizations, Physical Review Applied **3**, 037001 (2015).

[5] C. Pfeiffer and A. Grbic, Metamaterial huygens' surfaces: tailoring wave fronts with reflectionless sheets, Physical review letters **110**, 197401 (2013).

[6] C. Caloz, A. Lai, and T. Itoh, Wave interactions in a left-handed mushroom structure, in *IEEE Antennas and Propagation Society Symposium, 2004.*, Vol. 2 (IEEE, 2004) pp. 1403–1406.

[7] F. R. Morgenthaler, Velocity modulation of electromagnetic waves, IRE Transactions on microwave theory and techniques **6**, 167 (1958).

[8] J. R. Zurita-Sánchez, P. Halevi, and J. C. Cervantes-González, Reflection and transmission of a wave incident on a slab with a time-periodic dielectric function $\varepsilon(t)$, Physical Review A **79**, 053821 (2009).

[9] C. Caloz and Z.-L. Deck-Léger, Spacetime metamaterials—part i: general concepts, IEEE Transactions on Antennas and Propagation **68**, 1569 (2019).

[10] C. Caloz and Z.-L. Deck-Leger, Spacetime metamaterials—part ii: theory and applications, IEEE Transactions on Antennas and Propagation **68**, 1583 (2019).

[11] V. Pacheco-Peña, D. M. Solís, and N. Engheta, Time-varying electromagnetic media: opinion, Optical Materials Express **12**, 3829 (2022).

[12] A. M. Shaltout, V. M. Shalaev, and M. L. Brongersma, Spatiotemporal light control with active metasurfaces, Science **364**, eaat3100 (2019).

[13] T. J. Cui, M. Q. Qi, X. Wan, J. Zhao, and Q. Cheng, Coding metamaterials, digital metamaterials and programmable metamaterials, Light: science & applications **3**, e218 (2014).

[14] V. Pacheco-Peña and N. Engheta, Temporal aiming, Light: Science & Applications **9**, 129 (2020).

[15] N. Reiskarimian and H. Krishnaswamy, Magnetic-free non-reciprocity based on staggered commutation, Nature communications **7**, 11217 (2016).

[16] S. Taravati, N. Chamanara, and C. Caloz, Nonreciprocal electromagnetic scattering from a periodically space-time modulated slab and application to a quasisonic isolator, Physical Review B **96**, 165144 (2017).

[17] N. A. Estep, D. L. Sounas, J. Soric, and A. Alu, Magnetic-free non-reciprocity and isolation based on parametrically modulated coupled-resonator loops, Nature Physics **10**, 923 (2014).

[18] S. Taravati and G. V. Eleftheriades, Full-duplex nonreciprocal beam steering by time-modulated phase-gradient metasurfaces, Physical Review Applied **14**, 014027 (2020).

[19] Z. Wu, C. Scarborough, and A. Grbic, Space-time-modulated metasurfaces with spatial discretization: Free-space n-path systems, Physical Review Applied **14**, 064060 (2020).

[20] N. Engheta, Four-dimensional optics using time-varying metamaterials, Science **379**, 1190 (2023).

[21] E. Mikheeva, C. Kyrou, F. Bentata, S. Khadir, S. Cueff, and P. Genevet, Space and time modulations of light with metasurfaces: recent progress and future prospects, ACS photonics **9**, 1458 (2022).

[22] S. Taravati and G. V. Eleftheriades, Generalized space-time-periodic diffraction gratings: Theory and applications, Physical Review Applied **12**, 024026 (2019).

[23] E. Galiffi, R. Tirole, S. Yin, H. Li, S. Vezzoli, P. A. Huidobro, M. G. Silveirinha, R. Sapienza, A. Alù, and J. Pendry, Photonics of time-varying media, Advanced Photonics **4**, 014002 (2022).

[24] J. Gaxiola-Luna and P. Halevi, Growing fields in a temporal photonic (time) crystal with a square profile of the permittivity ε (t), Applied Physics Letters **122** (2023).

[25] X. Wu, X. Liu, M. D. Hickle, D. Peroulis, J. S. Gómez-Díaz, and A. Á. Melcón, Isolating bandpass filters using time-modulated resonators, IEEE Transactions on Microwave Theory and Techniques **67**, 2331 (2019).

[26] X. Wang, V. S. Asadchy, S. Fan, and S. A. Tretyakov, Space–time metasurfaces for power combining of waves, ACS Photonics **8**, 3034 (2021).

[27] S. Yin and A. Alu, Efficient phase conjugation in a space-time leaky waveguide, ACS Photonics **9**, 979 (2022).

[28] V. Pacheco-Peña, M. Fink, and N. Engheta, Temporal chirp, temporal lensing and temporal routing via space-time interfaces, arXiv preprint arXiv:2311.10855 (2023).

[29] Z. Li, X. Ma, A. Bahrami, Z.-L. Deck-Léger, and C. Caloz, Space-time fresnel prism, Physical Review Applied **20**, 054029 (2023).

[30] X. Zhou and A. S. Daryoush, An efficient self-oscillating mixer for communications, IEEE transactions on microwave theory and techniques **42**, 1858 (1994).

[31] Z. Tang, Y. Li, J. Yao, and S. Pan, Photonics-based microwave frequency mixing: methodology and applications, Laser & Photonics Reviews **14**, 1800350 (2020).

[32] S. Liu, P. P. Vabishchevich, A. Vaskin, J. L. Reno, G. A. Keeler, M. B. Sinclair, I. Staude, and I. Brener, An all-dielectric metasurface as a broadband optical frequency mixer, Nature communications **9**, 2507 (2018).

[33] S. Taravati, Aperiodic space-time modulation for pure frequency mixing, Physical Review B **97**, 115131 (2018).

[34] S. Taravati and C. Caloz, Mixer-duplexer-antenna leaky-wave system based on periodic space-time modulation, IEEE transactions on antennas and propagation **65**, 442 (2016).

[35] J. Zang, A. Alvarez-Melcon, and J. Gomez-Diaz, Nonreciprocal phased-array antennas, Physical review applied **12**, 054008 (2019).

[36] S. Taravati and G. V. Eleftheriades, Microwave space-time-modulated metasurfaces, ACS Photonics **9**, 305 (2022).

[37] G.-B. Wu, J. Y. Dai, Q. Cheng, T. J. Cui, and C. H. Chan, Sideband-free space–time-coding metasurface antennas, Nature electronics **5**, 808 (2022).

[38] S. Vosoughitabar and C.-T. M. Wu, Programming nonreciprocity and harmonic beam steering via a digitally space-time-coded metamaterial antenna, Scientific Reports **13**, 7338 (2023).

[39] S. A. Stewart, T. J. Smy, and S. Gupta, Finite-difference time-domain modeling of space–time-modulated metasurfaces, IEEE Transactions on Antennas and Propagation **66**, 281 (2017).

[40] Q. Zhao and C. D. Sarris, Space–time adaptive modeling and shape optimization of microwave structures with applications to metasurface design, IEEE Transactions on Microwave Theory and Techniques **70**, 5440 (2022).

[41] Y. Vahabzadeh, N. Chamanara, and C. Caloz, Generalized sheet transition condition FDTD simulation of metasurface, IEEE Transactions on Antennas and Propagation **66**, 271 (2017).

[42] V. Tiukuvaara, T. J. Smy, and S. Gupta, Floquet analysis of space-time modulated metasurfaces with lorentz dispersion, IEEE Transactions on Antennas and Propagation **69**, 7667 (2021).

[43] Y. Khorrami, D. Fathi, A. Khavasi, and R. C. Rumpf, Dynamical control of multilayer spacetime structures using extended fourier modal method, IEEE Photonics Journal **13**, 1 (2021).

[44] M. Rahmanzadeh, B. Rejaei, and A. Khavasi, Analysis of electromagnetic scattering from array of time-modulated graphene ribbons, Optics Express **31**, 21739 (2023).

[45] C. Scarborough and A. Grbic, Accelerated n-path network analysis using the floquet scattering matrix method, IEEE Transactions on Microwave Theory and Techniques **68**, 1248 (2020).

[46] P. A. Huidobro, M. G. Silveirinha, E. Galiffi, and J. Pendry, Homogenization theory of space-time metamaterials, Physical Review Applied **16**, 014044 (2021).

[47] M. Mostafa, A. Díaz-Rubio, M. Mirmoosa, and S. Tretyakov, Coherently time-varying metasurfaces, Physical Review Applied **17**, 064048 (2022).

[48] K. Pham and A. Maurel, Diffraction grating with space-time modulation, Journal of Computational Physics **469**, 111528 (2022).

[49] R. Rodriguez-Berral, C. Molero, F. Medina, and F. Mesa, Analytical wideband model for strip/slit gratings loaded with dielectric slabs, IEEE transactions on microwave theory and techniques **60**, 3908 (2012).

[50] C. Molero, A. Alex-Amor, F. Mesa, A. Palomares-Caballero, and P. Padilla, Cross-polarization control in fsss by means of an equivalent circuit approach, IEEE Access **9**, 99513 (2021).

[51] A. Alex-Amor, S. Moreno-Rodríguez, P. Padilla, J. F. Valenzuela-Valdés, and C. Molero, Analytical equivalent circuits for three-dimensional metamaterials and metagratings, Physical Review Applied **20**, 044010 (2023).

[52] A. Alex-Amor, S. Moreno-Rodríguez, P. Padilla, J. F. Valenzuela-Valdés, and C. Molero, Diffraction phenomena in time-varying metal-based metasurfaces, Physical Review Applied **19**, 044014 (2023).

[53] S. Moreno-Rodríguez, A. Alex-Amor, P. Padilla, J. F. Valenzuela-Valdés, and C. Molero, Time-periodic metallic metamaterials defined by floquet circuits, IEEE Access (2023).

[54] A. Alex-Amor, C. Molero, and M. G. Silveirinha, Analysis of metallic space-time gratings using lorentz transformations, Phys. Rev. Appl. **20**, 014063 (2023).

[55] L. Stefanini, D. Ramaccia, A. Toscano, and F. Bilotti, Temporal rainbow scattering at boundary-induced time interfaces, Applied Physics Letters **122** (2023).

[56] X. Fang, M. Li, Z. Lai, D. Ramaccia, A. Toscano, F. Bilotti, and D. Ding, Multifunctional space–time-modulated metasurface for direction of arrival estimation and rcs manipulation in a single system, IEEE Transactions on Microwave Theory and Techniques (2023).

[57] V. G. Ataloglou, S. Taravati, and G. V. Eleftheriades, Metasurfaces: physics and applications in wireless communications, National Science Review **10**, nwad164 (2023).

[58] L. Zhang, X. Q. Chen, S. Liu, Q. Zhang, J. Zhao, J. Y. Dai, G. D. Bai, X. Wan, Q. Cheng, G. Castaldi, *et al.*, Space-time-coding digital metasurfaces, Nature communications **9**, 4334 (2018).

[59] L. Zhang, Z. X. Wang, R. W. Shao, J. L. Shen, X. Q. Chen, X. Wan, Q. Cheng, and T. J. Cui, Dynamically realizing arbitrary multi-bit programmable phases using a 2-bit time-domain coding metasurface, IEEE Transactions on Antennas and Propagation **68**, 2984 (2019).

[60] X. Fang, M. Li, S. Li, D. Ramaccia, A. Toscano, F. Bilotti, and D. Ding, Diverse frequency time modulation for passive false target spoofing: design and experiment, IEEE Transactions on Microwave Theory and Techniques (2023).

[61] A. E. Cardin, S. R. Silva, S. R. Vardeny, W. J. Padilla, A. Saxena, A. J. Taylor, W. J. Kort-Kamp, H.-T. Chen, D. A. Dalvit, and A. K. Azad, Surface-wave-assisted nonreciprocity in spatio-temporally modulated metasurfaces, Nature communications **11**, 1469 (2020).

[62] Z. Liu, Z. Li, and K. Aydin, Time-varying metasurfaces based on graphene microribbon arrays, Acs Photonics **3**, 2035 (2016).

[63] X. Wang, A. Diaz-Rubio, H. Li, S. A. Tretyakov, and A. Alu, Theory and design of multifunctional space-time metasurfaces, Physical Review Applied **13**, 044040 (2020).

[64] N. Kinsey, C. DeVault, J. Kim, M. Ferrera, V. Shalaev, and A. Boltasseva, Epsilon-near-zero al-doped zno for ultrafast switching at telecom wavelengths, Optica **2**, 616 (2015).

[65] R. Rodriguez-Berral, F. Medina, F. Mesa, and M. Garcia-Vigueras, Quasi-analytical modeling of transmission/reflection in strip/slit gratings loaded with dielectric slabs, IEEE transactions on microwave theory and techniques **60**, 405 (2012).

[66] R. Dubrovka, J. Vazquez, C. Parini, and D. Moore, Equivalent circuit method for analysis and synthesis of frequency selective surfaces, IEE Proceedings-Microwaves, Antennas and Propagation **153**, 213 (2006).

[67] R. Rodriguez-Berral, F. Mesa, and F. Medina, Analytical multimodal network approach for 2-d arrays of planar patches/apertures embedded in a layered medium, IEEE Transactions on Antennas and Propagation **63**, 1969 (2015).

[68] C. Molero, Á. Palomares-Caballero, A. Alex-Amor, I. Parellada-Serrano, F. Gamiz, P. Padilla, and J. F. Valenzuela-Valdés, Metamaterial-based reconfigurable intelligent surface: 3d meta-atoms controlled by graphene structures, IEEE Communications Magazine **59**, 42 (2021).

[69] F. Mesa, R. Rodriguez-Berral, and F. Medina, Unlocking complexity using the eca: The equivalent circuit model as an efficient and physically insightful tool for microwave engineering, IEEE Microwave Magazine **19**, 44 (2018).

[70] L. Li, H. Zhao, C. Liu, L. Li, and T. J. Cui, Intelligent metasurfaces: control, communication and computing, Elight **2**, 7 (2022).

[71] A. Alex-Amor, F. Mesa, Á. Palomares-Caballero, C. Molero, and P. Padilla, Exploring the potential of the multi-modal equivalent circuit approach for stacks of 2-d aperture arrays, IEEE Transactions on Antennas and Propagation **69**, 6453 (2021).

[72] S. Zhang, H. Zhang, B. Di, Y. Tan, M. Di Renzo, Z. Han, H. V. Poor, and L. Song, Intelligent omni-surfaces: Ubiquitous wireless transmission by reflective-refractive metasurfaces, IEEE Transactions on Wireless Communications **21**, 219 (2021).

[73] M. Pérez-Escribano, S. Moreno-Rodríguez, C. Molero, J. F. Valenzuela-Valdés, P. Padilla, and A. Alex-Amor, Analytical framework to model reconfigurable metasurfaces including lumped elements, IEEE Transactions on Circuits and Systems II: Express Briefs (2023).

[74] A. C. Tasolamprou, A. D. Koulouklidis, C. Daskalaki, C. P. Mavidis, G. Kenanakis, G. Deligeorgis, Z. Viskadourakis, P. Kuzhir, S. Tzortzakis, M. Kafesaki, *et al.*, Experimental demonstration of ultrafast thz modulation in a graphene-based thin film absorber through negative photoinduced conductivity, ACS photonics **6**, 720 (2019).

[75] W. He, M. Tong, Z. Xu, Y. Hu, T. Jiang, *et al.*, Ultrafast all-optical terahertz modulation based on an inverse-designed metasurface, Photonics Research **9**, 1099 (2021).

2.4 Material Characterization

2.4.1 Reference-Plane Invariant Free Space Dielectric Material Characterization up to 330 GHz

In this contribution to an international congress, we outline the steps taken to characterize dielectric materials across the entire mmWave frequency range using a non-iterative and reference-plane invariant method. The measurement setup involves a free-space configuration with two facing horn antennas. Thru-Reflect-Line(TRL) and Gated-Reflect-Line (GRL) calibration methods along with Savitzky-Golay filters have been utilized to accurately extract and refine the scattering parameters. Furthermore, in extracting the constitutive parameters of the glass fiber and quartz slice, we have applied the classical Nicholson-Ross-Weir (NRW) and Baker-Jarvis (BJ) techniques. The results reveal a stable response across the entire frequency range, except for areas where resonances occur. Correctly addressing the resonances and managing the available power would enable the characterization of more complex materials with magnetic properties.

THIS IS A POSTPRINT VERSION OF THE PAPER:

S. Moreno-Rodríguez, M. Pérez-Escribano, S. Ortiz-Ruiz, A. Alex-Amor, B. Plaza-Gallardo, Francisco G. Ruiz, and C. Molero, "Reference-Plane Invariant Free Space Dielectric Material Characterization up to 330 GHz," *2024 4th URSI Atlantic Radio Science Meeting (AT-RASC)*, Meloneras, Spain, 2024.

Disclaimer:
This work has been published in 2024 4th URSI Atlantic Radio Science Meeting (AT-RASC)
DOI: 10.46620/URSIATRASC24/QSAS1331

4th URSI AT-RASC, Gran Canaria, 19 – 24 May 2024

Reference-Plane Invariant Free Space Dielectric Material Characterization up to 330 GHz

Salvador Moreno-Rodríguez[(1)], Mario Pérez-Escribano[(2)], Sergio Ortiz-Ruiz[(3)],
Antonio Alex-Amor[(4)], Borja Plaza-Gallardo[(5)], Francisco G. Ruiz[(3)] and Carlos Molero[(1)]
(1) Department of Signal Theory, Telematics and Communications,
Research Centre for Information and Communication Technologies (CITIC-UGR), University of Granada, Granada, Spain
(2) Telecommunication Research Institute (TELMA), Universidad de Málaga,
E.T.S. Ingeniería de Telecomunicación, 29010 Málaga, Spain
(3) Pervasive Electronics Advanced Research Laboratory (PEARL), Department of Electronics and Computer Science,
University of Granada, 18071 Granada, Spain
(4) University of Pennsylvania, Department of Electrical and Systems Engineering,
Philadelphia, Pennsylvania 19104, United States
(5) Radiofrequency Area, National Institute for Aerospace Technology (INTA), Madrid, Spain

Abstract

This paper describes the process followed to implement a system to characterize the complex permittivity of materials in the 10-330 GHz frequency band. Firstly, the method used and the system's calibration process are shown, consisting of a double calibration TRL (Thru-Reflect-Line) and GRL (Gated-Reflect-Line). Subsequently, a smoothing technique is used to improve the accuracy of the results. Finally, a test is performed on quartz and glass fiber samples, showing that the results are quite reliable over the entire measured bandwidth.

1 Introduction

In the communications industry, various materials are employed to design and manufacture devices. These materials exhibit diversity and can be tailored for specific purposes such as developing radiating, absorbing [1], or reflecting devices [2], among others. However, properly utilizing these materials requires a foundational understanding of their electromagnetic properties [3]. Notably, electrical permittivity and magnetic permeability play significant roles for non-conductive materials. Both are intricate parameters that distinctly elucidate the behavior of these materials in the presence of an electromagnetic field.

Traditionally, two main characterization methods can be found in the literature. On the one hand, resonant methods [4, 5] use cavity resonances to extract material properties at specific frequencies. These methods are highly accurate, although they have the disadvantage of providing a set of solutions in a discrete domain of frequencies corresponding to those at which resonances occur within a cavity. On the other hand, non-resonant or broadband methods [6] have traditionally been based on measurements of reflection and transmission of the material in free space. A notable approach in this category is the Nicolson-Ross-Weir (NRW) method [7], ideally functioning across an infinite bandwidth but practically limited by the transmission system of the waveguide and antenna. The challenge with such methods lies in demanding a high degree of alignment accuracy and the application of calibration techniques to isolate sample effects concerning propagation in free space. In this context, Baker-Jarvis et al. introduced a method in 1990 enabling the extraction of material characteristics from sample measurements [8]. This method requires precise knowledge of the distance between calibration planes and the sample thickness for accurate results. In recent years, with the new 5G and 6G frequency bands, the characterization of materials in bands beyond 100 GHz has become an interesting topic for researchers [9].

Generally, techniques for extracting material properties are further divided into three categories. The first one calculates permittivity, ε_r^*, and permeability, μ_r^*, from equations in which the unknowns are variables to be cleared, using transmission media, cavities, or free-space transmission and reflection [10]. The second group comprises genetic, evolutionary, or optimization algorithms and analytical equations [11], which cannot be solved directly. The last group of methods proposes using optimization algorithms using electromagnetic simulators, which try to find similarities between measurements and simulations to study the characteristics of materials [12].

In this contribution, we will use a broadband method based on the measurement in free space and reference-plane invariant, which starts from the solution of analytical equations for estimating the material parameters. Section 2 describes the measurement method, calibration process, and a technique to post-process the achieved results. In Section 3, an experimental validation is carried out with quartz and glass fiber samples in the 10-330 GHz band. Finally, Section 4 details the most important conclusions drawn from the work.

2 Method Description

2.1 Measurement Scheme

The starting point of the measurement method used was proposed in [10], corresponding to a variation of the one proposed in [8]. Specifically, the authors of [10] proposed the use of an air-dielectric coaxial guide, through which a TEM mode is propagated, knowing the distance between antennas perfectly, L_{air}, and the thickness of the material to be characterized, L. From this premise, they proposed a system invariant to the relative position of the material with the reference planes, i.e., in which the material could not be at the center of the transmission line. The main limitation of this method is the need to have an air-filled coaxial guide in which the material samples to be characterized could be inserted. To facilitate the measurement method, this work proposed using a free space measurement scheme, a system composed of horn antennas and lenses that generate a flat wavefront, as shown in the scheme in Fig. 1. In this case, the main difficulty is accurately knowing the air gap L_{air}. For this, it is necessary to address the calibration of the system.

2.2 Calibration

Two methods are proposed to be used together to perform the system calibration. First, a TRL calibration is performed at the end of the waveguide feeding the antenna. For this purpose, an aluminum kit has been designed for the WR-75, WR-51, WR-34, WR-22, and WR-15 standards, consisting of a short circuit, which will act as a reflect, and a 2 mm long line. The rest of the bands are calibrated using the millimeter-wave converter calibration kits, made by Rohde & Schwarz. This method places the reference planes just at the horns' entrance, specifically at the waveguide-horn transition. After the measurement, a free space GRL calibration is performed. Initially proposed in [13], this calibration consists of taking two measures: (i) of the empty sample holder and (ii) of the sample holder holding a metal plate, in which total reflection of the plane wavefront is assumed. A process similar to that followed in the TRL calibration is performed from both measurements. The main difference is that a time-gating process, a convenient technique used in both antenna and communications communities [14], is carried out to isolate the effects of propagation to the sample holder. This gating includes the effects of the antennas and lenses used to form the plane wavefront. After calibration, the reference planes are assumed to be in the material on which the normal incidence of a plane wave is occurring.

2.3 Post-processing

The measurement results are highly affected by spurious signals that can affect the estimation of the material parameters. In this sense, several techniques for smoothing the results to make them more reliable can be found in the literature. One of the most outstanding techniques is the one proposed in [15], using Savitzky-Golay filters. In this case, it has been demonstrated that using these filters is equivalent to, or even more efficient than, using other techniques, such as time-gating, when it comes to reducing possible signal interferences, such as reflections in the measurement system. That is why we have used this type of filter for this contribution, with polynomials of order two and 51-point windows for processing the results.

3 Validation

An experiment was carried out in the 10 to 330 GHz band to validate the proposed methodology. For this purpose, a setup consisting of the Keysight N5247B network analyzer, a set of transitions or frequency extenders, and horn antennas was mounted. In addition, two Greenlight lenses were positioned, with which a flat wavefront was created for frequencies below 50 GHz. Finally, a 0.94 mm thick quartz sample and a 1.22 mm thick glass fiber sample were placed in the center of the optical table without considering that they had to be located at the midpoint between the antennas. Fig. 2 shows a picture of the complete measurement scheme. The measurement process starts by setting the frequency limits of the analyzer and establishing 2001 measurement points with +5 dBm power at the ports and an intermediate frequency bandwidth of 1 kHz. Subsequently, a TRL calibration is performed on the analyzer with the kit mentioned in section 2.2. Once this is done, the antennas are connected and correctly aligned. Finally, placing the sample holder and taking measurements of the same vacuum, with a metal plate and the material to be characterized, is necessary. Once this process is finished, the GRL calibration is performed in MATLAB, allowing isolating the effects of the sample and the empty sample holder. The measured S-parameters of the two samples are shown in Fig. 3. As can be seen, the measurements are quite clean after performing the calibration. In addition, there is good continuity between adjacent bands, which shows that the measurement and calibration process has been completed correctly.

After performing both calibrations, it is time to apply the characterization method. At this point, it is important to note that the thickness of the metal plate used for calibration is slightly greater than that of the material to be measured ($L_{air} = 2$ mm), so we proceed to include this data in the characterization method. The results of the complex relative permittivity are shown in Figs. 4 and 5. As can be seen, they are similar to those expected from these materials. The real part of the permittivity obtained is quite flat and is only affected at points where the sample length coincides with a multiple of the wavelength and resonances that occur. This effect is common in this type of broadband method. The imaginary part, on the other hand, suffers more significant variations due to the position of the sample. When small misalignments occur, or normal incidence is not guaran-

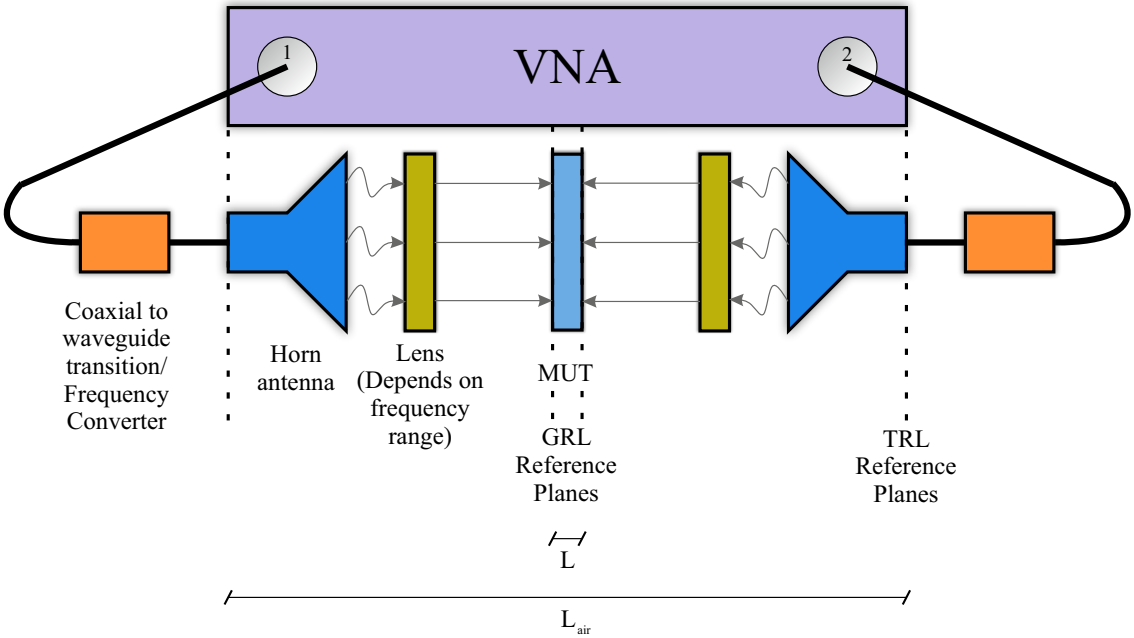

Figure 1. Measurement scheme used for characterization of materials in free space.

Figure 2. Photograph of the setup used for material characterization.

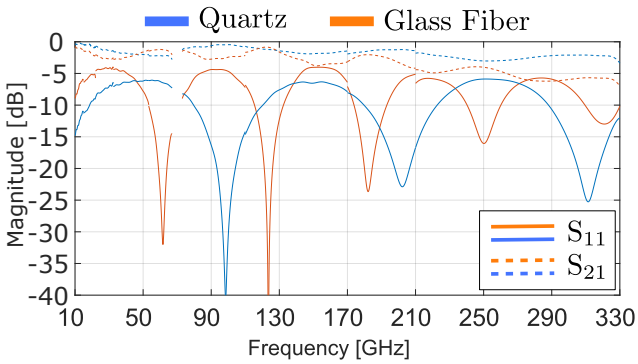

Figure 3. Measured S-parameters of the quartz (blue) and glass fiber (orange) samples, after the calibration process.

teed, the imaginary part, directly related to the losses, is seriously affected, so the estimation deteriorates considerably.

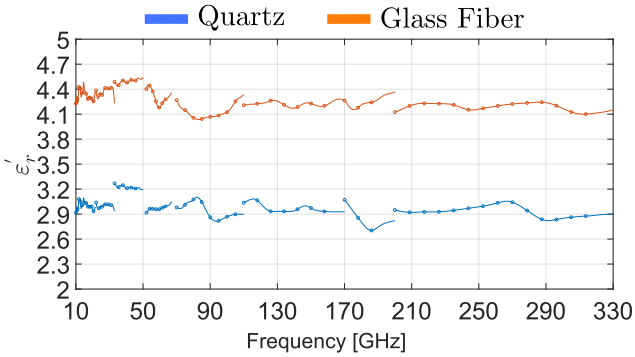

Figure 4. Estimated real part of the effective relative permittivity ($\varepsilon_r^{'}$) of the quartz (blue) and glass fiber (orange) samples.

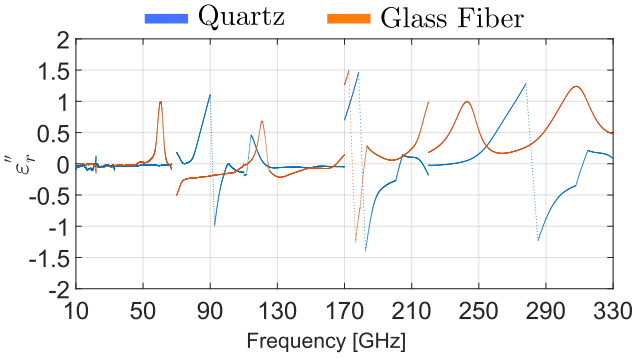

Figure 5. Estimated imaginary part of the effective relative permittivity ($\varepsilon_r^{''}$) of the quartz (blue) and glass fiber (orange) samples.

4 Conclusions

In this work, we have proposed a setup for characterizing materials' complex permittivity from 10 to 330 GHz.

To achieve this, we employed the classical NRW method and the Baker-Jarvis variant to implement a broadband approach invariant to the material's position during the measurement process. Following this, we explored the system's calibration to obtain the estimation. Furthermore, we applied a processing technique to enhance the response at frequency points affected by external factors, such as reflections on the optical table. Lastly, an experimental validation was performed using quartz and glass fiber samples. The results were verified to be accurate across the entire bandwidth.

Acknowledgements

This work has been supported by grant PID2020-112545RB-C54 funded by MCIN/AEI/10.13039/501100011033 and by the European Union NextGenerationEU/PRTR. It has also been supported by grants PDC2022-133900-I00, TED2021-129938B-I00, and TED2021-131699B-I00, and by Ministerio de Universidades and the European Union NextGenerationEU, under Programa Margarita Salas, and by MCIN/AEI/10.13039/501100011033 and the European Union NextGenerationEU/PRTR under grant IJC2020-043599-I.

References

[1] M. Gao, Q. Chen, Y. Zheng, L. Ding, D. Liao, and Y. Fu, "Ultrabroadband absorber based on layered inkjet-printing resistive film," *IEEE Antennas and Wireless Propagation Letters*, vol. 22, no. 2, pp. 228–232, 2023.

[2] A. Palomares-Caballero, C. Molero, P. Padilla, M. García-Vigueras, and R. Gillard, "Wideband 3-d-printed metal-only reflectarray for controlling orthogonal linear polarizations," *IEEE Transactions on Antennas and Propagation*, vol. 71, no. 3, pp. 2247–2258, 2023.

[3] M. Pérez-Escribano and E. Márquez-Segura, "Parameters characterization of dielectric materials samples in microwave and millimeter-wave bands," *IEEE Transactions on Microwave Theory and Techniques*, vol. 69, no. 3, pp. 1723–1732, 2021.

[4] C. Weil, C. Jones, Y. Kantur, and J. Grosvenor, "On rf material characterization in the stripline cavity," *IEEE Transactions on Microwave Theory and Techniques*, vol. 48, no. 2, pp. 266–275, 2000.

[5] M. Santra and K. Limaye, "Estimation of complex permittivity of arbitrary shape and size dielectric samples using cavity measurement technique at microwave frequencies," *IEEE Transactions on Microwave Theory and Techniques*, vol. 53, no. 2, pp. 718–722, 2005.

[6] L. A. Bronckers and A. B. Smolders, "Broadband material characterization method using a cpw with a novel calibration technique," *IEEE Antennas and Wireless Propagation Letters*, vol. 15, pp. 1763–1766, 2016.

[7] A. M. Nicolson and G. F. Ross, "Measurement of the intrinsic properties of materials by time-domain techniques," *IEEE Transactions on Instrumentation and Measurement*, vol. 19, no. 4, pp. 377–382, 1970.

[8] J. Baker-Jarvis, E. Vanzura, and W. Kissick, "Improved technique for determining complex permittivity with the transmission/reflection method," *IEEE Transactions on Microwave Theory and Techniques*, vol. 38, no. 8, pp. 1096–1103, 1990.

[9] M. Shu, X. Shang, N. Ridler, A. R. Calleau, A. I. Dimitriadis, and A. Zhang, "Improvements to millimeter-wave dielectric measurement using material characterization kit (mck)," *IEEE Transactions on Instrumentation and Measurement*, vol. 73, pp. 1–8, 2024.

[10] K. Chalapat, K. Sarvala, J. Li, and G. S. Paraoanu, "Wideband reference-plane invariant method for measuring electromagnetic parameters of materials," *IEEE Transactions on Microwave Theory and Techniques*, vol. 57, no. 9, pp. 2257–2267, 2009.

[11] J. Zhang, M. Y. Koledintseva, J. L. Drewniak, D. J. Pommerenke, R. E. DuBroff, Z. Yang, W. Cheng, K. N. Rozanov, G. Antonini, and A. Orlandi, "Reconstruction of dispersive dielectric properties for PCB substrates using a genetic algorithm," *IEEE Transactions on Electromagnetic Compatibility*, vol. 50, no. 3, pp. 704–714, 2008.

[12] A. Hosseinbeig, S. Marathe, and D. Pommerenke, "Characterization of relative complex permittivity and permeability for magneto-dielectric sheets," *IEEE Transactions on Electromagnetic Compatibility*, vol. 60, no. 6, pp. 1786–1794, 2018.

[13] P. Bartley and S. Begley, "Improved free-space s-parameter calibration," in *2005 IEEE Instrumentation and Measurement Technology Conference Proceedings*, vol. 1, 2005, pp. 372–375.

[14] A. Ramírez-Arroyo, A. Alex-Amor, C. García-García, A. Palomares-Caballero, P. Padilla, and J. F. Valenzuela-Valdés, "Time-gating technique for recreating complex scenarios in 5G systems," *IEEE Access*, vol. 8, pp. 183 583–183 595, 2020.

[15] D. Ma, X. Shang, N. M. Ridler, and W. Wu, "Assessing the impact of data filtering techniques on material characterization at millimeter-wave frequencies," *IEEE Transactions on Instrumentation and Measurement*, vol. 70, pp. 1–4, 2021.

Chapter 3

Conclusions and Future Work

This Doctoral Thesis has focused on the development of metamaterials for communications in the mmWave bands. Throughout this document, various techniques and prototypes have been proposed for the simulation, characterization, and validation of spacetime metamaterials. This final chapter summarizes the conclusions extracted from these studies and introduces potential future directions to continue this line of research.

3.1 Main Conclusions

The main conclusions to be highlighted from each work are listed below:

- In [J1], we presented a rotationally symmetric Fresnel lens-antenna operating at 60 GHz. The T-shaped design of the unit cell allows the construction of the lens in a plane as well as the tuning of the relative permittivity achieving lower values compared with the literature. The validation of the low-cost 3D printing technique for the manufacturing is corroborated since the measured results show good agreement with the simulations. Furthermore, the measurements demonstrate the capability of the lens to change the pointing angle for beam steering applications with a scanning loss of 0.18 dB/^{o}.

- Regarding [C1], a design method based on circuit models is proposed for creating ultra-wideband polarization converters using grounded metasurfaces. By taking advantage of the diagonal symmetries, independent control of the orthogonal components that form the electric field is available to tune the polarizer's response. The proposed static polarization converters show a fractional bandwidth of 80% and 55% at normal incidence. Thus, the same unit cell will be able to switch

between a rotator and a LP-to-CP polarizer, demonstrating potential reconfigurability for SatComs in K/Ka bands.

- Concerning [J2], a fully-analytical framework is presented for simulating 3D metadevices with 2D spatial periodicity. We analyzed the fields inside the 3D metastructure by distinguishing two classical regions: Rectangular Waveguides (RWGs) and Hard Waveguides (HWGs). The RWG is a classical waveguide formed by four metallic walls and the HWG is a metallic waveguide whose lateral walls are PMC. The fields are expressed in terms of a single mode due to their low-frequency regime and the non-excitation of higher-order modes. At the spatial discontinuities between each region, we applied the circuit approach explained in Section 1.1.6 for the periodic 2D spatial case. Thus, we were able to obtain similar results of the scattering parameters compared with full-wave commercial software for different configurations, even for oblique incidence. Moreover, with the aim of designing a 3D rotator, we studied the conditions under which a Slotted Waveguide (SWG) can be modeled as a HWG. This allowed us to set the resonance behavior of the complete structure depending on the polarization angle and to fix the desired phase shift between the main orthogonal components of the incident electric field. The results validate the excellent performance of the theoretical framework in simulating periodic full-metal metamaterials in the low-frequency regime, where the regions of the structure are monomodal and the periodicity of the cells is sub-wavelength, highlighting the low computation times (just a few seconds) compared with CST, which may take more than 10 minutes (even more for oblique incidence).

- Regarding [J3], the previously described analytical method is employed to analyze metasurfaces loaded with lumped elements. This approach facilitates the simulation of reconfigurable metasurfaces using equivalent circuit models of varactors or PIN diodes. We tested the performance of the analytical framework by including series and parallel RLC loads and varactor diodes, showing accurate results and faster simulation times compared to CST, even for oblique incidences (up to 40^{o}). Therefore, this framework reveals a promising alternative for simulating advanced prototypes like RIS. Moreover, it could serve as an excellent solution for simulating spacetime structures that involve time-varying responses of active lumped elements.

- In [J4], an analytical method based on transmission lines and Floquet's series expansions is detailed for time-varying metallic metasurfaces. Despite the lack of commercial software to simulate these structures, this model offers valuable physical insight into the frequency conversion and beam steering capabilities of these innovative proto-

types. This work reveals several differences compared to spatial cases. Firstly, the nature of the higher-order modes is different. In spatial cases, they are usually evanescent, whereas in time-varying cases, they are propagative. Secondly, the frequency of each temporal harmonic is different. It is an intrinsic property of time-varying system that can be exploited for frequency conversion. Furthermore, with the theoretical framework, we note that temporal high-order harmonics can only propagate within a semi-plane when the incident wave impinges on the metasurface under oblique incidence. It is highlighted that the simulation times of the proposed analytical method are on the order of only a few seconds. Additionally, these devices offer an alternative solution for pulsed sources or beamformers, depending on the modulation ratio, in emerging communication technologies such as 5G and 6G.

- In [J5], the previous Floquet circuit model applied to the analysis of time-modulated metasurfaces is extended with the inclusion of macroperiods and duty cycles. The macroperiods allow the simulation of new temporal cases when the ratio between the frequency of the incident wave and the modulation frequency of the metasurface is a rational number. On the other hand, the duty cycles break the time symmetry in each period, modifying the temporal electric field profile in the metasurface. This excites new temporal harmonics and alters the scattering parameters, such as the reflection and transmission coefficients. This expansion of the temporal parameters in the simulations enhances the beam steering capabilities of the time-varying metasurface since new temporal propagative harmonics are excited. Thus, it makes possible to achieve a richer diffraction pattern for future applications only controlling the modulation ratio and the duty cycles.

- Relating to [J6], a deep analysis of the physics of a spacetime metagrating is presented. The theoretical approach details the circuit topology of the structure when a monochromatic wave impinges on the spacetime-varying metasurface under TE/TM incidence. It allows us to know the evanescent/propagative nature of each spacetime harmonic, their amplitudes and their diffraction angles. Furthermore, by tuning the temporal parameters, it is possible to control the scattering parameters of the metasurfaces, facilitating beamforming for transmission, reflection, or both. These beamformers improve steering performance for future applications compared to previous time-only configurations since they enable beam coverage across the entire spatial region. On the other hand, leveraging the model's formulation, a methodology has been proposed for designing frequency mixers applicable to mmWave communications. Moreover, the simulation times

achieved with the circuit-based approach are significantly lower compared to those using the numerical FDTD technique.

- Finally, in [C2], we propose a non-iterative, broadband method for material characterization in free space, covering frequencies from 10 GHz to 330 GHz. Its main advantage lies in its ability to provide consistent results regardless of the material's position relative to the calibration planes. Thus, the reference-plane invariance of this method is particularly beneficial in mmWave bands, where even minor positional variations (as small as a few millimeters) can affect measurement accuracy. To accurately extract the normalized scattering parameters, TRL and GRL calibration techniques were employed. Additionally, Savitzky-Golay filters were used to refine the final results, demonstrating strong performance in dielectrics across the specified frequency range. This approach is anticipated to facilitate the extraction of constitutive parameters for new and complex materials, thus contributing to advancements in future communication technologies.

3.2 Future Work

Based on the research findings obtained in this Doctoral Thesis, the following opportunities for future lines of research are identified:

- **Inclusion of polarization control in the Fresnel lens-antenna**. The exploitation of diagonal symmetries for polarization control can be incorporated into the lens with an additional layer of resin and easily manufactured using a 3D printer. Furthermore, the beam steering properties of the lens can be mechanically exploited by implementing an automatically controlled positioner.

- **Implementation of reconfigurability between both polarizers**. The inclusion of materials such as graphene, which can be electronically reconfigured, could be a potential method to tune only the resonance in the top layer of the metasurface. Therefore, an easy conversion between the rotator and the LP-to-CP polarizer can be achieved. Moreover, the use of diagonal symmetries for independent polarization control has enabled the design of a novel absorber, as detailed in [OJ3], available on Authorea Preprints and recently submitted to a journal.

- **Development of metamaterials with PIN diodes or varactors in mmWave bands**. The circuit analysis of periodic metamaterials loaded with lumped elements depicted in [J3] facilitates the development of reconfigurable prototypes at high frequencies taking into account the parasitic effects. This opens up the opportunity to model

devices for isolation, beam steering, or polarity conversion across multiple bands by means of dynamic RIS.

- **Development of spacetime-modulated metamaterials with lumped elements**. We are now focused on the potential manufacturing of a spacetime metagrating with the inclusion of active elements that change their properties over time. Thus, we are working on incorporating time as a new variable into the analytical approach presented in [J3]. By adding external modulations to the bias of varactors, PIN diodes, or transistors, we aim to experimentally validate the future simulations and provide a powerful simulation tool for spacetime-varying metamaterials.

- **Expansion of the analytical framework to dispersive models and travelling-wave spacetime modulations**. To extend the applicability of the analytical framework, it is necessary to increase the range of frequencies available for simulation. For a more accurate tool, it is mandatory to account for dispersion in time-varying systems. This research line has already been explored in our latest paper [OJ2], available on ArXiv and recently submitted to an international journal. On the other hand, the inclusion of traveling-wave modulations will enable the simulation of nonreciprocal devices, efficient beamformers, and efficient frequency converters, among others.

Bibliography

[1] S. Morse, "Telegraph," Patent, June 20, 1840.

[2] A. G. Bell, "Improvement in telegraphy," Patent, March 7, 1876.

[3] G. Marconi, "Improvements in apparatus for wireless telegraphy," Patent, June 2, 1904.

[4] P. T. Farnsworth, "Television system," Patent, August 26, 1930.

[5] T. S. Rappaport, *Wireless communications: principles and practice*. Cambridge University Press, 2024.

[6] K. Shafique, B. A. Khawaja, F. Sabir, S. Qazi, and M. Mustaqim, "Internet of things (IoT) for next-generation smart systems: A review of current challenges, future trends and prospects for emerging 5G-IoT scenarios," *IEEE Access*, vol. 8, pp. 23 022–23 040, 2020.

[7] I. F. Akyildiz, A. Kak, and S. Nie, "6G and beyond: The future of wireless communications systems," *IEEE Access*, vol. 8, pp. 133 995–134 030, 2020.

[8] M. Banafaa, I. Shayea, J. Din, M. H. Azmi, A. Alashbi, Y. I. Daradkeh, and A. Alhammadi, "6G mobile communication technology: Requirements, targets, applications, challenges, advantages, and opportunities," *Alexandria Engineering Journal*, vol. 64, pp. 245–274, 2023.

[9] A. N. Uwaechia and N. M. Mahyuddin, "A comprehensive survey on millimeter wave communications for fifth-generation wireless networks: Feasibility and challenges," *IEEE Access*, vol. 8, pp. 62 367–62 414, 2020.

[10] T. S. Rappaport, S. Sun, R. Mayzus, H. Zhao, Y. Azar, K. Wang, G. N. Wong, J. K. Schulz, M. Samimi, and F. Gutierrez, "Millimeter wave mobile communications for 5G cellular: It will work!" *IEEE Access*, vol. 1, pp. 335–349, 2013.

[11] S. Rangan, T. S. Rappaport, and E. Erkip, "Millimeter-wave cellular wireless networks: Potentials and challenges," *Proceedings of the IEEE*, vol. 102, no. 3, pp. 366–385, 2014.

[12] Y. O. Imam-Fulani, N. Faruk, O. A. Sowande, A. Abdulkarim, E. Alozie, A. D. Usman, K. S. Adewole, A. A. Oloyede, H. Chiroma, S. Garba *et al.*, "5G frequency standardization, technologies, channel models, and network deployment: Advances, challenges, and future directions," *Sustainability*, vol. 15, no. 6, p. 5173, 2023.

[13] J. Gonzalez-Jimenez, A. Siligaris, A. Hamani, F. F. Manzillo, P. Courouve, N. Cassiau, C. Dehos, and A. Clemente, "An Energy-Efficient 56-Gb/s *D*-Band TX-to-RX Link Using CMOS ICs and Transmitarray Antennas," *IEEE Microwave and Wireless Technology Letters*, 2024.

[14] K. K. Vaigandla, B. S. Rani, K. Srikanth, T. Mounika, and R. Karne, "Millimeter wave communications: propagation characteristics, beamforming, architecture, standardization, challenges and applications," *Design Engineering*, vol. 9, pp. 10 144–10 169, 2021.

[15] Y. Zhang, C. R. Anderson, N. Michelusi, D. J. Love, K. R. Baker, and J. V. Krogmeier, "Propagation modeling through foliage in a coniferous forest at 28 GHz," *IEEE Wireless Communications Letters*, vol. 8, no. 3, pp. 901–904, 2019.

[16] T. Ohtsuki *et al.*, "Influence and mitigation of pedestrian blockage at mmwave cellular networks," *IEEE Transactions on Vehicular Technology*, vol. 69, no. 12, pp. 15 442–15 457, 2020.

[17] J. Du, D. Chizhik, R. Feick, G. Castro, M. Rodríguez, and R. A. Valenzuela, "Suburban residential building penetration loss at 28 GHz for fixed wireless access," *IEEE Wireless Communications Letters*, vol. 7, no. 6, pp. 890–893, 2018.

[18] F. Norouzian, E. Marchetti, M. Gashinova, E. Hoare, C. Constantinou, P. Gardner, and M. Cherniakov, "Rain attenuation at millimeter wave and low-THz frequencies," *IEEE Transactions on Antennas and Propagation*, vol. 68, no. 1, pp. 421–431, 2019.

[19] G. A. Siles, J. M. Riera, and P. Garcia-del Pino, "Atmospheric attenuation in wireless communication systems at millimeter and THz frequencies [wireless corner]," *IEEE Antennas and Propagation Magazine*, vol. 57, no. 1, pp. 48–61, 2015.

[20] H. T. Friis, "A note on a simple transmission formula," *Proceedings of the IRE*, vol. 34, no. 5, pp. 254–256, 1946.

[21] H. Whitworth, S. Al-Rubaye, and A. Tsourdos, "Utilizing Satellite Communication to Enable Robust Future Flight Data Links," in *2023 IEEE/AIAA 42nd Digital Avionics Systems Conference (DASC)*. IEEE, 2023, pp. 1–8.

[22] F. Ahmed, K. Singh, and K. P. Esselle, "State-of-the-art passive beam-steering antenna technologies: Challenges and capabilities," *IEEE Access*, 2023.

[23] D. d. S. Brilhante, J. C. Manjarres, R. Moreira, L. de Oliveira Veiga, J. F. de Rezende, F. Müller, A. Klautau, L. Leonel Mendes, and F. A. P. de Figueiredo, "A literature survey on AI-aided beamforming and beam management for 5G and 6G systems," *Sensors*, vol. 23, no. 9, p. 4359, 2023.

[24] Z. Wei, H. Qu, Y. Wang, X. Yuan, H. Wu, Y. Du, K. Han, N. Zhang, and Z. Feng, "Integrated sensing and communication signals toward 5G-A and 6G: A survey," *IEEE Internet of Things Journal*, vol. 10, no. 13, pp. 11 068–11 092, 2023.

[25] C. A. Fernandes, E. B. Lima, and J. R. Costa, "Dielectric lens antennas," *Handbook of antenna technologies*, pp. 1001–1064, 2016.

[26] T. A. Bressner, M. N. Johansson, A. B. Smolders, and U. Johannsen, "High-gain lens-horn antennas for energy-efficient 5G millimeter-wave communication infrastructure," *IEEE Transactions on Antennas and Propagation*, vol. 70, no. 5, pp. 3183–3194, 2021.

[27] O. Quevedo-Teruel, M. Ebrahimpouri, and F. Ghasemifard, "Lens antennas for 5G communications systems," *IEEE Communications Magazine*, vol. 56, no. 7, pp. 36–41, 2018.

[28] Q. Chen, F. Giusti, G. Valerio, F. Mesa, and O. Quevedo-Teruel, "Anisotropic glide-symmetric substrate-integrated-holey metasurface for a compressed ultrawideband Luneburg lens," *Applied Physics Letters*, vol. 118, no. 8, 2021.

[29] D. Pérez-Quintana, C. Bilitos, J. Ruiz-García, I. Ederra, J. Teniente-Vallinas, D. González-Ovejero, and M. Beruete, "Fully metallic luneburg metalens antenna in gap waveguide technology at v-band," *IEEE Transactions on Antennas and Propagation*, vol. 71, no. 4, pp. 2930–2937, 2023.

[30] P. Castillo-Tapia, O. Zetterstrom, A. Algaba-Brazalez, L. Manholm, M. Johansson, N. J. Fonseca, and O. Quevedo-Teruel, "Two-dimensional beam steering using a stacked modulated geodesic Luneburg lens array antenna for 5G and beyond," *IEEE Transactions on Antennas and Propagation*, vol. 71, no. 1, pp. 487–496, 2022.

[31] Z. Qu, S.-W. Qu, Z. Zhang, S. Yang, and C. H. Chan, "Wide-angle scanning lens fed by small-scale antenna array for 5G in millimeter-wave band," *IEEE Transactions on Antennas and Propagation*, vol. 68, no. 5, pp. 3635–3643, 2020.

[32] M. Imbert, A. Papió, F. De Flaviis, L. Jofre, and J. Romeu, "Design and performance evaluation of a dielectric flat lens antenna for millimeter-wave applications," *IEEE Antennas and Wireless Propagation Letters*, vol. 14, pp. 342–345, 2014.

[33] I. Munina, I. Grigoriev, G. O'donnell, and D. Trimble, "A review of 3D printed gradient refractive index lens antennas," *IEEE Access*, vol. 11, pp. 8790–8809, 2023.

[34] J. A. Vásquez-Peralvo, A. Tamayo-Domínguez, G. Pérez-Palomino, J. M. Fernández-González, and T. Wong, "3D Inductive Frequency Selective Structures Using Additive Manufacturing and Low-Cost Metallization," *Sensors*, vol. 22, no. 2, p. 552, 2022.

[35] A. Kapoor, R. Mishra, and P. Kumar, "Frequency selective surfaces as spatial filters: Fundamentals, analysis and applications," *Alexandria Engineering Journal*, vol. 61, no. 6, pp. 4263–4293, 2022.

[36] R. S. Anwar, L. Mao, and H. Ning, "Frequency selective surfaces: A review," *Applied Sciences*, vol. 8, no. 9, p. 1689, 2018.

[37] H. Li, C. Ma, T. Zhou, J. Wang, D. Ye, Y. Sun, W. Zhu, T. A. Denidni, and L. Ran, "Reconfigurable Fresnel lens based on an active second-order bandpass frequency-selective surface," *IEEE Transactions on Antennas and Propagation*, vol. 68, no. 5, pp. 4054–4059, 2019.

[38] Q. Xi, C. Ma, H. Li, B. Zhang, C. Li, and L. Ran, "A reconfigurable planar fresnel lens for millimeter-wave 5G frontends," *IEEE Transactions on Microwave Theory and Techniques*, vol. 68, no. 11, pp. 4579–4588, 2020.

[39] B. A. Munk, *Frequency Selective Surfaces: Theory and Design.* John Wiley & Sons, 2000, cited on pages 4, 9, 39, and 161.

[40] A. A. Omar, H. Huang, and Z. Shen, "Absorptive frequency-selective reflection/transmission structures: A review and future perspectives," *IEEE Antennas and Propagation Magazine*, vol. 62, no. 4, pp. 62–74, 2019.

[41] R. Panwar and J. R. Lee, "Progress in frequency selective surface-based smart electromagnetic structures: A critical review," *Aerospace Science and Technology*, vol. 66, pp. 216–234, 2017.

[42] A. Alex-Amor, F. Mesa, Á. Palomares-Caballero, C. Molero, and P. Padilla, "Exploring the potential of the multi-modal equivalent circuit approach for stacks of 2-D aperture arrays," *IEEE Transactions on Antennas and Propagation*, vol. 69, no. 10, pp. 6453–6467, 2021.

[43] C. Molero, A. Alex-Amor, F. Mesa, A. Palomares-Caballero, and P. Padilla, "Cross-polarization control in FSSs by means of an equivalent circuit approach," *IEEE Access*, vol. 9, pp. 99 513–99 525, 2021.

[44] A. Alex-Amor, Á. Palomares-Caballero, and C. Molero, "3-D metamaterials: Trends on applied designs, computational methods and fabrication techniques," *Electronics*, vol. 11, no. 3, p. 410, 2022.

[45] A. K. Rashid, B. Li, and Z. Shen, "An overview of three-dimensional frequency-selective structures," *IEEE Antennas and Propagation Magazine*, vol. 56, no. 3, pp. 43–67, 2014.

[46] M. A. Lopez, M. J. Freire, J. M. Algarin, V. C. Behr, P. M. Jakob, and R. Marqués, "Nonlinear split-ring metamaterial slabs for magnetic resonance imaging," *Applied Physics Letters*, vol. 98, no. 13, 2011.

[47] A. Suri and K. R. Jha, "Active frequency selective surfaces: a systematic review for sub-6 GHz band," *International Journal of Microwave and Wireless Technologies*, pp. 1–15, 2023.

[48] G. Bharti, K. R. Jha, and G. Singh, "Terahertz frequency selective surface for future wireless communication systems," *Optik*, vol. 126, no. 24, pp. 5909–5917, 2015.

[49] X. Chen, J. Tan, L. Kang, F. Tang, M. Zhao, and N. Kato, "Frequency Selective Surface towards 6G Communication Systems: A Contemporary Survey," *IEEE Communications Surveys & Tutorials*, 2024.

[50] N. Yogesh and Z. Ouyang, "Metamaterial Frequency Selective Surfaces As Polarizers," in *Handbook of Metamaterial-Derived Frequency Selective Surfaces*. Springer, 2022, pp. 1–28.

[51] T. Smith, U. Gothelf, O. S. Kim, and O. Breinbjerg, "An FSS-backed 20/30 GHz circularly polarized reflectarray for a shared aperture L- and Ka-band satellite communication antenna," *IEEE Transactions on Antennas and Propagation*, vol. 62, no. 2, pp. 661–668, 2013.

[52] M.-Q. Yang and Q.-Y. Guo, "An Ultra-Wideband Linear-to-Circular Polarizer Based on Phase Difference Complementary Scheme," *IEEE Transactions on Antennas and Propagation*, 2024.

[53] M. Saikia, S. Ghosh, and K. V. Srivastava, "Design and analysis of ultrathin polarization rotating frequency selective surface using

V-shaped slots," *IEEE Antennas and Wireless Propagation Letters*, vol. 16, pp. 2022–2025, 2017.

[54] M. A. Shukoor and S. Dey, "Wideband Via-less Reconfigurable Reflection and Transmission Linear-Circular/Linear-Cross Polarizer for Vehicular Satellite Communication Applications," *IEEE Transactions on Vehicular Technology*, 2023.

[55] W. A. Imbriale and L. Boccia, "Space Antenna Handbook," 2012.

[56] N. J. Fonseca and C. Mangenot, "High-performance electrically thin dual-band polarizing reflective surface for broadband satellite applications," *IEEE Transactions on Antennas and Propagation*, vol. 64, no. 2, pp. 640–649, 2015.

[57] M. Del Mastro, M. Ettorre, and A. Grbic, "Dual-band, orthogonally-polarized LP-to-CP converter for SatCom applications," *IEEE Transactions on Antennas and Propagation*, vol. 68, no. 9, pp. 6764–6776, 2020.

[58] J. Lundgren, O. Zetterstrom, F. Mesa, N. J. G. Fonseca, and O. Quevedo-Teruel, "Fully Metallic Dual-Band Linear-to-Circular Polarizer for K/Ka-band," *IEEE Antennas and Wireless Propagation Letters*, vol. 20, no. 11, pp. 2191–2195, 2021.

[59] M. Balmaseda-Márquez, S. Moreno-Rodríguez, P. Zapata, C. Molero, and J. Valenzuela-Valdés, "Fully-metallic 3-D cells for wideband applications," *IEEE Transactions on Antennas and Propagation*, vol. 71, no. 5, pp. 4588–4593, 2023.

[60] C. M. Jimenez, E. Menargues, and M. García-Vigueras, "All-metal 3-D frequency-selective surface with versatile dual-band polarization conversion," *IEEE Transactions on Antennas and Propagation*, vol. 68, no. 7, pp. 5431–5441, 2020.

[61] F. F. Manzillo, M. Ettorre, M. S. Lahti, K. T. Kautio, D. Lelaidier, E. Seguenot, and R. Sauleau, "A multilayer LTCC solution for integrating 5G access point antenna modules," *IEEE Transactions on Microwave Theory and Techniques*, vol. 64, no. 7, pp. 2272–2283, 2016.

[62] D. R. Jackson, C. Caloz, and T. Itoh, "Leaky-wave antennas," *Proceedings of the IEEE*, vol. 100, no. 7, pp. 2194–2206, 2012.

[63] F. Monticone and A. Alu, "Leaky-wave theory, techniques, and applications: From microwaves to visible frequencies," *Proceedings of the IEEE*, vol. 103, no. 5, pp. 793–821, 2015.

[64] V. Popov, F. Boust, and S. N. Burokur, "Beamforming with metagratings at microwave frequencies: Design procedure and experimental demonstration," *IEEE Transactions on Antennas and Propagation*, vol. 68, no. 3, pp. 1533–1541, 2019.

[65] Y. Ra'di, D. L. Sounas, and A. Alù, "Metagratings: Beyond the limits of graded metasurfaces for wave front control," *Physical review letters*, vol. 119, no. 6, p. 067404, 2017.

[66] V. Popov, F. Boust, and S. N. Burokur, "Controlling diffraction patterns with metagratings," *Physical Review Applied*, vol. 10, no. 1, p. 011002, 2018.

[67] V. S. Asadchy, Y. Ra'Di, J. Vehmas, and S. Tretyakov, "Functional metamirrors using bianisotropic elements," *Physical review letters*, vol. 114, no. 9, p. 095503, 2015.

[68] A. Díaz-Rubio, J. Li, C. Shen, S. A. Cummer, and S. A. Tretyakov, "Power flow–conformal metamirrors for engineering wave reflections," *Science advances*, vol. 5, no. 2, p. eaau7288, 2019.

[69] D. Berry, R. Malech, and W. Kennedy, "The reflectarray antenna," *IEEE Transactions on Antennas and Propagation*, vol. 11, no. 6, pp. 645–651, 1963.

[70] L. Dussopt, "Transmitarray antennas," *Aperture Antennas for Millimeter and Sub-Millimeter Wave Applications*, pp. 191–220, 2018.

[71] S. V. Hum, M. Okoniewski, and R. J. Davies, "Modeling and design of electronically tunable reflectarrays," *IEEE transactions on Antennas and Propagation*, vol. 55, no. 8, pp. 2200–2210, 2007.

[72] J. Y. Lau and S. V. Hum, "Reconfigurable transmitarray design approaches for beamforming applications," *IEEE Transactions on Antennas and Propagation*, vol. 60, no. 12, pp. 5679–5689, 2012.

[73] V. Pacheco-Peña, D. M. Solís, and N. Engheta, "Time-varying electromagnetic media: opinion," *Opt. Mater. Express*, vol. 12, no. 10, pp. 3829–3836, Oct 2022.

[74] A. M. Shaltout, V. M. Shalaev, and M. L. Brongersma, "Spatiotemporal light control with active metasurfaces," *Science*, vol. 364, no. 6441, p. eaat3100, 2019.

[75] T. J. Cui, M. Q. Qi, X. Wan, J. Zhao, and Q. Cheng, "Coding metamaterials, digital metamaterials and programmable metamaterials," *Light: science & applications*, vol. 3, no. 10, pp. e218–e218, 2014.

[76] V. Pacheco-Peña and N. Engheta, "Temporal aiming," *Light: Science & Applications*, vol. 9, no. 1, p. 129, 2020.

[77] E. Mikheeva, C. Kyrou, F. Bentata, S. Khadir, S. Cueff, and P. Genevet, "Space and time modulations of light with metasurfaces: recent progress and future prospects," *ACS photonics*, vol. 9, no. 5, pp. 1458–1482, 2022.

[78] A. Shaltout, A. Kildishev, and V. Shalaev, "Time-varying metasurfaces and Lorentz non-reciprocity," *Optical Materials Express*, vol. 5, no. 11, pp. 2459–2467, 2015.

[79] G. Ptitcyn, M. S. Mirmoosa, A. Sotoodehfar, and S. A. Tretyakov, "A tutorial on the basics of time-varying electromagnetic systems and circuits: Historic overview and basic concepts of time-modulation," *IEEE Antennas and Propagation Magazine*, vol. 65, no. 4, pp. 10–20, 2023.

[80] A. Alex-Amor, C. Molero, and M. G. Silveirinha, "Analysis of metallic space-time gratings using Lorentz transformations," *Physical Review Applied*, vol. 20, no. 1, p. 014063, 2023.

[81] V. Pacheco-Peña and N. Engheta, "Temporal equivalent of the Brewster angle," *Physical Review B*, vol. 104, no. 21, p. 214308, 2021.

[82] R. Tirole, S. Vezzoli, E. Galiffi, I. Robertson, D. Maurice, B. Tilmann, S. A. Maier, J. B. Pendry, and R. Sapienza, "Double-slit time diffraction at optical frequencies," *Nature Physics*, vol. 19, no. 7, pp. 999–1002, 2023.

[83] G. Ptitcyn, M. S. Mirmoosa, S. Hrabar, and S. A. Tretyakov, "Time-modulated circuits and metasurfaces for emulating arbitrary transfer functions," *Physical review applied*, vol. 20, no. 1, p. 014041, 2023.

[84] M. S. Mirmoosa, G. A. Ptitcyn, R. Fleury, and S. Tretyakov, "Instantaneous radiation from time-varying electric and magnetic dipoles," *Physical Review A*, vol. 102, no. 1, p. 013503, 2020.

[85] N. Reiskarimian and H. Krishnaswamy, "Magnetic-free non-reciprocity based on staggered commutation," *Nature communications*, vol. 7, no. 1, p. 11217, 2016.

[86] S. Taravati, N. Chamanara, and C. Caloz, "Nonreciprocal electromagnetic scattering from a periodically space-time modulated slab and application to a quasisonic isolator," *Physical Review B*, vol. 96, no. 16, p. 165144, 2017.

[87] N. A. Estep, D. L. Sounas, J. Soric, and A. Alu, "Magnetic-free non-reciprocity and isolation based on parametrically modulated coupled-resonator loops," *Nature Physics*, vol. 10, no. 12, pp. 923–927, 2014.

[88] J. Pendry, E. Galiffi, and P. Huidobro, "Gain in time-dependent media—a new mechanism," *JOSA B*, vol. 38, no. 11, pp. 3360–3366, 2021.

[89] J. Gaxiola-Luna and P. Halevi, "Growing fields in a temporal photonic (time) crystal with a square profile of the permittivity ε (t)," *Applied Physics Letters*, vol. 122, no. 1, 2023.

[90] X. Fang, M. Li, Z. Lai, D. Ramaccia, A. Toscano, F. Bilotti, and D. Ding, "Multifunctional Space–Time-Modulated Metasurface for Direction of Arrival Estimation and RCS Manipulation in a Single System," *IEEE Transactions on Microwave Theory and Techniques*, 2023.

[91] B. H. Kolner, "Space-time imaging, magnification, and time reversal of matter waves," *Applied Physics Letters*, vol. 117, no. 12, 2020.

[92] L. Li, H. Zhao, C. Liu, L. Li, and T. J. Cui, "Intelligent metasurfaces: control, communication and computing," *Elight*, vol. 2, no. 1, p. 7, 2022.

[93] X. Wu, X. Liu, M. D. Hickle, D. Peroulis, J. S. Gómez-Díaz, and A. Á. Melcón, "Isolating bandpass filters using time-modulated resonators," *IEEE Transactions on Microwave Theory and Techniques*, vol. 67, no. 6, pp. 2331–2345, 2019.

[94] Z. Li, X. Ma, A. Bahrami, Z.-L. Deck-Léger, and C. Caloz, "Space-time Fresnel prism," *Physical Review Applied*, vol. 20, no. 5, p. 054029, 2023.

[95] S. Taravati and C. Caloz, "Mixer-duplexer-antenna leaky-wave system based on periodic space-time modulation," *IEEE transactions on antennas and propagation*, vol. 65, no. 2, pp. 442–452, 2016.

[96] V. G. Ataloglou, S. Taravati, and G. V. Eleftheriades, "Metasurfaces: physics and applications in wireless communications," *National Science Review*, vol. 10, no. 8, p. nwad164, 2023.

[97] S. Taravati, "Aperiodic space-time modulation for pure frequency mixing," *Physical Review B*, vol. 97, no. 11, p. 115131, 2018.

[98] S. Taravati and G. V. Eleftheriades, "Pure and linear frequency-conversion temporal metasurface," *Physical Review Applied*, vol. 15, no. 6, p. 064011, 2021.

[99] C. Amra, A. Passian, P. Tchamitchian, M. Ettorre, A. Alwakil, J. A. Zapien, P. Rouquette, Y. Abautret, and M. Zerrad, "Linear-frequency conversion with time-varying metasurfaces," *Physical Review Research*, vol. 6, no. 1, p. 013002, 2024.

[100] L. Zhang, X. Q. Chen, R. W. Shao, J. Y. Dai, Q. Cheng, G. Castaldi, V. Galdi, and T. J. Cui, "Breaking reciprocity with space-time-coding digital metasurfaces," *Advanced Materials*, vol. 31, no. 41, p. 1904069, 2019.

[101] S. Taravati and G. V. Eleftheriades, "Full-duplex reflective beamsteering metasurface featuring magnetless nonreciprocal amplification," *Nature Communications*, vol. 12, no. 1, p. 4414, 2021.

[102] S. Vosoughitabar and C.-T. M. Wu, "Programming nonreciprocity and harmonic beam steering via a digitally space-time-coded metamaterial antenna," *Scientific reports*, vol. 13, no. 1, p. 7338, 2023.

[103] L. Zhang, X. Q. Chen, S. Liu, Q. Zhang, J. Zhao, J. Y. Dai, G. D. Bai, X. Wan, Q. Cheng, G. Castaldi *et al.*, "Space-time-coding digital metasurfaces," *Nature communications*, vol. 9, no. 1, p. 4334, 2018.

[104] L. Zhang, Z. X. Wang, R. W. Shao, J. L. Shen, X. Q. Chen, X. Wan, Q. Cheng, and T. J. Cui, "Dynamically realizing arbitrary multi-bit programmable phases using a 2-bit time-domain coding metasurface," *IEEE Transactions on Antennas and Propagation*, vol. 68, no. 4, pp. 2984–2992, 2019.

[105] X. Fang, M. Li, S. Li, D. Ramaccia, A. Toscano, F. Bilotti, and D. Ding, "Diverse frequency time modulation for passive false target spoofing: design and experiment," *IEEE Transactions on Microwave Theory and Techniques*, 2023.

[106] Z. Wu, C. Scarborough, and A. Grbic, "Space-time-modulated metasurfaces with spatial discretization: Free-space N-path systems," *Physical Review Applied*, vol. 14, no. 6, p. 064060, 2020.

[107] A. E. Cardin, S. R. Silva, S. R. Vardeny, W. J. Padilla, A. Saxena, A. J. Taylor, W. J. Kort-Kamp, H.-T. Chen, D. A. Dalvit, and A. K. Azad, "Surface-wave-assisted nonreciprocity in spatio-temporally modulated metasurfaces," *Nature communications*, vol. 11, no. 1, p. 1469, 2020.

[108] O. A. Abdelraouf, Z. Wang, H. Liu, Z. Dong, Q. Wang, M. Ye, X. R. Wang, Q. J. Wang, and H. Liu, "Recent advances in tunable metasurfaces: materials, design, and applications," *ACS nano*, vol. 16, no. 9, pp. 13 339–13 369, 2022.

[109] W. He, M. Tong, Z. Xu, Y. Hu, T. Jiang *et al.*, "Ultrafast all-optical terahertz modulation based on an inverse-designed metasurface," *Photonics Research*, vol. 9, no. 6, pp. 1099–1108, 2021.

[110] P. P. Vabishchevich, A. Vaskin, N. Karl, J. L. Reno, M. B. Sinclair, I. Staude, and I. Brener, "Ultrafast all-optical diffraction switching using semiconductor metasurfaces," *Applied Physics Letters*, vol. 118, no. 21, 2021.

[111] "CST Studio Suite — 3ds.com," https://www.3ds.com/products/simulia/cst-studio-suite.

[112] "Ansys HFSS — 3D High Frequency Simulation Software — ansys.com," https://www.ansys.com/products/electronics/ansys-hfss.

[113] Z.-X. Du, A. Li, X. Y. Zhang, and D. F. Sievenpiper, "A simulation technique for radiation properties of time-varying media based on frequency-domain solvers," *IEEE Access*, vol. 7, pp. 112 375–112 383, 2019.

[114] "COMSOL: Multiphysics Software for Optimizing Designs — comsol.com," https://www.comsol.com/.

[115] A. Taflove, S. C. Hagness, and M. Piket-May, "Computational electromagnetics: the finite-difference time-domain method," *The Electrical Engineering Handbook*, vol. 3, no. 629-670, p. 15, 2005.

[116] S. A. Stewart, T. J. Smy, and S. Gupta, "Finite-difference time-domain modeling of space–time-modulated metasurfaces," *IEEE Transactions on Antennas and Propagation*, vol. 66, no. 1, pp. 281–292, 2017.

[117] Y. Vahabzadeh, N. Chamanara, and C. Caloz, "Generalized sheet transition condition FDTD simulation of metasurface," *IEEE Transactions on Antennas and Propagation*, vol. 66, no. 1, pp. 271–280, 2017.

[118] E. Moreno, M. F. F. Pantoja, S. G. Garcia, A. R. Bretones, and R. G. G. Martin, "Time-domain numerical modeling of thz photoconductive antennas," *IEEE Transactions on Terahertz Science and Technology*, vol. 4, no. 4, pp. 490–500, 2014.

[119] S. F. Bass, A. M. Palmer, K. R. Schab, K. Kerby-Patel, and J. E. Ruyle, "Conversion matrix method of moments for time-varying electromagnetic analysis," *IEEE Transactions on Antennas and Propagation*, vol. 70, no. 8, pp. 6763–6774, 2022.

[120] J.-M. Jin, *The finite element method in electromagnetics*. John Wiley & Sons, 2015.

[121] Q. Zhao and C. D. Sarris, "Space–time adaptive modeling and shape optimization of microwave structures with applications to metasurface design," *IEEE Transactions on Microwave Theory and Techniques*, vol. 70, no. 12, pp. 5440–5453, 2022.

[122] V. Tiukuvaara, T. J. Smy, and S. Gupta, "Floquet analysis of space-time modulated metasurfaces with Lorentz dispersion," *IEEE Transactions on Antennas and Propagation*, vol. 69, no. 11, pp. 7667–7678, 2021.

[123] M. Rahmanzadeh, B. Rejaei, and A. Khavasi, "Analysis of electromagnetic scattering from array of time-modulated graphene ribbons," *Optics Express*, vol. 31, no. 13, pp. 21 739–21 752, 2023.

[124] K. Pham and A. Maurel, "Diffraction grating with space-time modulation," *Journal of Computational Physics*, vol. 469, p. 111528, 2022.

[125] J. R. Zurita-Sánchez, P. Halevi, and J. C. Cervantes-Gonzalez, "Reflection and transmission of a wave incident on a slab with a time-periodic dielectric function ε (t)," *Physical Review A—Atomic, Molecular, and Optical Physics*, vol. 79, no. 5, p. 053821, 2009.

[126] P. A. Huidobro, M. G. Silveirinha, E. Galiffi, and J. Pendry, "Homogenization theory of space-time metamaterials," *Physical Review Applied*, vol. 16, no. 1, p. 014044, 2021.

[127] A. Nicolson and G. Ross, "Measurement of the intrinsic properties of materials by time-domain techniques," *IEEE Transactions on instrumentation and measurement*, vol. 19, no. 4, pp. 377–382, 1970.

[128] W. B. Weir, "Automatic measurement of complex dielectric constant and permeability at microwave frequencies," *Proceedings of the IEEE*, vol. 62, no. 1, pp. 33–36, 1974.

[129] B. Salski, T. Karpisz, M. Warecka, P. Kowalczyk, P. Czekala, and P. Kopyt, "Microwave characterization of dielectric sheets in a plano-concave Fabry-Perot open resonator," *IEEE Transactions on Microwave Theory and Techniques*, vol. 70, no. 5, pp. 2732–2742, 2022.

[130] J. Barowski, M. Zimmermanns, and I. Rolfes, "Millimeter-wave characterization of dielectric materials using calibrated FMCW transceivers," *IEEE Transactions on Microwave Theory and Techniques*, vol. 66, no. 8, pp. 3683–3689, 2018.

[131] I. Vakili, L. Ohlsson, L.-E. Wernersson, and M. Gustafsson, "Time-domain system for millimeter-wave material characterization," *IEEE Transactions on Microwave Theory and Techniques*, vol. 63, no. 9, pp. 2915–2922, 2015.

[132] A. Passarelli, H. Bartosik, G. Rumolo, V. G. Vaccaro, M. R. Masullo, C. Koral, G. P. Papari, A. Andreone, and O. Boine-Frankenheim, "Novel measurement technique for the electromagnetic characterization of coating materials in the sub-THz frequency range," *Physical Review Accelerators and Beams*, vol. 21, no. 10, p. 103101, 2018.

[133] Y. Yashchyshyn and K. Godziszewski, "A new method for dielectric characterization in sub-THz frequency range," *IEEE Transactions on Terahertz Science and Technology*, vol. 8, no. 1, pp. 19–26, 2017.

[134] C. Yang, J. Wang, and C. Yang, "Estimation methods to extract complex permittivity from transmission coefficient in the terahertz band," *Optical and Quantum Electronics*, vol. 53, no. 8, p. 433, 2021.

[135] M. L. Kulygin and I. A. Litovsky, "Sub-Terahertz Complex Permittivity Measurement Method Using Cavity Switches," *Journal of Infrared, Millimeter, and Terahertz Waves*, vol. 41, pp. 1567–1575, 2020.

[136] J. C. Maxwell, "A Dynamical Theory of the Electromagnetic Field," *Philosophical Transactions of the Royal Society of London*, vol. 155, pp. 459–512, 1865.

[137] R. E. Collin, *Field theory of guided waves*. John Wiley & Sons, 1990, vol. 5.

[138] C. A. Balanis, *Modern antenna handbook*. John Wiley & Sons, 2011.

[139] J. L. Volakis and J. L. Volakis, *Antenna engineering handbook*. McGraw-Hill New York, 2007, vol. 1755.

[140] N. Marcuvitz, *Waveguide handbook*. Iet, 1951, no. 21.

[141] D. M. Pozar, *Microwave Engineering*. John Wiley & Sons, 1998.

[142] C. Caloz and Z.-L. Deck-Léger, "Spacetime metamaterials—part I: general concepts," *IEEE Transactions on Antennas and Propagation*, vol. 68, no. 3, pp. 1569–1582, 2019.

[143] C. Caloz and Z.-L. Deck-Leger, "Spacetime metamaterials—Part II: Theory and applications," *IEEE Transactions on Antennas and Propagation*, vol. 68, no. 3, pp. 1583–1598, 2019.

[144] Y. Xiao, D. N. Maywar, and G. P. Agrawal, "Reflection and transmission of electromagnetic waves at a temporal boundary," *Optics letters*, vol. 39, no. 3, pp. 574–577, 2014.

[145] Z. Hayran, J. B. Khurgin, and F. Monticone, "$\hbar\omega$ versus $\hbar k$: dispersion and energy constraints on time-varying photonic materials and time

crystals," *Optical Materials Express*, vol. 12, no. 10, pp. 3904–3917, 2022.

[146] D. M. Solís, R. Kastner, and N. Engheta, "Time-varying materials in the presence of dispersion: plane-wave propagation in a Lorentzian medium with temporal discontinuity," *Photonics Research*, vol. 9, no. 9, pp. 1842–1853, 2021.

[147] S. Taravati and G. V. Eleftheriades, "Generalized space-time-periodic diffraction gratings: Theory and applications," *Physical Review Applied*, vol. 12, no. 2, p. 024026, 2019.

[148] S. Edelberg and A. Oliner, "Mutual coupling effects in large antenna arrays: Part 1–Slot arrays," *IRE Transactions on Antennas and Propagation*, vol. 8, no. 3, pp. 286–297, 1960.

[149] V. G. Veselago, "The electrodynamics of substances with simultaneously negative values of ε and μ," *Sov. Phys. Usp.*, vol. 10, pp. 509–514, 1968.

[150] J. B. Pendry, A. J. Holden, D. J. Robbins, and W. Stewart, "Magnetism from conductors and enhanced nonlinear phenomena," *IEEE transactions on microwave theory and techniques*, vol. 47, no. 11, pp. 2075–2084, 1999.

[151] D. R. Smith, J. B. Pendry, and M. C. Wiltshire, "Metamaterials and negative refractive index," *science*, vol. 305, no. 5685, pp. 788–792, 2004.

[152] A. Boardman, "Pioneers in metamaterials: John pendry and victor veselago," *Journal of optics*, vol. 13, no. 2, p. 020401, 2010.

[153] C. Caloz and T. Itoh, *Electromagnetic metamaterials: transmission line theory and microwave applications*. John Wiley & Sons, 2005.

[154] M. Silveirinha and N. Engheta, "Tunneling of electromagnetic energy through subwavelength channels and bends using ϵ-near-zero materials," *Phys. Rev. Lett.*, vol. 97, p. 157403, Oct 2006.

[155] R. A. Depine, M. L. Martínez-Ricci, J. A. Monsoriu, E. Silvestre, and P. Andrés, "Zero permeability and zero permittivity band gaps in 1D metamaterial photonic crystals," *Physics Letters A*, vol. 364, no. 3-4, pp. 352–355, 2007.

[156] S. B. Glybovski, S. A. Tretyakov, P. A. Belov, Y. S. Kivshar, and C. R. Simovski, "Metasurfaces: From microwaves to visible," *Physics reports*, vol. 634, pp. 1–72, 2016.

[157] M. Chen, M. Kim, A. M. Wong, and G. V. Eleftheriades, "Huygens' metasurfaces from microwaves to optics: a review," *Nanophotonics*, vol. 7, no. 6, pp. 1207–1231, 2018.

[158] E. Martini and S. Maci, "Theory, analysis, and design of metasurfaces for smart radio environments," *Proceedings of the IEEE*, vol. 110, no. 9, pp. 1227–1243, 2022.

[159] M. Kadic, G. W. Milton, M. van Hecke, and M. Wegener, "3D metamaterials," *Nature Reviews Physics*, vol. 1, no. 3, pp. 198–210, 2019.

[160] C. Molero, Á. Palomares-Caballero, A. Alex-Amor, I. Parellada-Serrano, F. Gamiz, P. Padilla, and J. F. Valenzuela-Valdés, "Metamaterial-based reconfigurable intelligent surface: 3D meta-atoms controlled by graphene structures," *IEEE Communications Magazine*, vol. 59, no. 6, pp. 42–48, 2021.

[161] V. Torres, B. Orazbayev, V. Pacheco-Peña, J. Teniente, M. Beruete, M. Navarro-Cía, M. S. Ayza, and N. Engheta, "Experimental demonstration of a millimeter-wave metallic ENZ lens based on the energy squeezing principle," *IEEE Transactions on Antennas and Propagation*, vol. 63, no. 1, pp. 231–239, 2014.

[162] M. Beruete, N. Engheta, and V. Pacheco-Peña, "Experimental demonstration of deeply subwavelength dielectric sensing with epsilon-near-zero (enz) waveguides," *Applied Physics Letters*, vol. 120, no. 8, 2022.

[163] N. Engheta, "Four-dimensional optics using time-varying metamaterials," *Science*, vol. 379, no. 6638, pp. 1190–1191, 2023.

[164] X. Wang, A. Diaz-Rubio, H. Li, S. A. Tretyakov, and A. Alu, "Theory and design of multifunctional space-time metasurfaces," *Physical Review Applied*, vol. 13, no. 4, p. 044040, 2020.

[165] X. Wang, V. S. Asadchy, S. Fan, and S. A. Tretyakov, "Space–time metasurfaces for power combining of waves," *ACS Photonics*, vol. 8, no. 10, pp. 3034–3041, 2021.

[166] S. Yin and A. Alu, "Efficient phase conjugation in a space-time leaky waveguide," *ACS Photonics*, vol. 9, no. 3, pp. 979–984, 2022.

[167] H. Barati Sedeh, M. M. Salary, and H. Mosallaei, "Topological space-time photonic transitions in angular-momentum-biased metasurfaces," *Advanced Optical Materials*, vol. 8, no. 11, p. 2000075, 2020.

[168] E. Galiffi, R. Tirole, S. Yin, H. Li, S. Vezzoli, P. A. Huidobro, M. G. Silveirinha, R. Sapienza, A. Alù, and J. B. Pendry, "Photonics of time-varying media," *Advanced Photonics*, vol. 4, no. 1, pp. 014 002–014 002, 2022.

[169] S. Yin, E. Galiffi, and A. Alù, "Floquet metamaterials," *ELight*, vol. 2, no. 1, p. 8, 2022.

[170] J. E. Varela and J. Esteban, "Characterization of waveguides with a combination of conductor and periodic boundary contours: Application to the analysis of bi-periodic structures," *IEEE transactions on microwave theory and techniques*, vol. 60, no. 3, pp. 419–430, 2012.

[171] G. Floquet, "Sur les équations différentielles linéaires à coefficients périodiques," in *Annales scientifiques de l'École normale supérieure*, vol. 12, 1883, pp. 47–88.

[172] F. Bloch, "Über die Quantenmechanik der Elektronen in Kristallgittern," *Zeitschrift für Physik*, vol. 52, no. 7-8, pp. 555–600, 1929.

[173] Z. Zhang and S. Satpathy, "Electromagnetic wave propagation in periodic structures: Bloch wave solution of Maxwell's equations," *Physical review letters*, vol. 65, no. 21, p. 2650, 1990.

[174] F. Faisal and J. Kamiński, "Floquet-Bloch theory of high-harmonic generation in periodic structures," *Physical Review A*, vol. 56, no. 1, p. 748, 1997.

[175] A. Epstein and G. V. Eleftheriades, "Floquet-Bloch analysis of refracting Huygens metasurfaces," *Physical Review B*, vol. 90, no. 23, p. 235127, 2014.

[176] M. Valizadeh, L. Yousefi, and M. Miri, "Analytical formulation of spatiotemporal modulated graphene-based waveguides using Floquet-Bloch theory," *Scientific Reports*, vol. 14, no. 1, p. 7332, 2024.

[177] K. Yee, "Numerical solution of initial boundary value problems involving Maxwell's equations in isotropic media," *IEEE Transactions on antennas and propagation*, vol. 14, no. 3, pp. 302–307, 1966.

[178] A. Taflove, *Computational Electrodynamics: The Finite-Difference Time-Domain Method*. Artech House, 1995.

[179] B. Engquist and A. Majda, "Absorbing boundary conditions for numerical simulation of waves," *Proceedings of the National Academy of Sciences*, vol. 74, no. 5, pp. 1765–1766, 1977.

[180] R. Courant, K. Friedrichs, and H. Lewy, "Über die partiellen Differenzengleichungen der mathematischen Physik," *Mathematische annalen*, vol. 100, no. 1, pp. 32–74, 1928.

[181] R. Rodriguez-Berral, F. Medina, F. Mesa, and M. Garcia-Vigueras, "Quasi-analytical modeling of transmission/reflection in strip/slit

gratings loaded with dielectric slabs," *IEEE transactions on microwave theory and techniques*, vol. 60, no. 3, pp. 405–418, 2012.

[182] R. Rodriguez-Berral, C. Molero, F. Medina, and F. Mesa, "Analytical wideband model for strip/slit gratings loaded with dielectric slabs," *IEEE transactions on microwave theory and techniques*, vol. 60, no. 12, pp. 3908–3918, 2012.

[183] R. Rodriguez-Berral, F. Mesa, and F. Medina, "Analytical multimodal network approach for 2-D arrays of planar patches/apertures embedded in a layered medium," *IEEE Transactions on Antennas and Propagation*, vol. 63, no. 5, pp. 1969–1984, 2015.

[184] F. Mesa, R. Rodriguez-Berral, and F. Medina, "Unlocking complexity using the ECA: The equivalent circuit model as an efficient and physically insightful tool for microwave engineering," *IEEE Microwave Magazine*, vol. 19, no. 4, pp. 44–65, 2018.

[185] G. F. Engen and C. A. Hoer, "Thru-reflect-line: An improved technique for calibrating the dual six-port automatic network analyzer," *IEEE transactions on microwave theory and techniques*, vol. 27, no. 12, pp. 987–993, 1979.

[186] A. Ramírez-Arroyo, A. Alex-Amor, C. García-García, Á. Palomares-Caballero, P. Padilla, and J. F. Valenzuela-Valdés, "Time-gating technique for recreating complex scenarios in 5g systems," *IEEE Access*, vol. 8, pp. 183 583–183 595, 2020.

[187] P. G. Bartley and S. B. Begley, "Improved free-space S-parameter calibration," in *2005 IEEE Instrumentationand Measurement Technology Conference Proceedings*, vol. 1. IEEE, 2005, pp. 372–375.

[188] "MATLAB - El lenguaje del cálculo técnico — es.mathworks.com," https://es.mathworks.com/products/matlab.html.

[189] Smart, W. Applications, and T. G. (SWAT-UGR), "Facilities," https://swat.ugr.es/facilities-gear/.

Appendices

Appendix A

Introducción y conclusiones

Este apéndice presenta en español la parte introductoria de la Tesis Doctoral así como de las conclusiones obtenidas. Esto complementa el amplio resumen en español que está incluido al inicio del documento de Tesis para cumplir la normativa de la Universidad de Granada correspondiente a la redacción de la tesis doctoral en un idioma distinto al español.

Introducción

Desde sus inicios, la historia de las comunicaciones ha sido una búsqueda constante para mejorar la transmisión de información. Los primeros sistemas de comunicación, como el telégrafo [1] y el teléfono [2], utilizaban señales eléctricas a través de cables para enviar mensajes a distancias relativamente cortas. Con la invención de la radio [3] y la televisión [4], fue posible transmitir señales de audio y video a través de ondas electromagnéticas, lo que permitió una mayor cobertura geográfica y un mayor volumen de información. Con la llegada de la era digital y el crecimiento exponencial de Internet, la demanda de transmisión de datos ha aumentado drásticamente [5]. La necesidad de compartir grandes cantidades de información en tiempo real, como videos de alta definición, juegos en línea y aplicaciones de realidad aumentada y virtual, ha resaltado las limitaciones de los sistemas de comunicación tradicionales [6].

El aumento del ancho de banda es crucial para cubrir esta creciente demanda. Mayores anchos de banda permiten la transmisión de más datos a mayores velocidades, reduciendo la latencia y mejorando la calidad de los servicios de comunicación. Para lograr esto, es esencial que las antenas operen a frecuencias más altas, donde hay más ancho de banda disponible. Esto permite aumentar la capacidad de los sistemas, lo cual es esencial para las aplicaciones avanzadas y emergentes en las futuras comunicaciones 6G [7, 8]. Por lo tanto, el cambio a frecuencias más altas, como las bandas de mmWave y sub-Terahertz, abre la posibilidad de desbloquear nuevas

capacidades y soportar los requisitos de conectividad masiva del futuro.

La implementación de la tecnología 5G ha revelado numerosos desafíos que aún necesitan ser abordados, particularmente en escenarios urbanos [9–11]. Esta generación se caracteriza por el uso de las bandas de mmWave (de 30 a 300 GHz), donde la tasa de transmisión de datos podría alcanzar hasta 100 Gbps [12, 13]. No obstante, el uso de estas frecuencias presenta varios desafíos fundamentales en la comunicación [14]. Por nombrar algunos, se destaca la alta directividad inherente de las antenas que obliga a establecer enlaces P2P, la sensibilidad a los bloqueos producidos por el follaje [15], el bloqueo humano [16] o la penetración de materiales [17], la importante pérdida en la transmisión debido a la lluvia [18], las moléculas de gas en la atmósfera [19], y la atenuación general del canal impuesta por la fórmula de Friis [20]. Por ejemplo, varios de estos problemas se encuentran en las SatComs, donde también se añaden alteraciones de polarización por la rotación de Faraday en la ionosfera [21]. Además, con el crecimiento del IoT, han surgido nuevas comunicaciones D2D, incluyendo vehículos, usuarios móviles, redes e infraestructuras, donde las capacidades de direccionamiento de haces [22], formación de haces [23] y conversión de frecuencias [24] se vuelven cruciales.

Con todos estos desafíos, los ingenieros de RF han centrado sus esfuerzos en diseñar nuevos prototipos que mitiguen algunos de los inconvenientes presentados anteriormente. Por ejemplo, las antenas de lente [25] se han convertido en una excelente solución para enlaces P2P, ya que pueden concentrar la energía en regiones específicas, aumentando así la directividad de la antena y compensando las pérdidas en la trayectoria [26, 27]. Además de su capacidad para operar en una amplia gama de frecuencias [28, 29], tienen capacidades de direccionamiento de haces dependiendo, por un lado, del alimentador [30, 31]; y, por otro lado, de la relación entre la posición del elemento radiante y la lente [32]. Además, la mejora continua en la fabricación aditiva ha facilitado la fabricación de estos dispositivos utilizando materiales dieléctricos o metálicos a través de varias técnicas de impresión 3D [33, 34], como SLA, FDM, SLS, MJ, DLP, SLM o DMLS. Estas facilidades, junto con la inclusión de FSSs [35, 36], han permitido la creación de prototipos basados en lentes más sofisticados y reconfigurables, que son ideales para escenarios de comunicación donde se desea el direccionamiento de haces [37, 38].

Las FSSs son estructuras periódicas que de forma selectiva transmiten o reflejan ondas electromagnéticas a ciertas frecuencias [39]. Generalmente consisten en una matriz de elementos, como parches o aperturas, dispuestos en un patrón espacial periódico sobre un sustrato. El comportamiento de una FSS está determinado por la forma, tamaño y disposición de estos elementos (cuya periodicidad se establece como la distancia entre dos elementos o celdas consecutivos), así como por las propiedades dieléctricas del sustrato. En las últimas décadas, han ganado una importancia significativa debido a sus

múltiples aplicaciones, tales como filtros absorbentes [40], filtros de radomo en aeronaves, en los sectores médico y militar mediante textiles especiales, o su fácil implementación en antenas [41], entre otros. Además, el diseño de FSSs multicapa [42, 43] y el uso de la dimensión longitudinal para crear FSSs 3D [44], incrementa el ancho de banda operativo de los filtros y facilita la integración de elementos activos [45, 46]. Estos últimos conducen al desarrollo de AFSSs [47], resultando en un rendimiento superior en términos de reconfigurabilidad, respuestas de doble banda, direccionamiento de haces, formación de haces o conmutación de haces. La mejora en los métodos de fabricación, caracterización y medición de estos dispositivos ha permitido el desarrollo de FSSs en el rango de los subterahercios [48], permitiendo la creación de enlaces de alta capacidad con características de selección de frecuencia, reflexión, transmisión y absorción para las comunicaciones de la futura generación [49].

Las FSSs también se han propuesto en SatComs por su capacidad de ajustar la polarización y operar en diversas bandas de frecuencia [50, 51]. Su capacidad para cambiar entre LP-to-CP [52], o invertir la dirección de giro con rotadores [53], combinada con su funcionalidad en reflexión y transmisión [54], las convierte en una excelente opción para sistemas de comunicación donde las condiciones del canal pueden afectar la polarización de la señal electromagnética [55]. Particularmente, existe un interés especial en los terminales SatCom de las bandas *K/Ka* que operan en el rango de 17.7-21.2 GHz para enlace descendente y 27.5-31 GHz para enlace ascendente. Por lo tanto, el uso de FSSs ha hecho posible diseñar prototipos que funcionan en ambas bandas [56, 57]. Por otro lado, la aparición de polarizadores totalmente metálicos ha proporcionado una solución robusta para la integración satelital, utilizando FSSs multicapa [58] o empleando prototipos impresos en 3D [59, 60].

Las modulaciones espaciales han sido la técnica principal para adaptar los sistemas clásicos de formación de haces o conversión de polarización, como FSSs, antenas multicapa [61], LWAs [62, 63], metagratings [64–66], metamirrors [67, 68] o dispositivos basados en PA como reflectarrays [69], transmitarrays [70] o RISs [71, 72]. Sin embargo, la reciente inclusión de la modulación temporal ha abierto una nueva gama de aplicaciones intrigantes para las comunicaciones futuras [73–84]. Estas aplicaciones incluyen dispositivos no recíprocos [85–87], amplificación [88, 89], estimación de DoA [90], imágenes [91], computación digital [92], aislamiento [93], formación de lentes [94] o escaneo de haces en frecuencia a frecuencia de entrada fija en LWAs [95], por nombrar solo algunos. Muchas de estas aplicaciones serán muy útiles en 6G [96], destacando la conversión de frecuencia [97–99] y el direccionamiento de haces [100–102] para las futuras comunicaciones D2D. Varios de estos prototipos modulados espaciotemporalmente son capaces de modificar sus propiedades en el tiempo mediante diodos PIN [103–105] o varactores [106, 107] en el rango de mmWave. Además, la rápida mejora de

los sistemas de conmutación ha permitido la fabricación de nuevos prototipos incluso en el rango de los terahercios [108–110].

Con todas estas nuevas posibilidades que permiten los dispositivos modulados en el espacio y en el tiempo, es obligatorio desarrollar herramientas de simulación para comprender el sentido físico y comprobar la respuesta electromagnética de las estructuras diseñadas. Sin embargo, los software comerciales de onda completa clásicos, ampliamente utilizado por los ingenieros de RF, como *CST* [111] o *Ansys HFSS* [112], carecen de modulaciones temporales sin el soporte de herramientas externas [113]. Por lo tanto, hasta donde sabemos, el único software comercial disponible para simular la respuesta electromagnética de sistemas con variación temporal de manera convincente y práctica es *COMSOL* [114]. Sin embargo, presenta las limitaciones inherentes de los simuladores electromagnéticos de propósito general, como baja eficiencia o la complejidad de adaptación a problemas específicos. Además, *COMSOL* es una herramienta poderosa para resolver muchos problemas de física, pero no está específicamente diseñada para ser una herramienta fácil de usar para propósitos de ingeniería como *CST* o *HFSS*. Por estas razones, el desarrollo de métodos numéricos y analíticos para simular sistemas con variaciones en el espacio y en el tiempo se ha convertido en una prioridad.

Por lo tanto, para problemas que requieren conocimiento del comportamiento en el dominio del tiempo de los sistemas, la comunidad suele utilizar técnicas numéricas como FDTD [115–118], MoM [119] o FETD [120], entre otras, para analizar o comparar la respuesta electromagnética de estas estructuras. Debido al alto costo computacional de estos métodos, han surgido varias soluciones para reducir los tiempos de simulación, como el enfoque basado en mallas adaptativas [121]. No obstante, otras alternativas disponibles para simular sistemas variables en el tiempo que se encuentran en la literatura y que proporcionan una visión física de los problemas están basadas en modelos semianalíticos [122–124] o analíticos [125, 126]. La principal diferencia en comparación con los modelos heurísticos es que en estos casos, la topología y los elementos utilizados surgen de la formulación analítica misma, a diferencia de los modelos heurísticos en los que los componentes y la topología son predeterminados por el diseñador.

Para diseñar y simular todos los prototipos referenciados en esta sección, es vital conocer las propiedades electromagnéticas de cada material en la vida real. La extracción de las propiedades intrínsecas de los materiales a partir de la medición de los parámetros de dispersión en un medio circundante conocido es una técnica bien establecida. El método fue introducido en 1970 por Albert F. Nicholson y Glen F. Ross, quienes analizaron la respuesta al impulso de sistemas utilizando el modo TEM en una línea coaxial llena de aire [127]. Examinaron los coeficientes de transmisión y reflexión de una lámina de material colocada dentro del sistema, analizando estos parámetros en el dominio del tiempo. Cuatro años después, William B. Weir

extendió este método a frecuencias de microondas, donde la extracción de los parámetros de dispersión podía realizarse en una guía de ondas o en una línea de transmisión TEM [128]. El método se aplicó directamente en el dominio de la frecuencia utilizando los resultados extraídos del VNA. Desde entonces, se han propuesto muchos sistemas de caracterización de materiales para reducir la incertidumbre en la medición y extraer los parámetros constitutivos de los materiales a frecuencias más altas [129–131]. Además, la necesidad de determinar parámetros constitutivos en el rango de los subterahercios para desarrollar prototipos para futuras comunicaciones ha impulsado la propuesta de varios métodos de banda ancha en la literatura [132–135].

Por lo tanto, esta Tesis tiene como objetivo fundamental contribuir al campo de los dispositivos RF diseñados para las futuras comunicaciones en bandas mmWave. La organización del documento se divide en tres Capítulos:

- Capítulo 1: La Sección 1.1 se centra en la exposición de los principales desafíos encontrados en las generaciones móviles actuales y futuras: 5G y 6G. Además, ofrece una introducción preliminar a las soluciones propuestas en este documento. En las subsecciones siguientes, se consideran aspectos cruciales para la realización de esta Tesis Doctoral. Principalmente, en la Subsección 1.1.1, se presentan las relaciones constitutivas de los materiales lineales e isotrópicos utilizados en esta Tesis. A continuación, la Subsección 1.1.2 destaca la importancia de las condiciones de frontera (espaciotemporales) para resolver problemas electromagnéticos. Posteriormente, la Subsección 1.1.3 introduce brevemente los metamateriales y sus principales aplicaciones en la actualidad. En la Subsección 1.1.4, se discuten las estructuras periódicas y el teorema de Floquet-Bloch. Después, la Subsección 1.1.5 se enfoca en la técnica numérica utilizada para comparar los resultados de sistemas variables en el tiempo. En particular, se discute la implementación del método de diferencias finitas en el dominio del tiempo (FDTD). En la Subsección 1.1.6, se detalla la formulación general del análisis de circuitos propuesto en esta Tesis Doctoral. Finalmente, en la Subsección 1.1.7, se presentan los principales montajes configurados en el laboratorio para las validaciones experimentales.

- Capítulo 2: Publicaciones. Este capítulo se divide en cuatro secciones principales. Las secciones 2.1, 2.2 y 2.3 agrupan los artículos relacionados con la modulación espacial, temporal y espaciotemporal, respectivamente. La sección 2.4 está dedicada a explicar la configuración utilizada para la extracción de los parámetros de dispersión y los métodos aplicados para determinar los parámetros constitutivos de los materiales.

- Capítulo 3: Conclusiones y Trabajo Futuro. La sección 3.1 detalla las

principales observaciones de cada artículo publicado en esta Tesis Doctoral. Finalmente, la sección 3.2 describe posibles direcciones futuras de la línea de investigación para aplicaciones más complejas.

Conclusiones

Las principales conclusiones que se deben destacar de cada trabajo son las siguientes:

- En [J1], se presentó un conjunto lente-antena con simetría rotacional que opera a 60 GHz. El diseño en forma de T de la celda unitaria permite la construcción de la lente en un plano, así como el ajuste de la permitividad relativa, logrando valores más bajos en comparación con la literatura. La validación de la técnica de impresión 3D de bajo costo para la fabricación se confirma ya que los resultados medidos muestran una buena concordancia con las simulaciones. Además, las mediciones demuestran la capacidad de la lente para cambiar el ángulo de apuntado en aplicaciones de direccionamiento de haz con una pérdida de escaneo de 0.18 dB/º.

- En cuanto a [C1], se propone un método de diseño basado en modelos circuitales para crear convertidores de polarización con ultraanchos de banda a través de metasuperficies cortocircuitadas. Aprovechando las simetrías diagonales, se tiene un control independiente de los componentes ortogonales que forman el campo eléctrico, lo que permite ajustar la respuesta del polarizador. Los convertidores de polarización estáticos propuestos muestran un ancho de banda fraccional del 80% y del 55% en incidencia normal. Así, la misma celda unitaria podrá cambiar entre un rotador y un polarizador LP-to-CP, demostrando un potencial de reconfigurabilidad para SatComs en bandas *K/Ka*.

- Con respecto a [J2], se presenta un marco completamente analítico para simular metadispositivos 3D con periodicidad espacial 2D. Analizamos los campos dentro de la metastructura 3D distinguiendo dos regiones clásicas: RWGs y HWGs. El RWG es un guía de ondas clásica formada por cuatro paredes metálicas y el HWG es una guía de ondas metálica cuyas paredes laterales son PMC. Los campos se expresan en términos de un solo modo debido a su régimen de baja frecuencia y la no excitación de modos superiores. En las discontinuidades espaciales entre cada región, aplicamos el enfoque circuital explicado en la Sección 1.1.6 para el caso espacial 2D periódico. Así, pudimos obtener resultados similares de los parámetros de dispersión comparados con el software comercial de onda completa para diferentes configuraciones, incluso para incidencia oblicua. Además, con el objetivo de diseñar

un rotador 3D, estudiamos las condiciones bajo las cuales una SWG puede modelarse como una HWG. Esto nos permitió ajustar el comportamiento resonante de la estructura completa en función del ángulo de polarización y fijar el desplazamiento de fase deseado entre los componentes ortogonales principales del campo eléctrico incidente. Los resultados validan el excelente desempeño del marco teórico en la simulación de metamateriales metálicos periódicos en el régimen de baja frecuencia, donde las regiones de la estructura son monomodales y la periodicidad de las celdas es menor que la longitud de onda, destacando los bajos tiempos computacionales (solo unos pocos segundos) comparado con CST, que puede llevar más de 10 minutos (incluso más para incidencia oblicua).

- En cuanto a [J3], se emplea el método analítico previamente descrito para analizar metasuperficies cargadas con elementos concentrados. Este enfoque facilita la simulación de metasuperficies reconfigurables utilizando modelos equivalentes circuitales de varactores o diodos PIN. Probamos el rendimiento del marco analítico incluyendo cargas RLC en serie y en paralelo y diodos varactores, mostrando resultados precisos y tiempos de simulación más rápidos en comparación con CST, incluso para incidencias oblicuas (hasta 40º). Por lo tanto, este marco teórico revela una alternativa prometedora para simular prototipos avanzados como RIS. Además, podría servir como una excelente solución para simular estructuras espaciotemporales que involucran respuestas variables en el tiempo de los elementos activos concentrados.

- En [J4], se detalla un método analítico basado en líneas de transmisión y expansiones en series de Floquet para metasuperficies metálicas variables en el tiempo. A pesar de la falta de software comerciales para simular estas estructuras, este modelo ofrece una valiosa perspectiva física sobre las capacidades de conversión de frecuencia y direccionamiento de haces de estos novedosos prototipos. Este trabajo revela varias diferencias en comparación con los casos espaciales. Primero, la naturaleza de los modos de orden superior es diferente. En los casos espaciales, suelen ser evanescentes, mientras que en los casos variantes en el tiempo, son propagativos. En segundo lugar, la frecuencia de cada armónico temporal es diferente. Es una propiedad intrínseca del sistema variable en el tiempo que puede ser explotada para la conversión de frecuencia. Además, con el marco teórico, notamos que los armónicos temporales de alto orden solo pueden propagarse dentro de un semiplano cuando la onda incidente incide sobre la metasuperficie en incidencia oblicua. Se destaca que los tiempos de simulación del método analítico propuesto son del orden de solo unos pocos segundos. Además, estos dispositivos ofrecen una solución alternativa

para fuentes pulsadas o formadores de haces, dependiendo del ratio de modulación, en tecnologías de comunicación emergentes como 5G y 6G.

- En [J5], el modelo de circuitos de Floquet anteriormente aplicado al análisis de metasuperficies moduladas en el tiempo se extiende con la inclusión de macroperíodos y ciclos de trabajo. Los macroperíodos permiten la simulación de nuevos casos temporales cuando el ratio entre la frecuencia de la onda incidente y la frecuencia de modulación de la metasuperficie es un número racional. Por otro lado, los ciclos de trabajo rompen la simetría temporal en cada período, modificando el perfil del campo eléctrico temporal en la metasuperficie. Esto excita nuevos armónicos temporales y altera los parámetros de dispersión, como los coeficientes de reflexión y transmisión. Esta expansión de los parámetros temporales en las simulaciones mejora las capacidades de direccionamiento de haz de la metasuperficie variable en el tiempo, ya que se excitan nuevos armónicos propagativos temporales. Así, es posible lograr un patrón de difracción más rico para futuras aplicaciones controlando solo el ratio de modulación y los ciclos de trabajo.

- En relación con [J6], se presenta un análisis profundo de la física de un *metagrating* espaciotemporal. El enfoque teórico detalla la topología circuital de la estructura cuando una onda monocromática incide sobre la metasuperficie variable en el tiempo bajo incidencia TE/TM. Permite conocer la naturaleza evanescente/propagativa de cada armónico espaciotemporal, sus amplitudes y ángulos de difracción. Además, al ajustar los parámetros temporales, es posible controlar los parámetros de dispersión de las metasuperficies, facilitando la formación de haces para transmisión, reflexión o ambos. Estos formadores de haces mejoran el desempeño de direccionamiento para aplicaciones futuras en comparación con las configuraciones anteriores solo en el tiempo, ya que proporcionan la cobertura a través de toda la región espacial. Por otro lado, aprovechando la formulación del modelo, se ha propuesto una metodología para diseñar mezcladores de frecuencia aplicables a comunicaciones mmWave. Además, los tiempos de simulación logrados con el enfoque circuital son significativamente menores en comparación con los obtenidos utilizando la técnica numérica FDTD.

- Finalmente, en [C2], proponemos un método no iterativo y de banda ancha para la caracterización de materiales en espacio libre, cubriendo frecuencias desde 10 GHz hasta 330 GHz. Su principal ventaja radica en su capacidad para proporcionar resultados consistentes independientemente de la posición del material con respecto a los planos de calibración. Así, la invariancia del plano de referencia de este método es particularmente beneficiosa en bandas mmWave, donde in-

cluso variaciones menores en la posición (tan pequeñas como unos pocos milímetros) pueden afectar la precisión de las mediciones. Para extraer con precisión los parámetros de dispersión normalizados, se emplearon técnicas de calibración TRL y GRL. Además, se utilizaron filtros Savitzky-Golay para refinar los resultados finales, demostrando un rendimiento sólido en dieléctricos en el rango de frecuencia especificado. Se espera que este enfoque facilite la extracción de parámetros constitutivos para nuevos y complejos materiales, contribuyendo así a los avances en las futuras tecnologías de comunicación.